

Numerical and Experimental Investigation of Flow in Horizontal Axis Pelton Turbines



Sean Mark Petley

**This dissertation is submitted for the degree of
Doctor of Philosophy**

2018

Engineering Department
in collaboration with
Gilbert Gilkes & Gordon Ltd.

Declaration

The author declares that this thesis has not been previously submitted for award of a higher degree to this or any university, and that the contents, except where otherwise stated, are the author's own work.

Start date: 6th October 2014

Signed:

A handwritten signature in black ink, appearing to read 'J. M. Little', written in a cursive style.

Date: 4th September 2018

Abstract

The Pelton turbine is widely considered a mature technology, existing for more than a century. However, manufacturers concerns over operating efficiency are a key driver in the continued design development. In recent decades, the use of Computational Fluid Dynamics (CFD) has become well established in the field of hydro turbine design, analysis and optimisation. However, the complex flow phenomena within impulse turbines have meant that only recently the simulation of the operation of Pelton turbine injectors and runners has been possible. Modern advances in computer hardware enables larger models to be studied in shorter timescales, despite this the application of CFD to the full Pelton turbine including the casing is still very demanding and as far as the author is aware there are no available studies in the public domain, documenting how Eulerian mesh based CFD solvers can be used for this task.

The main objective of the present thesis is to understand the impact of the casing geometry on the performance of a twin jet Pelton turbine. This objective has been met by employing advanced CFD models, which has been complemented by experimental testing. In parallel these allowed the description and detailed understanding of the flow features within a horizontal axis Pelton turbine casing and the effects the geometry has on this flow and subsequently turbine performance.

The CFD analysis was carried out using the commercial code ANSYS® FLUENT® and included a number of numerical and physical assumptions to simplify the problems, including the usage of symmetry plane and modelling of only six (out of eighteen) consecutive buckets to reduce the size of the computational domain. The investigations can be split into two phases. In the first phase the CFD model was applied to a ‘naked – case’ and examined the impact of the addition of casing inserts such as a jet shroud and bolt on baffle and side shroud which direct the flow away from the injectors and runner, respectively. The second phase examined the variations of the casing width. The CFD models at this stage are only a visual indicative tool and cannot quantitatively predict efficiency as a result of variations in casing geometry, therefore experimental testing has been carried out to complement this work.

Experiments were carried out at the Laboratory of Hydraulic Machines within the National Technical University of Athens (NTUA). The first phase experimental testing has found that the addition of the inserts have an overall effect on efficiency of no more than 0.5%, for single and twin jet operation. Furthermore, some inserts and baffles have a positive impact and some are detrimental. The experimental testing of the second phase revealed that a more considerable reduction of as much as 3% in efficiency is experienced when reducing the casing width by 50% and efficiency reduces linearly with width.

The CFD results of the casing provide a visual assessment of the flow in the casing and a key outcome of the PhD has been learning how to interpret these patterns and then to make decisions on what experiments to carry out. As a second case study, further CFD analysis was applied to an in-house test rig at Lancaster University designed by the author, and based on this work further experimental testing was then carried out.

A second objective of the present thesis was to examine the influence of the injector spear and nozzle angle on the flow behaviour and hydraulic efficiency. The 3D CFD study has shown that injectors with noticeably steeper angles of 110° & 70° and 150° & 90° , respectively, attain a higher efficiency than the industry standard of 80° & 55° . Moreover, experimental testing of the upper jet at NTUA showed gains of $\approx 1\%$ in efficiency at the best efficiency point of the turbine can be achieved, however there appears to be an upper limit beyond which steeper designs are no longer optimal. Further insight was provided by carrying out additional simulations whereby the 3D velocity profiles obtained from the injector simulations are applied as an inlet boundary condition to a runner simulation and then examining the impact the jet shape has on the runner torque profile during the bucket cycle and the influence this had on turbine efficiency. It can be concluded that the secondary velocities, which contribute to the development of more significant free-surface degradations as the spear and nozzle angles are increased, result in a non-optimal jet runner interaction.

Further investigations were carried out in order to compare the absolute difference between the numerical runner efficiency and the experimental efficiency. In doing so, the various losses that occur during operation of the turbine can be appraised and a prediction of casing losses can be made. Firstly, the mechanical losses of the test rig are estimated to determine the experimental hydraulic efficiency. Following this the numerical efficiency of the runner can then be ascertained by considering the upstream pipework losses and the aforementioned runner simulations, which are combined with the 3D velocity profiles from the injectors. The results indicate that out of all of the experimental cases tested, in the best case scenario the casing losses can be approximated to be negligible and in the worst case scenario $\approx 3\%$.

Keywords

Renewable Energy, Hydropower, Impulse turbines, Pelton turbines, Computational Fluid Dynamics, Experimental Testing

Dedication

I would like to dedicate this research to the memory of my uncle and grandpa,

Lewis George Banks

1956 - 2015

Peter Baldwin Banks

1927 - 2015

Acknowledgements

*“As you set out for Ithaka
hope your road is a long one,
full of adventure, full of discovery.
Laistrygonians, Cyclops,
angry Poseidon - don't be afraid of them:
you'll never find things like that on your way
as long as you keep your thoughts raised high”*

‘Ithaka’, Constantine P. Cavafy, 1911.

This PhD has been a fascinating and truly worthwhile experience. It began as a self-deluding fantasy and ended as self-suffering lesson in humility. I would like to express my heartfelt thanks to those who have supported me along the way.

First and foremost, I would like to thank my supervisor Professor George Aggidis. From my very first week as an undergraduate in the Engineering Department at Lancaster you have been my mentor and encouraged me throughout my studies. I have greatly benefited from your wealth of experience.

My gratitude goes to Gilbert Gilkes & Gordon Ltd ¹ for sponsoring this research. I would specifically like to thank Jonathan Martin, Alan Robinson, Dr Jo Scott and Anthony Watson for providing their valuable insight. I would also like to thank Sam Clegg and Yiannis Kassanos for their support during the experimental testing.

My appreciation goes to my fellow labmates and friends Dr Shaun Benzon, Dr Nilla Karlsen-Davies and Simeon Doyle for putting up with my futile jokes. Έπειτα, θα ήθελα να ευχαριστήσω θερμά George Mousmoulis for hosting me in Athens and our interesting deliberations on Greek life!

I am most obliged to Dr Audrius Zidonis who in many ways paved the way for this research. I would also like to thank Dr Alexandros Panagiotopoulos and Professor John Anagnostopoulos and Professor Dimitris Papantonis for their guidance during the collaborative work at the Laboratory for Hydraulic Machines, National Technical University of Athens.

It goes without saying that I am indebted to my colleagues in the Engineering Department - academic staff; Dr Stephen Quayle and Dr Sergio Campobasso, whose pertinent questions have brought different perspectives to this research, and technicians; Jono Gates, Nick Renninson and Mark Salisbury.

Finally, I would like to express my love and thanks to Mum, Dad and my sister, Daisy.

¹ Referred to herein as ‘Gilkes’

List of Journal Publications

- **S. Petley**, A. Panagiotopoulos, D. S. Benzon, A. Židonis, G.A. Aggidis, J. S. Anagnostopoulos, D. E. Papantonis, “Out with the old, in with the new: Pelton hydro turbine performance influence utilising three different injector geometries” *ASME J. Fluids Eng*, vol. 141, no. 8, p. 081103, 2019

Under review:

- **S. Petley**, G.A. Aggidis, “Numerical and Experimental investigation of flow in Pelton turbine casings” – submitted to International Journal of Fluid Machinery and Systems

Also published by the author during the period of study:

- **S. Petley**, G.A. Aggidis, “Swansea Bay tidal lagoon annual energy estimation”, *Ocean Engineering*, vol. 111, pp. 348-257, 2016

List of Conference Publications

- **S. Petley**, G. A. Aggidis, “Transient CFD and experimental analysis for improved Pelton turbine casing designs” Proceedings of the 29th IAHR Symposium on Hydraulic Machinery and Systems, Kyoto, September 2018
- **S. Petley**, A. Panagiotopoulos, D. S. Benzon, A. Židonis, G.A. Aggidis, J. S. Anagnostopoulos, D. E. Papantonis, “Investigating the influence of the jet from three nozzle and spear design configurations on Pelton runner performance by numerical simulation.” Proceedings of the 29th IAHR Symposium on Hydraulic Machinery and Systems, Kyoto, September 2018
- A. Židonis, D. S. Benzon, A. Panagiotopoulos, **S. Petley**, G.A. Aggidis, J.S. Anagnostopoulos, D.E. Papantonis, “Experimental investigation and analysis of the spear valve design on the performance of Pelton turbines: 3 case studies” Proceedings of Hydro 2017, Seville, October 2017
- D. S. Benzon, A. Židonis, A. Panagiotopoulos, **S. Petley**, G.A. Aggidis, J.S. Anagnostopoulos, D.E. Papantonis, “Experimental investigation and analysis of three spear valve designs on the performance of Turgo impulse turbines” Proceedings of Hydro 2017, Seville, October 2017

Also published by the author during the period of study:

- G. Amato, S. Doyle, **S. Petley**, M.S. Campobasso, I.A. Milne, G.A. Aggidis, “Navier-Stokes CFD Analysis of a Tidal Turbine Rotor in Steady and Planar Oscillatory Flow” Proceedings of EWTEC 2017, Cork, August 2017

Contribution to Knowledge

The main contributions of the thesis are as follows:

1. CFD analysis of flow within Pelton turbine casings

Although some studies have recently started to utilise CFD in the analysis and optimisation of Pelton turbines, no mesh-based models have been able to successfully model the flow inside the casing. This research presents for the first time the flow development within the casing and provides an indicative visual assessment of the impact of different casing geometries on Pelton turbine performance.

.....

2. Experimental investigation of Pelton turbine casing design parameters

Since no historical experimental testing records were available the independent assessment provided in this thesis was a necessary learning outcome. The experimental testing has found that the efficiency of the Pelton turbine is strongly dependent on the geometry of the casing and in particular there appears to be a linear trend of decreasing width and efficiency, however beyond an upper limit the casing effect may be negligible.

.....

3. Influence of the injector spear and nozzle angle combination on jet – runner interaction in Pelton turbines

The numerical analysis of the injectors carried out during the course of this research presents for the first time the effects of much steeper nozzle and spear angles, than those presented in previous literature, on the hydraulic performance of the Pelton turbine. Overall steeper designs are shown to be more efficient in the 3D CFD simulations; however experimentally there appears to be an upper limit beyond which steeper designs are no longer optimal. Further numerical analysis of the runner, which has been coupled with the jet profile from the aforementioned injectors, indicates that the secondary velocities, which contribute to the development of more significant free-surface degradations as the spear and nozzle angles are increased result in a non-optimal jet runner interaction.

.....

Table of Contents

Declaration.....	i
Abstract.....	ii
Keywords	iii
Dedication	iv
Acknowledgements.....	v
List of Journal Publications.....	vi
List of Conference Publications.....	vi
Contribution to Knowledge.....	vii
List of Figures	xiii
List of Tables	xxi
Nomenclature.....	xxiii
Mathematical Notation.....	xxv
List of Acronyms	xxvi
1 Introduction.....	1
1.1 Hydropower	1
1.2 Background and Motivation.....	4
1.3 Aims of the Research	5
1.4 Structure of the Thesis	6
2 Background and Review of Previous Work.....	8
2.1 Invention and Early Development	8
2.2 Hydraulic Components of a Pelton Turbine Facility	9
2.3 Turbine Characteristics	10
2.3.1 Euler’s Turbomachinery Equation	11
2.3.2 Lancaster University Pelton Test Rig	14
2.4 Physical Flow Quantities and Equations.....	22
2.5 Multiphase Flows.....	26
2.5.1 Centrifugal Atomisation.....	26
2.5.2 Liquid Jet Disintegration.....	28

2.6	Literature Related to Pelton Turbine Development	30
2.6.1	Injector Research.....	30
2.6.2	Runner Optimisation	36
2.6.3	Casing Design	42
2.7	Computational Fluid Dynamics	48
2.7.1	A Note on the ANSYS® FLUENT® Solver	50
2.7.2	Fundamental Governing Equations.....	51
2.7.3	Implementation of Eulerian CFD solvers	52
2.7.4	Multiphase Modelling	60
2.8	Summary of Literature	63
3	Development of the Pelton Casing CFD Model	65
3.1	Choice of Solver.....	65
3.2	Simulation Setup.....	65
3.2.1	Domain Creation	65
3.2.2	Domain Meshing.....	69
3.2.3	Physics Definitions	74
3.2.4	Post Processing	79
3.2.5	Simulation Sequence.....	80
3.3	CFD Modelling Assumptions and Simplifications	84
3.3.1	Geometric Assumptions	84
3.3.2	Modelling Assumptions	90
3.4	Model Verification.....	95
3.4.1	Timestep Independence Study	95
3.4.2	Mesh Independence Study	97
3.4.3	Mesh Effects on Casing Flow	100
3.4.4	Estimating Efficiency Loss due to Casing	105
3.5	Correlating CFD Post Processing with Experiments	106
3.5.1	Visual Comparison of Results.....	106
3.6	Summary of Pelton turbine casing CFD Modelling.....	110
4	CFD Analysis of Pelton Casing Designs	112

4.1	Phase 1 - Pelton Shroud and Baffle Testing.....	114
4.1.1	The Naked Case	114
4.1.2	The Role of the Bolt on Baffle	129
4.1.3	The Role of the Side Shroud	133
4.2	Phase 2 – Analysis of Pelton Casing Width.....	137
4.2.1	Further Analysis of the Flow Sequence within the Casing – Upper Jet.....	138
4.3	Summary of CFD analysis of Pelton Casing Design	142
5	Experimental Testing of Pelton Turbine Casings	143
5.1	Phase 1 - Pelton Shroud and Baffle Testing.....	143
5.1.1	Technical Program	143
5.1.2	Program of Tests	144
5.1.3	Characteristic Equations	145
5.1.4	Test Points.....	146
5.1.5	Test Procedure.....	146
5.1.6	Normalised Efficiency	147
5.1.7	Uncertainty Analysis.....	148
5.1.8	Phase 1 Test Results Analysis and Discussion.....	149
5.2	Phase 1 Comparison with CFD.....	159
5.2.1	Flow Visualisation	160
5.2.2	The Naked Case – Test A.....	161
5.2.3	The Role of the Bolt on Baffle	164
5.2.4	The Role of the Side Shroud	166
5.2.5	Summary of Phase 1 testing	168
5.3	Phase 2 - Pelton Width Testing.....	168
5.3.1	Technical Program	168
5.3.2	Program of Tests	168
5.3.3	Phase 2 Results Analysis and Discussion	171
5.3.4	Summary of Phase 2 testing	176
5.4	Summary of Experimental Testing	176
6	Analysis of Flow through the Injectors.....	178

6.1	Numerical Investigation.....	178
6.1.1	2D Axisymmetric Analysis & Optimisation.....	178
6.1.2	3D Analysis.....	180
6.2	Experimental Investigation	186
6.2.1	Methodology	187
6.3	Experimental Test Results	191
6.4	Numerical and Experimental Comparison.....	193
6.4.1	Secondary Velocities in the Jet	194
6.4.2	Further Numerical Investigation of the Jet – Runner Interaction.....	200
6.5	Conclusions of Injector Research.....	211
7	Comparison of CFD and Experimental Results.....	213
7.1	Loss Analysis of a Typical Experiment	213
7.1.1	Mechanical Loss Estimation, η_M	213
7.1.2	Pelton Turbine System Modelling	220
7.2	Total Efficiency Analysis.....	223
7.3	Limitations of the CFD modelling	224
7.4	Summary of CFD and Experimental Comparison	226
8	Secondary Investigation of Casing Design	227
8.1	Lancaster University Test Rig.....	227
8.2	Proposed Tests	227
8.3	Results of Experimental Tests.....	234
8.4	Visual Documentation of Results	235
8.4.1	Analysis of Test #1	236
8.4.2	Analysis of Test #5	241
8.4.3	Analysis of Test #8	245
8.5	Summary of testing at Lancaster University	248
9	Summary and Conclusions.....	250
10	Recommendations for Future Work.....	253
10.1	Turbulence Modelling and Injector Simulations.....	253
10.2	Further Analysis of the Jet – Runner Interaction	253

10.3	Casing Simulations	254
10.4	Further Experimental Testing of Casing Widths	254
10.5	Nozzle and Spear Combinations and Jet Locations	254
	References.....	256

List of Figures

Fig. 1-1 Lester Pelton Patent Application no. 233,692	2
Fig. 1-2 Gilkes twin jet horizontal axis Pelton turbine	3
Fig. 1-3 Gilkes vertical axis Pelton turbine.....	3
Fig. 1-4 Typical application range for impulse and reaction turbines [7]	4
Fig. 2-1 Simple water wheel [16].....	8
Fig. 2-2 Schematised view of a Pelton turbine	9
Fig. 2-3 Bucket geometry [18]	10
Fig. 2-4 Pelton Turbine Velocity Triangles [20].....	12
Fig. 2-5 Gilkes Jubilee 9.5” runner	14
Fig. 2-6 Lancaster University Pelton test rig	15
Fig. 2-7 CAD of 9.5” Jubilee Pelton bucket showing the guide curves.....	16
Fig. 2-8 Velocity triangles drawn at the respective guide curve positions and velocity components: U (green), C_2 (red), and W_2 (black)	17
Fig. 2-9 Velocity streamlines through a stationary bucket using CFD [23]	18
Fig. 2-10 Illustrations of the flow in a Pelton bucket at selected relative angular positions of the runner [26]	18
Fig. 2-11 Bucket relative position during the jet cut in and cut out process	19
Fig. 2-12 Schematic of flow inside a Pelton bucket [27]	19
Fig. 2-13 Diagram showing absolute velocities W relative to bucket position during duty cycle	20
Fig. 2-14 Velocity triangles for different operating speeds	21
Fig. 2-15 Comparing flow patterns from the Lancaster Pelton test rig at different operating speeds.....	22
Fig. 2-16 Horizontal Axis Pelton Turbines at two scales.....	22
Fig. 2-17 Powerspout Pelton wheel in operation [29].....	25
Fig. 2-18 Atomisation modes of rotating discs [32]	27
Fig. 2-19 Atomisation modes for rotating cups [34].....	28
Fig. 2-20 Appearance of jet at $x/D = 104$ for air velocity a) 116 ft/s d) 4.8 ft/s water flow at 90 ft/s	30
Fig. 2-21 Axial velocities in the jet for an injector connected to a straight pipe [45].....	32
Fig. 2-22 Support for the LDA optics, (a) a traversing system to access jet flow from all possible position and (b) Plexiglas system to ensure laser was able to transmit through jet surface [45]	33
Fig. 2-23 Secondary flow due to the elbow in supply pipe [48]	34
Fig. 2-24 Representation of the surface jet [49].....	34
Fig. 2-25 Jet needle tip and nozzle seat ring modifications for jet quality improvements [43]35	35

Fig. 2-26 Flow visualisation with stationary buckets, front view (left) and side view (right) [53]	36
Fig. 2-27 Pressure sensor locations on inner and backside of bucket [26]	37
Fig. 2-28 Computational domain and boundary conditions applied [26]	38
Fig. 2-29 Computational mesh (A), field pressure effects (B) and phase distribution (C) [62]	39
Fig. 2-30 Comparison of the calculated air-water phase by the simulations on a coarse mesh (A) and fine mesh (B) [62]	40
Fig. 2-31 Comparison of torque variation exerted on a bucket for different timestep size [62]	40
Fig. 2-32 Horizontal axis Pelton turbine components [70]	43
Fig. 2-33 Details of the rectangular casing from [71]	44
Fig. 2-34 Splash water distribution at the wall of the rectangular casing [71]	44
Fig. 2-35 Cylindrical dome [71]	45
Fig. 2-36 Rectangular dome [71]	45
Fig. 2-37 Gilkes twin jet horizontal axis Pelton turbine [73]	46
Fig. 2-38 Free surface flow in a Pelton casing obtained by a SPH-ALE software of Andritz Hydro [79] (n.b. no velocity scale available in the paper)	47
Fig. 2-39 Free surface flow in a Pelton casing obtained by a SPH-ALE software of Andritz Hydro [77] (n.b. no velocity scale available in the paper)	48
Fig. 2-40 Numerical Fluid Flow calculation techniques [81]	50
Fig. 2-41 Overview of the iterative solution method	53
Fig. 2-42 Discretisation of the solution domain [84]	54
Fig. 2-43 Two typical cells with descriptive parameters in the FVM discretisation [84]	54
Fig. 2-44 A schematic representation of a portion of a fluid-fluid interface and related methods used to model its shape and motion. (a) Interface between two fluids. Interface tracking methods such as (b) the interface-fitted moving mesh method, and (c) the front tracking method. Interface capturing methods such as (d) the marker-and-cell method, (e) the volume-of-fluid method, and (f) the level-set method [94]	62
Fig. 3-1 CAD geometry of Gilkes twin jet horizontal axis Pelton indicating symmetry plane	66
Fig. 3-2 Gilkes Z120 runner type buckets	67
Fig. 3-3 Rotating fluid domain	67
Fig. 3-4 Stationary casing domain fluid region highlighting the location of the half cylinder representing the water jet	68
Fig. 3-5 Computational fluid model geometry	69
Fig. 3-6 Runner domain surface mesh details	70
Fig. 3-7 Detailed view of runner domain mesh	71

Fig. 3-8 Casing domain surface mesh details (tetrahedral mesh in yellow, swept hexahedral mesh in blue).....	72
Fig. 3-9 Detailed view of casing domain surface mesh	73
Fig. 3-10 Geometry indicating simulation boundary conditions for stationary casing domain	76
Fig. 3-11 Geometry indicating simulation boundary conditions for rotating runner domain ..	77
Fig. 3-12 Water volume fraction plot showing non-continuous liquid region.....	78
Fig. 3-13 Moment monitor wall zone definition – inside (orange) and outside (blue)	79
Fig. 3-14 Bucket duty cycle	80
Fig. 3-15 Jet initialisation process.....	81
Fig. 3-16 Jet feeding process – shown for 60°	82
Fig. 3-17 Entire separation of the jet process – shown for 70°	82
Fig. 3-18 Last stage of inflow process – shown for 90°	83
Fig. 3-19 Last stage of outflow process – shown for 130°	83
Fig. 3-20 Casing flow – shown for 200°	84
Fig. 3-21 External stroboscopic flow visualisation of water sheets from individual buckets [26]	86
Fig. 3-22 Torque curves for inside and outside of first bucket for different bucket number simulations	87
Fig. 3-23 Torque curves for inside and outside of the penultimate bucket for different bucket number simulations	88
Fig. 3-24 Water Volume Fraction 1% comparison at 360° Front View, clockwise from top left; a) 2-bucket, b) 4-bucket, c) 6-bucket and d) 18-bucket	89
Fig. 3-25 Water Volume Fraction 1% comparison at 360° Rear View, clockwise from top left; a) 2-bucket, b) 4-bucket, c) 6-bucket and d) 18-bucket	89
Fig. 3-26 Torque curves comparison of 2-bucket runner simulation with different turbulence models.....	91
Fig. 3-27 Comparing Volume Fraction for Compressive (left) and HRIC (right) through the jet	92
Fig. 3-28 Comparing Volume Fraction for Compressive (left) and HRIC (right) from a rear view at 360°	93
Fig. 3-29 Comparing 1% Water Volume Fraction for First-Order (left) and Second-Order (right)	94
Fig. 3-30 Torque curves comparison for First-Order and Second-Order time (or temporal) discretisation	94
Fig. 3-31 Torque curves comparison for varying timestep	96
Fig. 3-32 Mesh refinement study results: normalised efficiency against normalised grid spacing	98

Fig. 3-33 Mesh refinement study torque curves.....	99
Fig. 3-34 Volume fraction interface at the free surface for coarse, medium and fine meshes. Red indicated volume fraction within the rotating domain and blue in the stationary casing domain	102
Fig. 3-35 Comparing 1% water volume fraction plot at 240° rotation for coarse (blue), medium (red), fine (green) and extra fine (yellow) grids.....	103
Fig. 3-36 Comparing 1% water volume fraction plot at 360° rotation for coarse (blue), medium (red), fine (green) and extra fine (yellow) grids.....	104
Fig. 3-37 Impact of the water sheet on the roof of the casing with coarse (blue), medium (red), fine (green) and extra fine (yellow) grids (snapshot at 200° rotation)	105
Fig. 3-38 Comparing the torque curves for bucket 1 and 2 during four rotations.....	106
Fig. 3-39 Flow sequence of water leaving the bucket.....	107
Fig. 3-40 Upper Jet Experimental and 1% water VF plot comparison for 6-bucket coarse mesh at 200°, 360°, 560° rotations at BEP of 946 rpm	108
Fig. 3-41 Upper Jet Experimental and 1% water VF plot comparison for 6-bucket coarse mesh at 200°, 360°, 560° rotations at 847 rpm.....	109
Fig. 3-42 Upper Jet Experimental and 1% water VF plot comparison for 6-bucket coarse mesh at 200°, 360°, 560° rotations at 1040 rpm.....	110
Fig. 4-1 Gilkes twin jet horizontal axis Pelton turbine	112
Fig. 4-2 CAD of internal view of the Gilkes Pelton turbine with baffle plates.....	113
Fig. 4-3 Internal view of the Gilkes Pelton turbine with baffle plates	113
Fig. 4-4 The Naked Case.....	114
Fig. 4-5 Upper jet: casing flow for 100° rotation	115
Fig. 4-6 Upper jet: casing flow at 200° rotation.....	116
Fig. 4-7 Velocity triangle at maximum torque point from centre of bucket for axial and radial views U (green), C_2 (red), and W_2 (black) adapted from [107]	117
Fig. 4-8 Upper jet: casing flow at 240° rotation.....	117
Fig. 4-9 Upper jet: casing flow at 280° rotation.....	118
Fig. 4-10 Upper jet: casing flow at 320° rotation.....	118
Fig. 4-11 Upper jet: casing flow at 360° rotation.....	119
Fig. 4-12 Upper jet: wall contour plots of water volume fraction for 240° to 400° rotation showing evolution of flow along the casing walls.....	121
Fig. 4-13 Upper jet: casing flow at 400° rotation.....	122
Fig. 4-14 Upper jet: casing flow at 440° rotation.....	122
Fig. 4-15 Velocity vectors showing casing flow at 440° rotation.....	123
Fig. 4-16 Upper jet: casing flow at 480° rotation.....	123
Fig. 4-17 Lower jet: casing flow for 100° rotation	124

Fig. 4-18 Lower jet: casing flow at 240° rotation	125
Fig. 4-19 Lower jet: casing flow at 360° rotation	125
Fig. 4-20 Lower jet: wall contour plots of water volume fraction for 240° to 560° showing evolution of flow along the casing walls	128
Fig. 4-21 The Bolt on Baffle in-situ within the casing	129
Fig. 4-22 Lower jet with the BAF and SP: casing flow at 100° rotation	131
Fig. 4-23 Lower jet with the BAF and SP: casing flow at 200° rotation	131
Fig. 4-24 Lower jet with the BAF and SP: casing flow at 280° rotation	132
Fig. 4-25 Lower jet with the BAF and SP: casing flow at 360° rotation	132
Fig. 4-26 The Side Shroud in-situ within the casing.....	133
Fig. 4-27 Older casing design from the original Ganz drawing showing domed lower housing	134
Fig. 4-28 Upper jet with the SS: casing flow at 360° rotation	134
Fig. 4-29 Upper jet with the SS: volume fraction contour plot at 360° rotation.....	135
Fig. 4-30 Upper jet with the SS: casing flow at 400° rotation	135
Fig. 4-31 Upper jet with the SS: casing flow at 440° rotation	136
Fig. 4-32 Upper jet with the SS: casing flow at 480° rotation	136
Fig. 4-33 Velocity vector comparison between SS and naked case at 360° rotation.....	137
Fig. 4-34 Reduced width upper jet: casing flow at 240° rotation	138
Fig. 4-35 Velocity vectors for 240 mm casing at 240° rotation.....	138
Fig. 4-36 Reduced width upper jet: casing flow at 280° rotation	139
Fig. 4-37 Reduced width upper jet: casing flow at 360° rotation	139
Fig. 4-38 Velocity vectors at 360° rotation comparing casing width (black arrows indicating relative width).....	140
Fig. 4-39 Upper jet: wall contour plots for 240° to 440° rotation for 240 mm casing width.	141
Fig. 5-1 Pelton testing facility at NTUA.....	144
Fig. 5-2 Test points under consideration with BEP indicated as the red diamond.....	146
Fig. 5-3 Test E upper jet Q_{IIk} plotted against efficiency for constant unit speeds.....	150
Fig. 5-4 Test E lower jet Q_{IIk} plotted against efficiency for constant unit speeds.....	151
Fig. 5-5 Test E twin jet Q_{IIk} plotted against efficiency for constant unit speeds.....	151
Fig. 5-6 Experimental test results A – H at the BEP for twin jet operation.....	152
Fig. 5-7 Experimental test results A – H at the BEP for lower jet operation.....	153
Fig. 5-8 Experimental test results A – H at the BEP for upper jet operation.....	154
Fig. 5-9 Experimental test results A – H at the BEP for upper jet operation BEP error bars	155
Fig. 5-10 Experimental test results A – H at $n_{II} = 39$ for upper jet operation	156
Fig. 5-11 Experimental test results A – H at $n_{II} = 39$ for lower jet operation	157
Fig. 5-12 Experimental test results A – H at $n_{II} = 39$ for twin jet operation	157

Fig. 5-13 Location of pressure transducers in the NTUA test rig	159
Fig. 5-14 Snapshots of experimental operation at BEP for upper, lower and twin jet measurements.....	160
Fig. 5-15 CFD velocity vectors upper jet.....	161
Fig. 5-16 Experimental flow visualisation upper jet.....	162
Fig. 5-17 CFD velocity vectors lower jet.....	162
Fig. 5-18 Experimental flow visualisation lower jet.....	163
Fig. 5-19 Comparison of velocity vectors for upper and lower injector in the naked case....	164
Fig. 5-20 Comparison of experimental results for upper and lower injector with and without the BAF and SP.....	165
Fig. 5-21 Lower jet with BAF and SP	165
Fig. 5-22 Comparing snapshots taken during experimental testing of D (left) and E (right)	166
Fig. 5-23 Comparing CFD and experiment with the BAF and SP for lower jet operation....	166
Fig. 5-24 Experimental photograph of test F at BEP for upper jet operation	167
Fig. 5-25 Experimental photograph of test F at BEP for lower jet operation	167
Fig. 5-26 Test rig with components assembled for 240 mm width testing	170
Fig. 5-27 Test points under consideration with BEP indicated as the red diamond	170
Fig. 5-28 Experimental Test J upper jet operation.....	171
Fig. 5-29 Experimental Test J lower jet operation.....	172
Fig. 5-30 Experimental Test J twin jet operation.....	172
Fig. 5-31 Experimental results comparing casing widths at $n_{11} = 39$ for upper jet operation	173
Fig. 5-32 Experimental results comparing casing widths at $n_{11} = 39$ for lower jet operation	174
Fig. 5-33 Experimental results comparing casing widths at $n_{11} = 39$ for twin jet operation..	174
Fig. 5-34 Effect of changing casing width on efficiency at the BEP	175
Fig. 6-1 Two dimensional injector geometry showing fixed and variable operational and geometric parameters [98]	179
Fig. 6-2 Injector Loss contours for Nozzle and Spear Angles at $Q = 20$ kg/s (left) and 40kg/s (right) [96].....	180
Fig. 6-3 3D injector simulation showing the planes used in the analysis	182
Fig. 6-4 3D mesh for Standard injector design showing spear and nozzle around the exit ...	183
Fig. 6-5 3D Injector losses at different planes from nozzle exit	184
Fig. 6-6 Fluid power from conversion of static to dynamic pressure components for the three designs.....	185
Fig. 6-7 Static pressure contours for Standard and Novel 2 designs.....	186
Fig. 6-8 Dynamic pressure contours for Standard and Novel 2 designs.	186
Fig. 6-9 Pelton spears used for experimental tests.....	187
Fig. 6-10 Pelton nozzles used for experimental testing	187

Fig. 6-11 Gilkes twin jet Pelton test rig in operation at NTUA	188
Fig. 6-12 Pelton injector test plan	190
Fig. 6-13 Pelton injector flow curves comparison	191
Fig. 6-14 Pelton efficiency curves for 80/55, 110/70 and 150/90 injectors at $n_{II}=37$	192
Fig. 6-15 Pelton efficiency curves for 80/55, 110/70 and 150/90 injectors at $n_{II}=39$	192
Fig. 6-16 Pelton efficiency curves for 80/55, 110/70 and 150/90 injectors at $n_{II}=41$	193
Fig. 6-17 Pelton efficiency curves for 80/55, 110/70 and 150/90 injectors at $n_{II}=43$	193
Fig. 6-18 Vector plot of secondary velocities in the flow before the guide vanes for the Standard jet	195
Fig. 6-19 Vector plot of secondary velocities in the flow after the guide vanes for the Standard jet	195
Fig. 6-20 Comparing the secondary velocity vectors at different planes from nozzle exit....	196
Fig. 6-21 Experimental observation of upper jet detachment	197
Fig. 6-22 Vertical velocity profile comparison for Standard and Novel injector designs at plane $z/D = 1$	198
Fig. 6-23 Vertical velocity profile comparison for Standard and Novel injector designs at plane $z/D = 4$	198
Fig. 6-24 Comparing the 3D vertical, 3D horizontal and 2D axisymmetric axial velocity profiles for the Standard injector design at plane $z/D = 2$	199
Fig. 6-25 3D injector simulation showing the plane used in the analysis.....	202
Fig. 6-26 3D runner simulation showing the corresponding plane used in the analysis.....	202
Fig. 6-27 Moment monitor wall zone definition – inside (orange) and outside (blue)	202
Fig. 6-28 Mesh refinement study results (2): efficiency with respect to grid spacing	203
Fig. 6-29 Torque curves on the inside and outside of the bucket for 4 configurations	205
Fig. 6-30 Pressure coefficient distribution on the inside surface of bucket 1 at 80° rotation for two configurations	205
Fig. 6-31 Comparison of the CFD and experimentally obtained efficiency for the 3 real cases normalised to the ideal case	206
Fig. 6-32 Volume Fraction (free-surface) and vertical velocity vectors for Standard design	207
Fig. 6-33 Volume Fraction (free-surface) and vertical velocity vectors for Novel 1 design .	208
Fig. 6-34 Volume Fraction (free-surface) and vertical velocity vectors for Novel 2 design .	209
Fig. 6-35 Plane (red) indicating where remaining kinetic energy of the jet is calculated.....	210
Fig. 6-36 Three contour plots showing the jet remaining after interaction with the first bucket, coloured by kinetic energy	210
Fig. 7-1 Frictional torque vs rotational speed when $Q = 0 \text{ m}^3/\text{s}$	215
Fig. 7-2 Friction torque measurements with hub only [18]	215
Fig. 7-3 Loads on the runner [113]	216

Fig. 7-4 Pelton test rig bearing arrangement.....	217
Fig. 7-5 Bending moment diagram for showing radial loads on bearings	217
Fig. 7-6 SKF Bearing calculator tool, showing input values for BEP operation at 20°C	219
Fig. 7-7 The effect of temperature on bearing friction torque	219
Fig. 7-8 Pelton test rig loss features and straight pipe sections for 1.....	221
Fig. 7-9 Corrosion on the inside of L2 pipework.....	222
Fig. 7-10 Torque curves comparison of 6-bucket runner simulation with different turbulence models.....	225
Fig. 8-1 Side Shroud in construction in the Z120 test rig	228
Fig. 8-2 Twin jet testing results across a range of rotational speeds at 20 m head	234
Fig. 8-3 Lower jet testing results across a range of rotational speeds at 20 m head	234
Fig. 8-4 Upper jet testing results across a range of rotational speeds at 20 m head.....	235
Fig. 8-5 Lancaster Test rig locations.....	236
Fig. 8-6 Test #1 lower jet $n_{11} = 35$ rpm.....	237
Fig. 8-7 Test #1 lower jet $n_{11} = 39$ rpm.....	238
Fig. 8-8 Test #1 lower jet $n_{11} = 43$ rpm.....	238
Fig. 8-9 Droplets on casing roof	239
Fig. 8-10 Test #1 upper jet $n_{11} = 35$ rpm.....	239
Fig. 8-11 Test #1 Upper jet $n_{11} = 39$ rpm.....	240
Fig. 8-12 Test #1 Upper jet $n_{11} = 43$ rpm.....	240
Fig. 8-13 Comparing upper jet operation for test #1 with two different casing widths	241
Fig. 8-14 Lancaster test # 5 lower jet: casing flow at 240° rotation	242
Fig. 8-15 Lancaster test # 5 lower jet: casing flow at 320° rotation	242
Fig. 8-16 Lancaster test # 5 lower jet: casing flow at 440° rotation	243
Fig. 8-17 Test # 5 lower jet operation $n_{11} = 39$	244
Fig. 8-18 Comparing experimental and CFD snapshots for test #5 with lower jet.....	245
Fig. 8-19 Lancaster test # 8 upper jet: casing flow at 280° rotation	245
Fig. 8-20 Lancaster test # 8 upper jet: casing flow at 360° rotation	246
Fig. 8-21 Comparison of test #8 with standard case at 360° rotation	246
Fig. 8-22 Lancaster test # 8 upper jet: casing flow at 520° rotation	247
Fig. 8-23 Four photographs taken during test # 8 with upper jet showing flow progression.	248

List of Tables

Table 2-1 Outflow angle and velocity components for various guide curves.....	16
Table 2-2 Characteristic quantities of a Pelton turbine at two different scales.....	23
Table 2-3 Fluid Properties.....	24
Table 2-4 Characteristic scales of the flow in a Pelton turbine model.....	24
Table 2-5 Transition criteria of breakup regimes for rotating discs.....	27
Table 2-6 Housing dimensions according to Nechleba, Quartz and Raabe for horizontal axis Pelton turbines	42
Table 3-1 320 mm PCD Pelton BEP operating conditions used in analysis.....	75
Table 3-2 ANSYS material properties	75
Table 3-3 Simulation stationary and rotating domain boundary conditions	76
Table 3-4 Mesh sizing and normalised efficiency for different bucket number simulations...	90
Table 3-5 Timesteps chosen for study	95
Table 3-6 Average torque and efficiencies for changing timestep.....	96
Table 3-7 Mesh refinement study results normalised to coarse grid.....	97
Table 3-8 Mesh refinement study: Grid Conversion Indexes	99
Table 3-9 Known relative numerical error band introduced by various assumptions.....	111
Table 5-1 Program of experimental tests carried out indicating components used.....	145
Table 5-2 Spear position and associated flow rates	147
Table 5-3 Systematic error of each instrument	148
Table 5-4 Normalised control points used for uncertainty analysis.....	149
Table 5-5 Test efficiencies.....	156
Table 5-6 Pressure sensor readings test E twin jet operation.....	159
Table 5-7 Experimental width testing program indicating components	169
Table 5-8 Spear position and associated flow rates	171
Table 5-9 Percentage decrease in efficiency across test cases	175
Table 6-1 Details of the injector configurations	180
Table 6-2 Units used in the equation (6.2)	181
Table 6-3 Details of the boundary conditions for injector simulations.....	182
Table 6-4 Details of injector spear travel.....	183
Table 6-5 Systematic error of each instrument	189
Table 6-6 Pelton injector geometric details	190
Table 6-7 Details of the boundary conditions for runner simulations.....	201
Table 6-8 Mesh refinement study (2) results normalised to coarse grid.....	203
Table 6-9 Mesh refinement study (2): Grid Conversion Indexes.....	204
Table 6-10 Normalised efficiencies for the 4 case studies.....	206
Table 6-11 Kinetic energy remaining in the jet after the first cut-in process.....	210

Table 7-1 Bearing forces for single and twin jet operation.....	218
Table 7-2 Bearing friction torques and losses approximated from the SKF bearing calculator	220
Table 7-3 Head loss from loss features	222

Nomenclature

a	Acceleration	[m/s ²]
A	Nozzle opening diameter	[mm]
A_i	Cell area cross section	[m ²]
B	Bucket outer width	[mm]
B_c	Casing width	[mm]
\mathbf{C}	Absolute velocity vector	[m/s]
d_o	Jet diameter	[mm]
D	Runner pitch circle diameter	[mm]
D_s	Nozzle opening diameter	[mm]
E	Specific hydraulic energy	[m ² /s ²]
f	Fanning friction factor	[-]
F	Force	[N]
\mathbf{F}	External body forces vector	[N]
\mathbf{F}_J	Jet loading force	[N]
F_R	Total radial force acting on runner	[N]
g	Acceleration due to gravity	[m/s ²]
\mathbf{g}	Acceleration due to gravity vector	[m/s ²]
G	Injector opening diameter	[mm]
H	Hydraulic head	[m]
h_l	Individual head loss for hydraulic component	[m]
k	Turbulence Kinetic Energy	[m ² /s ²]
K	Loss factor	[-]
L_{ref}	Injector losses at a reference plane	[-]
m	Mass	[kg]
\dot{m}	Mass flow rate	[kg/s]
m_r	Runner mass	[kg]
M	Torque	[Nm]
M_B	Bearing friction torque	[Nm]
M_D	Disk friction torque	[Nm]
M_f	Friction torque of full runner in rotation	[Nm]
M_J	Torque induced by a single jet	[Nm]
M_M	Mechanical friction torque	[Nm]
M_s	Friction torque of only shaft in rotation	[Nm]
M	Measured torque	[Nm]
n	Rotational speed	[rpm]
n_{11}	Unit speed	[rpm]
N_j	Number of jets	[-]
p	Pressure	[Pa]
p_c	Order of convergence	[-]
p_i	Static pressure at individual mesh cell	[Pa]
P	Power	[W]
P_{in}	Power in	[W]
P_{out}	Power out	[W]
P_{ref}	Injector power at a reference plane	[W]
\mathbf{q}	Heat flux	[W/m ²]
Q	Flow rate	[m ³ /s]
Q_{11k}	Unit flow rate based on bucket width, B	[m ³ /s]
r	Streamline radius	[m]
r	Refinement Ratio	[-]

R_{B1}	Load on bearing 1	[N]
R_{B2}	Load on bearing 2	[N]
\mathbf{R}_{u1}	Resultant bearing force due to upper jet operation	[N]
\mathbf{R}_{u2}	Resultant bearing force due to twin jet operation	[N]
\mathbf{S}	Face area vector	[m ²]
s	Spear travel	[mm]
s_r	Random uncertainty at 95% confidence (Student's T distribution)	[-]
s_γ	Random uncertainty standard deviation	[-]
S_f	Safety Factor	[-]
t	Time for 1 revolution	[s]
t	Student's T factor	[-]
\mathbf{U}	Circumferential or bucket velocity vector	[m/s]
U	Jet velocity	[m/s]
U_{ideal}	Ideal jet velocity	[m/s]
u_i	Velocity of fluid at individual mesh cell	[m/s]
\mathbf{V}	Velocity vector	[m/s]
\mathbf{W}	Relative velocity vector	[m/s]
W	Work done	[J]
W_r	Force acting on runner from runner mass	[N]
Y^+	Dimensionless wall distance	[-]
β_2	Bucket outlet angle	[deg]
Δt	Timestep	[s]
δ	Percentage error	[%]
δ_M	Torque meter systematic error	[%]
δ_n	Speed sensor systematic error	[%]
δ_p	Pressure transducer systematic error	[%]
δ_Q	Flow meter systematic error	[%]
δ_r	Total random uncertainty in efficiency η	[%]
δ_s	Total systematic uncertainty in efficiency η	[%]
δ_t	Total uncertainty in efficiency η	[%]
ε	Turbulence eddy dissipation rate	[m ² /s ³]
η	Normalised Efficiency	[%]
η_0	Measured efficiency	[%]
η_{eh}	Total experimental hydraulic efficiency	[%]
$\eta_{h=0}$	Efficiency at zero grid spacing	[%]
η_C	Casing efficiency	[%]
η_M	Mechanical efficiency	[%]
η_N	Nozzle efficiency	[%]
η_P	Pipeline efficiency	[%]
η_R	Runner efficiency	[%]
η_{nh}	Total numerical hydraulic efficiency	[%]
θ	Rotated angle	[deg]
μ	Dynamic viscosity	[Pa.s]
ρ	Density	[kg/m ³]
σ	Surface tension coefficient	[N/m]
τ_{ij}	Reynolds stress tensor	[N/m ²]
τ_f	Torque experienced on fluid	[Nm]
τ_r	Torque experienced on a blade row	[Nm]
ω	Rotational frequency	[rad/s]
ω	Turbulence eddy frequency	[s ⁻¹]
ν	Kinematic viscosity	[m ² /s]

$\overline{u'_i u'_j}$	Reynolds stresses	[N/m ²]
------------------------	-------------------	---------------------

Mathematical Notation

∇	Del operator
∇^2	Laplacian operator
Φ	Tensor quantity
δ_{ij}	Kronecker delta function

List of Acronyms

BEP	Best Efficiency Point
CAD	Computer Aided Design
CFD	Computational Fluid Dynamics
CPU	Central Processing Unit
DES	Detached Eddy Simulation
DNS	Direct Numerical Simulation
DOE	Design of Experiments
ECL	Ecole Centrale de Lyon
EPFL	Ecole Polytechnique Fédérale de Lausanne
FVM	Finite Volume Method
GCI	Grid Convergence Index
HPC	High Performance Computing
HRIC	High Resolution Interface Capturing
LDA	Laser Doppler Anemometry
LES	Large Eddy Simulation
NTUA	National Technical University of Athens
PCD	Pitch Circle Diameter
PIV	Particle Image Velocimetry
RANS	Reynolds Averaged Navier Stokes Equation
RMS	Root Mean Squared
RSS	Root Sum Square
SIMPLE	Semi-Implicit Method for Pressure Linked Equations
SLR	Single Lens Reflex
SPH	Smoothed Particle Hydrodynamics
SRS	Scale Resolving Simulation
SST	Shear Stress Transport
URANS	Unsteady Reynolds Averaged Navier Stokes Equation
VOF	Volume of Fluid

1 Introduction

The world is currently moving towards renewable energy sources. This growth is driven by the twin challenges of energy security and regulatory policies to combat the ever growing concern posed by climate change, namely renewable energy targets such as the European Union Renewables directive, which aims to have 20% of the EU energy needs met by renewables in 2020 and most recently the Paris Agreement on Climate Change [1]. Hydropower is very promising as it delivers predictable energy and unlike other renewables such as wind and solar provides the necessary inertia required to maintain a stable energy grid. Hydropower is progressively becoming a prominent facet within the global supply of electricity. The World Bank reports that globally, hydropower is responsible for reducing annual emissions of CO₂ by some 2.8 billion tons and as of 2016 it represents 16.6% of the world's total electricity production while contributing 80% of the global renewable electricity mix [2]. In addition to eliminating carbon dioxide emissions and providing sustainable green energy contributing towards legal targets hydropower offers a unique benefit in responding to the needs of developing economies in the area of water security, as well as offering irrigation and flood management services.

1.1 Hydropower

Wherever there is water at an elevation higher than the nearest water course there is potential for hydropower generation. The available hydraulic energy is proportional to the sum of variations in potential energy and pressure energy between upstream and downstream basins.

Hydropower can be generated from a variety of sources, namely: rivers with run-of-river schemes, where the capacity is typically small (less than 20 MW [3]) and reservoirs where water is impounded by a dam and the turbines are typically large in capacity. The Itaipu hydroelectric plant on the Parana River, which consists of 20 x 700 MW Francis turbines, set a new world record in annual energy production of 103.09 million MWh in 2016 [4].

There are a number of different hydropower turbines, which can be categorised into two types: reaction turbines and impulse turbines.

Reaction turbines, such as the Francis and Kaplan, are usually completely submerged in fluid and utilise the pressure variations across rotating hydrofoil blades to extract the energy from the fluid.

Impulse turbines generate power by converting potential energy available from the pressure difference in water levels upstream and downstream into kinetic energy by discharging water into atmospheric pressure to act on the runner. The water jet hits each bucket, causing the runner

to rotate. To obtain optimal efficiency engineers have focussed on improving the design of the injector to enhance jet quality and the shape of the bucket to acquire optimal transfer of energy to the shaft [5].

One such impulse turbine, the Pelton turbine, was invented by Lester Pelton in 1880 [6], Fig. 1-1 is an illustration taken from the original patent application. Pelton turbines can be divided into two sub-categories: horizontal axis, which are suitable for at most three injectors² and vertical axis machines, which can be designed with up to six injectors, depicted respectively in Fig. 1-2 and Fig. 1-3. Henceforth, the work in this thesis and any reference to Pelton can be assumed to mean two jet horizontal axis machines only unless stated otherwise.

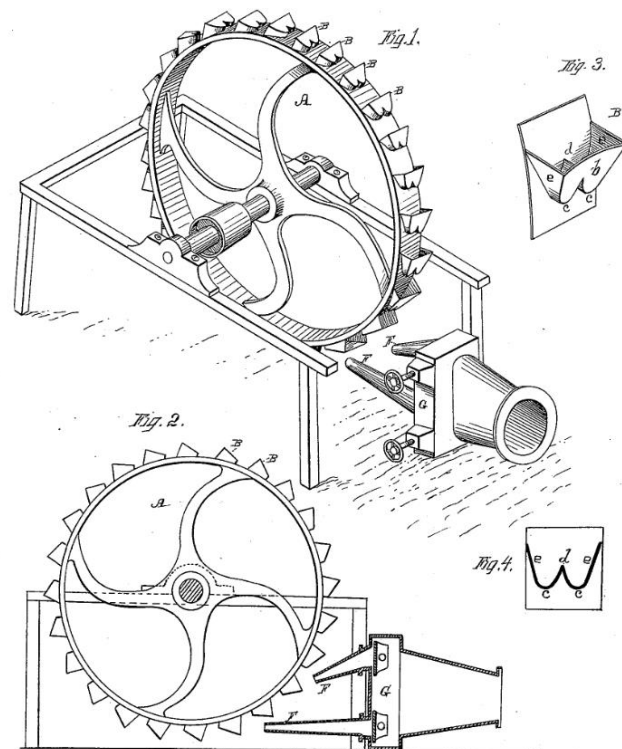


Fig. 1-1 Lester Pelton Patent Application no. 233,692

² This is true to a certain extent and historically has been the norm; however, in 2014 former Voith engineer Josef Erlach presented a design for a six jet horizontal axis Pelton, which he claims reduces costs by reducing the size of the runner and generator, casing and building requirements [99].

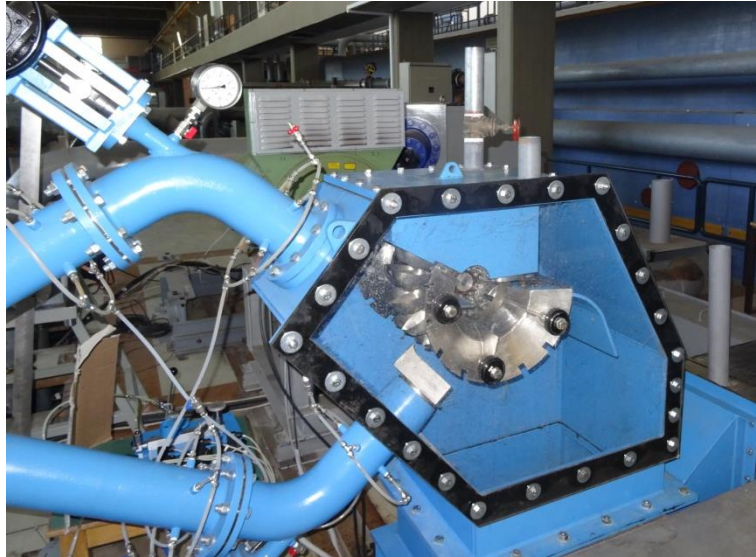


Fig. 1-2 Gilkes twin jet horizontal axis Pelton turbine



Fig. 1-3 Gilkes vertical axis Pelton turbine

The Pelton turbine is suitable for use in hydropower plants with high heads and operates efficiently over a wide range of flow rates, as shown in application range diagram in Fig. 1-4.

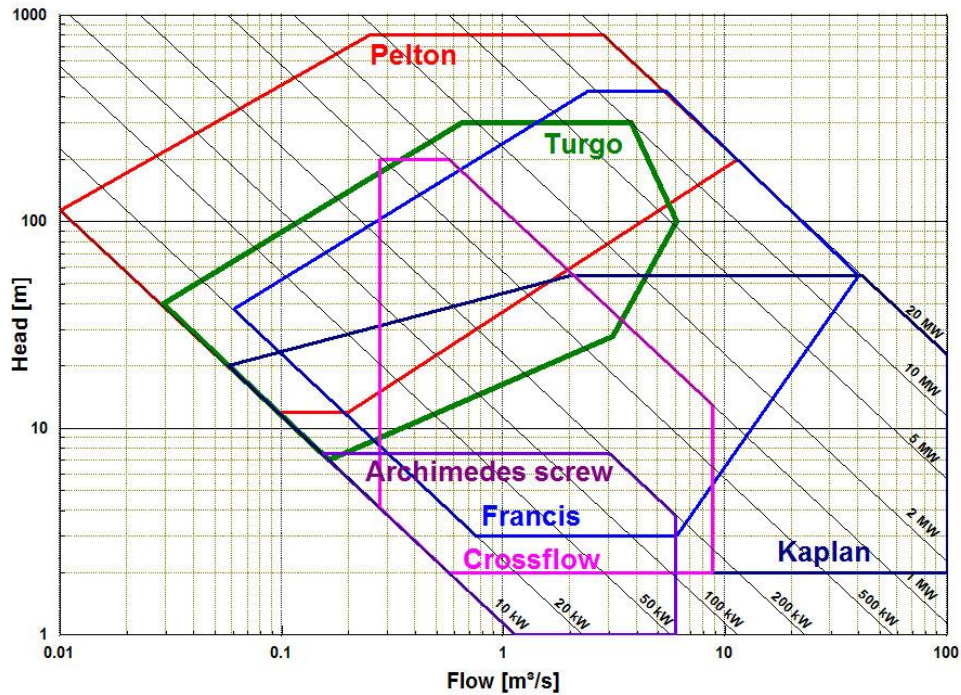


Fig. 1-4 Typical application range for impulse and reaction turbines [7]

1.2 Background and Motivation

The Pelton turbine remains one of the most efficient impulse turbines. Yet, despite its ubiquity, considerable effort continues to improve these machines to remain competitive in a market dominated by increasing concerns over energy production efficiency and mechanical reliability, and where new tools for analysis and optimisation are available.

For most of its existence it was developed based on theoretical or empirical guidance that was either limited by various assumptions or required extensive experimental testing, a very complex task in itself [8], that includes large costs and very long time scales. However, recent publications show a rapidly increasing use of numerical modelling known as Computational Fluid Dynamics (CFD) to better understand the details of the complex unsteady flow in the runner and the whole Pelton turbine [9], leading to significant design improvements.

However, the progress for Pelton turbines has remained behind other turbomachines due to the level of modelling complexity required [10]. Specifically, unsteady, multiphase, free surface flow in the jet-runner interaction and local flow separations in the bucket cut-out region and back-side flow, is difficult to simulate and predict accurately.

Furthermore the pipework and injector play an important role for jet quality, where the efficiency increase is clearly correlated with less disturbances seen on the jet surface and less jet dispersion is very important for efficiency of the whole system [11]. Likewise, the efficiency

of a turbine is affected by the bucket shape, which has already improved significantly since the original Pelton design [12] [13] [14] .

Moreover, the water leaving the buckets plays an important role. After exiting from the buckets the flow impacts and travels around the casing walls, some of which may cause interference with the runner and water jet, reducing the efficiency.

The design of the casing as a means to reduce this impact is therefore of interest to manufactures [15]. Despite this overarching purpose, there is no standard design guidelines and casing styles vary from manufacturer to manufacturer.

The cost of hydropower plant construction is very high resulting in the need to maximise energy production. Therefore, improving the turbine performance, even if it small, results in a significant improvement in the p/kWh investment. Moreover, the construction cost of the casing is significant and therefore efforts to reduce the overall size of the casing, while maintaining good efficiency and profits, is a primary concern of the project sponsors.

1.3 Aims of the Research

The aim of the present thesis was to better understand the flow in a horizontal axis twin jet Pelton turbine. More specifically the thesis focusses on the flow in the casing and aims to provide an overview of the design of Pelton turbine casings and the factors most important to maintaining high efficiency over a range of operating conditions. A secondary aim was to analyse the impact the injector nozzle and spear angle configuration have on Pelton turbine efficiency.

To achieve these aims the following objectives were set:

1. To develop a CFD model for studying the flow within the Pelton turbine casing;
2. To predict the effect that different casing geometries have on the flow and the subsequent interference with the runner and water jet and the impact on turbine efficiency using the CFD model;
3. To develop a CFD model for studying the flow through the injectors with different nozzle and spear angles;
4. To analyse the influence the different nozzle and spear angles have on the jet velocity profile, development of secondary flow structures and jet-runner interaction using the CFD model;
5. To verify these analyses with measurements obtained from a model Pelton experimental test rig;

6. To quantify the casing energy loss by comparison of the results obtained with the CFD models and experimental testing.

1.4 Structure of the Thesis

In Chapter 1, the motivation for research, a brief description of hydropower and the aims and objectives of the research are described.

In Chapter 2, a presentation of the background to the thesis is offered. Firstly a general description of the design of Pelton turbines and important equations is given. This is followed by an outline of the current state of research on Pelton turbines. Finally, an overview of the various modelling techniques applicable to Pelton turbines, more specifically a detailed description of the pertinent aspects of ANSYS FLUENT 17.2, the software used for the current study, is presented.

In Chapter 3, the development of the CFD model used for the present study is elaborated upon and the first set of results is presented. The effect of a number of different modelling assumptions on turbine performance has been examined and validated through mesh and temporal independency studies. Finally, in order to confirm the model effectiveness, results are compared to photographs obtained from an established test rig.

In Chapter 4, the CFD model is applied to the Gilkes Z120 Pelton design, more specifically the tool is applied to the casing design in two phases. The first phase considered the addition of casing inserts (baffles and shrouds), which direct the flow away from principle components and the second phase examined the variations of the casing width. In both phases the influence on the flow field and comments on the impact this will have on efficiency are provided.

In Chapter 5, the experimental performance testing of the Gilkes Z120 Pelton is presented, the testing procedure, uncertainties and performance curves are also provided. Firstly, the internal baffles and shrouds are tested with a systematic approach reflecting the models described in Chapter 4. Following this is a comparison between the qualitative flow predictions obtained from the CFD and the quantitative experimental data. A similar approach is then adopted for the second phase, which investigates a number of casing widths.

In Chapter 6, the Pelton turbine injectors, which have been optimised previously using a 2D-axisymmetric CFD simulation, were further investigated by examining a 3D model that included the branch pipe and guide vanes. This model was taken further by importing the jet profiles created into a runner simulation. An outline of the anticipated losses is presented.

In Chapter 7, the mechanical losses of the test rig are estimated by operating the turbine with the full runner, without the buckets and without the hub at zero flow to determine the disc friction torque. Combining with the injector losses from Chapter 6 an estimation of the casing losses can be ascertained.

In Chapter 8, the Lancaster University Pelton test rig is used as a second case study to establish the means to demonstrate the versatility of the CFD model and make similar predications of the effects of casing geometry, which can be verified by flow visualisations and experimental testing.

In Chapter 9, a summary of the research and conclusions are presented and finally Chapter 10 provides a list of recommendations for future work.

2 Background and Review of Previous Work

This chapter provides an overview of the published literature related to the state of the art in the field of interest. It gives a description of the history and components of the Pelton turbine. To follow, a summary of the more recent developments work carried in the optimisation of the principle components 1) injectors and 2) runner. Finally, specific literature related to Pelton turbine casing designs are presented.

2.1 Invention and Early Development

The invention of the Pelton turbine (or Pelton wheel as it was first known) originated through Lester Pelton's observations of water wheels being used by miners in the gold fields of California during the gold rush of the mid-19th century. These primitive devices were generally constructed of wood and consisted of triangular blocks arranged between a pair of circular casings, such that the inner edge resembled that of a saw blade, shown in Fig. 2-1. Water was then directed at the 'teeth' via an often square duct.

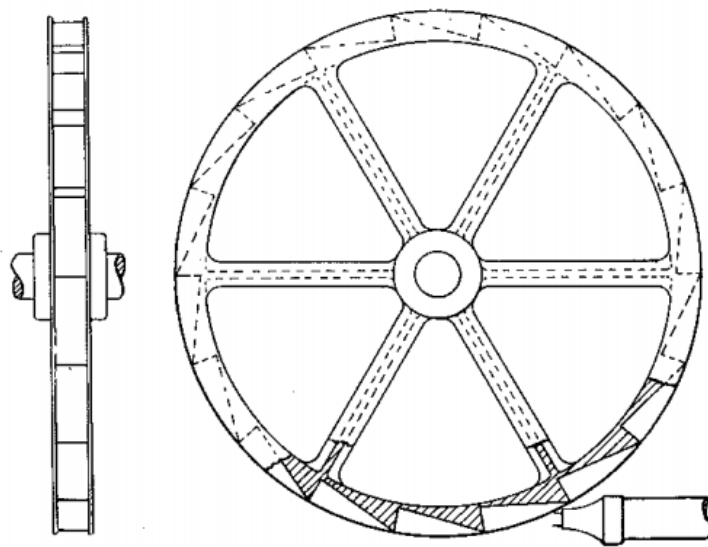


Fig. 2-1 Simple water wheel [16]

The efficiency of these devices were no more than 40%, the major fault being that due to the flat surfaced buckets closed in on both sides the water from the jet could not drain freely. Lester Pelton is credited as one of the first inventors to develop buckets that exhibited the jet splitting wedge that divides the water stream, which then follows the curve of the bucket passage, finally sweeping upwards and discharging the stream of the water jet out of the bucket. Pelton was awarded his patent in 1880 and since then many companies have independently carried out work to improve the efficiency of the turbine.

2.2 Hydraulic Components of a Pelton Turbine Facility

The modern Pelton turbine, shown in Fig. 2-2 is a hydraulic impulse machine, which extracts the energy from the water in two stages, firstly the available hydraulic head provides kinetic energy at the outlet of the nozzle, and the purpose of the spear is that it can move in and out to regulate the flow. As the water leaves the nozzle it strikes the bucket splitter, shown in Fig. 2-3, dividing the jet into two equal parts, which are deflected in accordance with the contours of the bucket. During this action the velocity of the jet is significantly decreased as the water jet's momentum is transferred to the runner as torque, which causes the runner to rotate. The transfer of the total energy from the nozzle exit into the casing occurs at atmospheric pressure, thus the mechanical energy transferred to the shaft comes from the impulse forces of the flow alone [17].

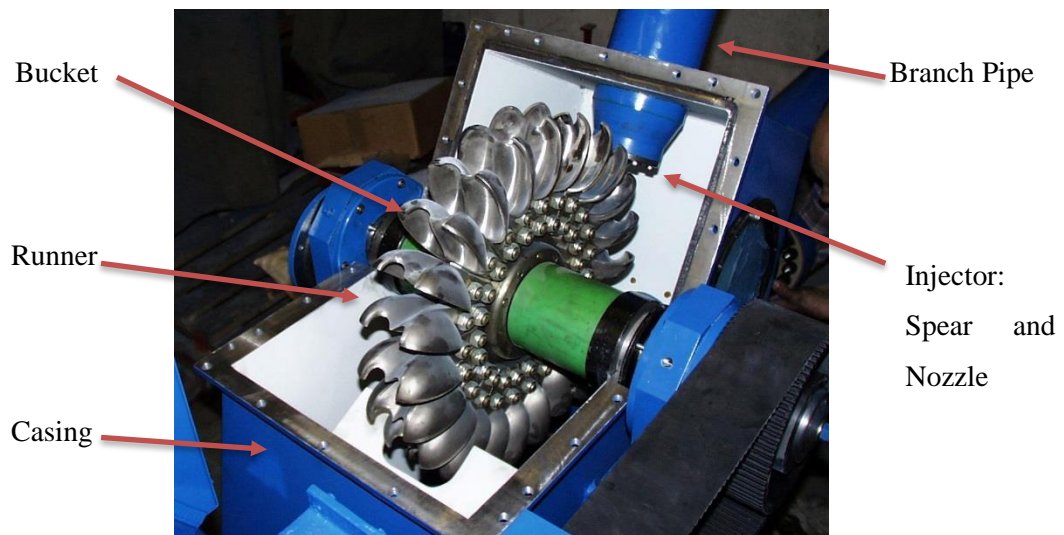


Fig. 2-2 Schematised view of a Pelton turbine

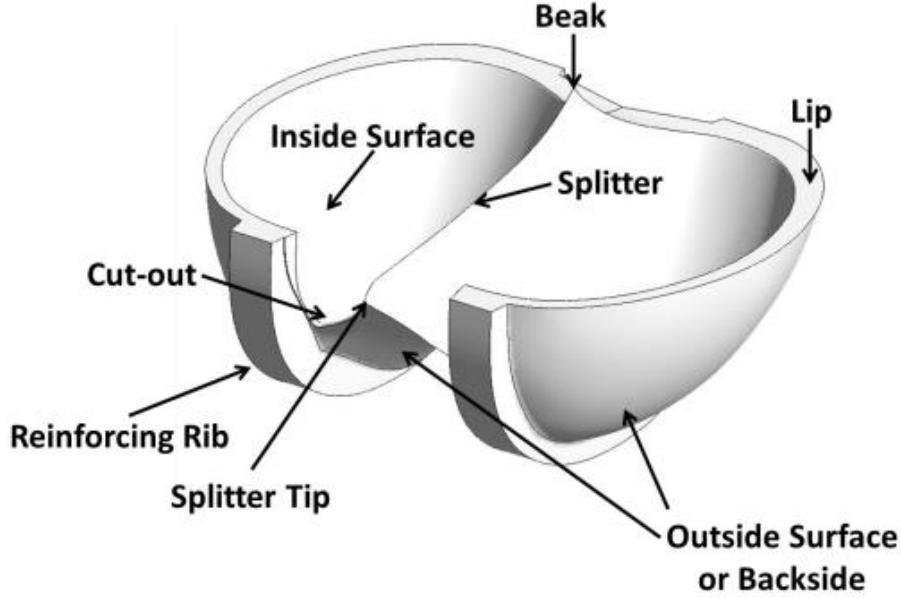


Fig. 2-3 Bucket geometry [18]

2.3 Turbine Characteristics

The following equations provide some basic definitions of hydraulic turbine coefficients in order to ensure a better understanding of this work;

The measure of the available potential energy is known as the hydraulic net head H [m]. The specific hydraulic energy, E , is calculated from the net head and the acceleration due to gravity g [m/s²].

$$E = g \cdot H \quad (2.1)$$

The available hydraulic power, P_h , can be calculated from the specific hydraulic energy, the density of the fluid, ρ [kg/m³] and the flow rate, Q [m³/s].

$$P_h = E \cdot (\rho \cdot Q) \quad (2.2)$$

In the field of turbomachinery a diverse array of dimensionless numbers are used in order to compare different turbines or to transfer model measurements to prototype size and to quantify the flow parameters. These dimensionless numbers can then, with the help of hydraulic similarity laws, be used to scale runners or compare one turbine against another. The specific speed, n_q , is the speed of a geometrically similar machine with a flow rate of $Q = 1$ [m³/s] and a hydraulic net head $H = 1$ [m] and is defined as follows [19]:

$$n_q = n \frac{\sqrt{Q}}{H^{0.75}} \quad (2.3)$$

Here the unit for the runner speed, n , is [1/s] and as such the resulting unit for n_q is [$\text{m}^{0.75} \text{s}^{1.5}$], which is complex and will therefore be avoided, Zhang [20] suggests normalising the values for Q and H . However, equation (2.4) for quasi-dimensionless unit speed, n_{11} and (2.5) for quasi-dimensionless unit flow rate, q_{11k} , which are used to establish the performance diagram, or hill chart [21], will be considered herein.

$$n = n_{11} \frac{\sqrt{H}}{D} \quad (2.4)$$

$$Q = q_{11k} B^2 \sqrt{H} \quad (2.5)$$

Where D [m], is the pitch circle diameter of the runner, and B [m], is the maximum bucket width.

2.3.1 Euler's Turbomachinery Equation

The impulse action, described in section 2.2 can be further explained by considering Euler's Turbomachinery equation. During operation the path of a water particle through a turbine sees it deviate from its initial direction resulting in a momentum change, which in turn induces a pressure on the blade surface causing the turbine shaft to rotate. Newton's Second Law can be applied to rotating systems to derive the Law of Moment of Momentum (2.6) [22].

$$\tau = \frac{d}{dt} (mr\mathbf{C}_u) \quad (2.6)$$

Here, $r\mathbf{C}_u$ is the specific angular momentum and $mr\mathbf{C}_u$ is the angular momentum. Because of the conservation of mass, it can be implied that the torque acting on the fluid in the streamtube is:

$$\tau_f = \dot{m}(r_2\mathbf{C}_{2u} - r_1\mathbf{C}_{1u}) \quad (2.7)$$

Where $\mathbf{C}_{2,1u}$ and $r_{2,1}$ is the circumferential flow velocity component and streamline radius at outlet (subscript 2) and inlet (subscript 1) stations and \dot{m} is the mass flow rate [kg s^{-1}]. The overall torque acting on the blades of the row is therefore:

$$\tau_r = -\tau_f = \dot{m}(r_1\mathbf{C}_{1u} - r_2\mathbf{C}_{2u}) \quad (2.8)$$

The produced mechanical power, P [W] of the turbine rotating at angular velocity, ω [rad s^{-1}] can be evaluated as (2.9), where it is known from convention that the circumferential velocity at the mean radius of station 1,2 is $\mathbf{U}_{1,2} = r_{1,2}\omega$

$$P = \tau_r \omega = \dot{m}(r_1\mathbf{C}_{1u} - r_2\mathbf{C}_{2u})\omega = \dot{m}(\mathbf{U}_1\mathbf{C}_{1u} - \mathbf{U}_2\mathbf{C}_{2u}) \quad (2.9)$$

Therefore Euler's Turbomachinery equation is the specific hydraulic energy, E [m^2/s^2]:

$$E = \frac{P}{\dot{m}} = (\mathbf{U}_1 \mathbf{C}_{1u} - \mathbf{U}_2 \mathbf{C}_{2u}) \quad (2.10)$$

2.3.1.1 Velocity Triangles Approach

Velocity triangles are used to represent the various velocity components of the working fluid and can be applied to the bucket of a Pelton turbine. Velocity triangles are drawn for the inlet (subscript 1) and outlet stations (subscript 2), shown schematically in Fig. 2-4.

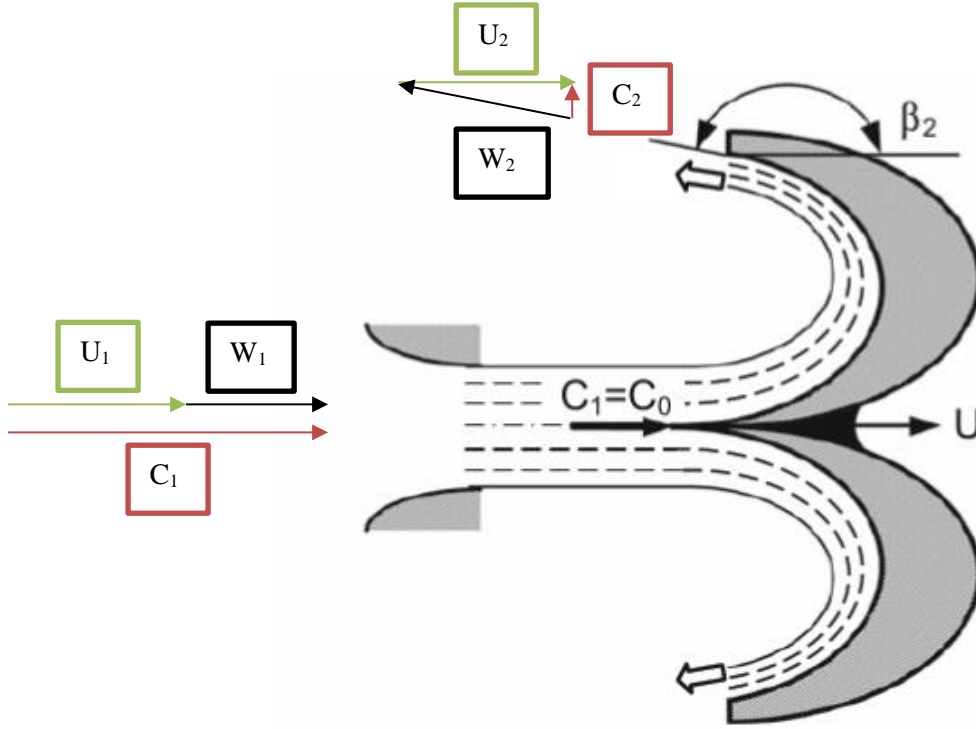


Fig. 2-4 Pelton Turbine Velocity Triangles [20]

From the inlet conditions, it can be ascertained that the absolute velocity \mathbf{C} is the sum of the relative velocity, \mathbf{W} and bucket velocity, \mathbf{U} . At the inlet of the bucket, the absolute velocity \mathbf{C}_1 and the entrainment velocity \mathbf{U} have the same direction and orientation, therefore the tangential component \mathbf{C}_{1u} is therefore equal in direction and magnitude to \mathbf{C}_1 .

The Euler equation (2.10) states that the kinetic energy available in the jet is entirely converted when the tangential component \mathbf{C}_{2u} of the outflow velocity is zero, this implies that \mathbf{W}_2 is equal in magnitude but opposite in direction to \mathbf{U} .

In practice, $\mathbf{W}_2 < \mathbf{W}_1$ due to the viscous losses associated with the fluid viscosity and friction generated when it interacts with solid surfaces, therefore one can introduce the loss factor $k_w = \mathbf{W}_2 / \mathbf{W}_1$, consequently the work per unit mass becomes:

$$E = \mathbf{U}(\mathbf{C}_1 - \mathbf{U})(1 - k_w \cos(\beta_2)) \quad (2.11)$$

To determine the optimal runner speed, set dE/dU to zero, this yields (2.12)

$$\begin{aligned} \frac{dE}{dU} &= \frac{d}{dU} (\mathbf{U}(\mathbf{C}_1 - \mathbf{U})(1 - k_w \cos(\beta_2))) = 0 \\ &\rightarrow \mathbf{C}_1 - 2\mathbf{U} = 0 \\ &\rightarrow \frac{\mathbf{U}}{\mathbf{C}_1} = 0.5 \end{aligned} \quad (2.12)$$

Indicating that the optimal runner speed is half the jet speed and that the angle $\beta_2 = 180^\circ$. This is of course practically impossible because it would imply that the water leaving the bucket strikes the underside of the following bucket, therefore designers will choose a smaller angle of β_2 to ensure the most efficient operation without causing flow interference.

Accordingly, the tangential component \mathbf{C}_{2u} of the outflow velocity is a function of the outflow angle β_2 :

$$\mathbf{C}_{2u} = \mathbf{U} + \mathbf{W}_2 \cos(\beta_2) \quad (2.13)$$

Therefore, the hydraulic efficiency can be evaluated as:

$$\begin{aligned} \eta_R &= \frac{\text{transferred energy}}{\text{theoretical available energy } (\beta_2 = 180)} = \frac{2E}{\mathbf{C}_1^2} \\ &= 2 \frac{\mathbf{U}}{\mathbf{C}_1} \left(1 - \frac{\mathbf{U}}{\mathbf{C}_1}\right) (1 - k_w \cos(\beta_2)) \end{aligned} \quad (2.14)$$

Furthermore, the efficiency of the turbine is the product of the hydraulic efficiency, pipeline efficiency (2.15), nozzle efficiency (2.16), where a head loss results due to viscous dissipation, mechanical efficiency, η_M which is a result of mechanical friction and also losses due to the casing, η_C .

The pipeline efficiency is found from the pipeline head loss h_p , with head H available between upstream basin and nozzle entry:

$$\eta_P = \frac{H - h_p}{H} = \frac{H_T}{H} \quad (2.15)$$

Nozzle head loss h_N , where discharge coefficient ϕ is defined as:

$$\eta_N = \phi^2 \text{ where } \phi = \frac{\mathbf{C}_1}{\mathbf{C}_{1,th}} \quad (2.16)$$

Where the theoretical jet velocity $\mathbf{C}_{1,th}$ can be calculated using Toricelli's law, defined as (2.17).

$$C_{1,th} = \sqrt{2gH_T} \quad (2.17)$$

Therefore, the overall efficiency of this turbine will be the product of the individual efficiency components.

2.3.2 Lancaster University Pelton Test Rig

During the PhD study a Pelton test rig was designed and established by the author within the Engineering Department at Lancaster University. The purpose of this test rig was to enable greater observation of the flow in the casing during operation than is normally possible, since very few examples of this exist in the published literature it was critical in the first instance to obtain an understanding of to what extent the casing influences the flow.

The runner was an existing 18-bucket “Jubilee design” supplied by Gilkes, with a pitch circle diameter of 9.5” (which corresponds to 241 mm) and cast from Aluminium bronze with a bucket width of 71 mm, shown in Fig. 2-5.



Fig. 2-5 Gilkes Jubilee 9.5” runner

The casing, designed by the author, was deliberately oversized, with respect to the runner and jet dimensions. Three of the walls are built from Perspex to allow for a greater area from which visual data could be obtained.

The test rig, as shown in Fig. 2-6, consists of a small fibreglass tank of 1.18 m³ volume, measuring 1.25 x 0.97 x 0.97 m. This is fed by a Sewabloc K 050-251 pump, which is controlled by a Hitachi L-300p variable speed drive. The pump supplies water to the nozzles via flexible

reinforced EPDM pipework, which can be regulated by two ball valves. Unlike a typical Pelton turbine, the nozzles are fixed and there is no spear or spear rod to regulate the flow, therefore only a single flow rate is obtainable from the set operating pressure.



Fig. 2-6 Lancaster University Pelton test rig

2.3.2.1 Calculating the Casing Flow from the Bucket Geometry and Velocity Triangles

Initial analysis of the flow in the Pelton turbine casing can be considered on a 1-D basis, by investigating the influence of bucket shape on the flow. In 2.3.1.1 the velocity triangle was introduced and a certain insight into the relative bucket flow can be obtained by considering the velocity triangle and the range of rotational speeds at which the Pelton can operate.

Firstly, the water impinging on the bucket will be deflected from its original direction and will follow the inner curvature of the bucket at a forced trajectory, the construction of this curvature at various sectors through the bucket geometry can be described by considering a number of guide curves, as shown in Fig. 2-7, labelled for convenience. Each curvature has a corresponding outflow angle, which relates directly with the β_2 angle necessary for creating the velocity triangles. Table 2-1 highlights a number of values each of the sectors, these are the value of β_2 , the corresponding diameter, d , the entrainment velocity, U , which is calculated from equation (2.18) using the BEP of the turbine.

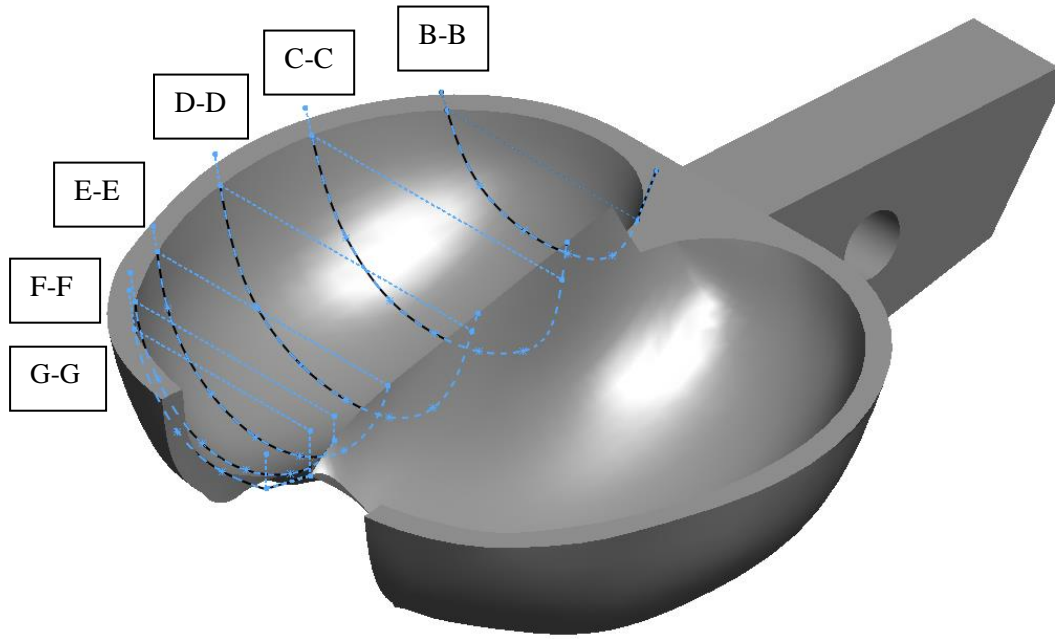


Fig. 2-7 CAD of 9.5" Jubilee Pelton bucket showing the guide curves

$$U = \frac{n\pi d}{60} \quad (2.18)$$

In this idealised case it is assumed that there are no viscous losses in the bucket, therefore the absolute velocity will remain constant along the streamline, such that $\mathbf{W}_1 = \mathbf{W}_2$, however the velocity vector \mathbf{W}_2 is not parallel to \mathbf{W}_1 but will be deflected by the aforementioned outflow angle. Therefore, the peripheral component of the absolute velocity, C_{2u} can also be calculated from equation (2.13).

Since testing is carried out at 20 m head, the jet speed C_1 can be calculated from equation (2.17), where the nozzle coefficient $\phi = 0.98$, such that $C_1 = 19.413$ m/s

Location	β_2	Diameter, d	U	W	W_{2u}	C_{2u}
	°	m	m/s	m/s	m/s	m/s
B-B	157	0.2019	7.88	11.54	-10.62	-2.74
C-C	163	0.2253	8.79	10.62	-10.16	-1.37
D-D	167	0.2487	9.70	9.71	-9.46	0.24
E-E	168	0.2721	10.61	8.80	-8.61	2.01
F-F	169	0.2862	11.16	8.25	-8.10	3.07
G-G	169	0.2926	11.41	8.00	-7.85	3.56

Table 2-1 Outflow angle and velocity components for various guide curves

The velocity triangles are then drawn at the respective guide curve position, as shown in Fig. 2-8.

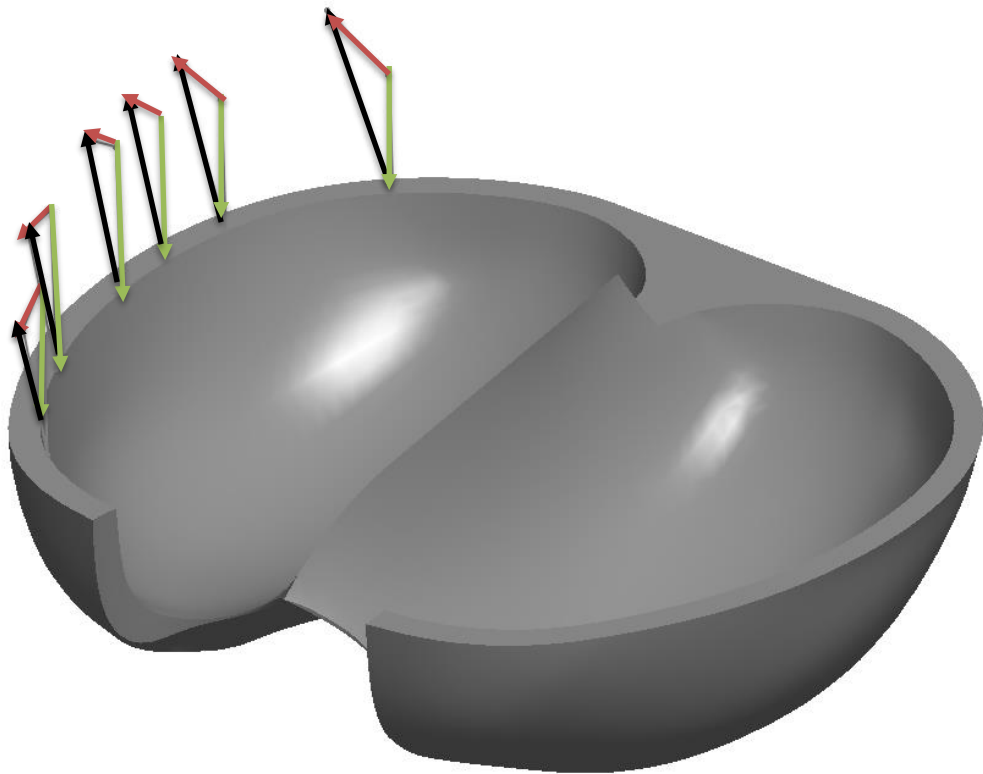


Fig. 2-8 Velocity triangles drawn at the respective guide curve positions and velocity components: U (green), C_2 (red), and W_2 (black)

For a stationary bucket, one can consider very simple streamlines emanating from a single point at which the jet strikes the splitter blade, an example of this from the literature is shown in Fig. 2-9.

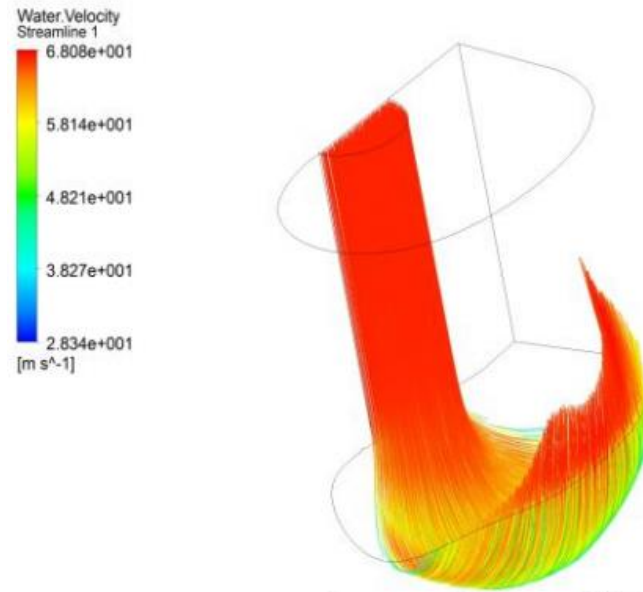


Fig. 2-9 Velocity streamlines through a stationary bucket using CFD [23]

However, in order to consider the flow in the casing one must consider the relative bucket flow during the entire jet cut in and cut out process as this will affect where the water leaves the runner in relation to the casing geometry and time. A more detailed description of the flow in a Pelton bucket is as follows. Firstly, the water leaves the bucket close to its root, Fig. 2-10b, then mainly on its sides, and towards the end of a cycle close to the cut-outs, Fig. 2-10d. In addition, splashing water and strings of droplets may occur depending on the bucket design [24]. After the bucket passage, a part of the water interacts with the turbine casing. Finally, the decelerated water falls into the tailrace channel [25].

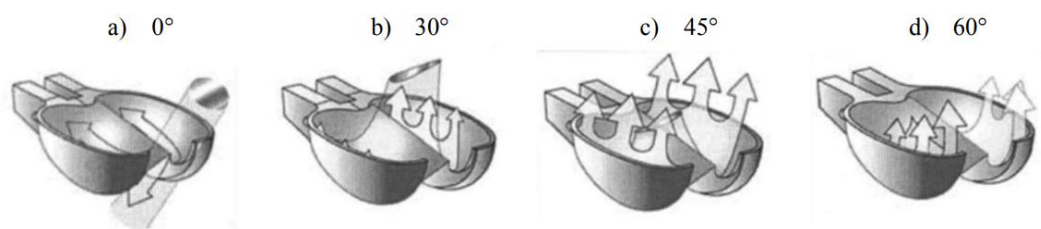


Fig. 2-10 Illustrations of the flow in a Pelton bucket at selected relative angular positions of the runner [26]

Fig. 2-11 shows five representative positions of the bucket relative to the jet.

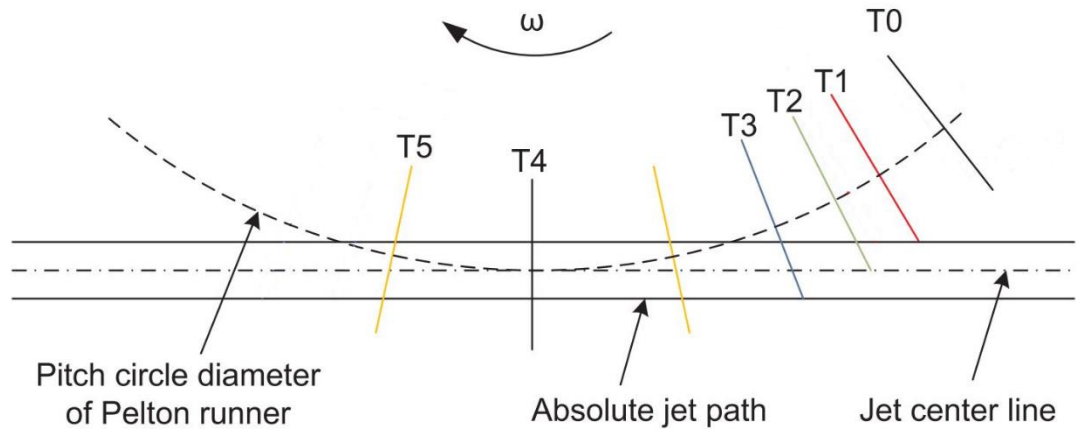


Fig. 2-11 Bucket relative position during the jet cut in and cut out process

It is known from experience that the streamlines along the bucket surface from these locations can be represented in Fig. 2-12.

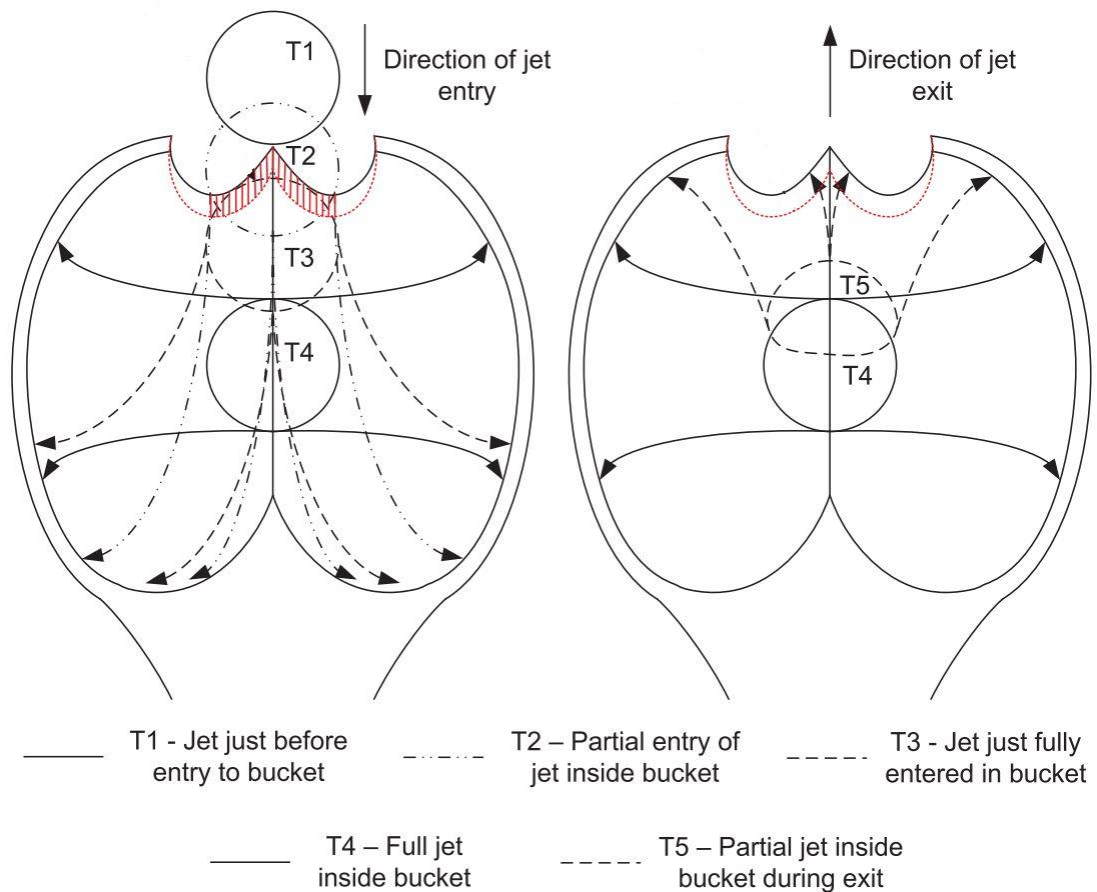


Fig. 2-12 Schematic of flow inside a Pelton bucket [27]

As a result the velocity triangles can be shown in relation to the relative bucket position in Fig. 2-13. The triangle is drawn parallel to the tangent made with point on the diameter, which

corresponds to the respective guide curve. Therefore, one may superimpose the casing on top of this to give an idea of where the water leaving the bucket will travel and at what time during the bucket cycle.

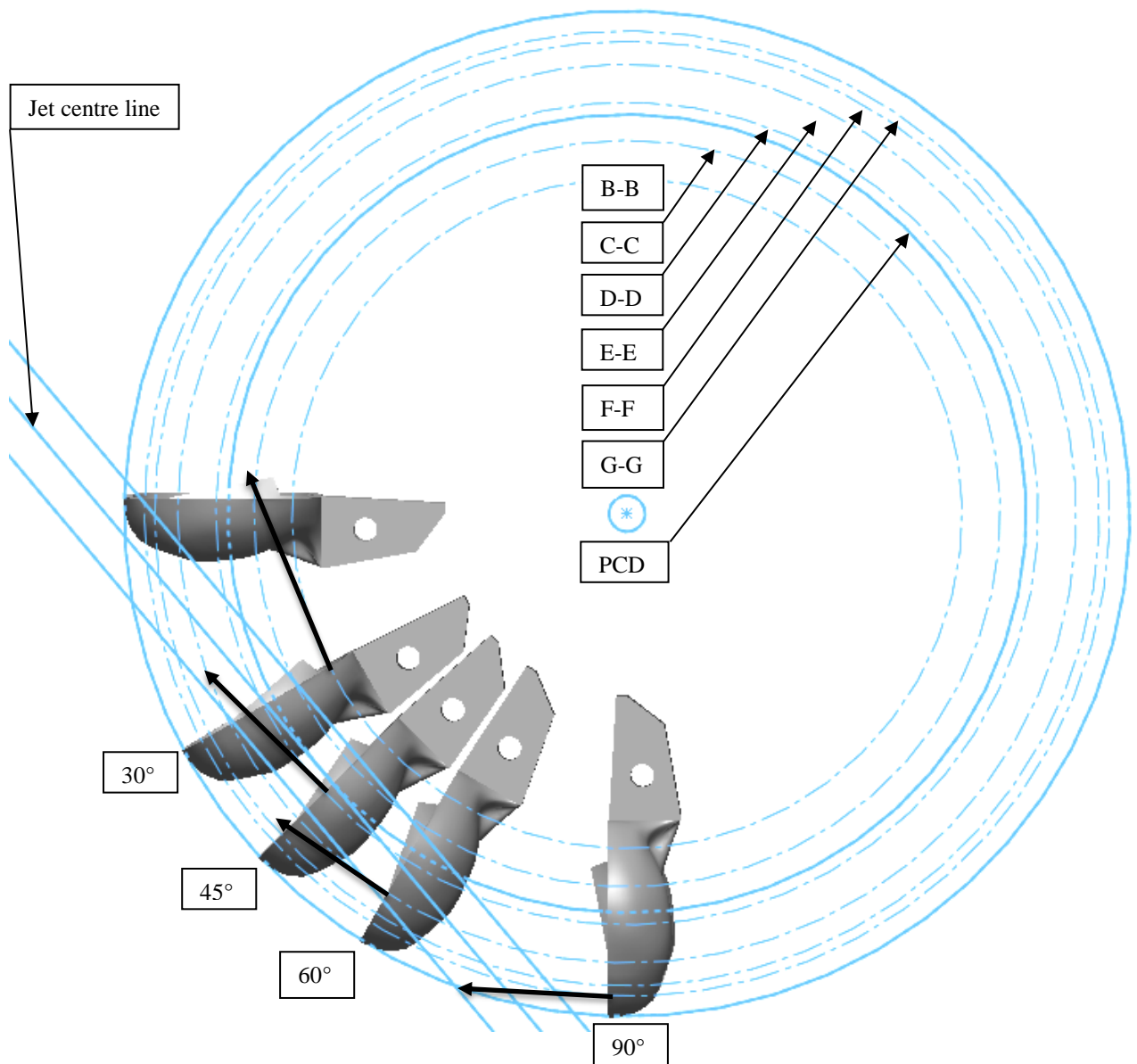


Fig. 2-13 Diagram showing absolute velocities \mathbf{W} relative to bucket position during duty cycle

In some cases, the turbine will be operated at a non-optimal speed, known as off-design conditions and indeed the experimental testing will be carried out at a range of rotational speeds in Chapter 5. At a non-optimal speed the direction of the water leaving the turbine will be affected. It is shown in Fig. 2-14 that as the speed changes, the peripheral speed changes and thus the entire velocity triangle changes, such that when $U < 0.5 C_1$, the water leaving the runner will be in a direction opposite to the rotational speed, and for $U > 0.5 C_1$, the reverse is true.

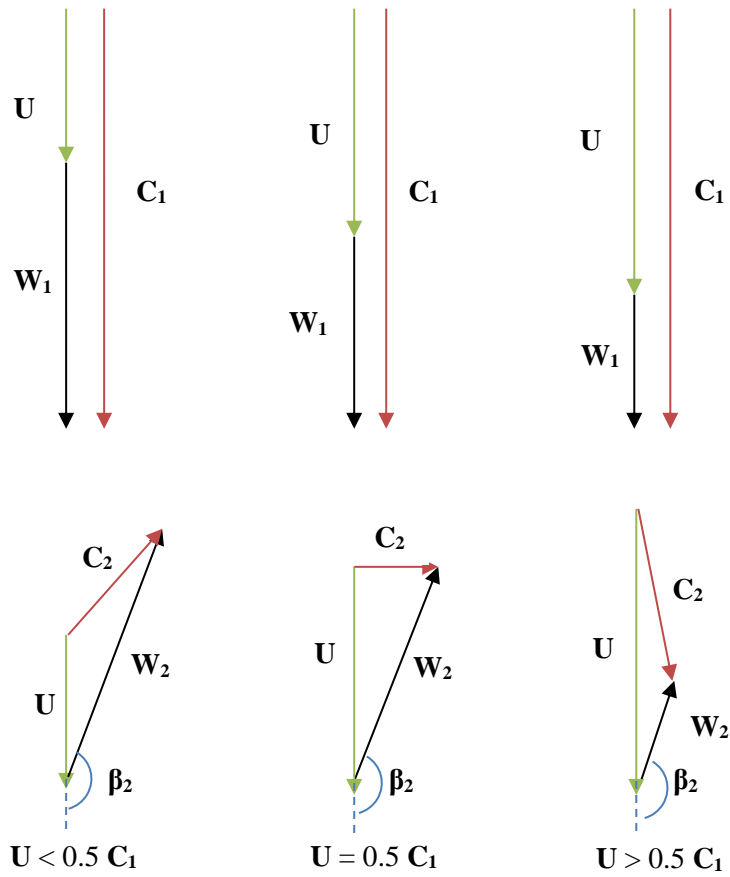


Fig. 2-14 Velocity triangles for different operating speeds

Full flow patterns have been photographed from the Lancaster University Pelton test rig in Fig. 2-15, which clearly shows the change of the absolute outflow angle relative to velocity (angle between U and C_2). This angle and the magnitude of the speed C_2 represent the influencing variables of the turbine on the casing flow. At the optimum unit speed the flow is characterised by almost rotation free outflow angle $= 90^\circ$, where the absolute speed is minimal, as shown in Fig. 2-15(b), the absolute outflow velocity is close to zero. When the unit speed is lower than the optimum as shown in Fig. 2-15(a), the absolute outflow velocity is very large and its direction is opposite to jet. In the case of higher unit speed the reverse is true as shown in Fig. 2-15(c).

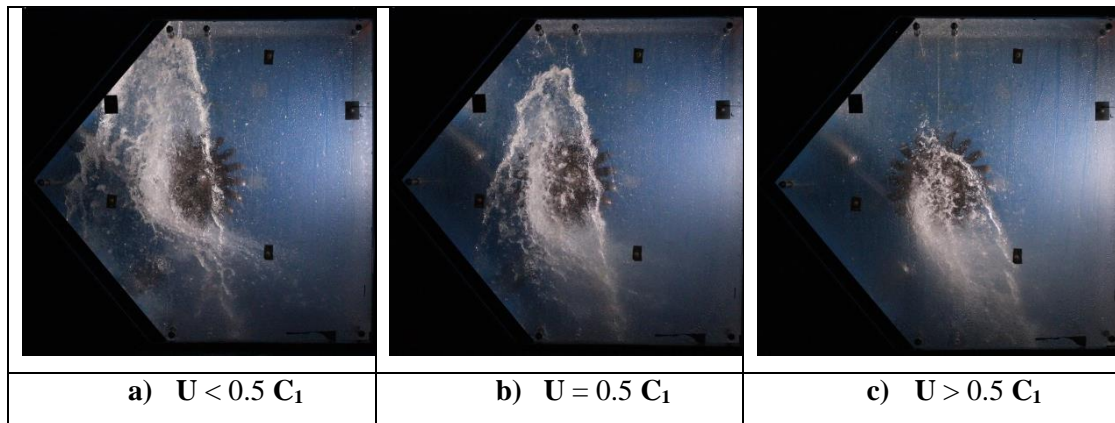


Fig. 2-15 Comparing flow patterns from the Lancaster Pelton test rig at different operating speeds

2.4 Physical Flow Quantities and Equations

For the study of the hydraulic phenomena related to the operation of Pelton turbines, two scales can be distinguished. The first relates to ‘full-scale’ machines, that is to say turbines that are connected to the electricity grid. The second scale relates to experiments that take place in the laboratory, which are model-scale, such as that which has been established at Lancaster University, detailed in Fig. 2-16 a) and b) respectively.

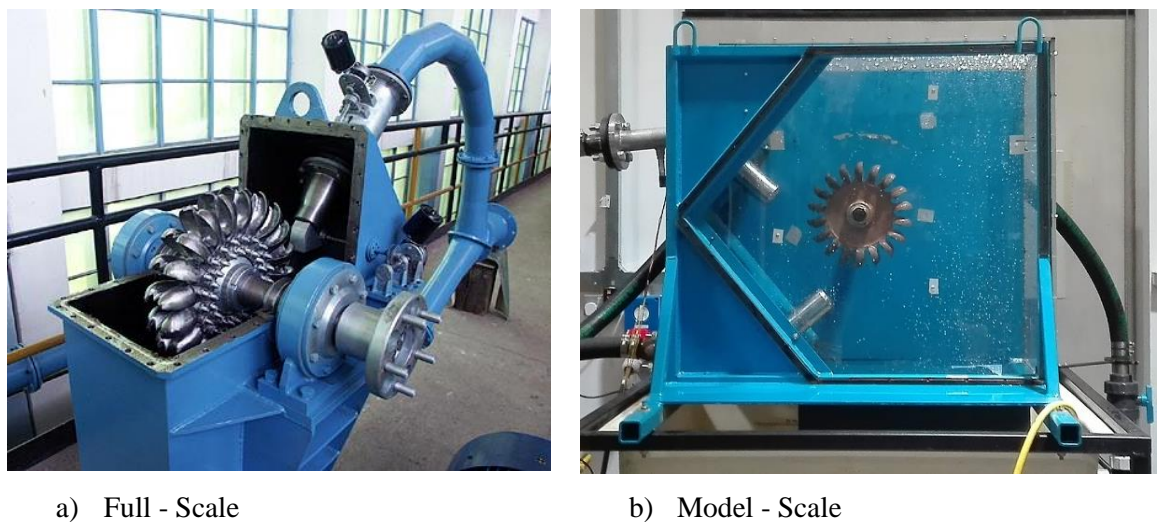


Fig. 2-16 Horizontal Axis Pelton Turbines at two scales

For these two scales, certain characteristic quantities, such as pressure, flow, velocity and diameter have been highlighted in Table 2-2.

Scale	Flow rate [m ³ /s]	Pressure head [m]	Velocity [m/s]		Diameter [mm]	
			Pipe	Jet	Pipe	Jet
Model	0.05 - 0.5	20 - 80	1 - 6	20 - 40	100	10 - 40
Full	0.1 - 20	100 - 2000	3 - 60	45 - 200	200 - 500	30 - 200

Table 2-2 Characteristic quantities of a Pelton turbine at two different scales

The flow at various stages during of operation of the Pelton turbine can be described by the following non-dimensional numbers [28] obtained from these quantities:

1. Reynolds Number

The Reynolds number (2.19) compares the magnitude of the inertia forces to the viscous forces

$$Re = \frac{\rho CD}{\mu} \quad (2.19)$$

2. Froude Number

The Froude number (2.20) measures the importance of the inertia forces relative to the gravity force

$$Fr = \frac{C}{\sqrt{gD}} \quad (2.20)$$

3. Weber Number

The Weber number (2.21) is the ratio between the inertia forces and the surface tension forces

$$We = \frac{\rho C^2 D}{\sigma} \quad (2.21)$$

4. Ohnesorge Number

The Ohnesorge number (2.22) relates the viscous forces to inertial and surface tension forces

$$Oh = \frac{\mu}{\sqrt{\rho D \sigma}} \quad (2.22)$$

Table 2-4 outlines the range of values of the non-dimensional numbers (2.19) - (2.22) that have been calculated from the typical dimensions (length scale) and values in Table 2-2 for a model-scale Pelton during operation, highlighting the relative importance of different forces, which dominate the flow in these sections. For each of the four flow regimes: i) confined steady-state flows in the upstream pipes and the distributor, ii) free jets past the injector, iii) transient

free surface flow in the buckets and iv) dispersed 2-phase flow in the casing there are different values for the characteristic variables of length, D and velocity, C . The density, ρ , viscosity, μ and surface tension coefficient, σ , for the two the fluids is given in Table 2-3.

Fluid	Density [kg m^{-3}]	Viscosity [$\text{kg m}^{-1} \text{s}^{-1}$]	Surface Tension [N m^{-1}]
Air	1	2×10^{-5}	0.0735
Water	1000	1.1×10^{-3}	

Table 2-3 Fluid Properties

The Weber (calculated for both the liquid and gas phase) and Ohnesorge numbers using the surface tension coefficient of the two phases can only be defined for jet, bucket and casing flow, where the two phases are present.

Flow regime	Typical Dimension	Velocity Scale	Reynolds number	Froude number	Weber number	Weber number	Ohnesorge number
	D [mm]	C [m s^{-1}]	Re [-]	Fr [-]	We_L [-]	We_G [-]	Oh [-]
Pipe flow	100	1 - 6	$1e5 - 6e5$	1 - 6	-	-	-
Water jet	15 - 30	20 - 40	$3e5 - 1e6$	50 - 70	$8e4 - 7e5$	$8e2 - 7e2$	$1e-3 - 7e-4$
Bucket flow	100	10 - 20	$1e6 - 2e6$	10 - 20	$1e5 - 5e5$	$1e2 - 5e2$	$4e-4$
Isolated water droplet	1	2	$2e3$	20	50	$5e-2$	$4e-3$

Table 2-4 Characteristic scales of the flow in a Pelton turbine model

For the jet and bucket flow we can thus observe from Table 2-4 that the Reynolds number is always greater than 1×10^5 , this shows the preponderance of the inertial phenomena with respect to the viscous forces. The order of magnitude of the Weber number also shows the significance of the inertial phenomena dominating over surface tension. Finally, the small Ohnesorge numbers highlights the weak dynamic role of the viscosity, especially in the cases where there are surface tension effects.

However, since we are interested in casing flow, probably the most pertinent of the obtained non-dimensional quantities is the Weber number, which is small for the isolated water droplet. For two phase flow in the casing the jet disturbance and the degree of atomisation of the water

droplets leading to windage (i.e. the significant circulation of air) losses is all dependant on the Weber number. Fig. 2-17 shows a small Powerspout Pelton turbine operating at 900 rpm with part of the casing wall removed. Here, when unconfined the water sheets leaving the turbine travels ~ 5 m and eventually the sheet breaks up into small liquid fragments. The distance of travel may seem particularly large, however, the overall efficiency of the turbine is $\sim 50\%$. Nevertheless, the figures demonstrate the complex hydrodynamic behaviour of the flow within the casing.



Fig. 2-17 Powerspout Pelton wheel in operation [29]

The flow observations made within the casing available in the literature are performed with conventional SLR digital cameras and in some cases the lenses will be protected by tubing if the camera is within the casing. These methods have provided thus far limited information about the flow structures due to 3 reasons: (i) the observation distance is too far, providing only low resolution images. (ii) The stroboscopic lighting systems provides only averaged snapshots of the flow. (iii) The typical duration of one stroboscope pulse is about $30\text{--}40\ \mu\text{s}$, which is insufficient to avoid motion blur, even if the pressure head of the turbine is significantly reduced. Moreover, accurate flow visualisations are difficult to perform. The space between the Pelton runner and the casing is very chaotic due to the spray and splash water, making visualisations of either the jet, bucket flow or indeed observations of the flow within the casing a challenging task. It is noted that the visibility is poor due to the atmosphere surrounding the runner, which consists of (i) water sheets ejected from the buckets, (ii) a significant number of different sized droplets originating from the water sheets breaking up and the collision of the water sheets with the casing walls, and (iii) fog and spray, which occurs due to ‘windage’ where the air in the casing becomes rapidly saturated.

2.5 Multiphase Flows

Multiphase flows are ubiquitous in nature and unsurprisingly the quantity of available literature documenting them would result in a bibliography vastly longer than this entire thesis. Nonetheless, in order to make a study of hydropower turbines it is necessary to provide some details of the type of fluid dynamics present that has previously been studied. Indeed, the nature of this thesis subject – casing flow in Pelton turbines – requires explication of the interesting phenomena, which occur throughout the entire operation of the turbine.

Multiphase flow, by definition is used to refer to any fluid flow consisting of more than one phase or component, such as air and water. Predicting the outcome of the interaction between a bulk fluid and gaseous flow is challenging as the process is governed by many complex parameters.

To offer a broader introduction to the fluid dynamics within a Pelton turbine, two areas will be introduced, namely; centrifugal atomisation and fluid jets injected into atmosphere. Describing the mechanisms that leads to aerodynamic jet breakup, disintegration and droplet formation is still a major study and as such two PhD thesis offer a much larger literature review into these topics [30] [31].

2.5.1 Centrifugal Atomisation

A centrifugal atomiser comprises a high speed rotating disk into which liquid is introduced, generally through the centre causing it to travel radially from the centre to the edge of the disc due to the centrifugal force. The disintegration of the ligament created by the atomiser is a complicated phenomenon not yet fully understood, however research tends to suggest that it is a result of Kelvin – Helmholtz and Rayleigh – Taylor instabilities. Depending on the geometry of the disc there two main types of rotary atomisers: spinning cups and discs.

Fig. 2-18 shows three atomisation modes for rotating discs described by Frost [32]. The first a) occurs for low liquid flow rate and is described as direct droplet formation originating from the periphery of the disc. An increase in flow rate, leads to the formation of ligaments, which originate from the periphery of the rotating disc and atomisation occurs at some distance away from its rim, as shown in b). Finally, for c) where there is a further increase in the liquid flow rate, ligament formation no longer occurs and sheets of liquid are formed. The transition from the direct droplet formation to the sheet formation could occur due to changes in the fluid properties, such as with an increase in the rotational speed and liquid viscosity, density and liquid flow rate or by decreasing the surface tension or the diameter of the disc [33].

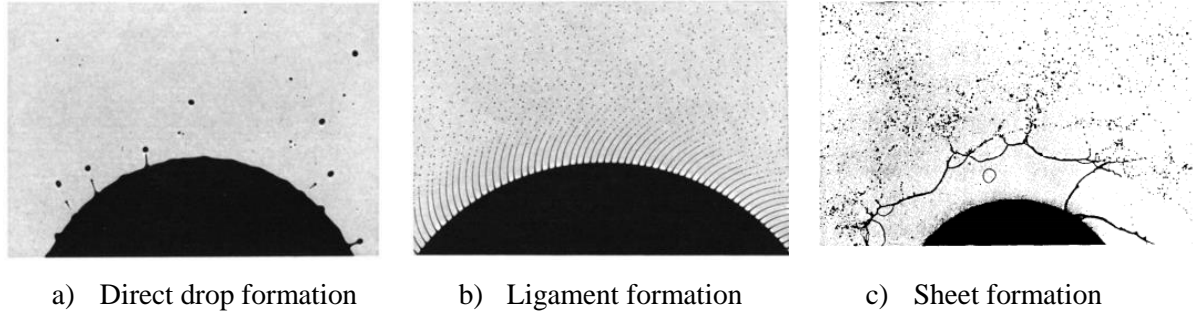


Fig. 2-18 Atomisation modes of rotating discs [32]

In this experiment, Frost was able to determine a number of non-dimensional numbers that described the conditions under which the transition occurs, namely A_1 (2.23), A_2 (2.24) and A_3 (2.25), and criteria for the transition is shown in Table 2-5.

$$A_1 = \frac{\omega \rho D^2}{\mu} \quad (2.23)$$

$$A_2 = \frac{\sigma D \rho}{\mu^2} \quad (2.24)$$

$$A_3 = \frac{Q \rho}{\mu D} \quad (2.25)$$

Breakup regime	Transition Criteria
Direct droplet formation	$\frac{A_3 A_1^{0.95}}{A_2} < 1.52$
Ligament formation	$\frac{A_3 A_1^{0.63}}{A_2^{0.9}} > 0.46$
Sheet formation	$\frac{A_3 A_1^{0.84}}{A_2^{0.9}} > 19.8$

Table 2-5 Transition criteria of breakup regimes for rotating discs

Where σ [N/m] is the surface tension coefficient, μ [Pa · s] is the dynamic viscosity, D is the diameter of the rotating disc and Q is the liquid volume flow rate.

A number of other researchers have carried out similar experiments with rotating discs of different geometries and with different fluids, noting similar values for the boundaries of the atomisation regimes. Liu et al [34] carried out a comparable experimental investigation of the liquid disintegration for rotating cups, noting that three different types of disintegration formation occur as the angular speed increases in a given flow rate, shown in Fig. 2-19.

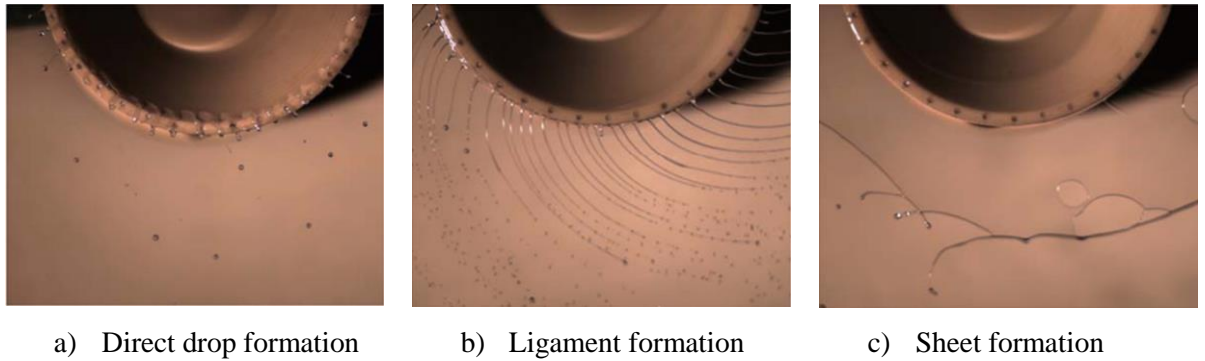


Fig. 2-19 Atomisation modes for rotating cups [34]

Liquid atomisation, or the transformation of bulk fluid into droplets, ligaments and sheets is a phenomenon found and easily observable in everyday life and is particularly present in the casing of a Pelton turbine during operation. The purpose of highlighting this theory is twofold, firstly to provide some insight into the mechanisms that generate particular fluid flow phenomena relevant to the study of impulse turbines and to offer a framework of definition, which will be used later in the thesis to describe casing flow.

2.5.2 Liquid Jet Disintegration

The design of a nozzle and the influence this has on the ensuing liquid jet has been widely studied as it has implications in an extensive range of industries. A liquid jet originating from a nozzle is sensitive to a number of disturbances, which of a certain frequency cause the jet to break up into a series of successive droplets originating at the free surface. The mechanism of this has been widely studied and is still not fully understood, however it is agreed that turbulence is the main cause of free surface disturbances. There are wide differences in the free surface behaviour at different length scales since surface tension is important for small length scales and gravity for large length scales [35]. In addition, the break up process also depends on fluid density, nozzle radius and initial disturbance amplitude [36]. The earliest investigations date back to Bidone and Savart in the early decades of the 19th century. Savart proposed two laws related to jet degradation namely: 1) for constant diameter, the length of the continuous part of the jet is directly proportional to the square root of the head driving the jet (i.e. also proportional to jet velocity) and 2) for constant velocity, the length of the jet is proportional diameter [37]. Soon later, Plateau noted the instability arose when the liquid column length exceeded the column diameter by a factor close to pi. Lord Rayleigh later corroborated Plateau's work, giving an analytical explanation of this physical observation, the culmination of this work is known as the Plateau-Rayleigh instability law [38].

By 1909 Niels Bohr had extended Rayleigh's analysis to include viscous effects and the effects of surface tension. Weber went further to demonstrate the breakup length for a viscous jet in 1936 [39].

McCarthy and Malloy show that the level of jet turbulence and also the velocity profile contribute to the disintegration process [40]. The state of the jet leaving the nozzle may be considered as laminar, semi-turbulent or fully turbulent. In a fully developed laminar jet the velocity profile can be assumed to follow a parabola, with the maximum velocity along the centre line of jet³. When the jet is turbulent the velocity profile is characterised by a much flatter appearance. A semi turbulent jet consists of a turbulent core enveloped by a laminar outer region. Initially the laminar layers inhibit the turbulent elements from reaching the free surface, however eventually the momentum is redistributed between the two layers, the velocity profile flattens and the radial components of turbulence result in the jet breakup. As the Reynolds number is increased the thickness of the laminar layer decreases until zero, when the jet can be considered fully turbulent [41].

For the purposes of comparison with the water jet of a Pelton turbine the experimental work of Hoyt and Taylor noted that high Reynolds number water jets discharging into air exhibit axisymmetric instabilities, which accompany the transition from laminar to turbulent flow at the exit [42]. This leads to spray formulation at some distance from the exit and further downstream helical disturbances which result in the jet assuming a helical form. Hoyt also noted that amplification of the disturbances also occurs when there is a mismatch between the speed of the jet at the free surface and the ambient air into which the jet discharges. The resulting mismatch induces aerodynamic form drag on the surface. A much more stable water jet with little surface disturbances was visible when a column of air is arranged to surround the water jet travelling at the same velocity. Fig. 2-20 compares the images of the water jet at different air speeds.

³ N.b., the inclusion of the spear in a Pelton injector means that there are two boundary layers to consider, one at the wall and one at the centre of the water jet.

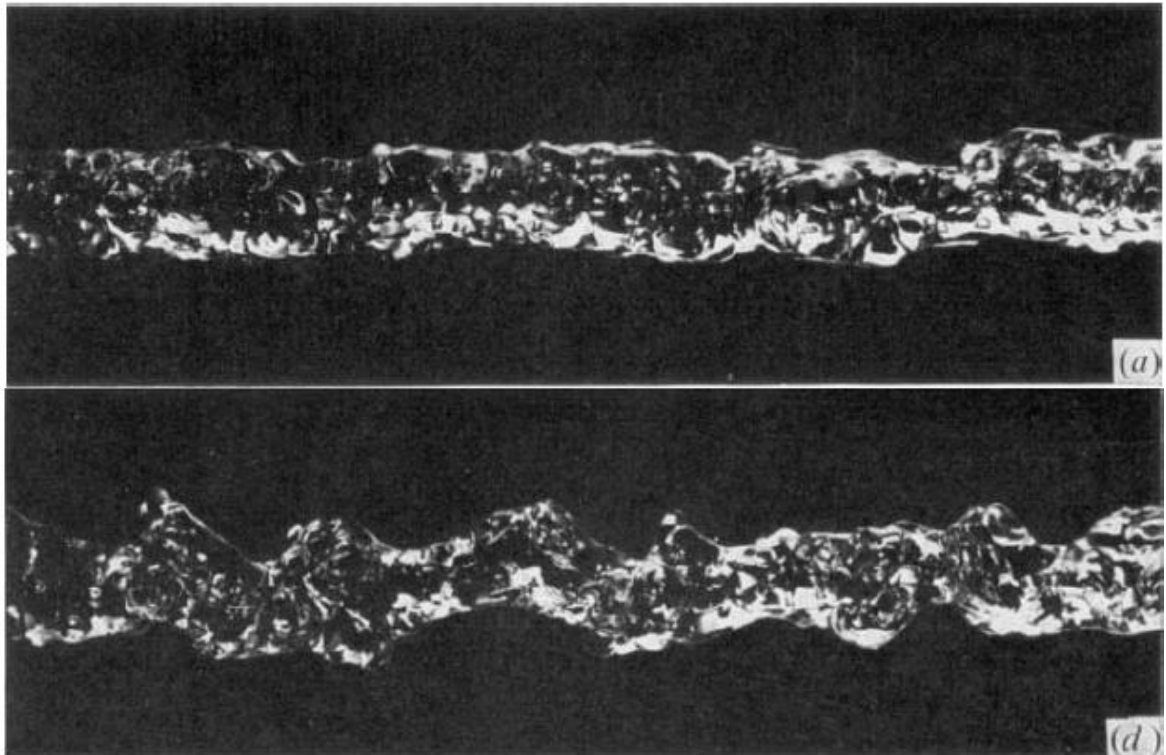


Fig. 2-20 Appearance of jet at $x/D = 104$ for air velocity a) 116 ft/s d) 4.8 ft/s water flow at 90 ft/s

2.6 Literature Related to Pelton Turbine Development

According to a number of global surveys the Pelton turbine represents one of the most widely employed hydropower turbine types [20]. In the last twenty or so years modern tools, such as CFD, have been applied to the design of these machines in order to achieve maximum exploitation of the available hydraulic energy. Based on the present state of the art, hydraulic efficiencies of around 90% are routinely quoted by manufacturers, both from new constructions and through refurbishment of existing installations. This achievement can be attributed to the operational optimisation of both the jet quality and the jet – runner interaction. The following subsections cover the available literature related to Pelton turbine development, more specifically related to the design optimisation of the injector and runner. This is followed by an overview of casing designs, which demonstrates that there are no clear conclusions or guidelines available in the literature and casing styles vary from manufacturer to manufacturer, demonstrating the need for this research.

2.6.1 Injector Research

As the efficiency of the Pelton turbine depends highly on the quality of the jet, the disturbances that arise from the upstream flow conditions in the distributor, injector and the nozzle are of

great concern to designers [43]. These disturbance mechanisms tend to generate secondary flow structures, which are inherently connected to energy losses, moreover a suboptimal jet interaction with the runner will result in not only a reduction in the efficiency but studies have shown an increase in the risk of cavitation [44].

An idealised jet is defined as having uniformity in the velocity distribution within the jet, the absence of secondary flows and compactness of the jet, it may be gleaned that jet quality is a measure of the relationship between the real and idealised jet conditions [11]. Staubli et al have indicated through studies of a number of Swiss Pelton power plants that gains in efficiency of between 0.5 - 1% could be achieved by improving the jet quality. It was found that the upstream flow history was hard to predict though the complex local Froude, Weber and high Reynolds numbers guarantee the turbulent nature of the secondary flow generated in bends, bifurcations hardly decay before reaching the nozzle.

Staubli et al. [11] describe three key indicators governing the quality of jets, namely: jet dispersion, which is the widening of the jet with distance from the nozzle; jet deviation, which is the deviation of the jets centre line from the theoretical axis; and jet deformation, which is the disturbance of the jet free surface. Zhang and Casey [45] expand this list to include the effect of the downstream interaction of the jet with the surrounding air, which causes the highly turbulent free surface of the jet to entrain air leading to the deformation of the surface of the jet.

Both papers [45] and [11] present experimental techniques used to quantify the flow conditions at the nozzle inlet, the effect this has on the jet quality and behaviour across a number of different inlet flow conditions. Typically these experiments have mainly been performed by employing photographic methods and measurement by means of Pitot tubes, however more recently Laser Doppler Anemometry (LDA) has been used to obtain a more accurate detail of the flow distribution and types of flows present in the jet [46]. Zhang and Casey [45] carry out experiments on the Pelton nozzle using LDA, first a straight pipe was connected to the model nozzle, which will be used as a reference case to study basic flow phenomena. The second, the model nozzle is connected to a 90° bend, this is used to study the effects of vortices and rotational secondary flows. The final experiment sees the model nozzle connected to the actual distributor of a Pelton turbine.

The results of the first experiment show the typical velocity distribution of the jet at different lengths along the jet axis. A typical example of the velocity distribution in the jet at different sections along the jet axis is shown in Fig. 2-21.

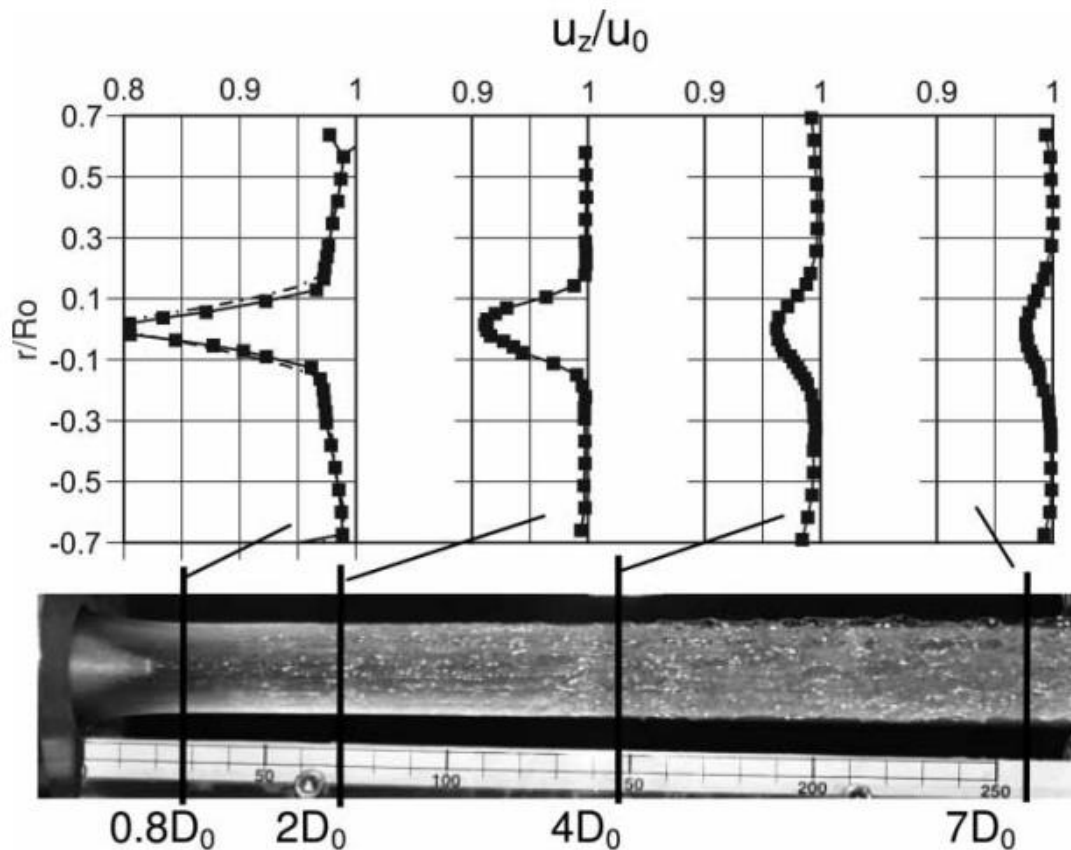


Fig. 2-21 Axial velocities in the jet for an injector connected to a straight pipe [45]

The authors make the following observations:

- The velocity is lower at the centre of the jet, this is attributed to the wake generated in the boundary layers on the needle surface. As the head increases the velocity deficit in the core becomes narrower, indicating a dependence on the Reynolds number;
- At section $0.8D_0$, close to the nozzle, the velocity distribution is non-uniform, indicating that the flow is highly dependent on the curvature and geometry of the nozzle. This is supported by the theory that states that when the water jet emerges from the nozzle its diameter decreases due to contraction, and its velocity increases up to the least cross section [5]. At this point the flow has not yet reached a maximum and is still accelerating.

As already mentioned when the jet emerges from the nozzle its diameter contracts slightly, however beyond this the diameter begins to increase gradually, this is due to the influence of the exchange of impulses between the jet and the ambient air, which acts to retard the velocity of the outer particles [5]. The point at which the diameter converges is known as the ‘waist’, photographic estimations of this location are frequently incorrect and LDA can be used to confirm or find the correct location of the jet waist.

Despite the presence of secondary flow structures being mainly responsible for jet instability, they only contribute between 0 – 5% of the overall flow, therefore their detection is increasingly difficult. The second experiment was used to quantify the effect secondary flows, the apparatus for the experiment is outlined in Fig. 2-22, and shows the LDA setup, enabling measurement of the fluid flow before and after it has left the nozzle, which is intern, connected to a 90° bend [47].

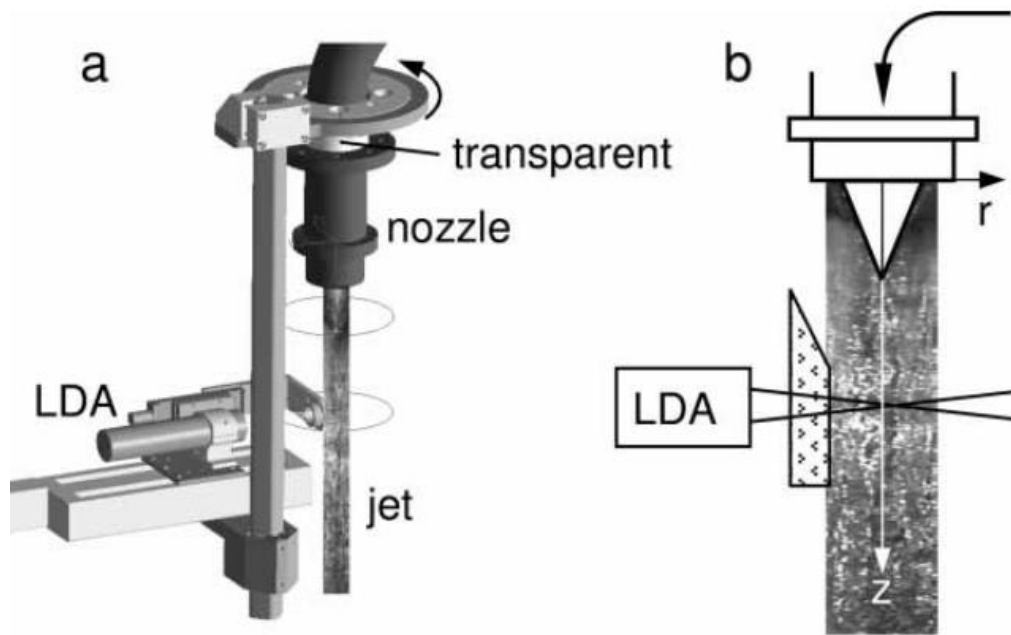


Fig. 2-22 Support for the LDA optics, (a) a traversing system to access jet flow from all possible position and (b) Plexiglas system to ensure laser was able to transmit through jet surface [45]

The presence of secondary flow can be confirmed by measuring the tangential velocity both upstream and downstream of the injector. In general cases, such as Fig. 2-23 [48], two recirculation vortices can be observed as a result of the presence of the elbow upstream, they meet at the stagnation point (Staupunkt) and the flow is generally unsteady as it is the collision of two almost equal flows. As the jet leaves the injector a similar tangential velocity profile can be observed, however since the jet is now unrestrained by the containing walls the surface is free to deform and deviate around the stagnation point.

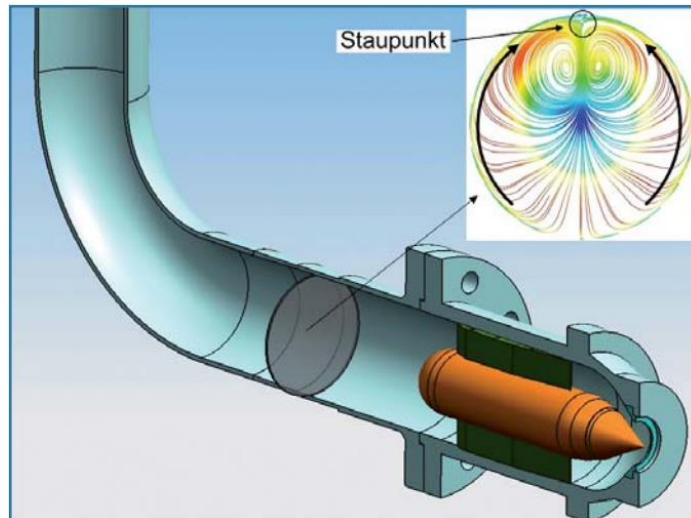


Fig. 2-23 Secondary flow due to the elbow in supply pipe [48]

CFD simulation of the deformation of the surface of the jet that are the end result of secondary flows created by the elbow is shown in Fig. 2-24 [49].

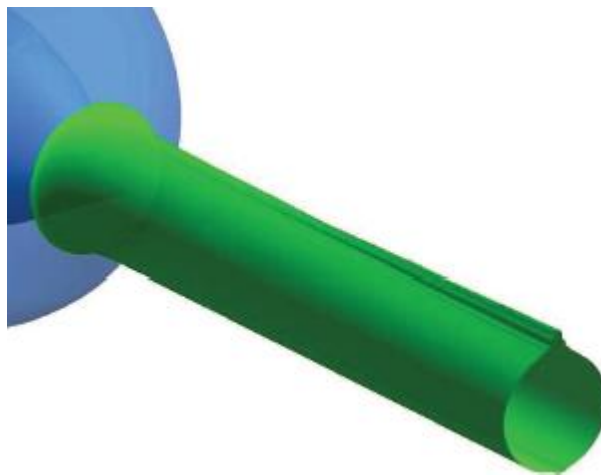


Fig. 2-24 Representation of the surface jet [49]

CFD simulations have been validated using an experimental setup that includes a tactile measurement probe. It consists of a pair of linear guides mounted at the nozzle body, a slide with a rotary ring and a micrometer onto which different probes may be attached [50].

In the course of research detailed in [15] on experiments at HPP Rothenbrunnen by Andritz Hydro it was demonstrated that there are differences between the efficiency of the two jets, this is due to different supply pipe layouts having an effect on the jet, the lower jet experienced a greater increase in jet diameter and exhibits a lower efficiency. This demonstrates that jet dispersion correlates to jet efficiency. Additionally, at Rothenbrunnen replacement of the

injector and introducing new internals to the casing reduced the number of droplets seen in the visualisation studies and led to reduced jet dispersion. Overall thermodynamic efficiency was increased by 1.4%, which is significant considering the minimal expense incurred.

The LDA method does have some drawbacks, for example the rough jet surface scatters so much light it makes it difficult to determine the edge of the jet and therefore the jet thickness. In addition to this turbulence in the flow often makes the jet opaque, therefore a thin film of Perspex must be placed adjacent to the jet surface to ensure that the laser beams are able to transmit through the water. The Perspex slightly influences the flow in the immediate vicinity, however it has been determined that this does not affect the measurements.

2.6.1.1 Nozzle Modifications

It has been noted that older Pelton designs often used shallower nozzle and spear angles indicating that the jet quality may not be optimum [11]. During the improvement works at Moccasin Power Plant, California, it was identified that the injector design contributed significantly to suboptimal jet-runner interaction and poor jet flow quality [43]. The original 1969 injector had an 80° nozzle, this was increased to 90° and spear of 60° , which was decreased to 50° , as shown in Fig. 2-25 [51]. It was argued that the original combination might produce a good jet in a model test scenario but not produce a high quality jet in a scaled up Pelton of the size required at the site. The results of the jet modification with the new geometry showed an improvement of 0.5% at 60% load and 0.9% at full load [52].

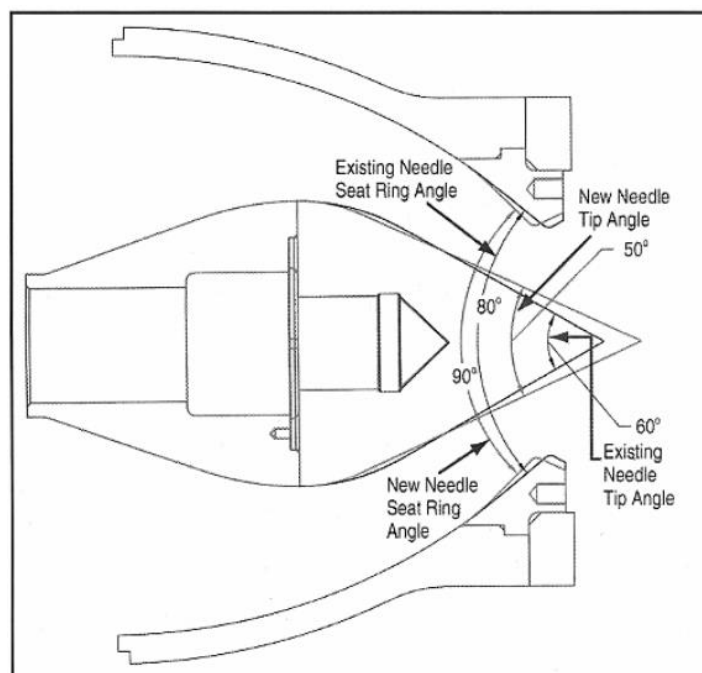


Fig. 2-25 Jet needle tip and nozzle seat ring modifications for jet quality improvements [43]

2.6.2 Runner Optimisation

Until very recently much of the development work of the buckets in a Pelton runner were carried out through long term experimental testing on a trial and error basis. Few experimental investigations of the flow in Pelton turbines are presented in the literature. Those available can be divided in 2 classes, i.e. (i) flow observations, and (ii) pressure measurements.

The first experiments with flow observations were carried out using stationary buckets, an example of which is shown in Fig. 2-26 display the front and side face views, which were obtained through tubes to prevent the splashing water flowing along the test bed walls to mask the bucket [53]. These visualisations give good information about the flow pattern and flow angles. The flow observations also offered details of the part of the flow escaping from the cut-out as well as the lateral sheet flow for which the direction and angle of the flow is easily observed.

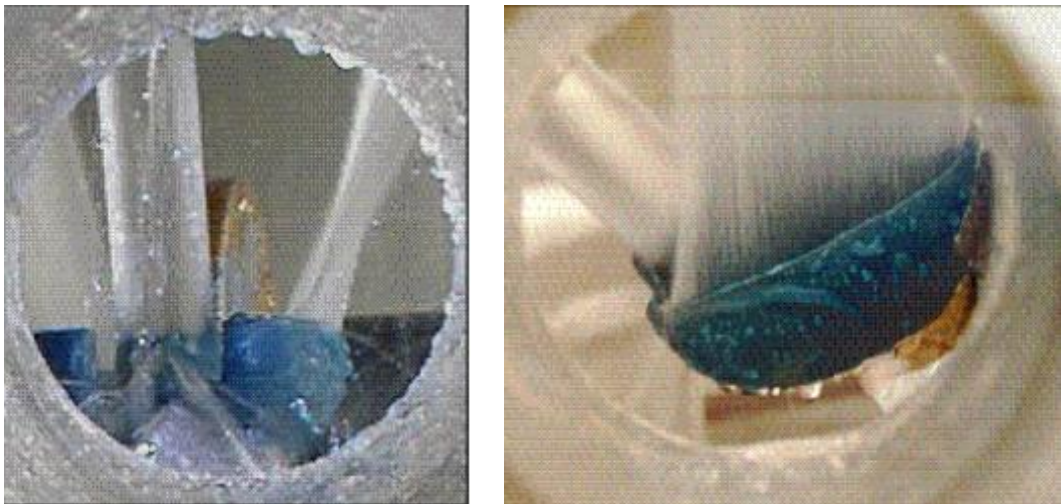


Fig. 2-26 Flow visualisation with stationary buckets, front view (left) and side view (right) [53]

Later, rotating buckets were modelled and Bachman et al. [24] documented the flow pattern in and around a bucket of a model Pelton runner performed using external flow visualisations obtained with a stroboscopic flash. Perrig, in a PhD thesis from Ecole Polytechnique Fédérale de Lausanne (EPFL) [26] fitted small rigid endoscopes both in a bucket, to observe the relative flow, and in the casing to observe the jet/bucket interaction.

The first measurement of the unsteady pressure in a rotating bucket was carried out by Avellan et al. [53]. Three piezo-electric pressure sensors were installed in a bucket. These results permitted to enhance the design of the Pelton turbines. Kvicinsky [54] fitted a reduced scale Pelton runner with 32 flush-mounted unsteady pressure sensors, providing the first set of unsteady pressure measurement in a runner under normal operating conditions. According to

the shape of the measured signals, 5 distinct zones could be defined on the bucket inner surface. Perrig [26] documented the power budget associated with the cut-in and outflow procedure of the jet using on board wall pressure measurements, which included 43 piezo-resistive pressure sensors that were distributed on the bucket inner surface, backside and sides as shown in Fig. 2-27.

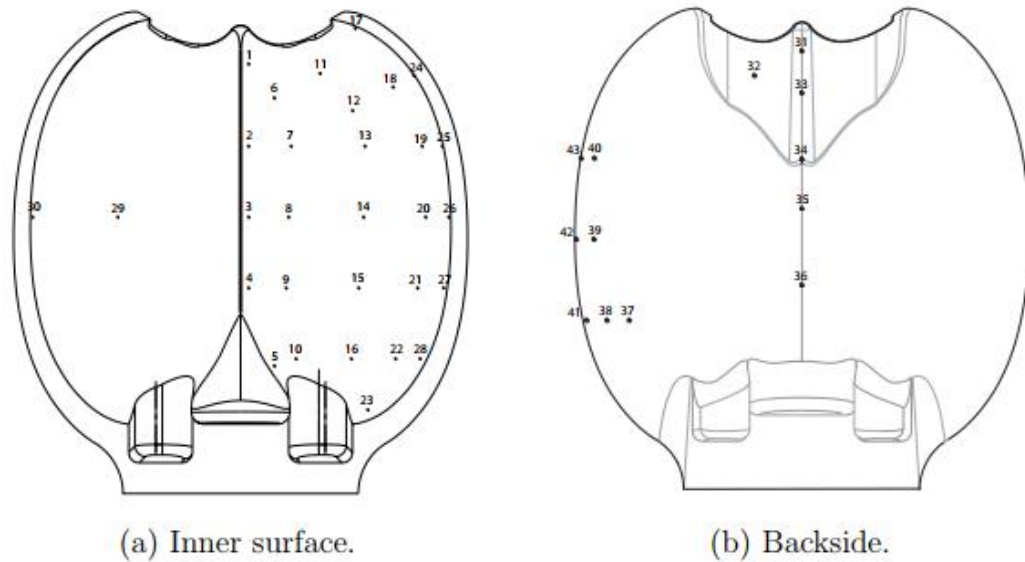


Fig. 2-27 Pressure sensor locations on inner and backside of bucket [26]

The two sensors on the left hand side of the inner surface are to observe the symmetry phenomenon. The sensors on the back side are to calculate the flow that adheres to the backside of the bucket as a result of the Coanda effect. Finally, the sensors on the left hand side of the back are to calculate the flow that exits the preceding bucket and impinges on the following bucket.

To date, Zidonis et al. [10] has published the most comprehensive review of the modelling research of Pelton turbines using CFD. By far the largest amount of publications use commercial mesh-based Eulerian codes developed by ANSYS: CFX and FLUENT.

Early applications by Kvicinsky et al. [55] measured the pressure distribution on a stationary Pelton bucket cut by an ideal jet and verified different suitability of two multiphase models; the Volume of Fluid (VOF) available in FLUENT and the homogeneous model available in CFX, to the simulation of such a configuration by comparison with experimental pressure data from sensors located on the bucket inner surface. These comparisons show that the force on the steady bucket is well captured. Zoppé et al. [56] used the VOF model to analyse numerically the influence of the variation in head, incidence conditions and jet diameter on the fluid dynamics

in a fixed Pelton bucket and the experimental flow visualisations highlighted that VOF underestimates the leakage through the bucket cut-out region.

Later attempts to numerically analyse the flow in a rotating Pelton turbine bucket were carried out by Perrig et al. [57], with Perrig's thesis [26] presenting a more complete analysis of the energy exchange in a rotating multi-jet Pelton turbine bucket, which simulated an ideal jet striking a rotating runner and compared the results to the experimental data.

The simulation was performed with the commercial solver, ANSYS CFX and multiphase modelling was carried out using the homogeneous Model and the 2-Fluid Model. A quarter runner model was used and the domain and boundary conditions are indicated in Fig. 2-28. In this research the jet was simulated as half a cylinder. The results obtained from both models are compared with the experimental data in terms of unsteady pressure, water film thickness, and water film topology. The 2-Fluid Model appears to provide the best results, while the homogeneous model is too dispersive.

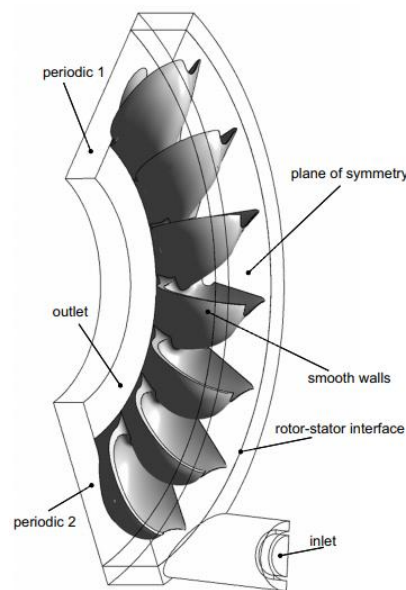


Fig. 2-28 Computational domain and boundary conditions applied [26]

The heavy computational cost of Pelton turbine CFD simulations is the main reason why Perrig and many other researchers [18], [58], [59] consider simulations with a reduced number of buckets. All authors always use a symmetry plane along the centre line of the bucket to split the bucket in half. The main justification for this is that since the locations of the injectors are fixed the bucket will experience a periodic torque from the contact with the water jet [60]. Nevertheless, some researchers opt to model the full runner. For example further research simulating the performance of a Pelton runner with a real jet was performed by Santolin et al. at the University of Padova [61], taking into account the flow effects in the jet downstream of

the nozzle and spear. In this work a full runner was modelled using the CFX solver and the homogenous model to compute the time history of the torque and analysed the influence of the water jet profile.

The above procedure was also applied by Jošt et.al [62] where the flow through the Pelton turbine was simulated using the CFX software. More specifically, the flow in the pipework and injector system of a twin jet Pelton horizontal axis turbine injectors was initially simulated and then used as an input for simulating a rotating runner with 23 buckets, as shown in Fig. 2-29A.

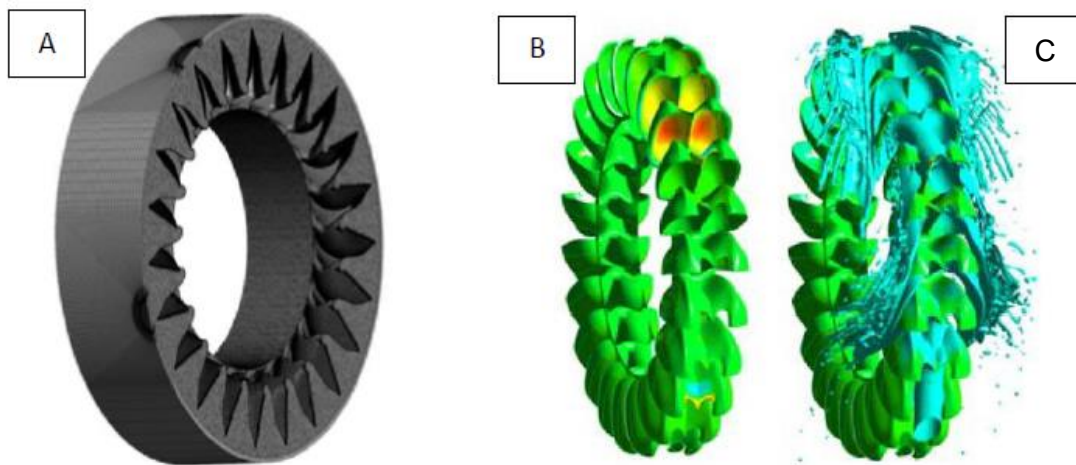


Fig. 2-29 Computational mesh (A), field pressure effects (B) and phase distribution (C) [62]

The calculation of the fluid-mechanical magnitudes, such as the pressure and phase distribution, shown in Fig. 2-29B-C provides an indicative snapshot. Then the torque curves were plotted and the efficiency was calculated. However, the density of the mesh used was inadequate, as suggested by the comparison of the simulation result with a coarse and fine mesh, highlighted in Fig. 2-30. Also, the timestep used seems to have a great effect on the results, as shown in Fig. 2-31, indicating that more computational cost is needed to more accurately simulate the flow.

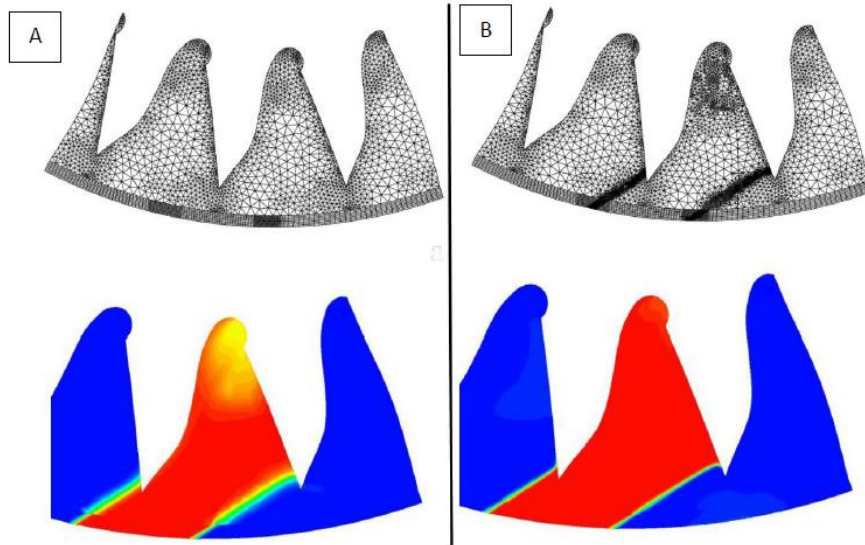


Fig. 2-30 Comparison of the calculated air-water phase by the simulations on a coarse mesh (A) and fine mesh (B) [62]

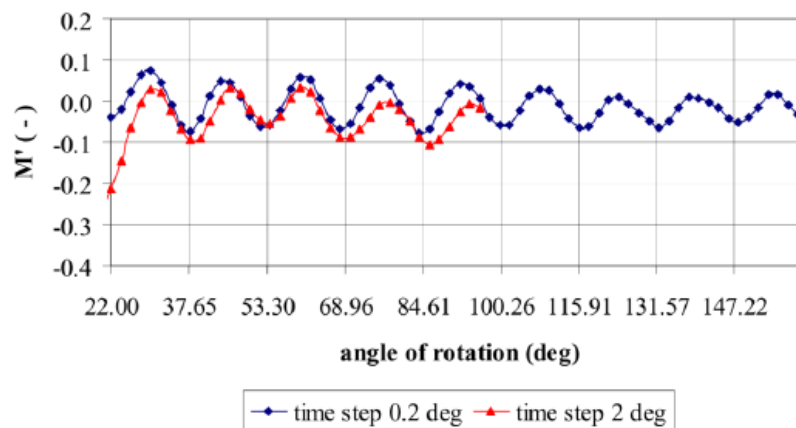


Fig. 2-31 Comparison of torque variation exerted on a bucket for different timestep size [62]

A number of studies using FLUENT have also been reported for rotating bucket simulations, incorporating the VOF multiphase model, with both reduced runner [59] and the full runner being modelled [63], [64].

In terms of turbulence modelling all studies report the use of two-equation RANS models. Early works carried out in CFX used the $k-\epsilon$ turbulence model [57], which was later swapped exclusively for the $k-\omega$ SST model, nevertheless all simulations in FLUENT use the realisable and RNG $k-\epsilon$ respectively [63], [64].

All of the research reported thus far considers the flow in Pelton turbines to be incompressible, however Perrig [26] is the only example where artificial compressibility was employed due to the under prediction of the shear stress and jet disturbance during the jet-cut in process in the

initial work. However, it was found to have very little effect on the overall prediction of efficiency and since it added additional computational time is considered unnecessary in the present work.

Examples of the application of other commercial codes beyond the ANSYS packages are very limited in the literature, there is one very early example of FLOW-3D from the year 2000 [65], however it is noted by the author that “FLOW-3D was probably the only commercial CFD code capable of this kind of computation.” Since then significant developments in the capabilities of CFD have taken place. There has been one published example of modelling the Pelton turbine using OpenFOAM [66], a mesh based open-source code. Despite OpenFOAM’s capability in implementing the multiphase models used by both CFX and FLUENT: homogeneous, inhomogeneous and VOF [67], the simulated Pelton turbine showed significant over predictions of the torque on the bucket in comparison to both the same simulation carried out with CFX and the experimental results. Furthermore, several numerical instabilities were reported and ultimately the simulation time was far in excess (30 x) of that with CFX, demonstrating the need for further OpenFOAM code development if it is to become an accurate alternative to commercial codes.

In all cases there will be a discrepancy between the CFD and experimental results, generally in these models, which only consider the jet and runner, the CFD will over predict the efficiency since it does not take into account losses from the pipework, injector, casing, bearing and windage. The following papers report an over prediction of between 1.5 and 6% [57] [26] [18] [61]. In some cases there CFD will under predict the efficiency compared to experiments, by 2% [62] and 3.5% [58] respectively. This is largely attributed to insufficient mesh resolution, which can in some cases impact the jet shape and thickness and subsequent jet-runner interaction.

More recently, a number of researchers have developed independent design methodologies for Pelton turbine buckets. Zidonis [18] defined a number of key design parameters, which were analysed using a Design of Experiments technique where each element was systematically simulated using CFX and then later combined such that an optimised design was obtained. For Solemslie [14] the bucket surface was theoretically defined by a series of Bézier curves and required a high degree of user interaction during the design process. In both cases an experimental turbine with buckets, designed with the presented methods were manufactured and tested. The flow in the designed bucket were analysed and improvements to the design method presented [60].

2.6.3 Casing Design

Though casing studies are limited it is implied in the general literature that the casing is an essential part of the turbine and that further studies are needed to determine optimum shape and dimension. The casing is important and should have the appropriate design to reduce as far as possible the losses due to the splash water interaction with the runner and jet.

Measurement of the efficiency of a Pelton turbine has so far been determined based on calculating the ratio of available hydraulic energy and the power transferred at the shaft, and it is therefore not readily possible to obtain detailed information about the losses that arise from flow losses due to the casing, such as swirling, exit, friction and windage losses.

Since the rotor operates in an air environment at atmospheric pressure, the rotation of the runner at high speeds leads to the water leaving the buckets being highly turbulent causing droplets and fine mist to dissipate throughout the casing. Thus, the aerodynamic resistance of the air causes small but not insignificant ventilation losses.

To date, investigations of the flow in the casing of Pelton turbines is limited to visual documentation of splash water distribution, using standard photographic methods and those more advanced such as Particle Image Velocimetry (PIV) and Laser Doppler Anemometry (LDA), where based on observation a case can be considered good or not good at achieving the principle aim of draining water coming from the buckets without hindering the runner and jet.

Older designs of Pelton casings tend to have complex geometrical features as shown in Fig. 2-20. In general, the case is split along the axis of the runner and consists of a semi-circular upper housing, which can be removed to allow access to the runner and a domed lower housing. The dimensions of these sections according to Nechleba [5], Quartz [68] and Raabe [69] are related to the jet diameter and bucket outer width as shown in Table 2-6, where lower part and upper part refer to 1 and 2 in Fig. 2-20 respectively.

	Housing Upper Part	Housing Lower Part
Nechleba	$B_C = 3 - 5 \cdot d_0$	$B_C = 12 - 18 \cdot d_0$
Quartz	$B_C = 1.2 - 1.4 \cdot B$	$B_C = 3 - 4 \cdot B$
Raabe	$B_C = 11 - 13 \cdot d_0$	$B_C = 11 - 13 \cdot d_0$

Table 2-6 Housing dimensions according to Nechleba, Quartz and Raabe for horizontal axis Pelton turbines

Where B_c is the casing width, d_0 the jet diameter and B the bucket outer width.

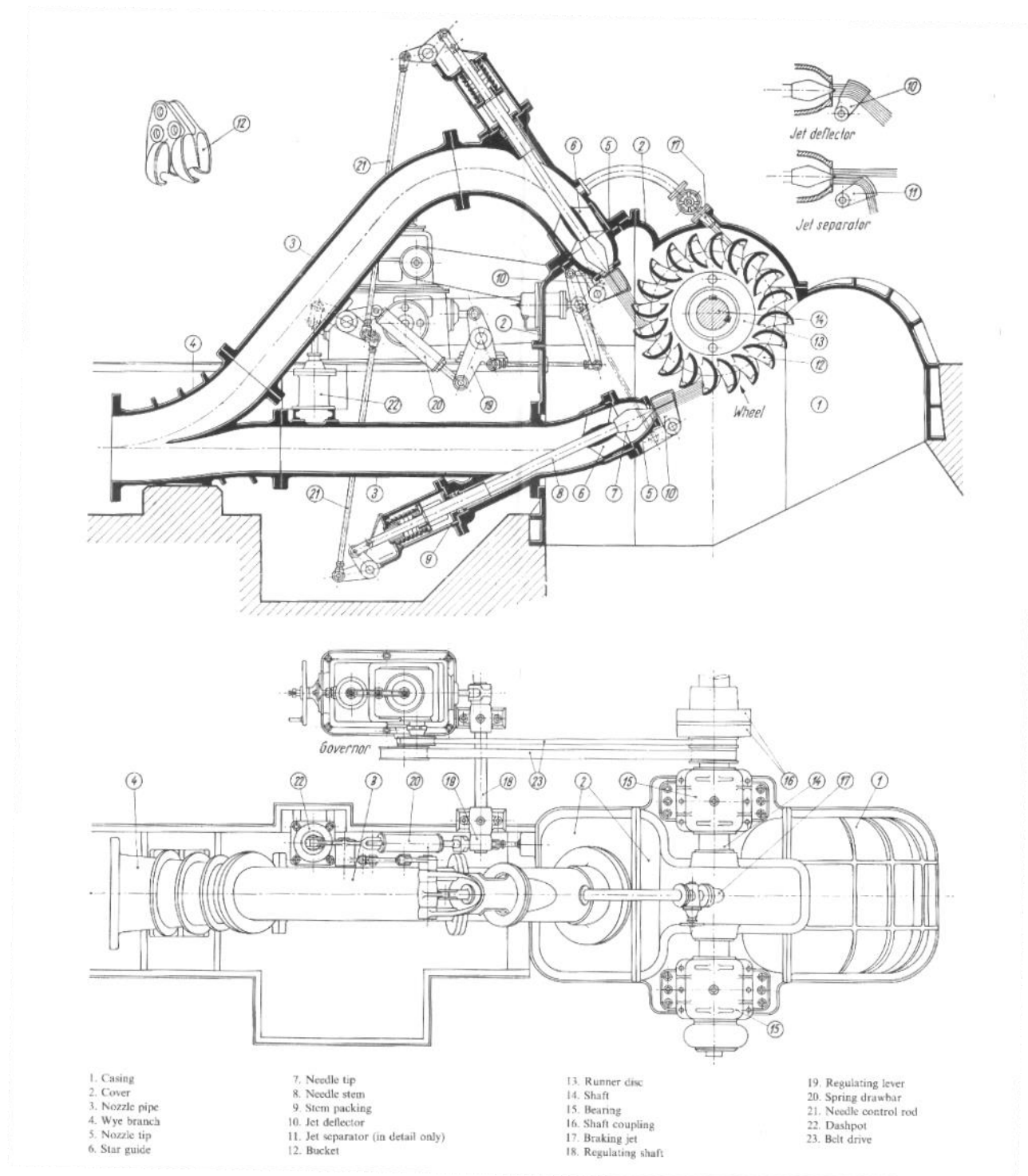


Fig. 2-32 Horizontal axis Pelton turbine components [70]

More recently, Vienna University of Technology published a paper [71] that investigated the influence of the casing design by observing the flow in Pelton turbine casings. The researchers made a systematic classification of the flow distribution by observing the flow in a rectangular case, details of which are outlined in Fig. 2-33.

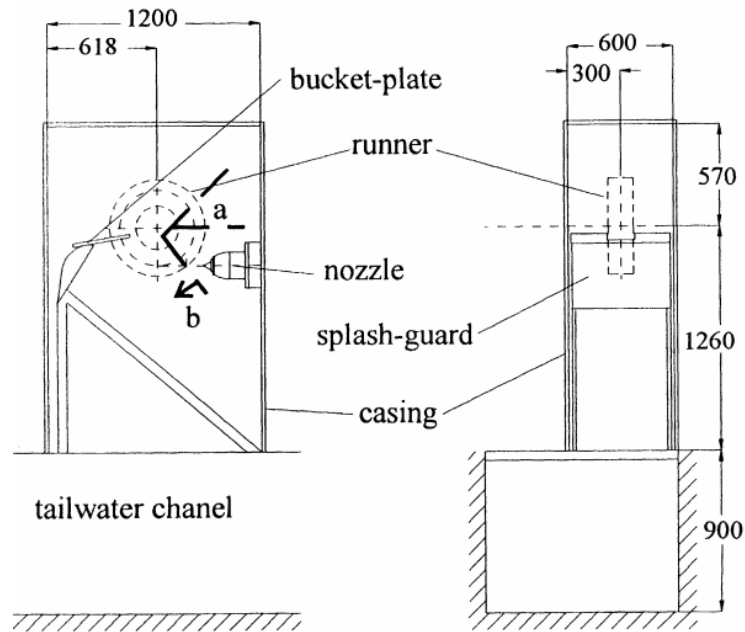


Fig. 2-33 Details of the rectangular casing from [71]

The paper categorised the flow patterns observed into four criteria:

1. Fig. 2-34 (a), here the pattern is independent of the flow and can only be observed at low rotational speeds. (low unit speed – optimal unit speed)
2. Fig. 2-34 (b), here the pattern is independent of the flow and can only be observed in the optimal range of operating rotational speeds. (optimal unit speed – high unit speed)
3. Fig. 2-34 (c), here the pattern is dependent on the flow and is observed at high rotational speeds beyond the optimal.
4. The final category is that, which can be observed at the runaway speed of the turbine.

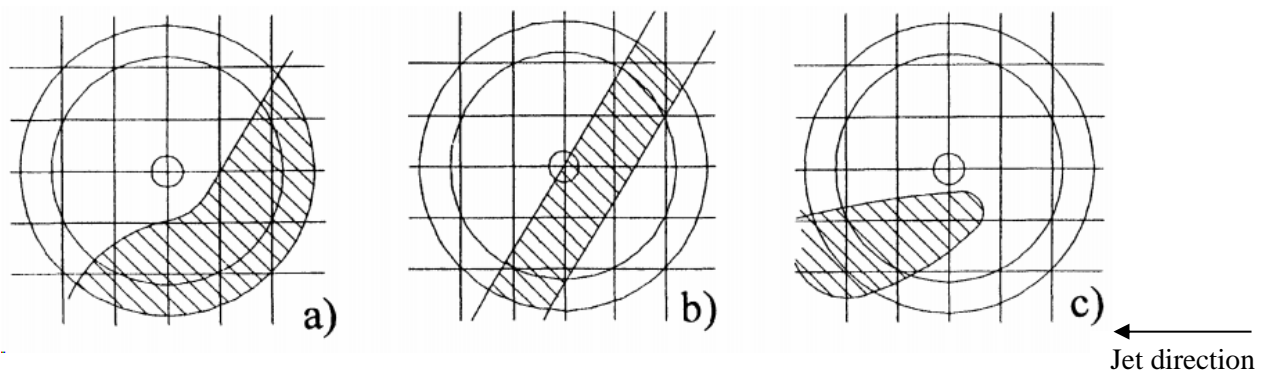


Fig. 2-34 Splash water distribution at the wall of the rectangular casing [71]

Following this a second study varied both the radius, R_g , and width of a cylindrical domed shaped casing, and also the width of a rectangular casing, examples of which are shown in Fig. 2-35 and Fig. 2-36 respectively.

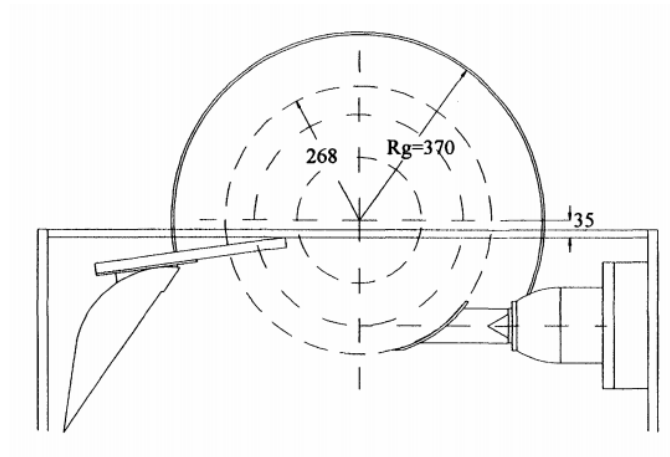


Fig. 2-35 Cylindrical dome [71]

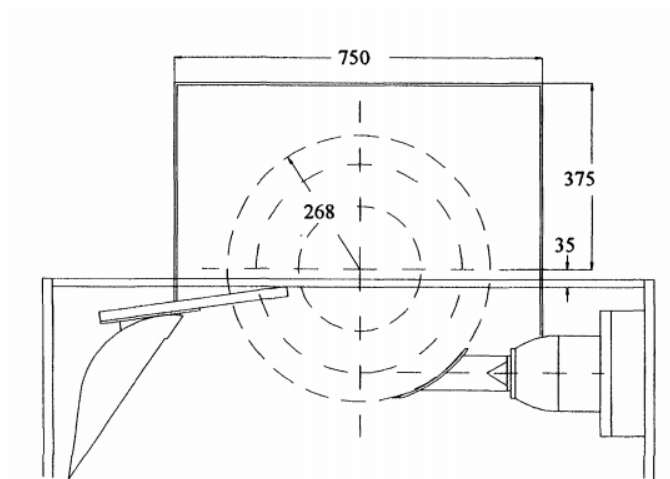


Fig. 2-36 Rectangular dome [71]

It was demonstrated that a cylindrical dome with small axial and radial width or a rectangular case with a small width is suitable for high flows. It was found that for most scenarios the turbine efficiency was nearly equal, therefore the authors defined the ‘efficiency factor’ as being radius of curvature at the peak of the efficiency chart, high efficiency factor means high efficiency away from the optimum. The case with the highest efficiency factor was the cylindrical dome with a small width and large R_g .

Later, splash water in the casing of the Pelton turbine was documented using a PIV system and the priority of the project was the analysis of the influence of different guiding plates on the efficiency of the turbine. The photos recorded provided useful information on the flow direction along the walls of the casing. PIV was chosen to give a more fundamental analysis of the flow direction and velocities of the droplets leaving the bucket and travelling in the casing [72]. This

paper provided the method undertaken in PIV documentation, however no comments are made about the findings or guidelines listed for casing design, simply anticipated as future work.

Upgrade works by Staubli et al. [15] at the Swiss hydro plant, HPP Rothenbrunnen, have included the provision to document and analyse the casing flows in detail and areas where flow returns from the casing to the runner and jet were detected and eliminated by modifying the casing locally. In addition, the injectors were replaced with steeper angles, which led to a combined efficiency improvement of 1.4%. The efficiency increase is clearly correlated with less disturbances seen on the jet surface, less jet dispersion and a smaller amount of splashing water.

Modern Pelton turbine casings tend to forgo the rather elaborate casing design depicted in Fig. 2-20 and consist generally of a more rectangular shape with at least two sides perpendicular to the axis of the jet generally separated by the angle between the injectors, usually 80° , as shown in Fig. 2-37. Experimental experience has shown that it is often necessary to include a certain number of internal casing components, known as baffles, to help remove vagrant spray away from the runner and jet, these include but not limited to; injector shrouds, side shrouds and as noted by Nechleba [5] ‘a wiper must be arranged behind the discharge side of the wheel’ to reduce ventilation losses, this also stops vagrant spray entering the roof of the casing.

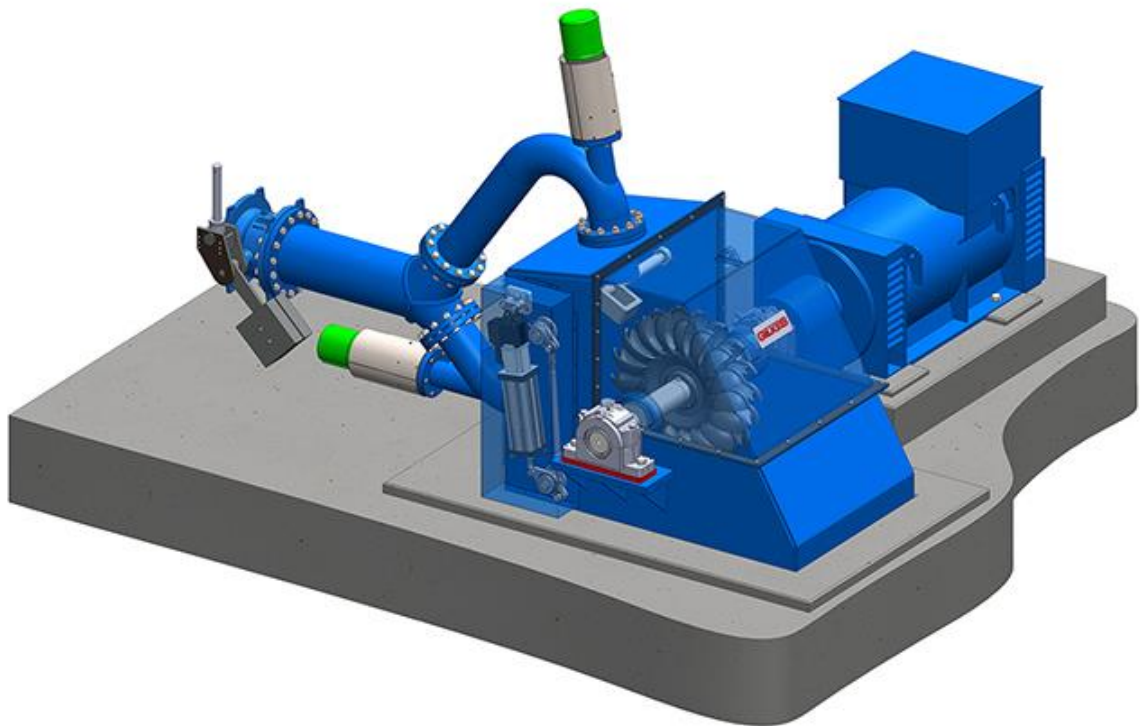


Fig. 2-37 Gilkes twin jet horizontal axis Pelton turbine [73]

Due to the heavy computational resource requirements to compute accurately a Pelton turbine using an Eulerian multiphase CFD model researchers have now developed particle based methods. One such method is Smoothed Particle Hydrodynamic (SPH), a meshless method, whereby the motion equations are solved using a set of arbitrarily distributed nodes, so called particles, which allows the use of a Lagrangian formulation [74]. Marongiu first used SPH to model the free surface flow in a Pelton bucket by comparing the computed results with the obtained pressure profile distribution obtained from experiments and ANSYS CFX [75]. Later the accuracy and stability of the SPH model was improved by adopting a hybrid SPH – Arbitrary Lagrangian-Eulerian (ALE) model [76].

Most recently Neuhauser in a thesis from Ecole Centrale de Lyon (ECL) [77] and Rentschler et al. [78] both of Andritz Hydro have documented how the in-house SPH-ALE solver can be used to model the complex free surface flow in the casing of a Pelton turbine, with the aim of evaluating the potential for improvement of efficiency by additional casing components in rehabilitation project. Examples of the water sheets are shown in Fig. 2-38 and Fig. 2-39.

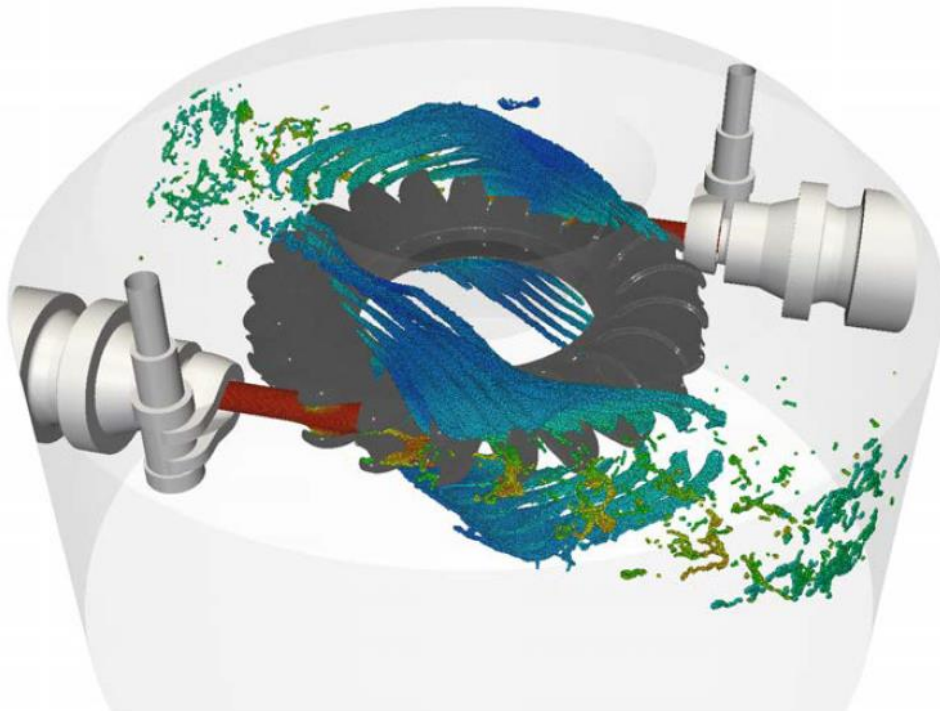


Fig. 2-38 Free surface flow in a Pelton casing obtained by a SPH-ALE software of Andritz Hydro [79] (n.b. no velocity scale available in the paper)

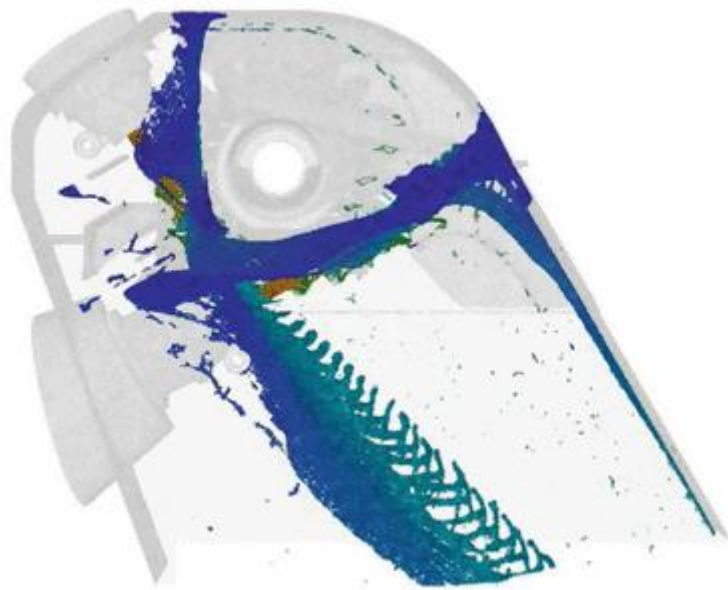


Fig. 2-39 Free surface flow in a Pelton casing obtained by a SPH-ALE software of Andritz Hydro [77] (n.b. no velocity scale available in the paper)

While Rentschler et al. notes that it is technically feasible to simulate free surface flows inside a Pelton turbine with classical mesh-based CFD tools, the tracking of the water inside the casing with adequate resolution is very computationally demanding. Additionally, mesh-based techniques naturally diffuse the free surface and producing a mesh quality, which reduces the influence on the simulated flow, requires time and expertise. Therefore, these intrinsic characteristics push classical CFD tools to the limit of their cost-effectiveness. However, SPH does not come without its drawbacks, firstly it is a relatively new concept and there are no commercially and fully validated codes available. Independent researchers have developed their own SPH codes, which requires specific knowledge of coding in addition to fluid dynamics. Indeed, Andritz note that the in-house SPH-ALE algorithm has been in development for twelve years.

2.7 Computational Fluid Dynamics

Computational Fluid Dynamics (CFD) is a branch of fluid mechanics that uses computers to implement numerical methods to obtain a solution for the general fluid flow equations. Anderson describes CFD as the art of replacing the integrals or partial differential equations (PDE's), which describe the conservation of mass, momentum and other scalar quantities into discretised algebraic forms, which, in turn may be solved numerically [80]. The equations have a strong dependence on the fluid properties, are coupled and time dependant and as such no

analytical solution has yet been found to resolve them fully, and the Clay Mathematical Institute offers \$1 million to anyone who can do so.

The desired approach in the Eulerian frame of reference uses a control volume, where the flow within a certain geometric volume is studied and the equations are recast in the conservative form allowing integration or differentiation over the control volume. Typically, numerical methodologies can be classified according to several features such as [81]:

- Discretisation of the space: the computational grid or mesh⁴ is generated and consists of a number of discrete control volumes or cells.
- Discretisation of fluid flow equations: the conservative form of the equations are expressed as a series of algebraic equations used to approximate the fluid flow properties at the nodes of the mesh.
- Time-integration method.
- Method of pressure-velocity-density coupling: an equation for pressure is derived numerically from a combination of the continuity and momentum equations.

Some of the methods are listed in Fig. 2-40 below:

⁴ Very often it will be called the ‘grid’, this is in my mind is due to historical reasons. In the early stages of development, CFD could only be used for 2D problems, however ‘mesh’ seems a more appropriate name when considering 3D geometries.

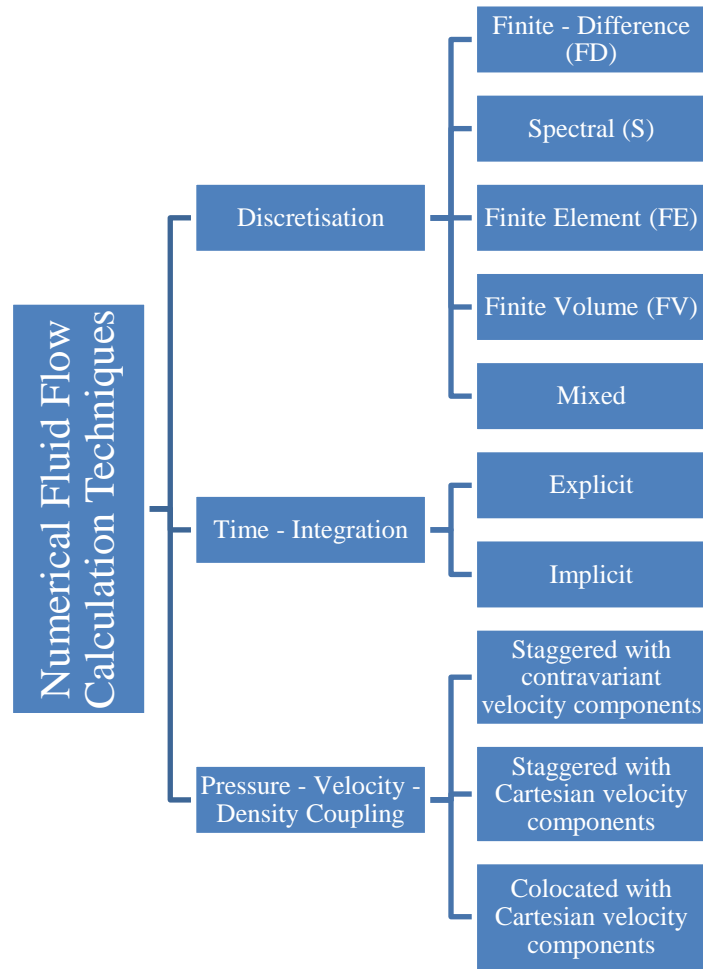


Fig. 2-40 Numerical Fluid Flow calculation techniques [81]

2.7.1 A Note on the ANSYS® FLUENT® Solver

The ANSYS® FLUENT® solver used in this study is a general purpose commercial CFD software. It is capable of handling flow types that involve both laminar and turbulent regions, single phase and multiphase, compressible and incompressible, steady state and transient. The FLUENT solver uses a Finite Volume Method (FVM) based approach and can handle both 2D and 3D meshes in an unstructured manner and is therefore capable of supporting meshes with arbitrary element shapes (in 2D: triangular/quadrilateral cells and in 3D: tetrahedral/hexahedral/pyramid/wedge/polyhedral cells or a combination of cell types known as hybrid meshes) [82].

The following subsections will therefore cover informative description pertinent to the settings that are available and will be implemented in FLUENT. The author directs readers to the ANSYS FLUENT solver theory guide [82] for the full mathematical detail and descriptions of the techniques used by the solver.

2.7.2 Fundamental Governing Equations

In fluid dynamics, there are three governing equations for compressible flow, which may be summarised as follows:

- i. Conservation of mass or the Continuity equation, which states that the mass of a closed system will remain constant over time, that mass is neither destroyed nor created;

$$\frac{\partial \rho}{\partial t} + \nabla \cdot (\rho \mathbf{V}) = 0 \quad (2.26)$$

where ρ is the fluid's density [kg/m³] and \mathbf{V} the velocity vector.

- ii. Conservation of momentum, is obtained from Newton's Second Law and states that the rate of change of momentum of a system is equal to the sum of the forces on the system;

$$\frac{\partial(\rho \mathbf{V})}{\partial t} + \rho(\mathbf{V} \cdot \nabla) \mathbf{V} = -\nabla p + \nabla \cdot \tau_{ij} + \rho \mathbf{g} \quad (2.27)$$

Where: p is the static pressure, τ_{ij} is the viscous stress tensor and $\rho \mathbf{g}$ is the gravitational external body forces per unit volume respectively.

Newtonian fluids, such as water and air both exhibit a linear relationship between the stress component and the velocity gradient. Moreover, if the fluid is isotropic, i.e. the fluid properties are independent of direction, the stress and velocity components can be related using only two fluid properties, the dynamic viscosity, μ [Pa s], and the second coefficient of viscosity, λ . The stress-velocity gradient relations, sometimes known as the constitutive relations, are given in equation (2.28)

$$\tau_{ij} = \left(\frac{\partial v_i}{\partial x_j} + \frac{\partial v_j}{\partial x_i} \right) + \delta_{ij} \lambda (\nabla \cdot \mathbf{V}) \quad (2.28)$$

Where $\lambda = -\frac{2\mu}{3}$ and δ_{ij} is the Kronecker delta function, $\delta_{ij} = 1$, if $i = j$ and $\delta_{ij} = 0$, if $i \neq j$, with indices i and j representing the three dimensional space.

The final law:

- iii. Conservation of energy, is obtained from the First Law of Thermodynamics, which states that the total energy of an isolated system remains constant.

However, the energy conservation only needs resolving for flows involving heat transfer or compressibility, since flows within impulse turbines can be considered incompressible⁵ several

⁵ The International Standard states that the speed of sound is 343 m/s in dry air at mean sea level, standard temperature of 20°C [121]. Later it will be shown in the thesis that the maximum flow velocity in the simulation is 34.31 m/s. The effects of compressibility are negligible when the Mach number ≤ 0.1 [122]

simplifications can be made. For an incompressible fluid, equations (2.26) and (2.27) simplify to the following forms:

$$\nabla \cdot \mathbf{V} = 0 \quad (2.29)$$

$$\frac{\partial(\rho \mathbf{V})}{\partial t} + \rho(\mathbf{V} \cdot \nabla) \mathbf{V} = -\nabla p + \mu \nabla^2 \mathbf{V} + \rho \mathbf{g} \quad (2.30)$$

For neatness the incompressible system of fluid equations have been expressed as two equations (2.29) and (2.30), however eventually will be considered as a series of four equations comprising four variables. Three of the equations regarding the momentum balance and one resulting from the continuity equation, while the unknown variables are the three components of velocity (in Cartesian or cylindrical coordinate system) and the static pressure.

2.7.3 Implementation of Eulerian CFD solvers

As mentioned previously there is no analytical solution for the non-linear partial differential equations that describe the conservation laws in the Navier-Stokes equations, therefore the time and space has to be discretised in order to obtain numerical solutions. A commonly used approach in the FVM is the ‘method of lines’ [83]. In this method the PDE’s for the conservation of mass and momentum are integrated over the space to obtain an algebraic equation. The computer then solves the algebraic equation by iterative methods resulting in a value of the flow field at discrete locations in space. The general procedure for solving the problem using CFD is as follows [82]:

- Division of the domain into a number of discrete control volumes, by creating a suitable number of mesh cells at preselected points called nodes.
- Integration of the governing equations by converting them to algebraic equations at the interior node of the cells of the mesh for the discrete dependent variables such as velocities, pressure, temperature, and conserved scalars.
- Linearisation of the discretised equations and solution of the resultant linear equation system to yield updated values of the dependent variables.

This whole calculation process requires several iterations since the governing equations are solved sequentially and therefore the solution must satisfy all of the equations. The whole solution procedure for each iteration can be neatly summarised in the following flow diagram shown in Fig. 2-41.

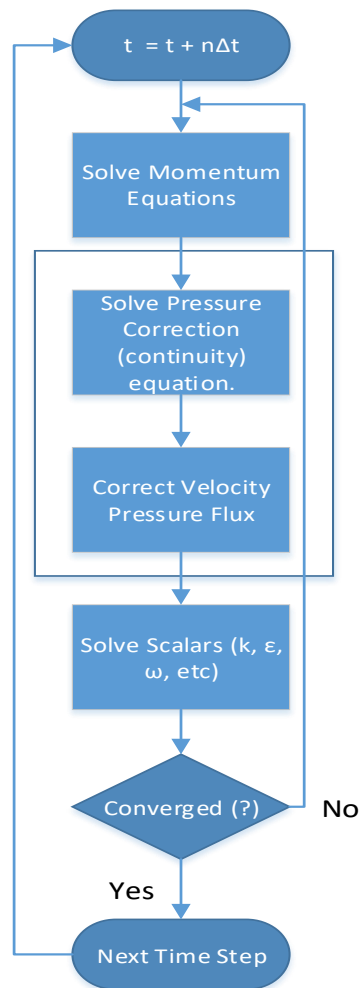


Fig. 2-41 Overview of the iterative solution method

Fig. 2-42 introduces the two fundamental concepts in the discretisation of the space and time domain. The first is the concept of space discretisation, where the domain has been subdivided into a number of control volumes, called the mesh. The second is time discretisation, where the solution time is broken down into a number of timesteps Δt .

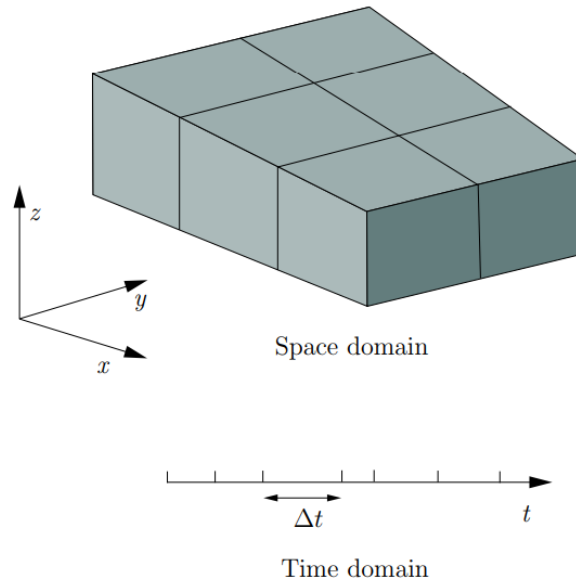


Fig. 2-42 Discretisation of the solution domain [84]

2.7.3.1 *Spatial discretisation*

Since the FLUENT solver uses the FVM, each control volume (cell) within the mesh has a node at its centre, and the variables of interest, such as velocity and pressure are stored at the centre of the cells, known as collocated arrangement. In Fig. 2-43 two typical cells are bounded by faces, f , the cells have a single face that divides the two, known as internal faces, and boundary faces which correspond with the boundary of the domain.

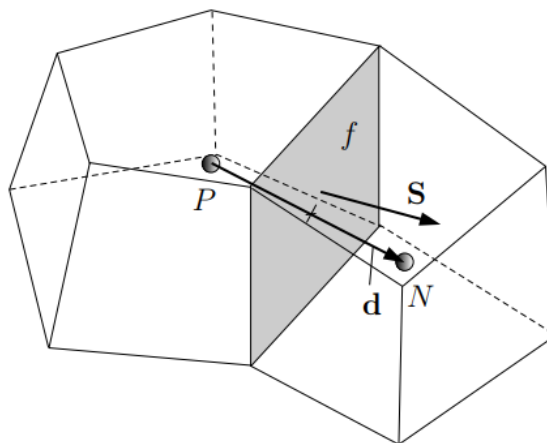


Fig. 2-43 Two typical cells with descriptive parameters in the FVM discretisation [84]

In the description above \mathbf{S} is the face area vector normal to the face with magnitude equal to the area of the face. It points outwards from the cell of interest P into the neighbouring cell N . The

unit vector \mathbf{n} normal to the face is defined as and denotes the vector between P and N , i.e. $\mathbf{d} = \mathbf{x}_N - \mathbf{x}_P$.

Consider the unsteady transport equation (2.31) for any tensor quantity ϕ for the arbitrary control volume V ;

$$\int_V \frac{\partial \phi}{\partial t} dV + \oint \mathbf{v} \phi \cdot d\mathbf{S} = \oint \Gamma_\phi \nabla \phi \cdot d\mathbf{S} + \int_V S_\phi dV \quad (2.31)$$

Where: Γ_ϕ is the diffusion coefficient for ϕ , and S_ϕ is the source of ϕ per unit volume.

In order for the computer to solve this continuous function it must be converted to an algebraic form, which is accomplished by discretisation yielding the following equation:

$$\frac{\partial \phi}{\partial t} V + \sum_f^{N_{faces}} \mathbf{v}_f \phi_f \cdot \mathbf{S}_f = \sum_f^{N_{faces}} \Gamma_\phi \nabla \phi_f \cdot \mathbf{S}_f + S_\phi V \quad (2.32)$$

Where N_{faces} is the number of faces enclosing the cell, ϕ_f is the value of ϕ convected through the cell face and V is the cell volume.

Since dependant variables are stored at the cell centres, however from (2.32) the face values are required for the convection terms, the values at cell centres must be interpolated. FLUENT has a number of different schemes for accomplishing this and the accuracy of the solution is highly dependent on selecting the correct scheme for the application. The most widely used is an upwind scheme, which develops a Taylor series expansion of the computed of the cell-centred value about the cell centroid.

The simplest upwind scheme is the First Order Upwind Differencing, which was first proposed by Courant, Issacson and Rees [85]. The scheme derives quantities at cell faces that are determined by assuming that the cell-centre values of any field variable represent a cell-average value and hold throughout the entire cell. The value of ϕ_f is determined according to the direction of flow, such that;

$$\phi_f = \begin{cases} \phi_P & \text{for } F \geq 0 \\ \phi_N & \text{for } F < 0 \end{cases} \quad (2.33)$$

Where: F can be taken as the flow direction.

The discretised transport equation can then be rearranged to provide an expression for the concentration at the centre of cell P as a function of the concentrations in the surrounding cells and can be simplified as follows:

$$a_P \phi = \sum_f^{N \text{ faces}} a_f \phi_f + b \quad (2.34)$$

Where the subscript f refers to the neighbouring cells (i.e. sum of ϕ_f through all faces (4 in 2D and 6 in 3D)), and a_P and a_f are the linearised coefficients for ϕ and ϕ_f .

Similar equations arise for each cell in the grid creating a set of algebraic equations and a point implicit (Gauss-Seidel) linear equation solver is then used to solve the equations by sweeping through the domain cell-by-cell in an iterative manner. For large meshes however it can take a very long time to see the effect of values at the domain boundaries, therefore an algebraic multigrid (AMG) method is employed to speed up convergence. The AMG uses a number of meshes going from fine (original mesh) to coarse. The solution on the coarse mesh is used initially to account for the influence of the boundaries and far neighbouring cells and superimposed on the fine mesh from which the final solution is obtained. The AMG method only accelerates the convergence and does not influence the final result.

The same procedure for the discretisation of the momentum equation follows from the method used to solve the convection-diffusion equations as outlined above. By replacing ϕ with u in equation (2.34), this results in the linearised momentum equation in direction, x .

$$a_P u = \sum_f^{N \text{ faces}} a_f u_f + \sum p_f A \cdot \hat{i} + S \quad (2.35)$$

It is evident that the pressure gradient, p_f appears in the momentum equation, however FLUENT stores the velocity and pressure in the centre of the computing cells. Thus, solving the momentum equation system requires the value of the pressure levels on the boundary surface between adjacent cells. As a result, the pressure estimate is first required to then resolve the momentum equation system. The estimation of the pressure field is using by using some interpolation pattern. If the VOF multiphase model (described in 2.7.4.1) is used, the available interpolations patterns for finding the pressure values at the cell boundaries are PRESTO! and body force weighted. The former is preferred for use in high-turbulence flows, large Reynold numbers, steep pressure gradients, and flow-through volumes with strongly curved domains. In contrast, the second method is preferred in flows that are affected by strong forces exerted throughout the body (such as gravity or electromagnetic forces).

Following the sequence in the flow diagram as described in Fig. 2-41 the discretisation of the continuity equation takes place after to the discretisation of the momentum equation and more specifically the pressure is calculated from the continuity equation. However, since the flow is

considered incompressible, density does not appear in the continuity equation and therefore pressure does not appear explicitly in the continuity equation.

Therefore, numerous algorithms have been developed to overcome this issue, the algorithms are iterative and generally consist of momentum and pressure corrector steps. The momentum predictor refers to the calculation of a new velocity field with the momentum equations, based on the pressure of the previous timestep or the initial guess. The pressure corrector on the other hand, corresponds to a correction of the pressure field with the help of the continuity equation [30].

Within FLUENT there are a number of different coupling algorithms (solved either in a segregated or fully coupled manner), however within this thesis the segregated SIMPLE algorithm was implemented. The SIMPLE (Semi – Implicit Method for Pressure Linked Equations) algorithm was developed by Spalding and Patankar at Imperial College in the early 1970's [86]. The solutions steps can be summarised as follows;

1. Guess a pressure field
2. Solve the momentum equations using this pressure field, thus obtaining velocities which satisfy momentum, but not necessarily continuity
3. Construct continuity errors for each cell : inflow – outflow
4. Solve a pressure-correction equation, p' , by substituting the continuity errors into the continuity equation

$$a_p p' = \sum_f^{N \text{ faces}} a_f p'_f + \sum J_f^* \quad (2.36)$$

Where $\sum J_f^*$ is the net flow rate into the cell.

5. The pressure-correction equation may be solved using the AMG method. Once a solution has been adjust the pressure field and face flowrate can be calculated using:

$$p = p^* + \alpha_p p' \quad (2.37)$$

$$J_f = J_f^* + d_f (p'_{c0} - p'_{c1}) \quad (2.38)$$

Where p^* is the guessed pressure term, α_p is the under-relaxation factor for pressure, p'_{c0} and p'_{c1} are the corrected pressures within the two cells on either side of the face and term d_f is a function of the average of the momentum equation a_p coefficients for the cells on either side of face f .

6. Adjust the velocity fields corresponding, thus obtaining velocities which satisfy continuity, but not momentum.
7. Go back to step 2, and repeat with the new pressure field. Repeat until continuity and momentum errors are acceptably small.

2.7.3.2 Temporal discretisation

Since the governing equations must be discretised in both space and time, temporal discretisation is therefore necessary. For transient simulations the discretisation of the time derivative term, $\frac{\partial \Phi}{\partial t}$ in equation (2.32), is performed by integration of every term in the differential equations over a timestep, Δt .

In FLUENT both implicit and explicit temporal discretisation is available, however using the Pressure Based solver, which will be described in section 3.4.1, only Euler implicit time differencing is available.

A generic expression for the linear variation of Φ within a timestep is given by

$$\int_V \frac{\partial \Phi}{\partial t} dV = F(\Phi) \quad (2.39)$$

If the time derivative is discretised using backward differences, the first order accurate temporal discretisation is given by:

$$F(\Phi) = \frac{\Phi^{n+1} - \Phi^n}{\Delta t} \quad (2.40)$$

And second order discretisation is given by:

$$F(\Phi) = \frac{3\Phi^{n+1} - 4\Phi^n + \Phi^{n-1}}{\Delta t} \quad (2.41)$$

Where Φ is a scalar quantity, $n+1$ is the value at the next time level, $t + \Delta t$, n is the value at the current time level, t , and $n-1$ is the value at the previous time level, $t - \Delta t$.

One method is therefore to evaluate $F(\Phi)$ at the future time level and therefore the implicit method implies that Φ^{n+1} in a given cell is related to Φ^{n+1} in a neighbouring cell through $F(\Phi^{n+1})$:

$$\Phi^{n+1} = \Phi^n + \Delta t F(\Phi^{n+1}) \quad (2.42)$$

Equation (2.42) can be solved iteratively by initialising Φ^i to Φ^n and iterating equation (2.43), until Φ^i converges, at which point Φ^{n+1} is set to Φ^i .

$$\Phi^i = \Phi^n + \Delta t F(\Phi^i) \quad (2.43)$$

2.7.3.3 Turbulence modelling

Turbulent flows are universal and are characterised by unsteady, aperiodic motion in which transported quantities such as mass and momentum fluctuate in space and time. Richardson noted that turbulent flow is composed of eddies of different sizes. The size of the eddies define a characteristic length scale, which are also characterised by flow velocity and time scales dependent on the length scale [87]. For most engineering applications the full resolution of these fluctuations are too computationally expensive to simulate directly, specifically the non-linear convective acceleration term, $(\mathbf{V} \cdot \nabla)\mathbf{V}$, therefore the concept of Reynolds averaging can be introduced. The Reynolds-averaged Navier Stokes (RANS) equations yield six additional unknown variables, which require supplementary turbulence models to ‘close’ the system of equations.

A modified form of the continuity and momentum equation in (2.29) and (2.30) can be described in (2.46) and (2.47) respectively, where the fully resolved fluctuating flow variable, Φ is decomposed into steady mean component, $\bar{\Phi}$, and a time varying fluctuating component, Φ' , which itself has zero mean value [88]:

$$\Phi(t) = \bar{\Phi} + \Phi' \quad (2.44)$$

Where;

$$\bar{\Phi} = \frac{1}{\Delta t} \int_0^{\Delta t} \Phi(t) dt \quad (2.45)$$

Substituting this expression for the form of the flow variables into the continuity and momentum equations and taking the time average yields the so-named RANS equations:

$$\nabla \cdot \mathbf{V} = 0 \quad (2.46)$$

$$\frac{\partial(\rho \mathbf{V})}{\partial t} + \rho(\mathbf{V} \cdot \nabla)\mathbf{V} = -\nabla p + \mu \nabla^2 \mathbf{V} - \rho \frac{\partial}{\partial x_i} (\overline{u'_i u'_j}) + \rho \mathbf{g} \quad (2.47)$$

Where \mathbf{V} is the time mean velocity, p is the time mean static pressure, and u'_i denotes the fluctuating velocity component and the overbar represents the time average. Here, the Reynolds stresses $-\rho(\overline{u'_i u'_j})$ can be related to the mean velocity gradients by the Boussinesq hypothesis [89] in (2.48)

$$-\rho(\overline{u'_i u'_j}) = \mu_t \left(\frac{\partial V_i}{\partial x_j} + \frac{\partial V_j}{\partial x_i} \right) - \frac{2}{3} \rho k \delta_{ij} \quad (2.48)$$

Where the turbulent kinetic energy, $k = \frac{1}{2}(\overline{u'^2} + \overline{v'^2} + \overline{w'^2})$ and μ_t is the turbulent viscosity, typically calculated as a function of the transport variables in the turbulence closure equations.

The two-equation models are most commonly employed methodology for solving the RANS equations and the FLUENT solver theory guide [82] provides further mathematical details on the composition of each model along with a list of the closing coefficients, which are used by the solver. The turbulence models under consideration in this study are briefly outlined as follows:

The Realisable k- ϵ model attempts to account for the different scales of motion through changes to the formulation for the turbulent viscosity. This differs significantly from the standard k- ϵ model where the eddy viscosity is determined from a single turbulence length scale and the coefficient of viscosity, C_μ is a constant rather than a variable. These improvements lead to a better ability to predict the spreading of jets, and capture the mean flow of complex structures involving rotation, separation, recirculation and flows undergoing severe pressure gradients.

The k- ω based shear stress transport (SST) by Menter [90] provides the advantages of both the k- ω model [91] (in the near wall region) and the k- ϵ in the free stream region. Therefore, the model benefits from using a low-Reynolds number near the wall without extra damping functions near the wall. By switching to the k- ϵ formulation in the free stream it limits the k- ω problem that the model is too sensitive to the inlet free-stream turbulence properties. The SST model also presents a more superior prediction of the shear stress transport behaviour by limiting the over prediction of eddy viscosity. The model has found extensive application in flows with adverse pressure gradients [82].

2.7.4 Multiphase Modelling

Impulse turbines are naturally multiphase and within the Pelton turbine two primary phases are to be modelled; air and water. The air and water interact with each other with high complexity through the interface, often referred to as the ‘free-surface’. In cases where the flow is highly turbulent, or where surface tension is no longer dominant for example, this interface can break down leading to air entrainment and droplet formation respectively. The entrained air alters the properties of the flow, namely the density and compressibility and as a consequence the turbulent nature of flow, and the droplet formation requires the modelling of the discrete particles as an additional third phase.

In most CFD solvers the free surface is modelled by approximation, this is due to the computational effort required to completely resolve the 3D Navier-Stokes equations. The nature of time marching simulations is that numerical viscosity (often called numerical or false

diffusion) smears sharp interfaces between phases. Consequently, in cases that involve complex fluid dynamics, the solution of the complete Navier-Stokes is requisite and approximation techniques to track or capture the interface are needed. Several methods are available to predict the location of the free-surface using both the Eulerian frame (in the case of static meshes and dynamic meshes) and also mesh free methods in the Lagrangian frame, summarised in Fig. 2-44.

Fig. 2-44 demonstrates how the interface can be constructed using two sub-techniques; 1) interface tracking, where the interface is modelled as a sharp boundary between the two fluids and the motion is explicitly tracked through the domain (b, c) and 2) interface capturing, where the interface is implicitly represented on a regular fixed mesh by marking the fluid on both sides of the interface (d, e, f).

The moving mesh method offers the advantage of treating the interface as a sharp discontinuity, which can lead to a more accurate representation, however when the interface undergoes large deformations significant errors can be introduced due to the correspondingly large mesh distortions. Furthermore the requirement for remeshing introduces significant simulation time. The front tracking method, where the flow is computed on a stationary mesh while the dynamic evolution of the interface (front) is explicitly tracked using Lagrangian-based approach also is hindered by computational time due to the many necessary operations to delete, insert reordering of the interface particles to preserve the resolution of the interface.

Interface-capturing methods offer significant advantages since they implicitly represent the interface on a regular fixed mesh by marking the fluids on either side of the interface using the following methods; d) virtual particles (marker and cell method), e) and indicator function usually volume fraction (Volume of Fluid (VOF) method), and f) a signed distance function (level set method). As the name implies the marker and cell method uses particles to mark the fluids, these are coupled and advected by the flow, the downside of this method is the high cost of the additional transport equations for the particles, and nevertheless this method does enforce mass conservation. The VOF method uses an indicator function, which physically represents the volume fraction of the one of the two phases, where the free surface is represented with the cell volume occupied by exactly half of each phase. The VOF method ensure mass conservation and since only one phase needs to be advected through the domain is more computationally efficient, however in coarser meshes the interface sharpness can become diffused over time [92]. Lastly, the level set method uses a signed distance function to represent the interface as a sharp boundary and therefore captures the interface more accurately than the VOF method. However, since it is not inherently mass conservative additional calculations are necessary to correct this leading to additional effort [93]. Based on the above descriptions a decision was

made to use the VOF method for multiphase modelling since it combines the best compromise between accuracy and simulation time.

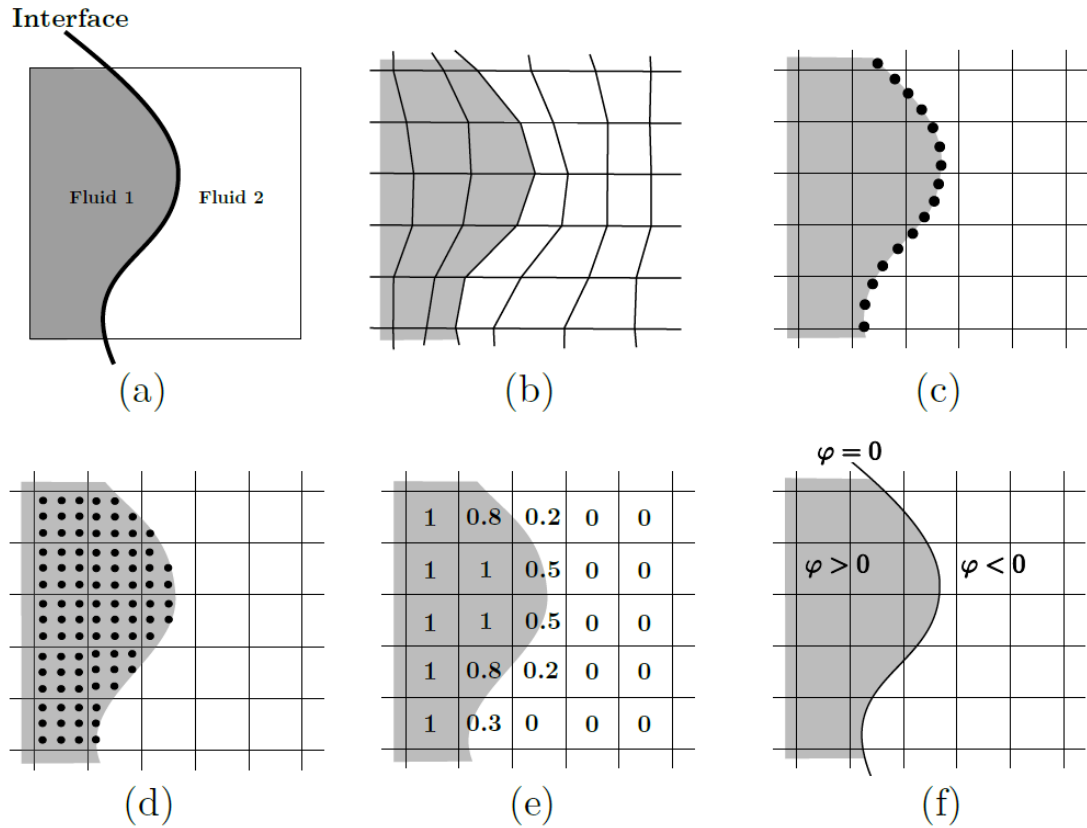


Fig. 2-44 A schematic representation of a portion of a fluid-fluid interface and related methods used to model its shape and motion. (a) Interface between two fluids. Interface tracking methods such as (b) the interface-fitted moving mesh method, and (c) the front tracking method. Interface capturing methods such as (d) the marker-and-cell method, (e) the volume-of-fluid method, and (f) the level-set method [94]

2.7.4.1 Volume of Fluid

Volume methods the entire domain is marked by an indicator function. An indicator function is defined on a set X (in this case the mesh cells) that indicates membership of an element in a subset of A of X , having the value 1 for all elements of A (those where one phase is totally present) and value 0 for all elements of X not in A (those where the same phase is totally not present). In the Volume method the exact position of the interface is a posteriori and therefore special techniques that form part of the solution algorithm, need to be applied to capture the interface. In the case for FLUENT the indicator function is known as the volume fraction and it is implemented by Hirt and Nichols' Volume of Fluid (VOF) algorithm [95]. Fig. 2-44 gives an example of how the VOF records the interface in the cell as indicated by the volume fraction distinguishing the presence of the phase fluid. The volume fraction of one of the two fluids can

be defined as, α_n , which varies smoothly between 0 and 1. The sum of the volume fraction of the n phases must therefore be:

$$\sum_{n=1}^2 \alpha_n = 1 \quad (2.49)$$

The free surface interface can be defined when the value of $\alpha_n = 0.5$. The indicator function is evolved using the following advection equation:

$$\frac{\partial \alpha}{\partial t} + \nabla \cdot (\alpha_n \mathbf{V}) = 0 \quad (2.50)$$

The VOF has a clear advantage over a number of other techniques as the volume of fluid occupying the cell enforces continuity as that volume cannot be occupied by the other phase. The flow properties (i.e. density, viscosity) are a weighted function of the properties of both phases and since these properties from the continuity equation are then used to solve a single momentum equation through the domain, the attained velocity field is shared among the fluids. The precision of the VOF model is therefore dependant on the interface reconstruction technique and the advection scheme selected, which will be explored in more detail in 3.3.2.2. In summary the VOF offers the best compromise between the accuracy of the reconstruction of the interface and simulation time.

2.8 Summary of Literature

After Lester Pelton had filed a patent for the Pelton wheel in 1880, for the following century little work was carried out to improve the understanding of and further develop Pelton turbines. The majority of research in the early stages was carried out through experimental testing on a trial and error basis.

Within a Pelton turbine facility there are four major sections of interest for efficiency analysis each with a corresponding flow regime: i) confined steady-state flows in the upstream pipes and the distributor, ii) free jets past the injector, iii) transient free surface flow in the buckets and iv) dispersed 2-phase flow in the casing. The distributor and nozzle play an important role for jet quality, where the efficiency increase is clearly correlated with less disturbances seen on the jet surface and less jet dispersion is very important for both efficiency of the whole system [11]. In recent years trends towards steeper angled injector and nozzles have improved jet quality and efficiency significantly [96] [97]. Likewise, the efficiency of a turbine is affected by the bucket shape, which has already improved significantly since the original Pelton design [12] [13] [14]. Moreover, the water leaving the buckets plays an important role. After exiting from the buckets the flow impacts and travels around the casing walls, some of which may cause interference

with the runner and water jet, reducing the efficiency. The design of the casing as a means to reduce this impact is therefore of interest to manufactures [15].

In the last decade, the advent of computational tools, such as CFD, has inspired a renewed interest in the design and efficiency optimisation of the Pelton runner and injector. By far the most popular CFD software used to model Pelton turbines are the commercial codes developed by ANSYS: CFX and FLUENT [10], since it offers the most accurate results in a reasonable time scale. Furthermore the ANSYS packages are constantly updated and widely used in industry making them very suitable for research purposes and this industrially funded PhD.

The capability of solving impulse turbine related problems that include multiphase with free surfaces has been demonstrated by number of previous studies [17] [18] [26] [54] [98]. However, while it has been noted that it is technically feasible to simulate free surface flows inside a Pelton turbine with classical mesh-based CFD tools, thus far this has only focussed on injector and runner and neglected to simulate the casing, since the tracking of the water inside the casing is a very computationally demanding task. Additionally, mesh-based techniques naturally diffuse the free surface and producing a mesh quality, which reduces the influence on the numerical flow, requires time and expertise making it difficult to produce a CFD model which can accurately simulate the flow within the Pelton turbine in a timescale that makes optimisation studies feasible. These intrinsic characteristics highlight some of the limitations of classical CFD methods, which can only improve in time with faster and more robust computer hardware. As a response to drawbacks of this researchers from ECL working alongside turbine manufacturer Andritz Hydro have employed a meshless based CFD approach called SPH [79]. However, SPH does not come without its drawbacks, firstly it is a relatively new concept and there are no commercially and fully validated codes available. Independent researchers have developed their own SPH codes, which requires specific knowledge of coding in addition to fluid dynamics. Indeed, Andritz note it has taken twelve years to develop the code. Moreover, thanks to the recent improvement in computer hardware, larger two-phase unsteady models can be studied in shorter timescales, despite this the ability to predict the efficiency of the full turbine, including the casing, is pushing towards the limits of CFD. As such there are no available studies in the public domain, documenting how Eulerian mesh based CFD solvers can be used for this task, highlighting the knowledge gap and novelty of this research.

3 Development of the Pelton Casing CFD Model

In this chapter the Gilkes Z120 runner and casing is modelled using the chosen commercial CFD solver, ANSYS FLUENT, at the best efficiency point (BEP). The fluid domain around the runner and within the casing is created using a series of modelling assumptions in order to simplify the model and reduce computation times⁶.

3.1 Choice of Solver

Although still within the early stages of application to impulse turbines, the use of CFD to model the Pelton runner has been documented by a number of researchers. Based on the available literature reviewed in section 2.6, ANSYS CFX and FLUENT is currently the most widely used and experimentally validated CFD codes for Pelton turbine analysis where a jet is interacting with the rotating runner. However, to date there have been no attempts to simulate the flow within the casing using an Eulerian solver, highlighting the knowledge gap and novelty of this work. The challenges that this poses include, highly turbulent energy exchanges, multiphase fluid interactions within the rotating runner geometry and dispersed phase flow within the casing all to be simulated simultaneously.

Nevertheless, the commercial code FLUENT will now be considered herein. The choice of solver was largely influenced by the experience of the industrial sponsors, Gilkes and ultimately CFX and Fluent are very similar, solving the same equations, however CFX has a stronger history for turbo-machinery whereas FLUENT offers more schemes for multiphase modelling. The version of FLUENT was 17.2 and it was used in standalone mode.

3.2 Simulation Setup

This section describes the geometry creation, mesh generation and setup of the runner and casing simulation. Domain geometries were created using SolidWorks 2016 and imported to ANSYS Design Modeller®.

3.2.1 Domain Creation

Based on previous examples outlined in the literature review, several simplifications can be made to the geometry that will have minimal effect on the predicted flow but which significantly reduce the model size and therefore computational time:

⁶ While computational time is an important factor to consider, computer architecture is constantly improving and as such I consider the academic practice of listing solve time and the processor name etc to be pretty much cargo cult science. Therefore, where possible this will be avoided.

- The mounting arms at the rear of the buckets were removed since this will not interact with the water
- Only six (out of the full 18 buckets) were modelled because after some initial noise the flow will interaction with each bucket will be repeatable. Almost all available studies in the literature use a reduced number of buckets [10], and this will be further analysed in section 3.3.1.3.
- Only one side of the injector, runner and casing are modelled since the flow can be assumed to be symmetrical, as shown in Fig. 3-1.

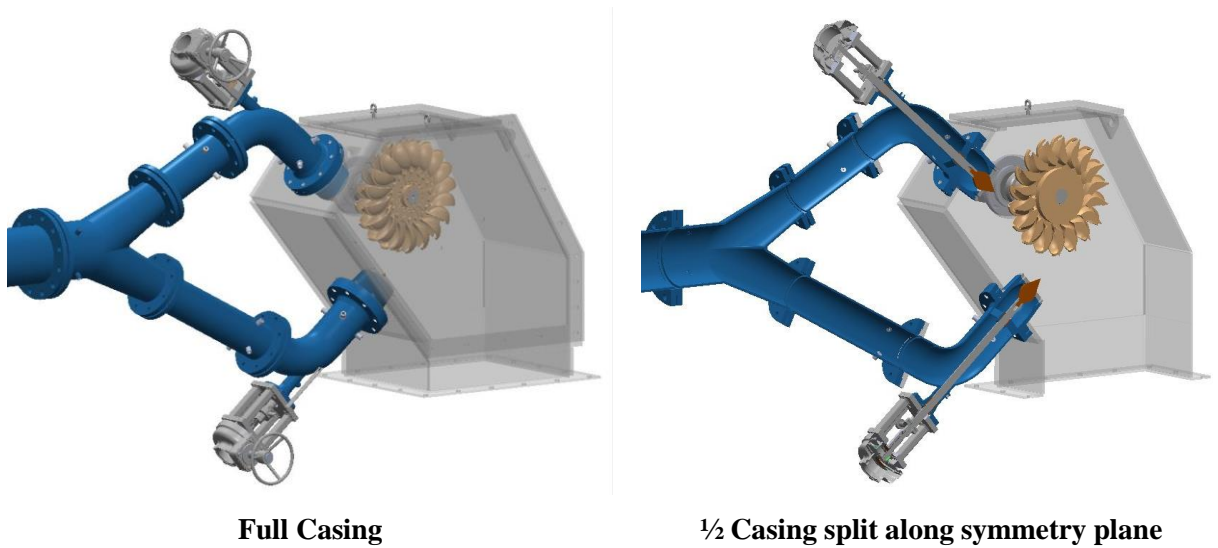


Fig. 3-1 CAD geometry of Gilkes twin jet horizontal axis Pelton indicating symmetry plane

The domain of interest can be split into two sub-domains, namely the rotating runner domain and stationary casing domain. The rotating domain used in the numerical analysis was created using the CAD geometry of the 320 mm nominal pitch circle diameter 18- bucket runner with Z120 type buckets, provided by the industrial sponsors Gilkes, as shown in Fig. 3-2.

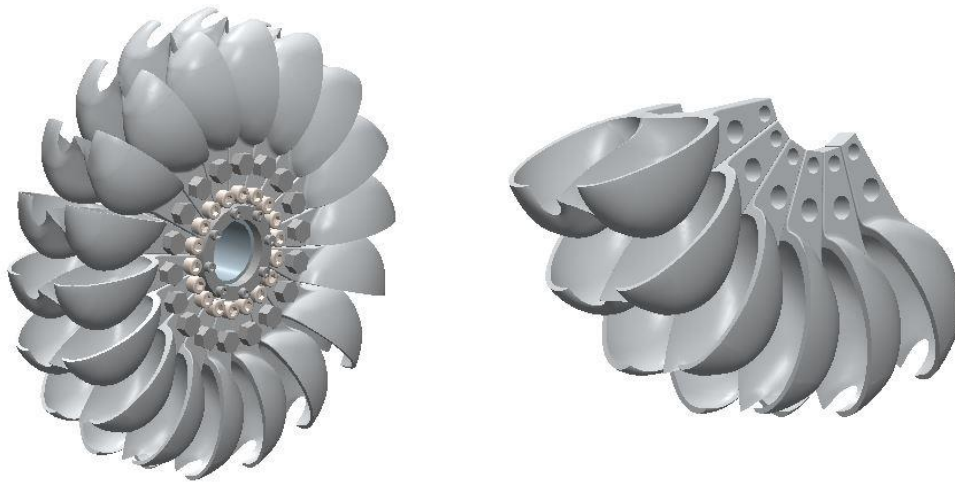


Fig. 3-2 Gilkes Z120 runner type buckets

The Z120 buckets form the most up to date and efficient runner that Gilkes manufacture. It has been developed over the past eight years as a result of another PhD project that used CFD and a Design of Experiments technique where each element was systematically simulated and then later combined such that an optimised design was obtained [18].

The runner domain was then obtained by creating a fluid region around the buckets, as shown in Fig. 3-3.

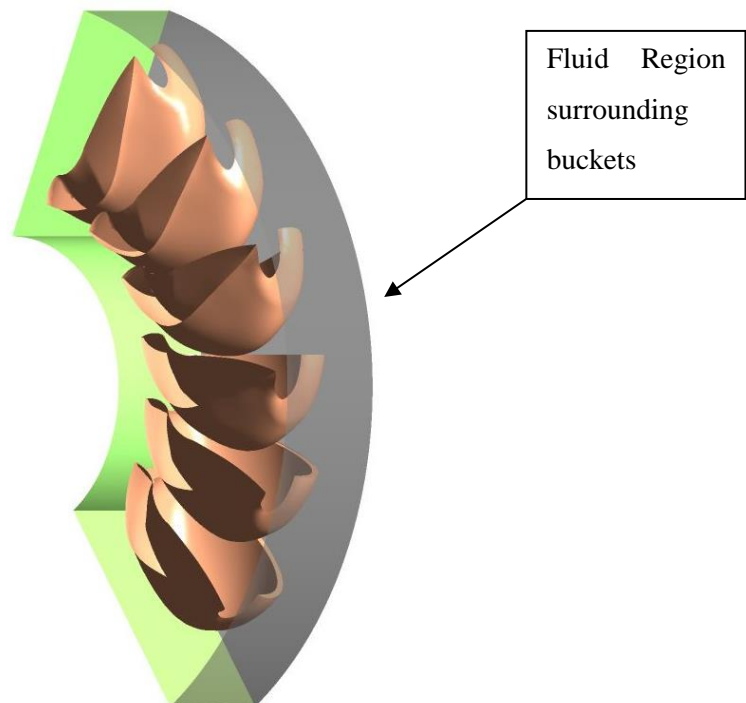


Fig. 3-3 Rotating fluid domain

For all simulations used in this chapter an ideal jet with uniform velocity was used. The injector in reality comprises a nozzle and spear, however this would add unnecessary complexity therefore the water jet is represented as a half cylinder in the stationary casing domain. The jet dimensions were created using the BEP flow rate conditions to determine the diameter of the cylinder.

The casing domain, shown in Fig. 3-4, was created by means of the CAD geometry of the casing supplied with the Z120 runner, which has a standard width of 520 mm. The casing also contains cut-out regions representing the nozzles.

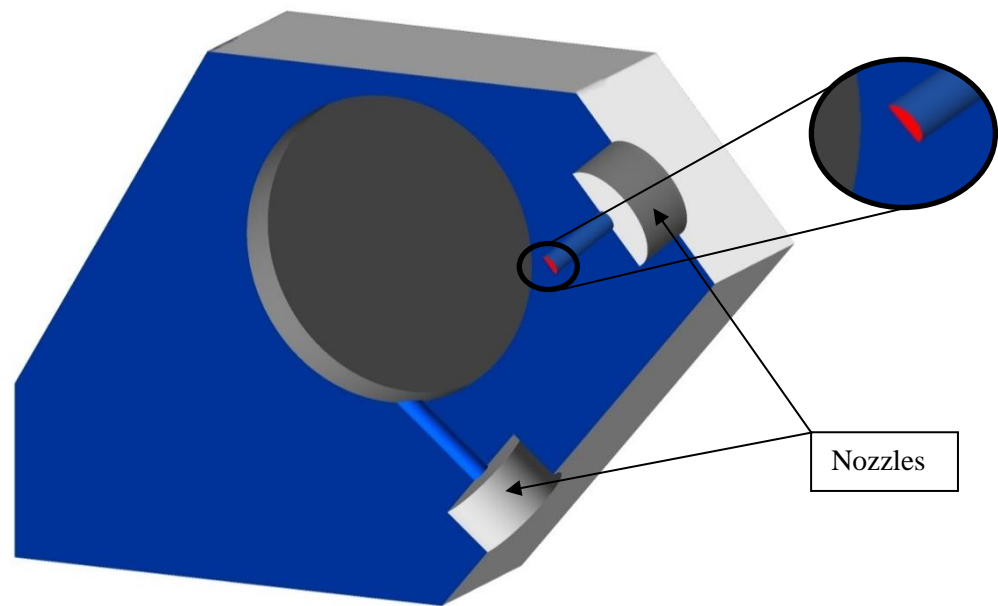


Fig. 3-4 Stationary casing domain fluid region highlighting the location of the half cylinder representing the water jet

The full fluid domain used for the computational analysis combining the stationary casing and rotating runner domains is depicted in Fig. 3-5, with the axis and direction of rotation indicated.

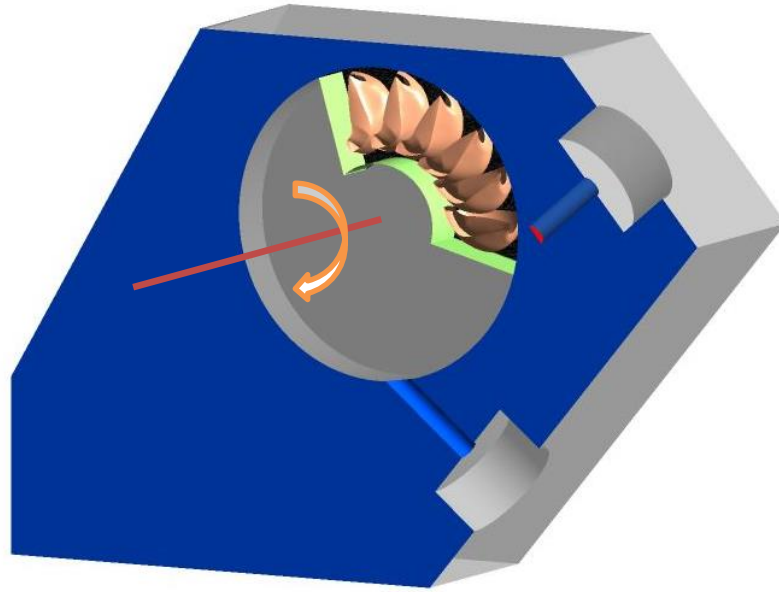


Fig. 3-5 Computational fluid model geometry

3.2.2 Domain Meshing

The two sub-domains were meshed separately using the ANSYS Meshing® tool within Workbench⁷.

The runner domain was meshed as an unstructured tetrahedral mesh with 5 inflation layers on the bucket wall boundaries⁸. Face element sizing was applied to the bucket surfaces where the torque is measured as well as edge sizing around the splitter, cut-out and inner surface edge of the bucket in order to capture the flow field accurately in this region. This sizing is depicted in the surface mesh shown in Fig. 3-6 and the inflation layers and mesh density regions are shown in Fig. 3-7.

⁷ The mesh depicted and used for analysis is the coarse mesh, the decision to use this mesh will be outlined later in 5.4.2.

⁸ The inflation layer is the structured cell zone adjacent to wall boundaries used in order to achieve a more accurate resolution of the boundary layer.

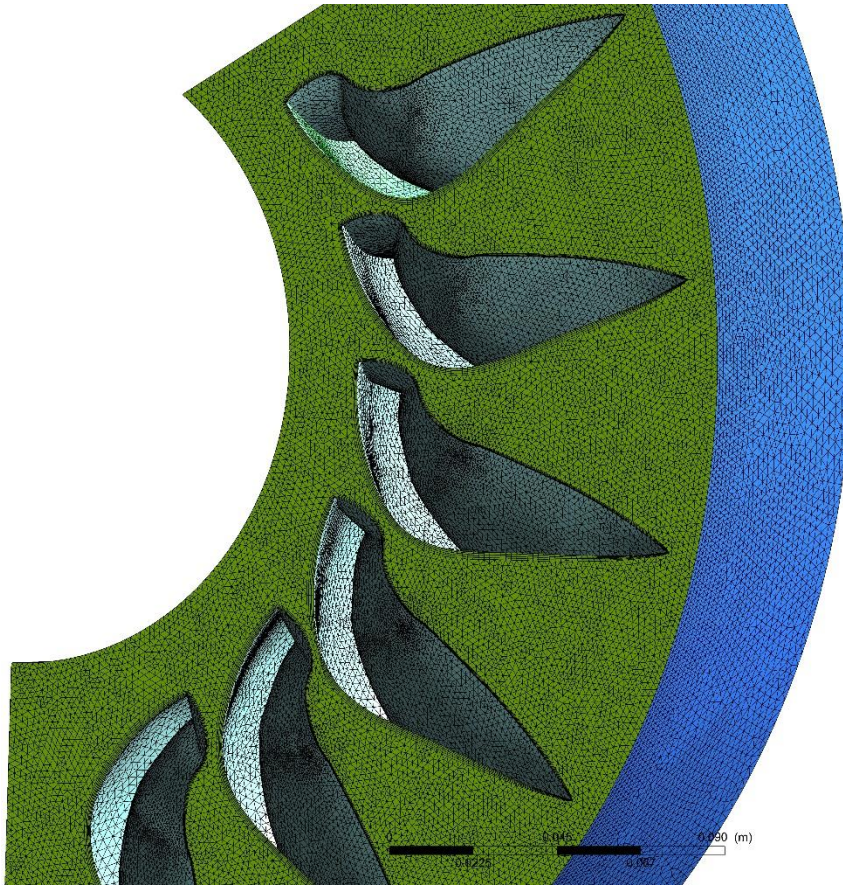


Fig. 3-6 Runner domain surface mesh details

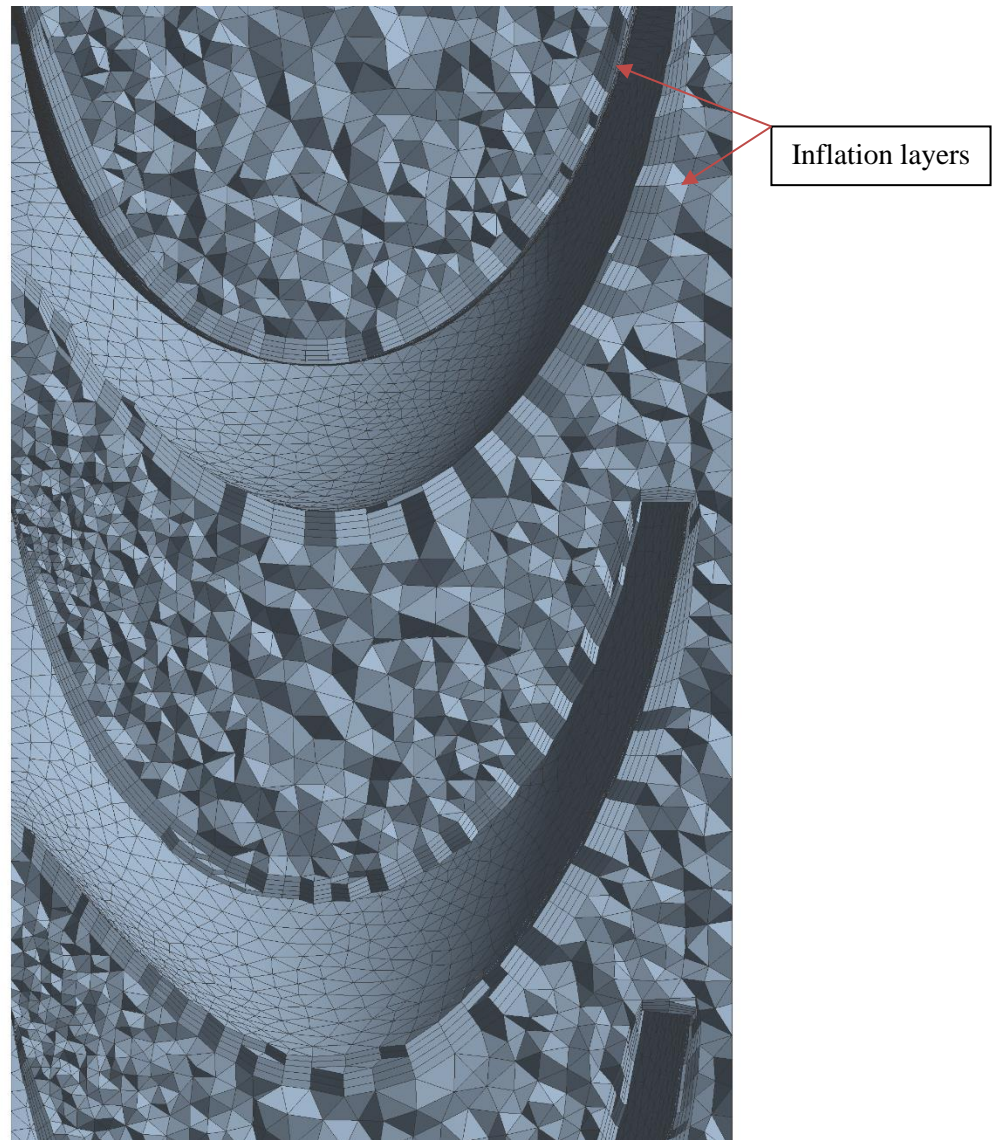


Fig. 3-7 Detailed view of runner domain mesh

Since the project is interested in the flow in the casing care had to be taken to ensure that the mesh resolution was fine enough to capture the air-water interface whilst still being able to generate results in an efficient time. the volume fraction of water as a percentage is very small compared to the overall volume of the casing therefore dense mesh regions are required to capture the air-water interface accurately otherwise artificial/numerical diffusion of the water will occur. Numerical diffusion can be minimised when the mesh cells are aligned with the flow, therefore a hybrid tetrahedral - hexahedral mesh was chosen. The majority of the flow leaves the bucket and travels towards the outer wall of the casing in the axial direction, therefore a swept structured mesh was generated in this direction. Again, 5 inflation layers were applied to the wall boundaries. Face sizing was applied to the interface to match the cell sizing on the corresponding faces of the runner mesh. In this area a tetrahedral mesh was generated and the mesh was conformal at the face between the structured and unstructured region. The jet, which

is represented as a half cylinder could be meshed using structured hexahedral elements. For the initial analysis the upper jet only was considered, however the lower jet will be analysed later in section 4.1.1.2. The sizing is depicted in the surface mesh shown in Fig. 3-8 and the inflation layers and mesh density regions are shown in Fig. 3-9.

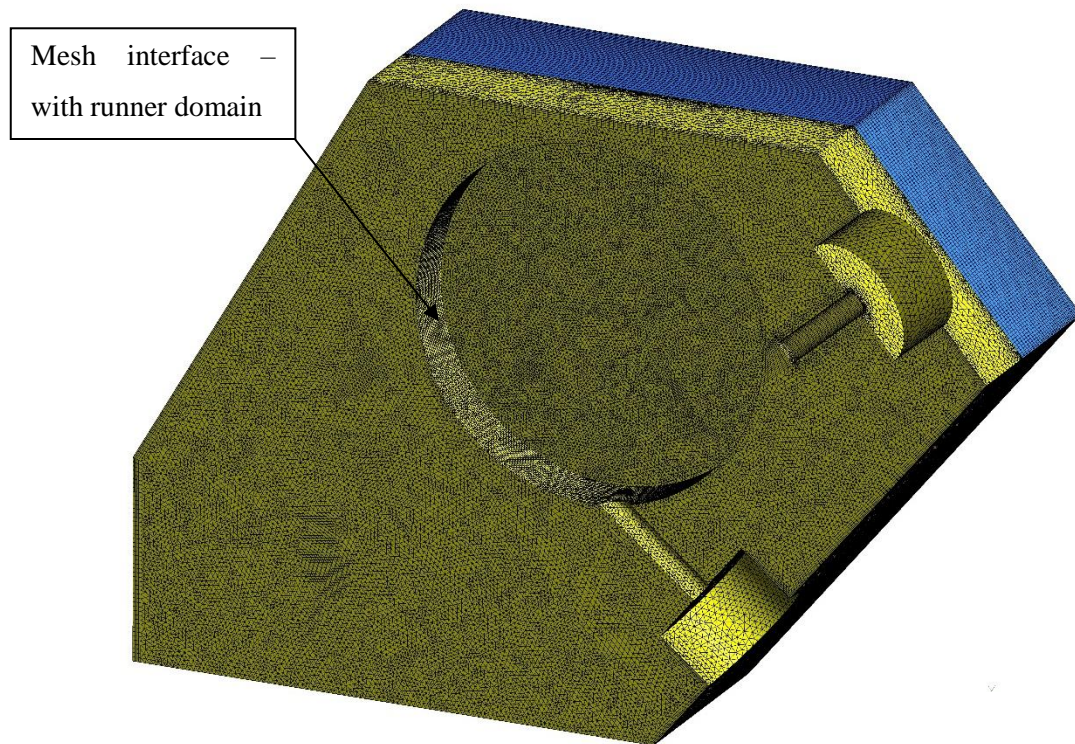


Fig. 3-8 Casing domain surface mesh details (tetrahedral mesh in yellow, swept hexahedral mesh in blue)

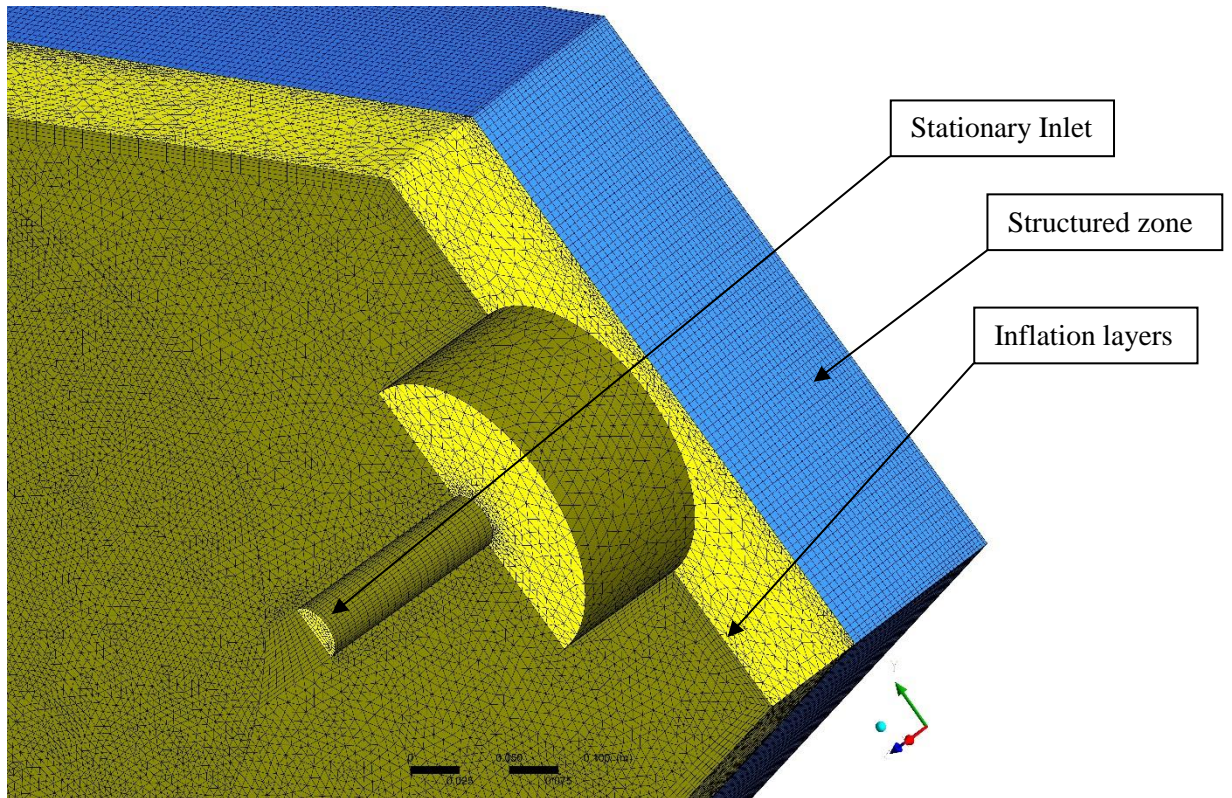


Fig. 3-9 Detailed view of casing domain surface mesh

The added benefit of structured meshes is that the hexahedral cells, with 6 faces compared to 4 in tetrahedral are much more efficient way of filling the available space with cell edges of similar sizes. In the first instance the casing mesh was generated as fully tetrahedral and consisted of 14.1 million elements compared to the first hybrid mesh as described above, which had 3.9 million elements.

In both runner and casing sub-domains the mesh was of acceptable quality; skewness was kept below 0.9, orthogonal quality was above 0.1, and aspect ratios of greater than 5:1 were avoided.

3.2.2.1 A note on y^+

The non-dimensionalised minimum wall distance, also known as the y^+ value, is an important value to consider when generating a mesh for turbulent flows as it determines the quality of resolution of the turbulent boundary layer. The relationship of the y^+ value to the turbulence modelling approach will be discussed later in section 3.3.2.1. The equation used to calculate y^+ is given in (3.1) [82]. For values of $y^+ \approx 1$ the turbulence model is fully resolved, however to achieve a $y^+ \approx 1$, a very dense mesh is required, since the growth ratio away from the wall needs also to be small. Moreover, when modelling turbulence there is a balance between achieving good convergence and results in a reasonable timescale, and as such in many cases it is not feasible to fully resolve turbulence.

In order to overcome this in all subsequent simulations wall functions were used. Wall functions utilise the predictable dimensionless logarithmic boundary layer profile to allow conditions at the wall (e.g. shear stress) to be determined by when the centroid of the wall adjacent mesh cell is located in the log-layer. Wall functions are therefore suitable for a typical value, as such $30 < y^+ < 300$, however in the cases where very high Reynold's numbers higher values of y^+ are acceptable [99].

$$y^+ = \frac{u_* y}{\nu} = \frac{y}{\nu} \sqrt{\frac{\tau_w}{\rho}} \quad \tau_w = \mu \left(\frac{\partial u}{\partial y} \right)_{y=0} \quad (3.1)$$

Where u_* and u are the friction velocity and velocity parallel to the nearest wall respectively, y is the wall normal distance to the centre of the first cell, ν is the local kinematic viscosity of the fluid, ρ is the fluid density and τ_w is the wall shear stress.

During the mesh generation of the runner the required minimum wall distance was calculated using an online y^+ tool, such as Pointwise [100]. Specifying the wall velocity as the theoretical jet velocity and the characteristic length scale as 0.12 m (bucket width) the near wall mesh resolution was found to be 0.25 mm to achieve $y^+ = 300$, which is the upper limit of wall functions applicability, for $y^+ = 1$ this would be 0.00075 mm. This demonstrates that the boundary layers are very thin and unlikely to be fully resolvable with an affordable resolution, therefore wall functions will be applied and the targeted y^+ value was chosen to be 100.

Indeed it should be noted that under-resolved turbulence might cause excessive damping leading to under prediction of energy exchange between the jet and the runner. For this reason, other researchers have neglected turbulence effects and chosen an inviscid solver [78]. Nevertheless, in this case, where there is viscous fluid flow despite the viscous effect being almost negligible due to high inertial forces, then it is recommended that turbulence modelling is indeed mandatory. However, it is important to bear in mind this key relationship between minimum wall distance and torque prediction.

3.2.3 Physics Definitions

3.2.3.1 Operating Conditions

The jet velocity can be approximated from the theoretical jet velocity formula, given in (2.17), when in this instance the test head is 60 m. The operating conditions used to calculate the jet diameter to provide the turbine operating conditions are listed in Table 3-1.

		Z120 runner BEP
PCD	[mm]	320
Rotational Speed	[rpm]	946.46
Head	[m]	60
Ideal jet velocity	[m/s]	34.4104
Flow Rate	[m ³ /s]	0.0231
Jet Area	[m ²]	0.000693
Jet Radius	[m]	0.01485

Table 3-1 320 mm PCD Pelton BEP operating conditions used in analysis

3.2.3.2 Materials

Since the simulations are multiphase they contain two fluids; air and water. The fluids were defined as isothermal and under constant fluid properties. The material options for each fluid are given in Table 3-2.

<i>Fluid Name</i>	<i>Density ρ</i>	<i>Dynamic Viscosity μ</i>
	[kg/m ³]	[kg/m.s]
Water	998.2	0.001003
Air	1.225	0.000017894

Table 3-2 ANSYS material properties

3.2.3.3 Defining Boundary Conditions

In order for FLUENT to solve the discretised form of the governing equations, they have to be closed by specifying boundary conditions, these are listed in Table 3-3. These are also highlighted in Fig. 3-10 and Fig. 3-11 for the casing and runner domains respectively.

	Boundary Name	Type	Boundary Details	Fluid Value
Casing Domain	S_Symmetry	Symmetry	N/A	N/A
	S_Inlet	Velocity Inlet	Magnitude: 34.4104 m/s Normal to Boundary Turbulence: Intensity: 1% Length Scale: 0.01 m	Air Volume Fraction: 0 Water Volume Fraction: 1
	S_Outlet	Pressure Outlet	Relative Pressure: 0 Pa Turbulence:	Air Volume Fraction: 1 Water Volume Fraction: 0

			Backflow Intensity: 1% Length Scale: 0.01 m	
	S_Interface	Pressure Outlet	Relative Pressure: 0 Pa Turbulence: Backflow Intensity: 1% Length Scale: 0.01 m	N/A
	S_Walls	Wall	No Slip Wall	N/A
Runner Domain	R_Symmetry	Symmetry	N/A	N/A
	R_Opening	Pressure Outlet	Relative Pressure: 0 Pa Turbulence: Backflow Intensity: 1% Length Scale: 0.01 m	Air Volume Fraction: 1 Water Volume Fraction: 0
	R_Interface	Pressure Outlet	Relative Pressure: 0 Pa Turbulence: Backflow Intensity: 1% Length Scale: 0.01 m	N/A
	R_BucketIn_1-6	Wall	No Slip Wall	N/A
	R_BucketOut_1-6	Wall	No Slip Wall	N/A

Table 3-3 Simulation stationary and rotating domain boundary conditions

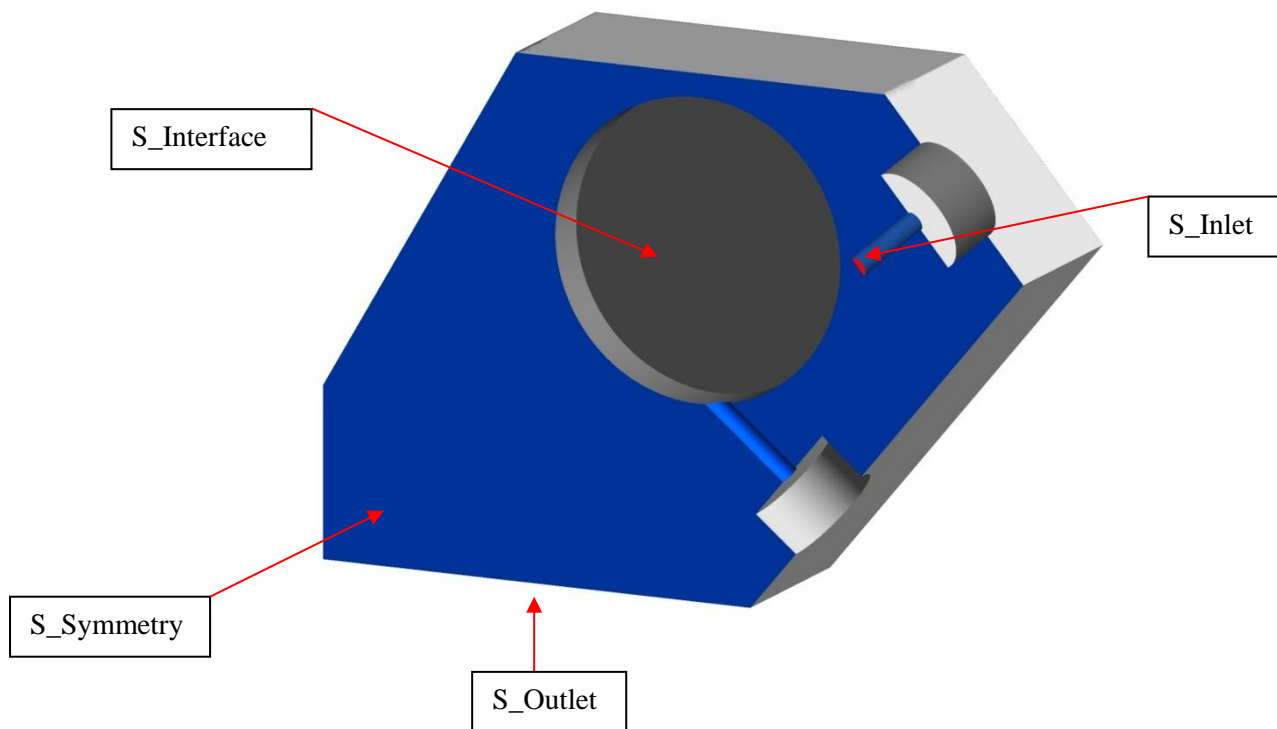


Fig. 3-10 Geometry indicating simulation boundary conditions for stationary casing domain

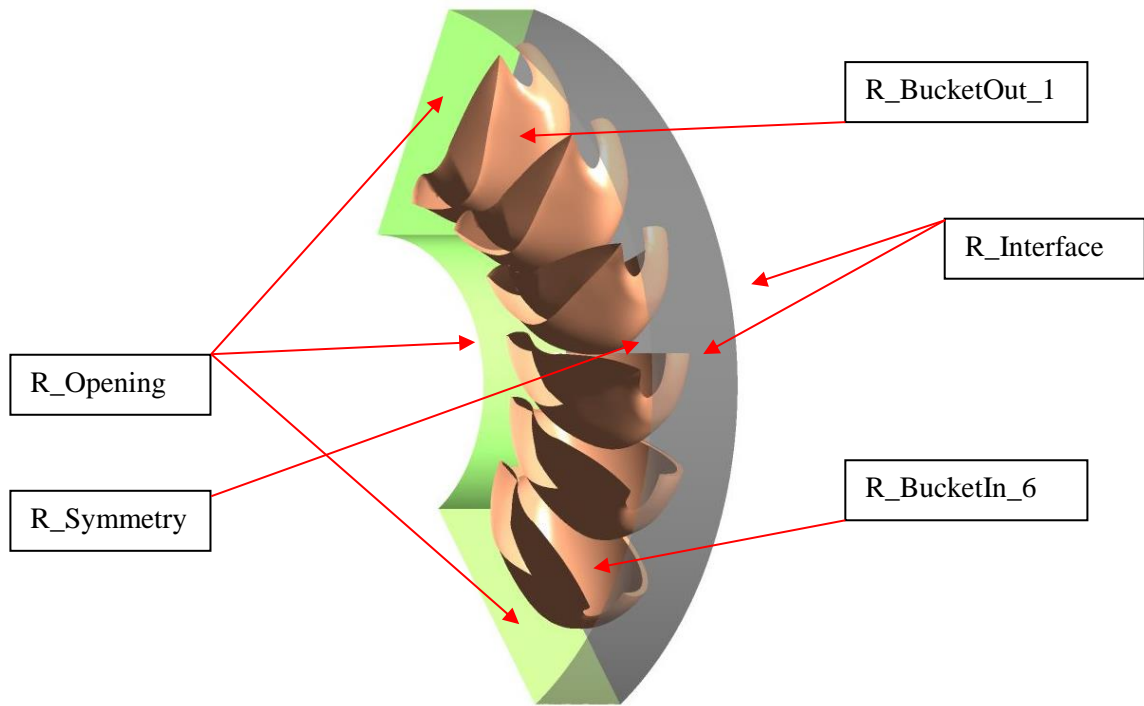


Fig. 3-11 Geometry indicating simulation boundary conditions for rotating runner domain

3.2.3.4 *Defining Interfaces*

Since the nature of Pelton turbine operation is unsteady and transient it is necessary to model the runner rotation. Within FLUENT cases involving rotating meshes are simulated using the Sliding Mesh approach [82]. The location of the interfaces has been shown for both the rotating and stationary domains in Fig. 3-11. As the name implies the two domains slide (i.e., rotate) relative to one another along the mesh interface in discrete steps. Interfaces enable information to be passed between the two different computational domains. At each timestep, the intersection of the two interfaces is determined; the intersection is considered as an interior face (i.e. a face with fluid cells at its both sides), while the remaining parts of the interface faces are considered as a pre-determined boundary type, which in the present study are pressure outlets in order to allow the fluid to exit.

3.2.3.5 *Surface Tension*

Since the diffusion of the air water interface is related to the surface tension it is important to implement this in the calculations. An indication of this is demonstrated in Fig. 3-12, which shows the volume fraction contour plot of the water sheet leaving the first bucket on the runner-casing interface, as the maximum water volume fraction is below 100%, this is indicative of a non-continuous liquid, which results in liquid breakup and the formation of droplets.

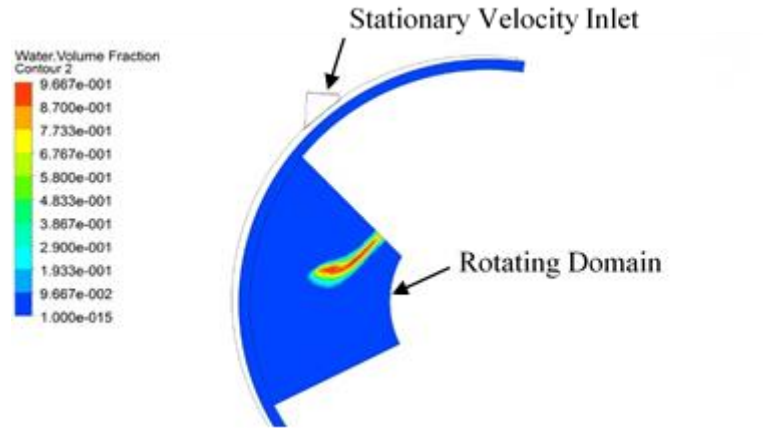


Fig. 3-12 Water volume fraction plot showing non-continuous liquid region

In addition in the case of flow where the Weber number tends to 0 as is true where the (absolute) velocity of the water sheet leaving the bucket tends to 0 (or is certainly of 1 order smaller than the jet velocity), the inertial forces becomes small and surface tension force becomes dominant. The surface tension model in FLUENT is the continuum surface force (CSF) model proposed by Brackbill et al [101]. The surface tension coefficient for water in contact with air at 15°C was taken as 0.0735 N/m.

3.2.3.6 Results Processing – Torque

Although detailed analysis of the flow in the casing consists of plotting the volume fraction as an isosurface and looking at contour plots of pressure for example, the primary integral quantity that can be measured from these simulations is the runner torque, which allows for the calculation of the runner hydraulic efficiency, as follows. The torque value calculated will be used to compare the effects of mesh and timestep.

In FLUENT a moment monitor is defined to measure the torque, which writes out the final value of the moment for each timestep. The total moment vector about a specified centre (in this simulation the axis of rotation) is computed by summing the cross products of the pressure and viscous force vectors for each face with the moment vector (3.2), which is the vector from the specified moment centre to the force origin [82]. The monitor is defined for both the inside and outside surfaces (wall zones) of each bucket 1 – 6, highlighted for a representative bucket in Fig. 3-13.

$$\underbrace{\mathbf{M}_A}_{\text{total moment}} = \underbrace{\mathbf{r}_{AB} \times \mathbf{F}_P}_{\text{pressure moment}} + \underbrace{\mathbf{r}_{AB} \times \mathbf{F}_V}_{\text{viscous moment}} \quad (3.2)$$

Where A is the specified moment centre and B is the force origin.

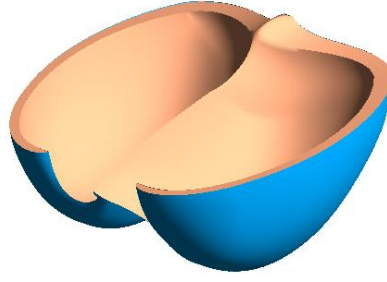


Fig. 3-13 Moment monitor wall zone definition – inside (orange) and outside (blue)

The torque is then numerically integrated using the trapezium rule to give the area under the total torque curve or the work done by a single bucket.

$$W = \int_b^a M(\theta) d\theta = \frac{1}{2} \sum_{i=1}^n (M(\theta_{i+1}) + M(\theta_i)) (\theta_{i+1} - \theta_i) \quad (3.3)$$

The time for a single revolution is calculated is given by equation (3.4)

$$t = \frac{2\pi}{\omega} \quad (3.4)$$

Using equations (3.3) and (3.4), the power produced by the runner, where N_B is the total number of buckets that make up the runner, can be calculated as shown in equation (3.5).

$$P_{Out} = \frac{N_B \times W}{t} \quad (3.5)$$

However, in order to calculate the runner efficiency, the hydraulic power is also required, which can be expressed as equation (3.6). Where \dot{m} is the jet mass flow rate [kg s^{-1}] and u is the jet velocity [m s^{-1}], which is defined by the inlet boundary conditions.

$$P_{in} = \frac{\dot{m} \times u^2}{2} \quad (3.6)$$

Therefore, the efficiency is the ratio of equation (3.5) and (3.6).

3.2.4 Post Processing

In general two different post processing techniques will be used, firstly isosurfaces are used to represent the water volume fraction. An isosurface is a surface within the domain upon which a particular variable has a constant value. Unless otherwise stated an isosurface of 1% water volume fraction (that is a volume fraction of 1% in each cell) will be used. Therefore no colour spectrum indicating the range is required since is at a constant value. The second are contour plots, which are made up of a series of lines linking points with equal values of a given variable.

The whole range of variable values will be divided into a number of contours. These are plotted on surfaces and a colour spectrum of the variable will be provided.

3.2.5 Simulation Sequence

The simulation is modelling a very short portion of time. In physical terms it models to at least 360° rotation, which represents a simulation time of just 0.08 s. While it is sufficient to calculate the torque and then construct the total torque produced by the runner, assumed to be steady state, in approximately 140° rotation, much more time is required in order to visualise the flow in the casing. For the standard casing width of 520 mm the water does not reach the casing walls until at least 200° rotation, nor leave the casing entirely until long beyond that.

A FLUENT Journal .jou file was written that contained all of the necessary commands to execute the simulation, such as switching the water jet on and off, specifying the runner rotational speed and timestep etc. In addition to switching the jet velocity to 0 m s^{-1} , it was determined that it was important to reduce to water volume fraction to 0 to give better convergence and make the simulation more robust. For all simulations considered herein a convergence target of an rms of 1×10^{-4} was chosen for the residuals of the momentum equations for every timestep. The simulation sequence can be divided into five subsections that relate to the specific physical flow condition outlined in Table 2-4 and detailed by the bucket duty cycle in Fig. 3-14, these are; inflow, flow development, jet separation, end of cycle and finally casing flow, as described below.

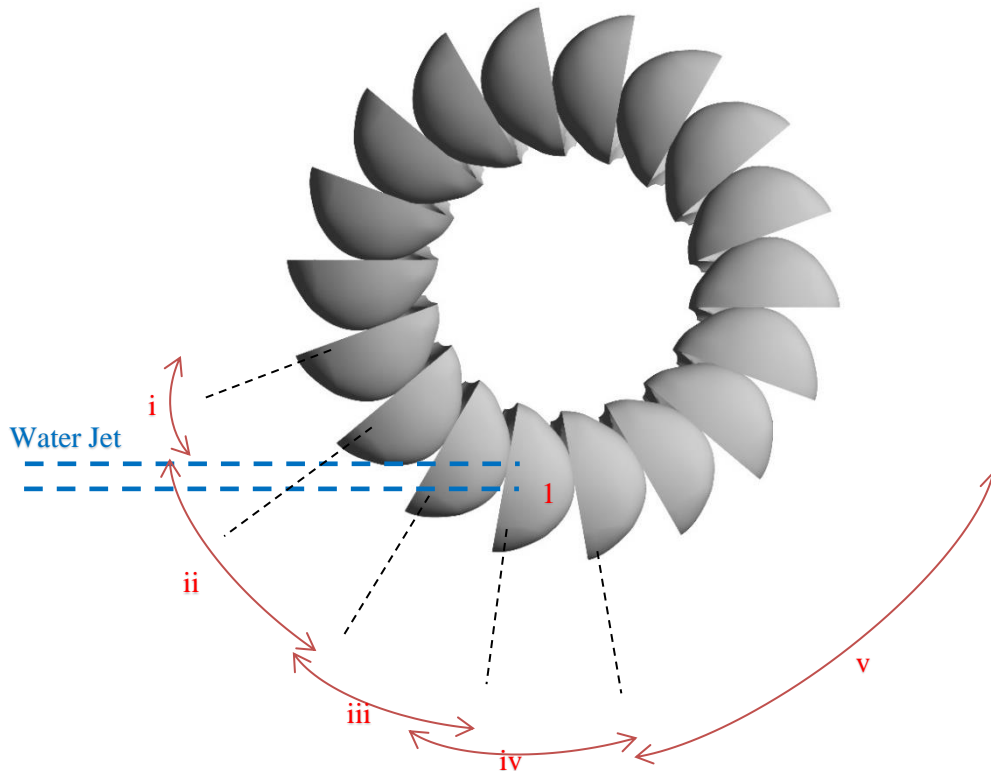


Fig. 3-14 Bucket duty cycle

1. ($\theta = 36^\circ$) At time, $t = 0$ there is no water in the turbine. Prior to inflow the jet is allowed to initialise, this is done by setting the rotational velocity of the runner domain to 0 rpm and waiting for the jet to pass through the runner domain. A timeframe showing this initialisation is presented in Fig. 3-15.

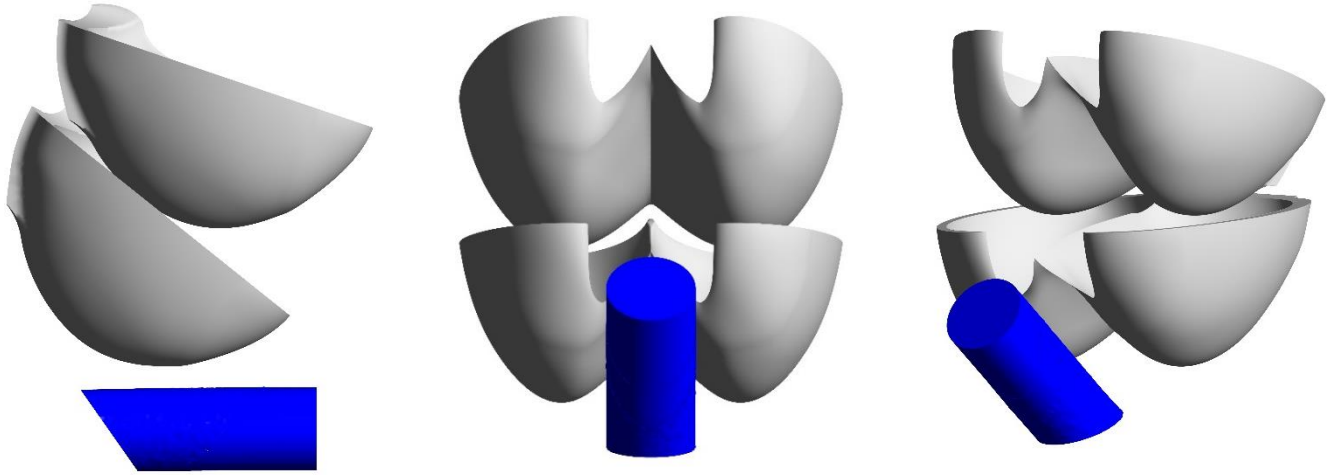


Fig. 3-15 Jet initialisation process

3. ($\theta = 40^\circ - 60^\circ$) The initial feeding process (ii) then begins, where the upper surface of the jet comes into contact with the underside of the first bucket and then the jet begins to flow through the cut-out before into the inside of bucket 1. As the jet makes contact with the splitter the jet then starts to separate accordingly. Thereafter, the flow evolves into the expected film flow following the contour of the bucket surface moving first slightly towards the root and then laterally towards the outer edge, as shown in Fig. 3-16.
2. ($\theta < 40^\circ$) Following this the runner rotational velocity is set to the BEP velocity and the first bucket tip approaches the jet (i).

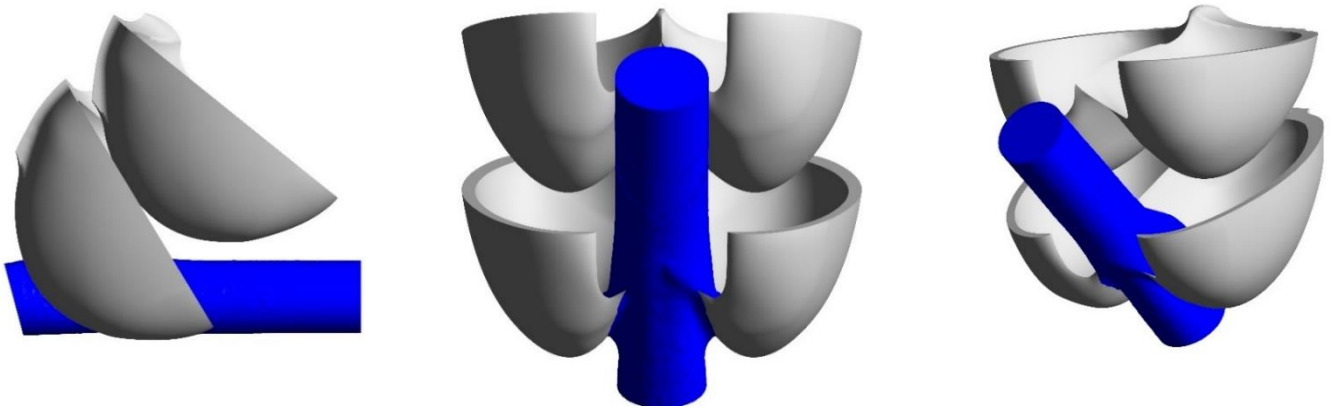


Fig. 3-16 Jet feeding process – shown for 60°

- 4) ($\theta = 60^\circ - 70^\circ$) Entire separation of the jet (iii), at this point the jet is almost entirely cut by the first bucket. The now entirely separated portion of the jet remains attached to bucket 2 backside far in the duty cycle. Once the tip and the cut-out lips are in contact with the jet upper surface, the jet starts to separate in 2 branches, i.e. the upper one, that flows in bucket 2, and the lower one that continues to feed bucket 1, as shown in Fig. 3-17.

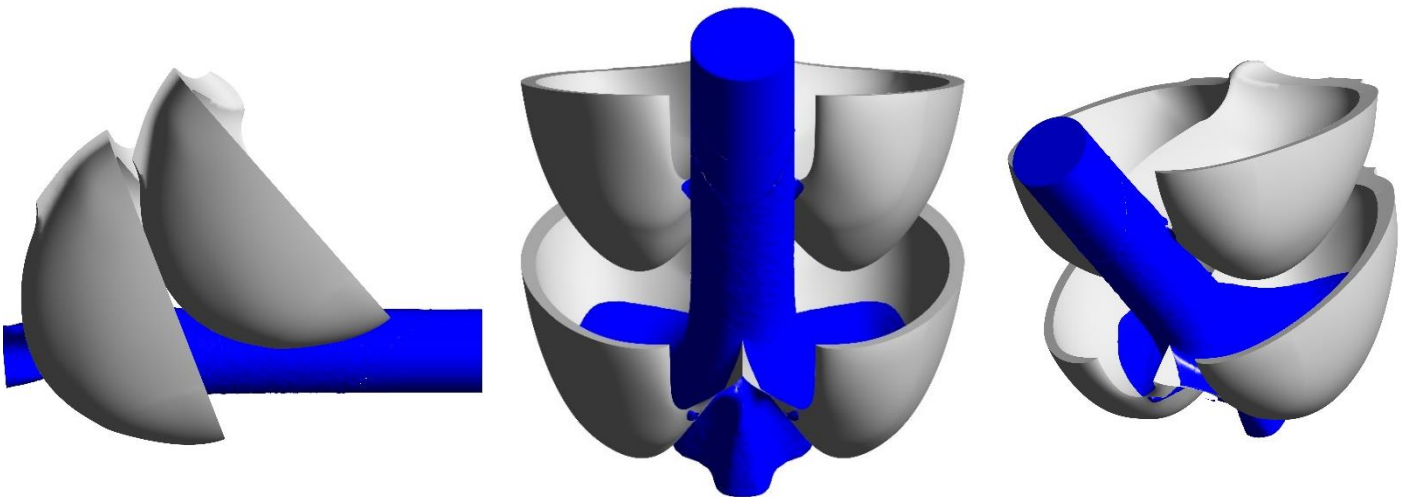


Fig. 3-17 Entire separation of the jet process – shown for 70°

- 5) ($\theta = 70^\circ - 90^\circ$) Last Stage of inflow (iv), at this point the axis of the jet will be orthogonal with the lip of the first bucket and water will continue to enter bucket 2 until the process described in 4) repeats itself with bucket 3 and so on and so on. The water has started to exit bucket 1, detailed in Fig. 3-18.

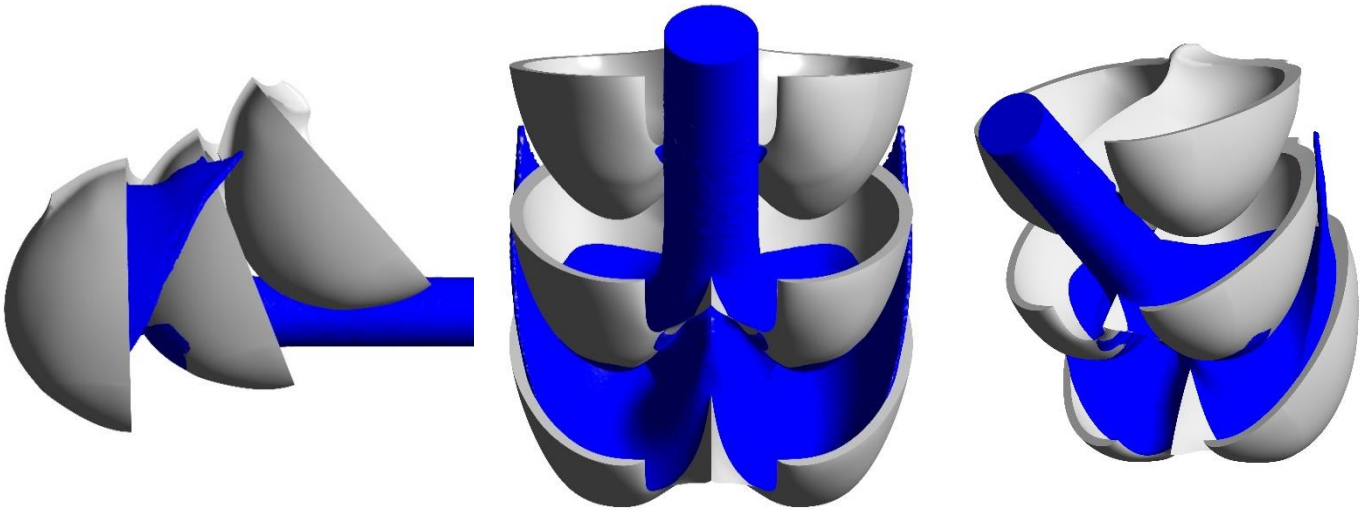


Fig. 3-18 Last stage of inflow process – shown for 90°

- 6) ($\theta = 90^\circ - 130^\circ$) Last stage of outflow (v), during this process the majority of the water has left bucket 1, now the outflow sheet is fully developed, with the flow from bucket 1 and bucket 2 appearing first as thin water sheets and then they will merge as they progress into the casing before eventually becoming thinner and breaking up into droplets. After this point when the water sheets start to disintegrate (130°) it is no longer possible to plot the isosurface of water volume fraction = 0.5 (i.e. the free surface) and therefore smaller volume fractions will be used.

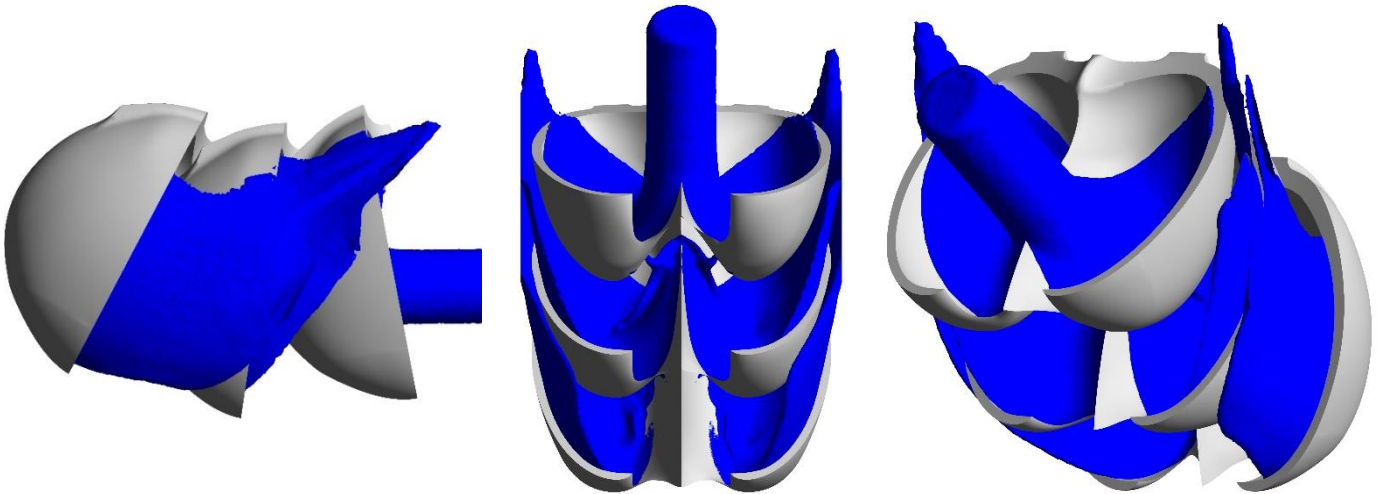


Fig. 3-19 Last stage of outflow process – shown for 130°

- 7) Casing flow ($\theta = 130^\circ - \infty$) It is from this point that the water sheets start appearing in the casing before interacting with the casing walls. The last remaining part of water leaving the first few buckets, encircled in green, appear. This is the water that will

eventually impact the right hand side of the casing. It is here that much lower volume fractions are required (1% water) in order to visualise the casing flow. However, since in reality at this point the physical conditions within the casing are a combination of striated surface, droplets and mist.

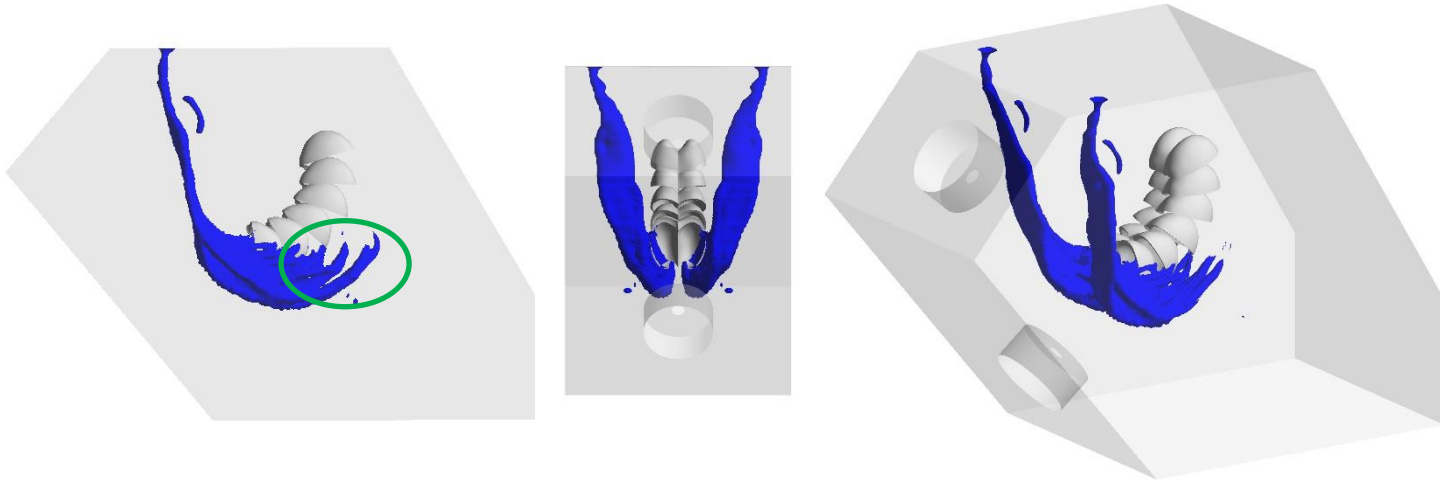


Fig. 3-20 Casing flow – shown for 200°

3.3 CFD Modelling Assumptions and Simplifications

From the outset it was apparent that a number of simplifications were required in order to produce results from a model in an economic time frame. The model focusses on the turbine operating at BEP conditions, which allow a direct comparison to experimental data. A number of initial modelling techniques were investigated, which were later improved for increased accuracy and reduced computational cost creating an efficient platform to investigate a number of casing configurations.

There are several modelling assumptions and simplifications that can be made in order to generate a computational model that can accurately simulate the flow within the Pelton turbine, within timescales that are feasible. These assumptions are listed below and detailed in the following chapters.

3.3.1 Geometric Assumptions

A transient simulation of the full runner and casing with both upper and lower jet operation is a computationally heavy exercise, which makes it unfeasible for the investigation of a number of different casing configurations. For this reason, several simplifications have been made to the Pelton geometry in order to reduce the size of the computational domain and simulation time.

3.3.1.1 Symmetry

Since the runner and casing are symmetrical along the plane of the bucket splitter it is assumed that the casing flow modelled will be symmetrical. This reduces mesh size by one half as shown in Fig. 3-1.

3.3.1.2 Jet profile

Previous studies, detailed in the literature review, document the unsteady nature of the water jet leaving from the injector, particularly the non-uniform velocity profile and presence of secondary velocities generated by the upstream pipework. It has been found that this can have a significant effect on the performance of impulse turbines. Despite the importance of the jet velocity profile it was decided from the outset that all CFD studies should assume an ideal jet velocity profile.

3.3.1.3 Number of Buckets

A question of periodicity was asked; in order to reduce the size of the computational domain and therefore reduce the simulation time an assessment was carried out to determine if a reduced number of buckets could be used.

It has been shown in previous studies that when the runner is operating under steady state conditions the torque acting on each individual bucket can be considered periodic and therefore many researches use a reduced number of buckets to predict the runner performance [18], [26], [57], [60]. However, since this study is concerned with the flow within the casing it is not known whether it is feasible to use a reduced number of buckets to observe the casing flow. High speed photography has made it possible to capture the flow that leaves the runner from each bucket in sheets, as depicted in Fig. 3-21 and it is possible to infer from this that flow leaving one bucket will be the same as the flow that leaves the next bucket and so on, yet when viewed with the naked eye the flow appears to be ‘steady – state’. However, it is not known is to whether the flow leaving the buckets will interact with each other and have an influence on the performance of the turbine, therefore in order to determine a number of buckets that will adequately capture the interaction of the flow leaving consecutive buckets a periodicity study was carried out.

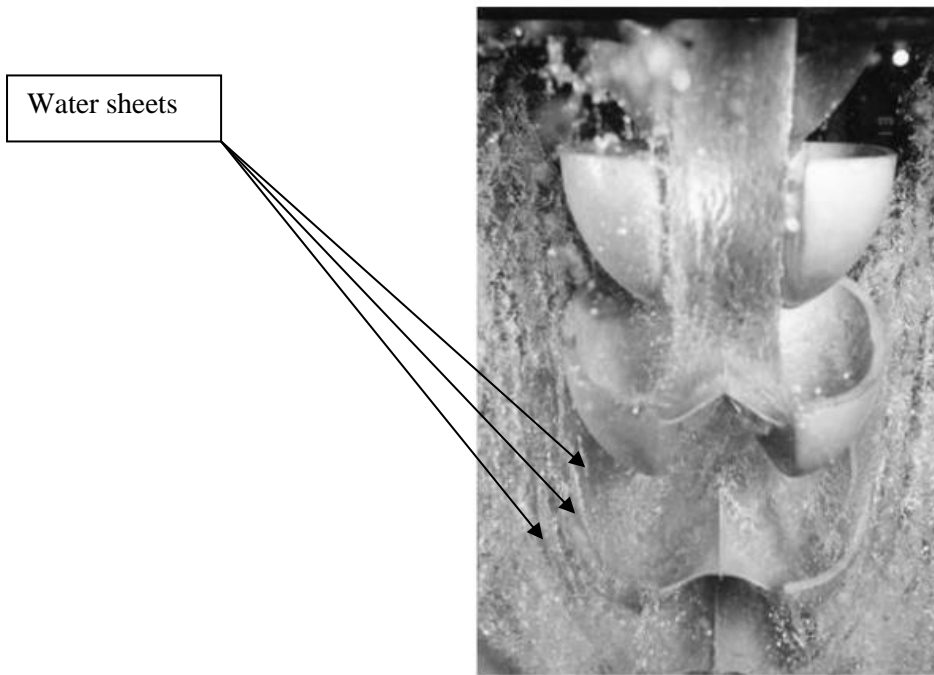


Fig. 3-21 External stroboscopic flow visualisation of water sheets from individual buckets [26]

In order to assess the differences between using a reduced number of buckets and a full runner, simulations were carried out with 2, 4, 6 and 18 buckets respectively. The rotating domains were created by taking a periodic fluid region around the buckets, which was swept with equal distance from the first and last buckets in each case. The fluid regions were then meshed with equal body, surface and edge element sizing and with 5 inflation layers around the bucket surfaces, as outlined in 3.2.2.

The torque from the first bucket of each simulation is plotted in Fig. 3-22 and penultimate bucket in Fig. 3-23.

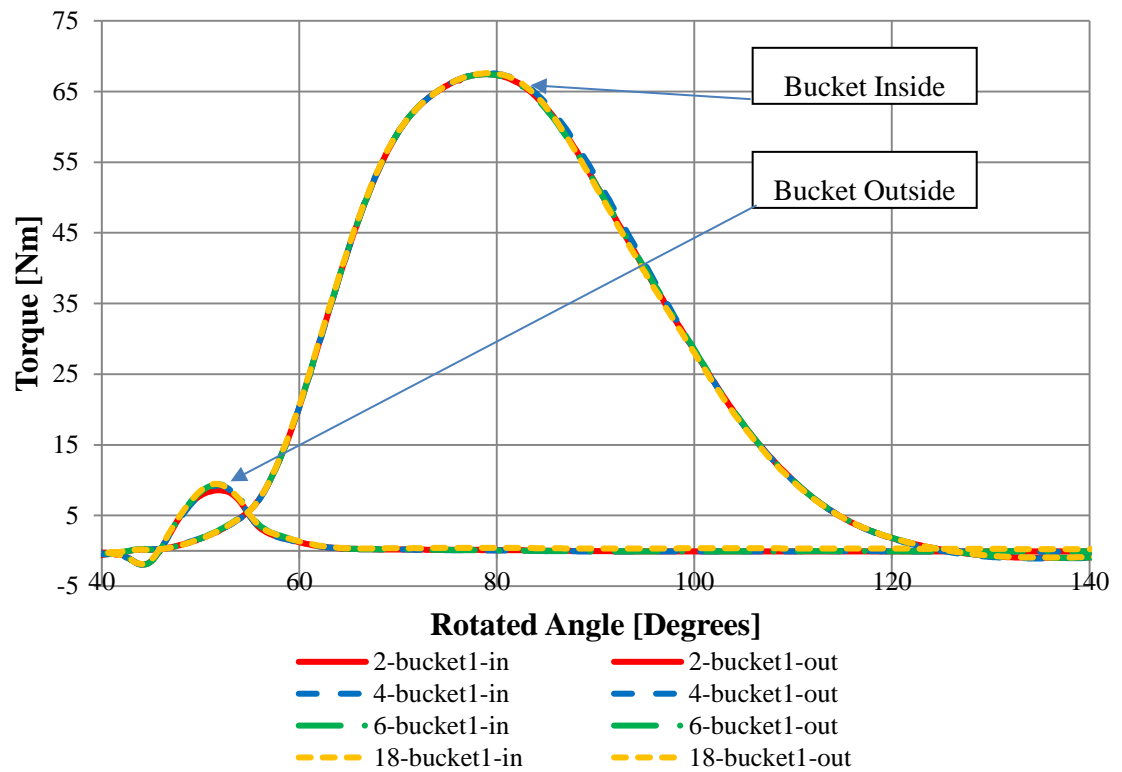


Fig. 3-22 Torque curves for inside and outside of first bucket for different bucket number simulations⁹

⁹ N.B. the slight negative torque on the outside of the bucket (40° - 45° for the outside) is due to the negative pressure that is pulling the bucket, which arises during the jet cutting process as a result of the Coanda effect. This has been documented experimentally in [54], [97].

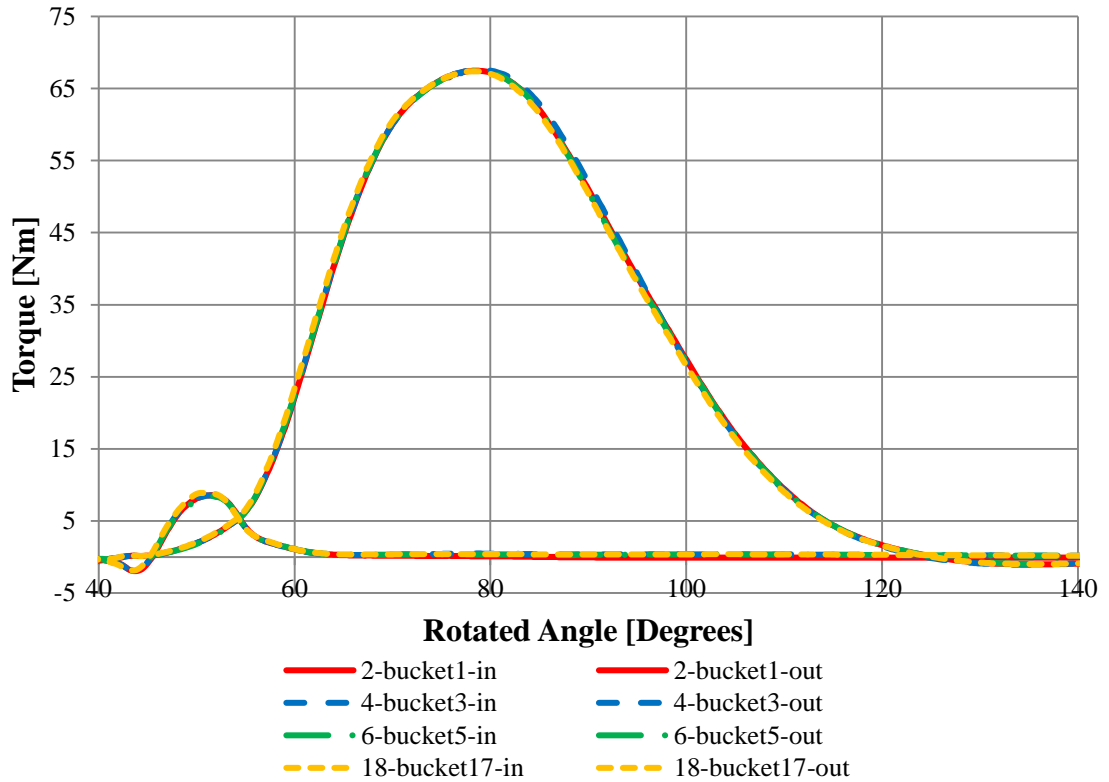


Fig. 3-23 Torque curves for inside and outside of the penultimate bucket for different bucket number simulations

It can be observed from Fig. 3-22 and Fig. 3-23 that the torque curves are identical for the first and penultimate bucket are identical. It can be concluded then that given the same mesh generation settings the torque calculated is periodic and as a result the shape of the flow leaving the bucket should therefore be identical whether x buckets or y buckets are modelled. The normalised efficiency calculated for the different buckets appears in Table 3-4 showing a negligible difference of 0.05% efficiency difference between the simulations. The only difference will be how that flow then appears as it moves through the casing mesh.

Fig. 3-24 and Fig. 3-25 show the front and rear view respectively of the isosurface of water Volume Fraction at 1% within the casing after the runner has rotated a full 360° for from top left clockwise 2-bucket, 4-bucket, 6-bucket, and 18-bucket simulations. In general the shape and direction of the water interfaces are very similar. However, the definition of the water sheets in the right hand side of the casing in Fig. 3-25 towards the symmetry plane appear more washed out in the 2-bucket and 4-bucket simulations, though as will be shown later in 3.5.1, this flow is largely a fine mist and therefore its influence on the turbine efficiency is negligible. Given the modest increase in mesh sizing between 2-bucket, 4-bucket and 6-bucket simulations, as outlined in Table 3-4, but more significant between 18-bucket and the fact that a significant

portion of the flow is captured with 6-bucket simulation, all future simulations will use this number.

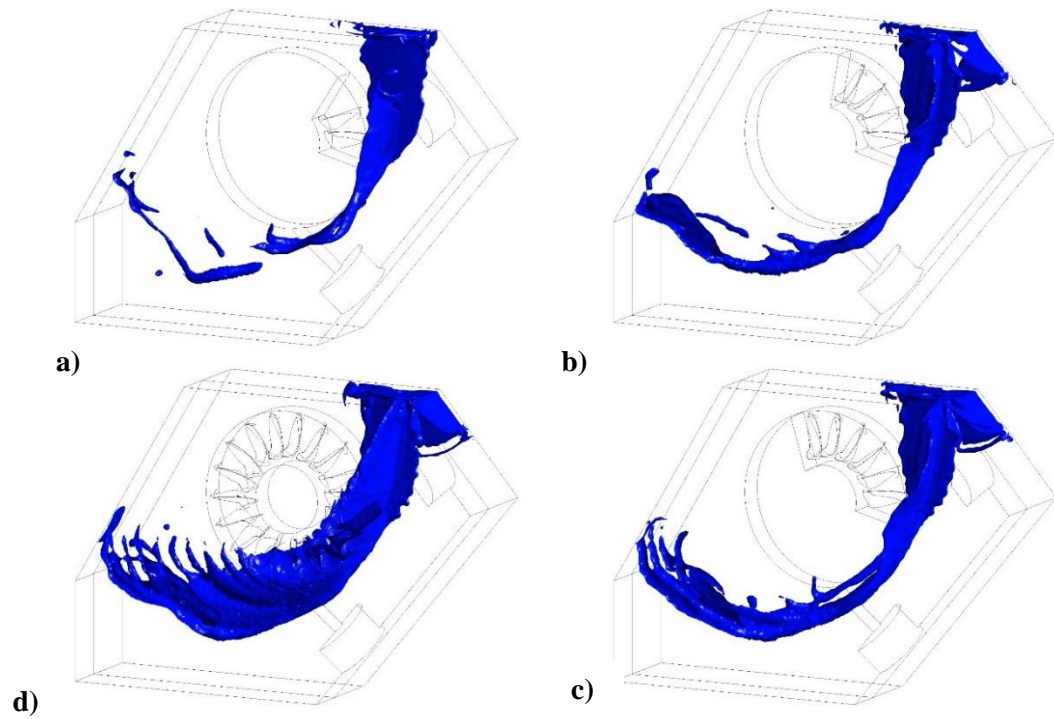


Fig. 3-24 Water Volume Fraction 1% comparison at 360° Front View, clockwise from top left; a) 2-bucket, b) 4-bucket, c) 6-bucket and d) 18-bucket

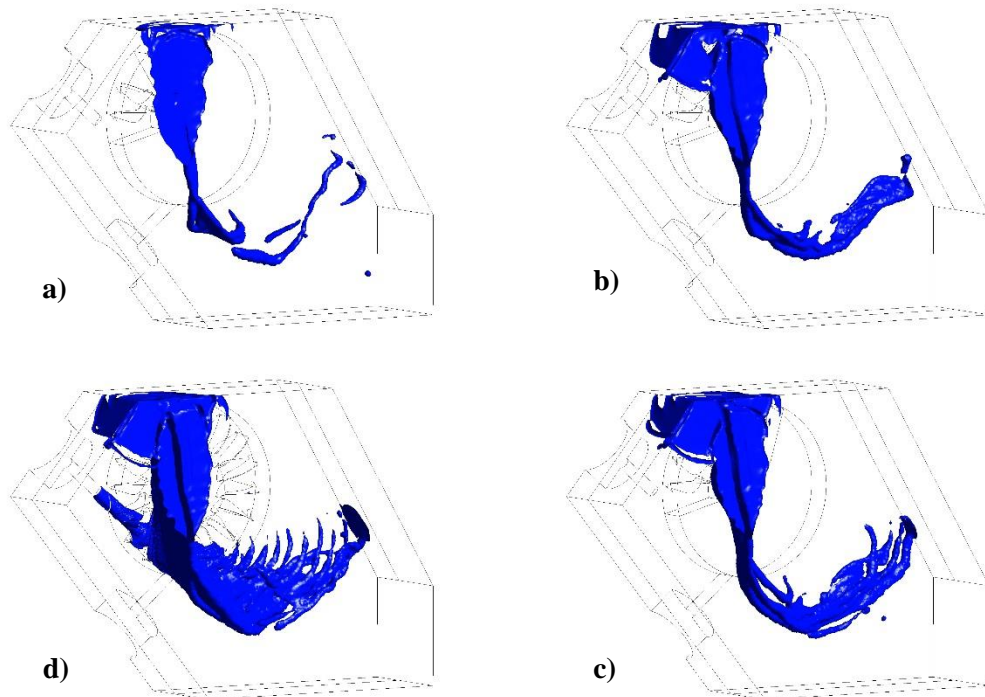


Fig. 3-25 Water Volume Fraction 1% comparison at 360° Rear View, clockwise from top left; a) 2-bucket, b) 4-bucket, c) 6-bucket and d) 18-bucket

Mesh #	Number of Elements Runner + Casing [million]	Normalised Efficiency [%]
2-bucket	1.05 + 3.90	99.88¹⁰
4-bucket	1.96 + 3.90	100.05
6-bucket	2.87 + 3.90	100
18-bucket	8.35 + 3.90	99.95

Table 3-4 Mesh sizing and normalised efficiency for different bucket number simulations

3.3.2 Modelling Assumptions

As well as the geometric assumptions several modelling assumptions were made based on the definition of the physics used to describe the problem and the numerical techniques chosen to analyse them. The modelling assumptions can be detailed as follows.

3.3.2.1 Turbulence Model

A number of turbulence models employing the Boussinesq approach have been developed and FLUENT implements many of these. Typically, these turbulence models are categorised according to the number of additional transport equations they use to compute the turbulent viscosity. According to the literature the most popular of these approaches applied to the modelling of impulse turbines are the two-equation models.

Typically, in the two-equation models, the turbulence kinetic energy, k , is one of the transported variables and the common choices for the second are the dissipation rate of turbulent kinetic energy, ε , or the specific dissipation rate, ω .

The most widely used two-equation models in FLUENT are the Realisable k - ε and Menter's k - ω Shear Stress Transport (SST) model [90]. The two models are only subtly different since the SST model is a combination of pure two equation models, namely k - ε is used in the free stream zone, while the k - ω is used near the wall. In order to determine which model to choose two simulations were run using a 2-bucket Pelton runner to assess their influence on performance and computational cost. Fig. 3-26 shows the differences in the torque curves for each of the

¹⁰ Also significant for 2-bucket flow is the final bucket sees the jet switch off, such that there will be a slight reduction in the torque developed on that bucket since the flow into a bucket is significantly affected by how it interacts with the underside of the next bucket. Therefore, as a result the power generated will be lower and hence the efficiency will also be lower. One may conclude that the slightly larger reduction in efficiency can be attributed to this and the real value will in fact be ~99.95%.

turbulence models. Based on these results going forward the Realizable $k-\epsilon$ was used as it solved marginally faster.

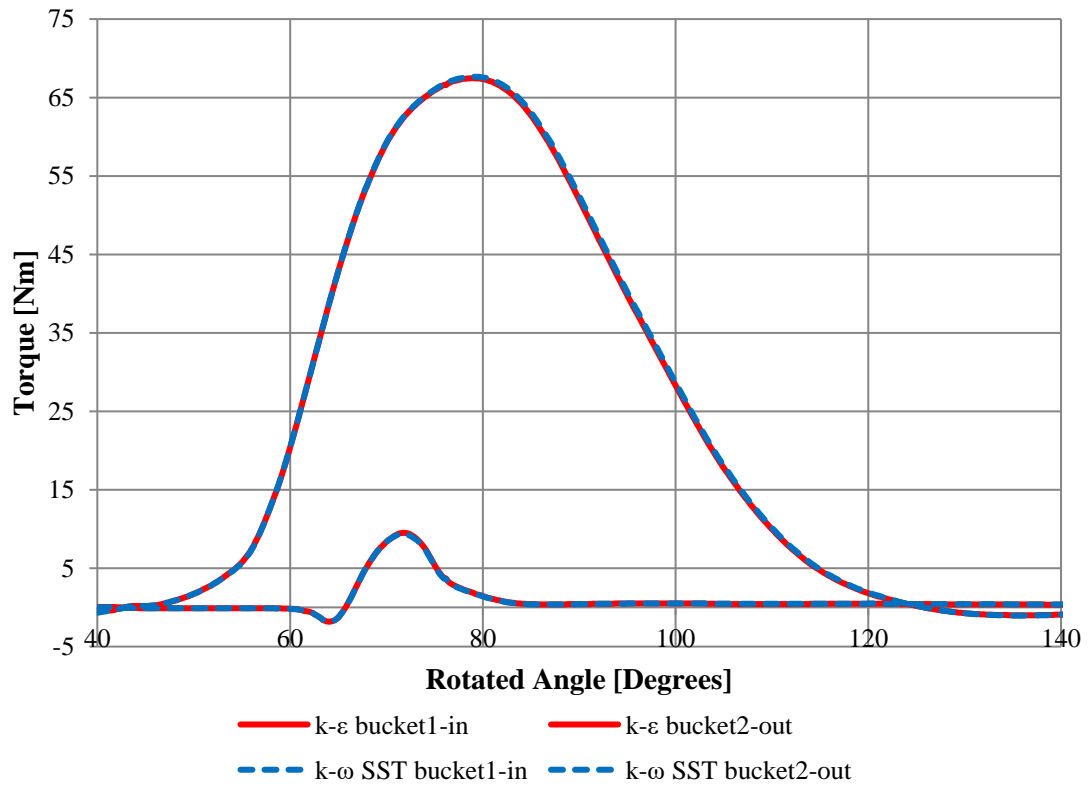


Fig. 3-26 Torque curves comparison of 2-bucket runner simulation with different turbulence models

3.3.2.2 Discretisation Methods

It has been mentioned previously in 3.2.3.5 that surface tension is an important factor to consider when modelling Pelton turbines. However, a typical VOF scheme has deficiencies in calculating a smooth surface tension force along the liquid–gas interface and under several conditions induces high numerical diffusion [102]. Therefore selecting a discretisation model that limits numerical diffusion is an important factor to consider in multiphase modelling

When using FLUENT with the implicit pressure-based solver, there are two options for the VOF volume fraction discretisation; the Compressive scheme and the HRIC (High Resolution Interface Capturing) scheme. In the absence of clear recommendations a study was performed to determine the most appropriate choice. Fig. 3-27 shows a water volume fraction plot through the jet as it passes through the rotating runner domain, for the Compressive (left) and HRIC (right) discretisation schemes. In all simulation cases the interface is treated as sharp and the Interfacial Anti-Diffusion option is enabled. The width of the air-water interface as measured

at the arrows as a percentage of the overall jet diameter is 20% for Compressive and 27.9% for HRIC, indicating slightly higher diffusion for the HRIC scheme. Similarly Fig. 3-28, shows an isovolume plot of the water leaving the runner after 360° rotation, coloured between 0% and 10% water volume fraction. For Compressive (left) there is much more red, indicating less diffusion of the water volume fraction and furthermore there is less smearing of the water in the right hand side of the casing as it travels towards the symmetry plane. In addition, Compressive solved marginally faster.

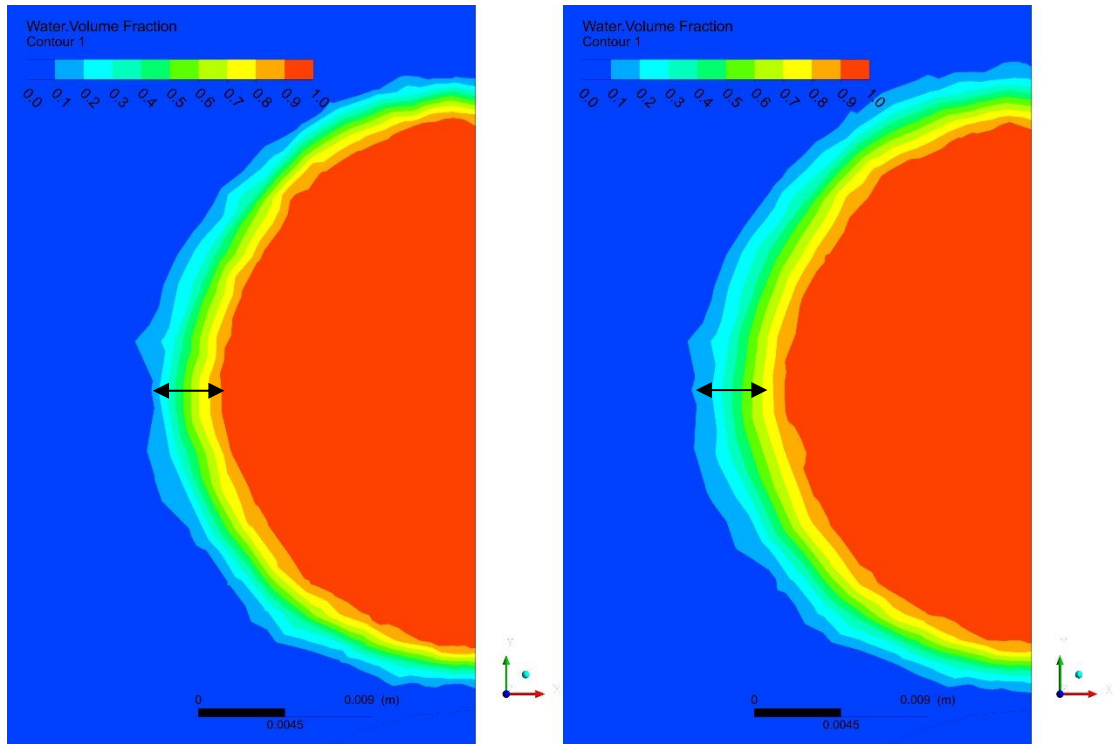


Fig. 3-27 Comparing Volume Fraction for Compressive (left) and HRIC (right) through the jet

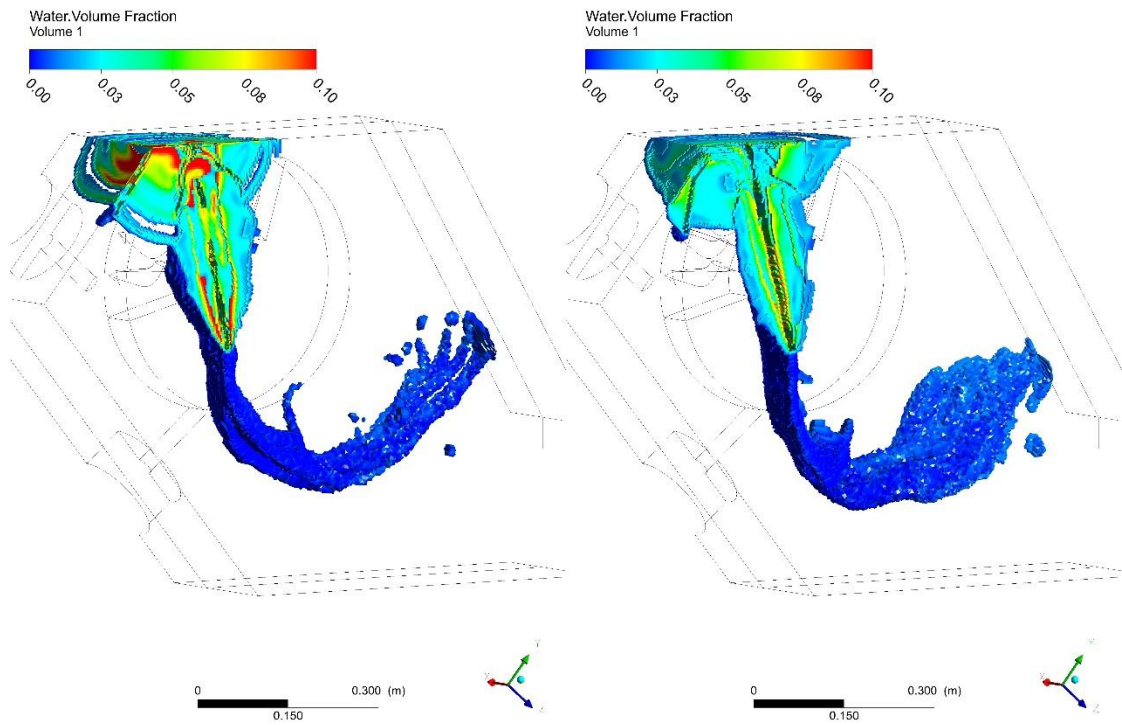


Fig. 3-28 Comparing Volume Fraction for Compressive (left) and HRIC (right) from a rear view at 360°

For this reason, it was decided to proceed with the Compressive discretisation scheme.

3.3.2.3 Solver Control

FLUENT offers two upwind schemes for the temporal transient formulation, First-Order accurate and Second-Order accurate. It is known from the theory that Second-Order will generally obtain more accurate results, but it may be more difficult to obtain convergence. Both cases were run for the same step size and to a similar degree of convergence. Fig. 3-29 shows an isosurface plot of the water leaving the runner after 360° rotation displayed at a water Volume Fraction of 1%. Likewise, the torque curves for these simulations are shown in Fig. 3-30. It can be concluded that the torque curves are almost identical, with the Second-Order scheme predicting a higher torque for the outside of the bucket, similarly the isosurfaces appear very similar in shape and capture to a comparable level the water sheets from each bucket, shown as distinct streaks in the right hand side of the casing.

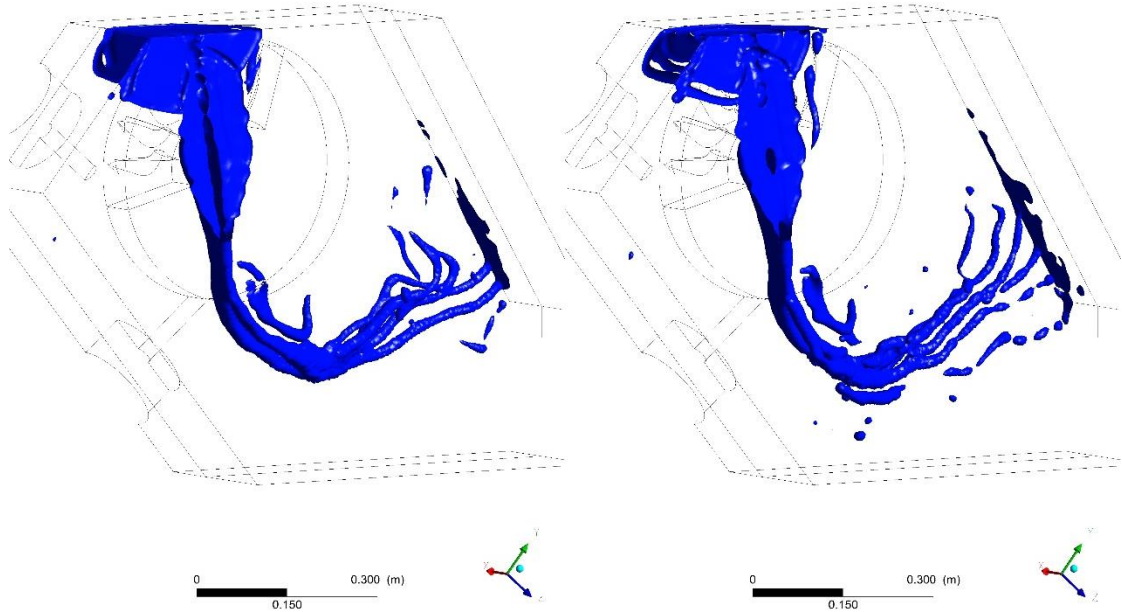


Fig. 3-29 Comparing 1% Water Volume Fraction for First-Order (left) and Second-Order (right)

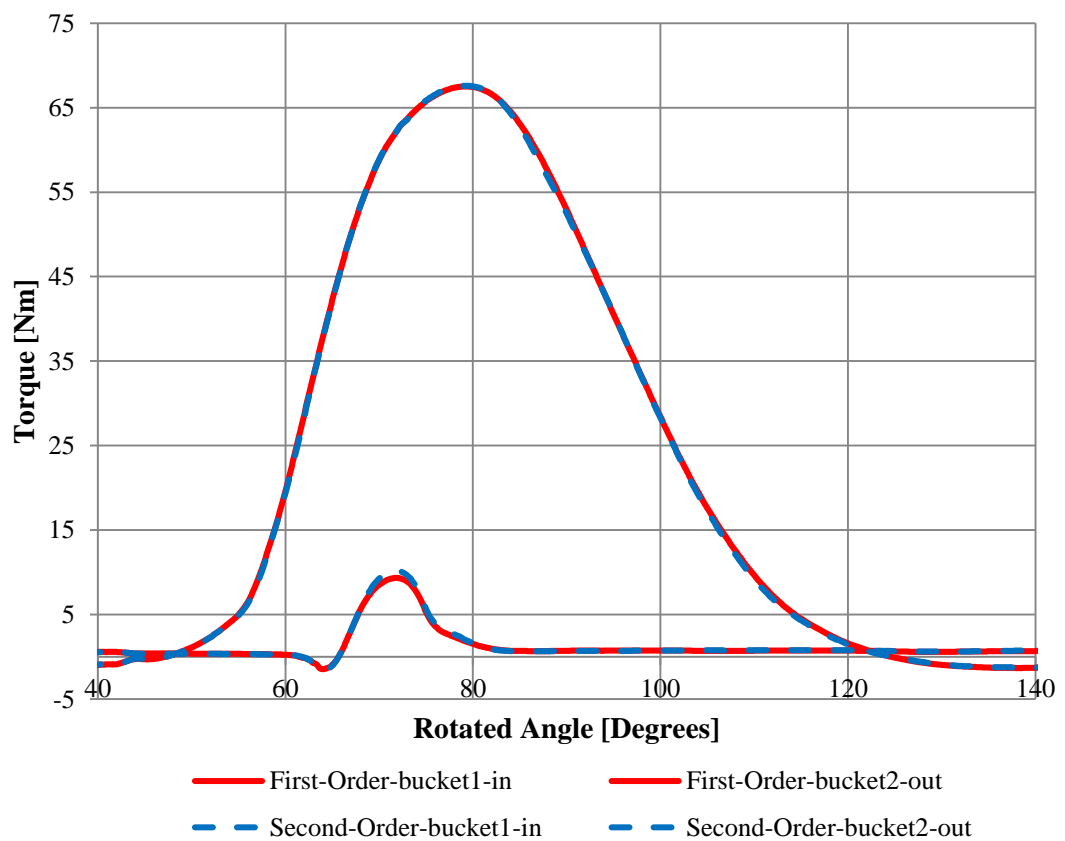


Fig. 3-30 Torque curves comparison for First-Order and Second-Order time (or temporal) discretisation

Since it took marginally longer to obtain similar residual targets for the Second-Order schemes all simulations will be carried out to First-Order accuracy.

3.4 Model Verification

3.4.1 Timestep Independence Study

Since the nature of the Pelton turbine simulation is transient it is therefore necessary to define a timestep. In general a number of CFD textbooks suggest that in order to be numerically stable it is required to maintain a Courant number of 1 or below. The Courant number is expressed in equation (3.7).

$$\text{Courant Number} = \frac{u \, dt}{dx} \quad (3.7)$$

Where u , is the 1-dimensional flow velocity, dt is the timestep size and dx is the typical mesh spacing in the direction of u .

Without reference to the mesh size or timestep the Courant number will of course be largest when the flow velocity is the highest, as is the case in phase i of the bucket duty cycle. In accordance with this, the mesh spacing defined above was monitored with respect to the Courant number.

Nevertheless, all simulations presented in the thesis were solved using the implicit based solver where the restriction on the Courant number is not as severe as when using an explicit solver and it was found that the stability of the simulation was generally not affected if the Courant number exceeded 1.

In phase ii of the bucket duty cycle the timestep is controlled by the angle rotated in each timestep, in the first instance a conservative timestep of 0.1 degree rotation (i.e. $\frac{1}{946.46 \div 60 \times 3600} = 1.7609 \text{ e-05 s}$) was initially chosen to give an RMS Courant number of 1. However to try and reduce the computational time a timestep study was carried out to try and use as large a timestep as possible without effecting the computational results. Details of the timesteps studied are shown in Table 3-5.

Rotation Angle [deg/timestep]	0.1	0.2	0.4	0.8
Physical time [s]	1.7609 e-05	3.5219 e-05	7.0438 e-05	1.4088 e-04

Table 3-5 Timesteps chosen for study

Table 3-6 shows the differences in normalised efficiency for the 4 timestep variations and the torque curves for these simulations are shown in Fig. 3-31.

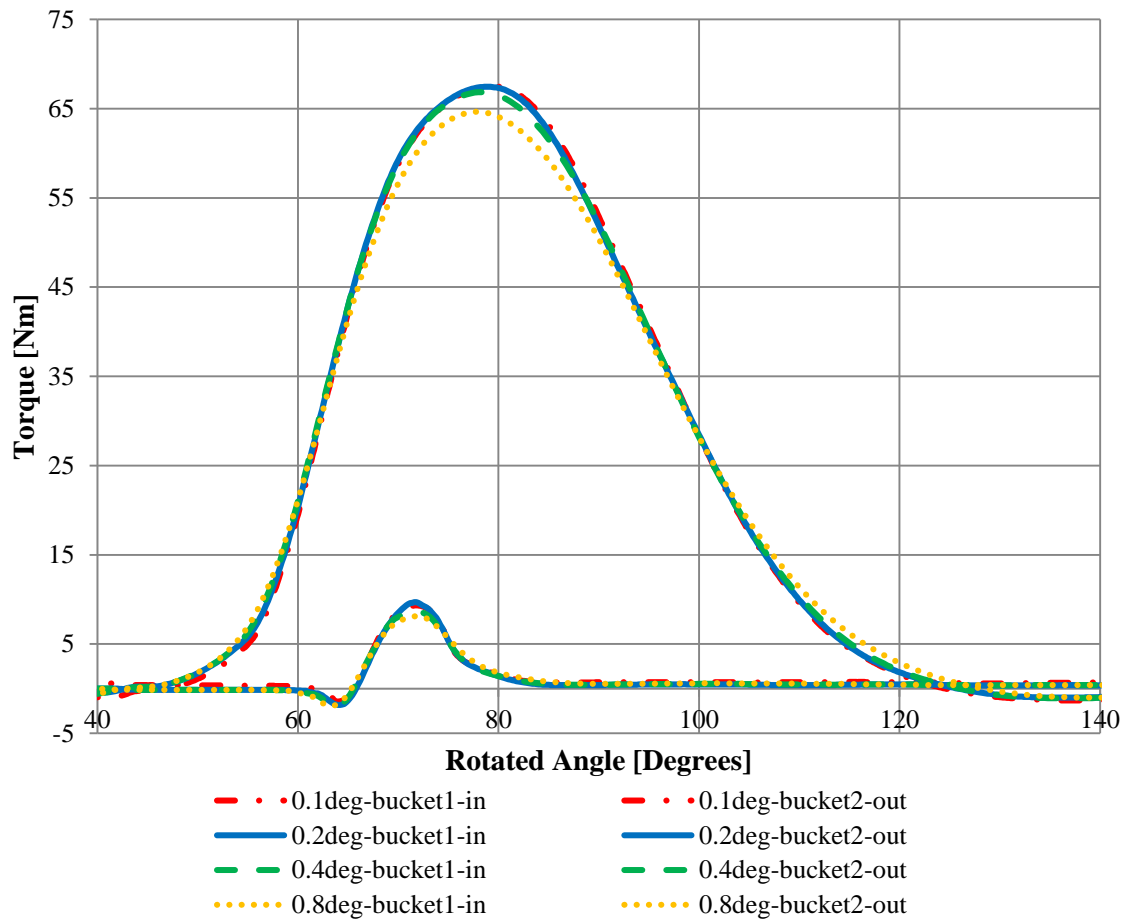


Fig. 3-31 Torque curves comparison for varying timestep

		Timestep= 0.1 deg	Timestep= 0.2 deg	Timestep= 0.4 deg	Timestep= 0.8 deg
Normalised efficiency	[%]	100.00%	99.503%	99.105%	98.14%

Table 3-6 Average torque and efficiencies for changing timestep

Although the shape of the torque curve for the different timestep is very similar, the difference in normalised efficiency for each timestep is more pronounced, showing a fairly substantial drop of 1.86% for 0.8 deg. The difference between 0.1 deg and 0.2 deg and 0.2 deg and 0.4 deg is negligible and therefore based on these results a timestep of 0.2 deg will be used.

3.4.2 Mesh Independence Study

“CFD is only as good as the mesh”¹¹, a wise man once said, but which wise man originally said it has been lost in the sands of time. The adage is now ubiquitous and naturally a large portion of time is spent determining the effect the mesh has on results.

In order to investigate the discretisation errors introduced by the mesh a Grid Convergence Index (GCI) study was carried out using the 2.87 million element runner mesh and the 3.9 million element casing mesh described in section 3.2.2¹². This method to examine the discretisation errors with respect to mesh refinement was suggested by Roache [103], and involves performing the simulation on two or more successively finer meshes. As the mesh is refined (mesh cells become smaller and the number of cells in the flow domain increase) the spatial discretisation errors should asymptotically approach zero, excluding computer round-off error [104].

Three meshes were created using a refinement ratio $r=1.2$ with the coarsest mesh containing 6.77 million elements and the finest mesh containing 11.92 million elements. The results of the three meshes, normalised to the coarsest mesh result are shown in Table 3-7 below. The results are also plotted in Fig. 3-32. Furthermore, Table 3-7 also indicates the time taken for each simulation run using the Lancaster University High End Computing (HEC) cluster on four dedicated 16-core servers (each with two Intel(R) Xeon(R) E5-2640 v3 @ 2.6 GHz processors).

Mesh #	Normalised Grid Spacing	Number of Elements Runner + Casing [million]	Normalised Efficiency [%]	Wall clock time
Coarse	1.000	2.87 + 3.90	100	31 hr 12 mins
Med	0.833	3.70 + 4.55	100.688	56 hr 49 mins
Fine	0.694	5.11 + 6.81	100.942	122 hr 08 mins

Table 3-7 Mesh refinement study results normalised to coarse grid

¹¹ Matthew 7:24-25

¹² These mesh sizes may seem modest in the ‘grand scheme of things’, however it must be acknowledged that since simulations are solved on a relatively moderate sized HPC cluster and small timestep sizes are required, then solve times would become unfeasible should the meshes be more dense.

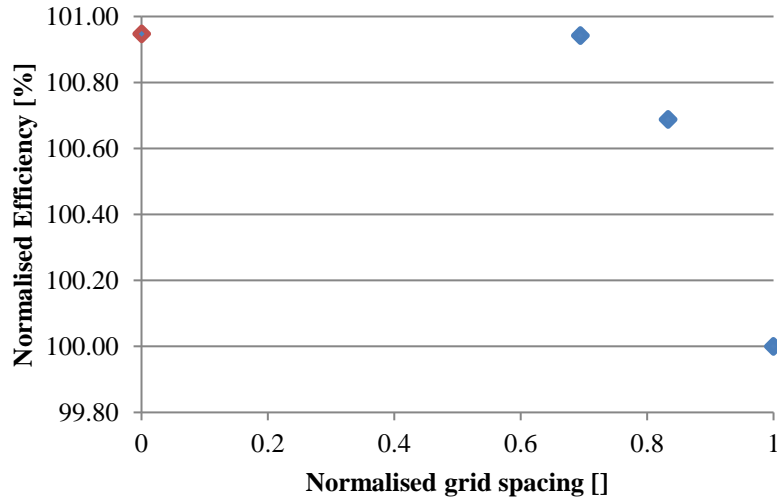


Fig. 3-32 Mesh refinement study results: normalised efficiency against normalised grid spacing

As the grid spacing is reduced, the efficiency approaches the asymptotic zero grid spacing value. The order of convergence, p_c , can be calculated using equation (3.8) below.

$$p_c = \frac{\ln\left(\frac{\eta_1 - \eta_2}{\eta_2 - \eta_3}\right)}{\ln(r)} \quad (3.8)$$

Where η_n is the efficiency for each mesh and n is the mesh number.

Using the order of convergence obtained, the efficiency at zero mesh spacing, $\eta_{h=0}$, can be determined using a Richardson extrapolation of the two finest meshes.

$$\eta_{h=0} = \eta_3 + \frac{\eta_3 - \eta_2}{2^{p_c} - 1} \quad (3.9)$$

This gives a zero mesh spacing of 100.947 %, which is also plotted in Fig. 3-32.

The order of convergence can also be used to calculate the GCI using a safety factor F_s of 1.25 as suggested by [103] for grid convergence studies using three or more grids. The GCI for Mesh 3 & 2 and Mesh 3 & 1 can be calculated as follows:

$$GCI_{3,2} = \frac{F_s(\eta_3 - \eta_2)/\eta_3}{r^{p_c} - 1} \quad (3.10)$$

$$GCI_{3,1} = \frac{F_s(\eta_3 - 1)/\eta_3}{r^{p_c} - 1} \quad (3.11)$$

The grid convergence indexes are given in Table 3-8 below.

Refinement Ratio	r	1.2
Order of Convergence	P_c	5.4688
Safety Factor	F_s	1.25
GCI for meshes 3 and 2	$GCI_{3,2}$	0.001838
GCI for meshes 2 and 1	$GCI_{2,1}$	0.004994
GCI for meshes 3 and 1	$GCI_{3,1}$	0.006820

Table 3-8 Mesh refinement study: Grid Conversion Indexes

To check whether the solution is within an asymptotic range, the following equation (3.12) can be used;

$$\frac{GCI_{2,1}}{r^{P_c} \times GCI_{3,2}} = 1.0025 \quad (3.12)$$

The result is very close to 1 which indicates that the solutions are well within the asymptotic range.

Fig. 3-33 shows the torque curves on the inside and outside of the first two buckets of the six bucket runner simulation for each mesh used in the mesh refinement study. The timestep used for each was 0.2 deg, which was shown to produce accurate results in 3.4.1.

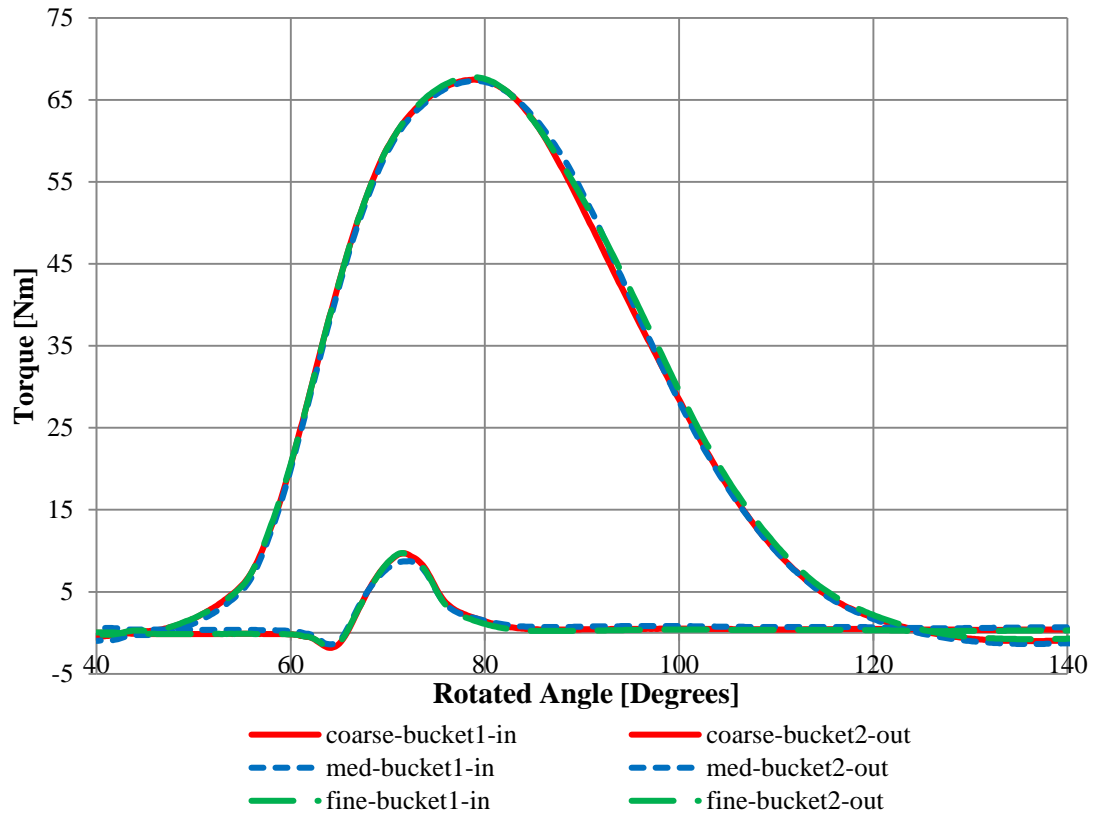


Fig. 3-33 Mesh refinement study torque curves

The results show a systematic difference in the peak torque on the outside of each bucket and also a slight difference during the final portion of water leaving each bucket (i.e $80^\circ - 120^\circ$ etc). It is important to note that although the magnitude of the torque differs as the number of elements increases, the general shape of the torque curve is still captured with the coarse mesh.

3.4.3 Mesh Effects on Casing Flow

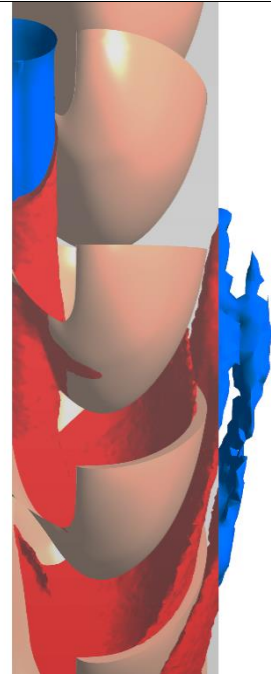
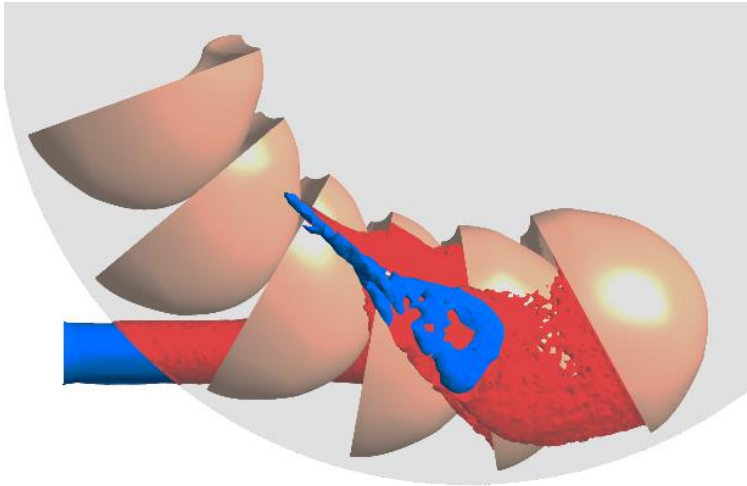
Thus far, spatial and temporal convergence has been judged by considering the effects these parameters have on the torque curve. This is a very importance factor to assess since it can be used to calculate the numerical efficiency, which can be validated¹³ against experimental data. However, to verify¹⁴ whether the CFD model developed in this chapter is suitable to achieve the stated aim, it is important to consider to what extent the mesh has on altering the appearance of the flow in the casing. As we wish to develop a tool, which can predict the flow passage in the casing it is therefore critical to determine whether this will be affected by the level of mesh refinement and if indeed the coarse mesh is suitable for this task.

Fig. 3-34 shows the free surface isosurface (water volume fraction = 50%) plotted at the same timestep (80° rotation) for the coarse, medium and fine mesh. The part of the isosurface plotted in blue is the fluid in the casing domain and in red in the rotating runner domain, with the grey denoting the interface. It can be observed that the overall shape of the free surface is broadly the same, since the meshes are torque independent then one can conclude that the shape of the water leaving the buckets will be alike as obtaining accurate torque results ensures the correct angle of deflection and the correct energy dissipation. In addition, there appears to be very little difference in the level of diffusion within the runner domain, however there is some diffusion experienced as the water sheets pass the interface and enter the casing domain. This will largely be because of the two simultaneous features, the influence of the tetrahedral cells, which naturally diffuse the free surface (introducing numerical diffusion errors) and the rotating sliding mesh leading to non-conformal interfaces, which inherently also introduce numerical diffusion issues.

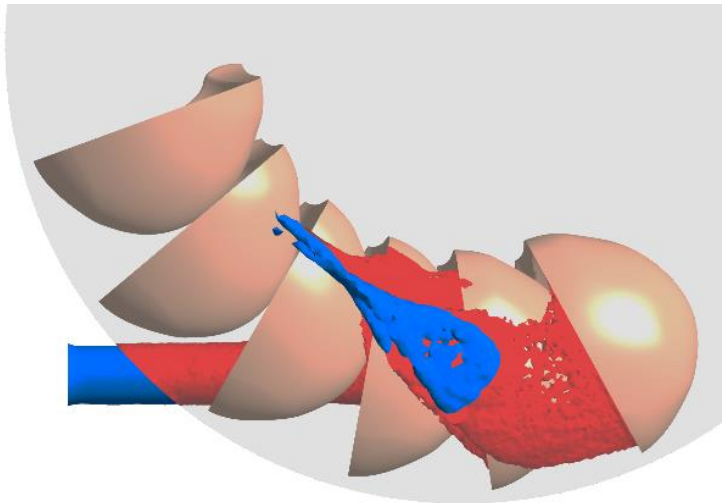
¹³ The process of determining if a mathematical model of a physical event represents the actual physical event with sufficient accuracy [122].

¹⁴ The process of determining if a computational model obtained by discretising a mathematical model of a physical event and the code implementing the computational model can be used to represent the mathematical model of the event with sufficient accuracy [122].

Coarse Mesh



Medium Mesh



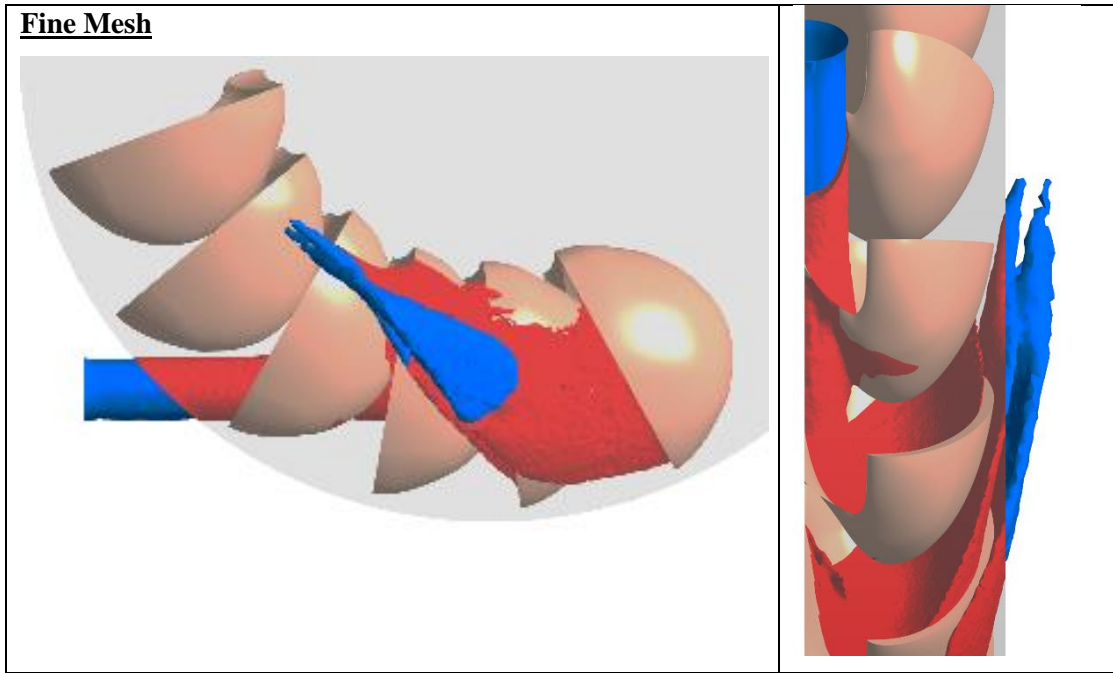


Fig. 3-34 Volume fraction interface at the free surface for coarse, medium and fine meshes. Red indicated volume fraction within the rotating domain and blue in the stationary casing domain

Based on the plots in Fig. 3-34 for the three meshes with respective levels of refinement, the coarse mesh was deemed to be of suitable resolution to predict the water overall shape and direction of the water leaving the runner. However, since the project is interested more specifically in how the flow develops within the casing, it is more appropriate to also include some plots of the flow for the different meshes at the same timestep after the flow has travelled some distance from the runner. At this stage in the project, further mesh refinement was applied, referred to as the extra-fine mesh, which consists of a 7.2 million element runner mesh and 11.23 million element casing mesh.

Fig. 3-35 and Fig. 3-36 show three comparison plots at timesteps representing 240° and 360° rotation respectively. In both, water volume fraction isosurfaces of 1% are plotted for the four different meshes, where the blue represents the coarse mesh, red is the medium mesh, green is the fine mesh and yellow the extra fine mesh. The three comparisons in Fig. 3-35, show that the overall shape and direction of the water sheet highlighted in the red circle is well represented and does not alter as a result of mesh refinement and to indicate that the coarse mesh is suitable for analysing different casing configurations. In all meshes there are five/six fingers, highlighted in the green circle, which are smoother and sharply defined in the finer meshes. Overall, the coarse mesh is shown to provide a good approximation of the casing flow and the level of mesh refinement (i.e. edge, wall and body element sizing) will be applied to all subsequent analysis.

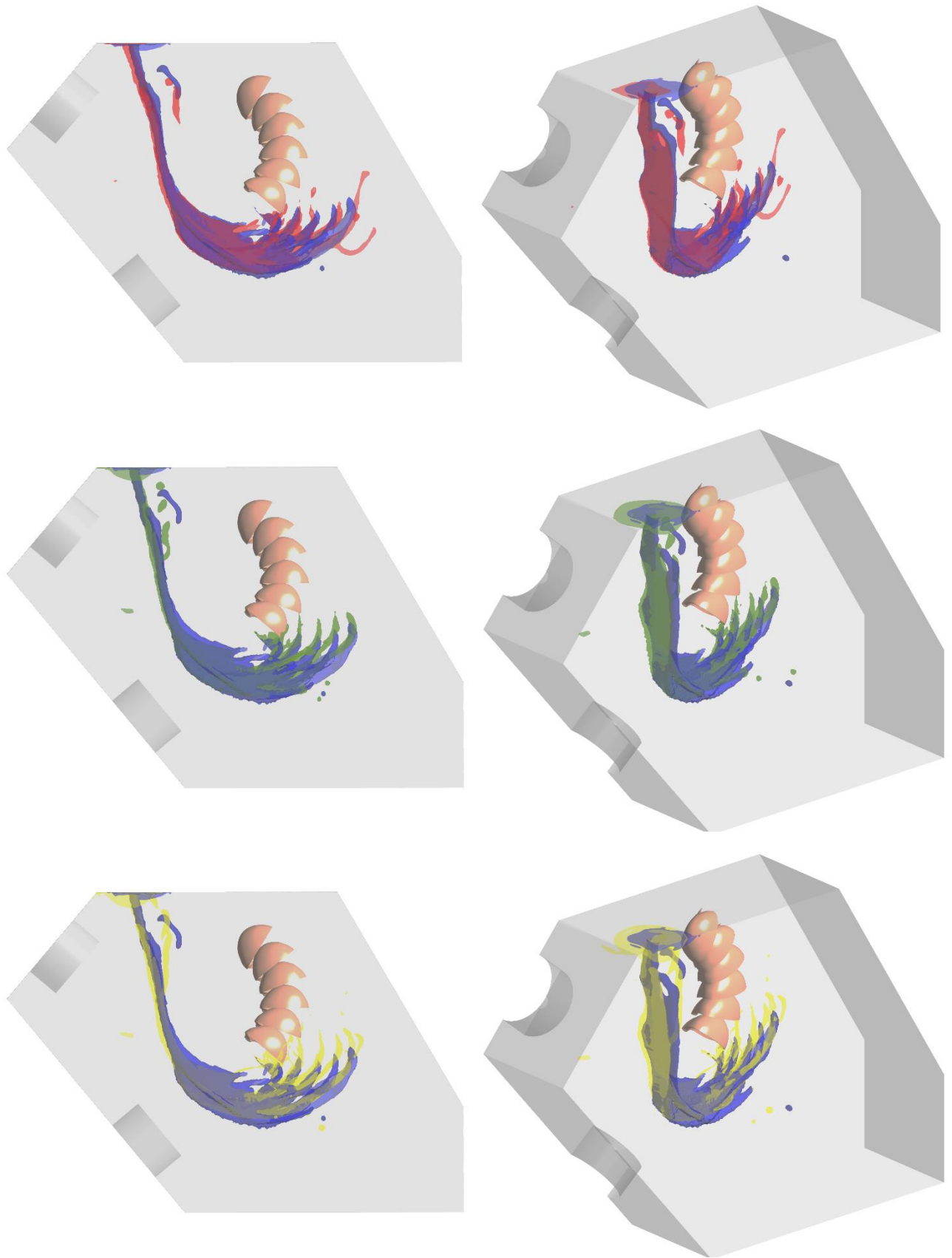


Fig. 3-35 Comparing 1% water volume fraction plot at 240° rotation for coarse (blue), medium (red), fine (green) and extra fine (yellow) grids

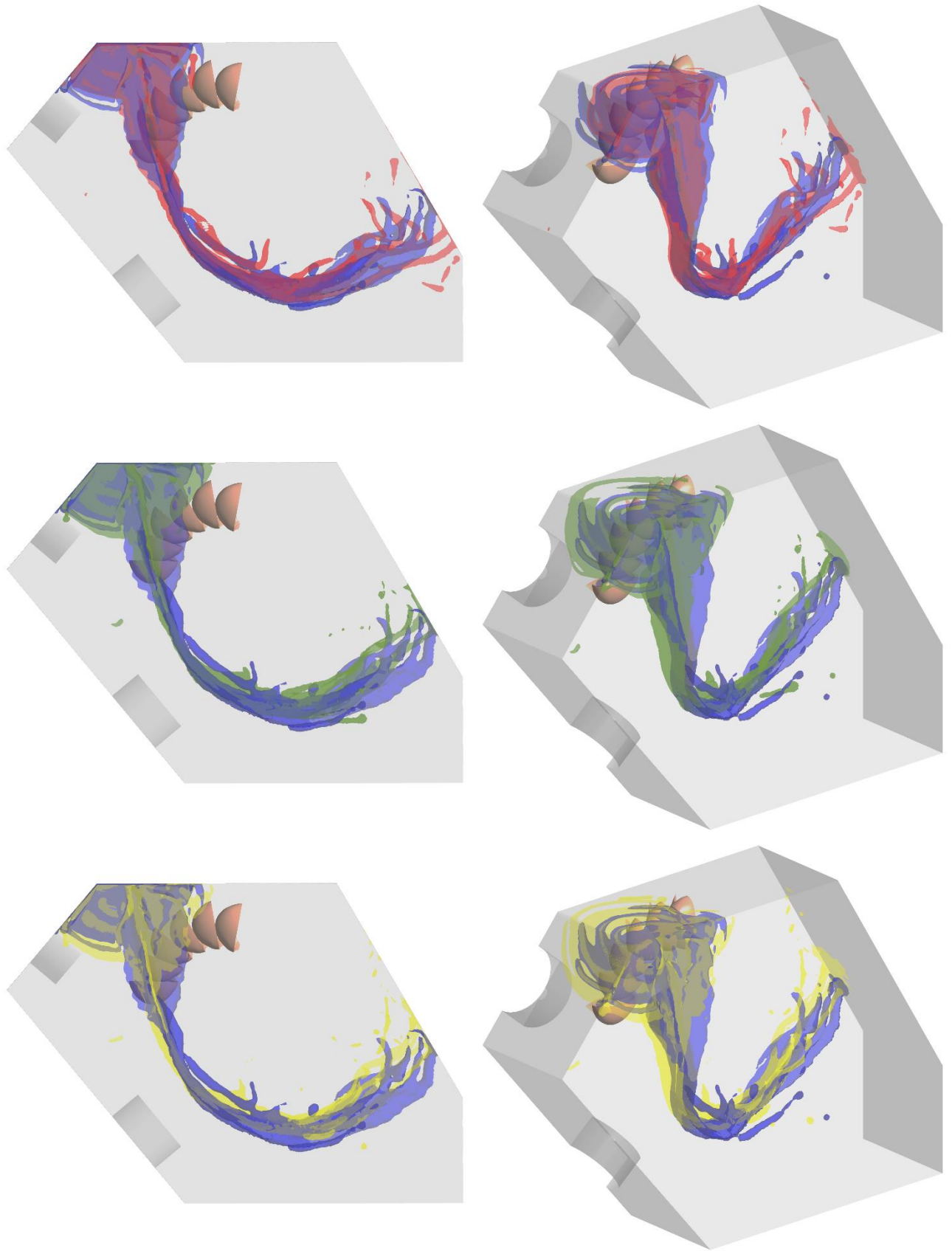


Fig. 3-36 Comparing 1% water volume fraction plot at 360° rotation for coarse (blue), medium (red), fine (green) and extra fine (yellow) grids

A further comparison between the four meshes is shown in Fig. 3-37, which depicts the water volume fraction isosurface as viewed from the roof of the casing, in each mesh the impact point of the vertical water sheet has been highlighted in a black arrow. As the mesh is refined the impact point moves closer to the runner. This is logical since the predicted efficiency also increases with the level of refinement, therefore the kinetic energy of the water and thus velocity for the fine grids will be lower, hence impacting the roof of the casing slightly closer to runner.

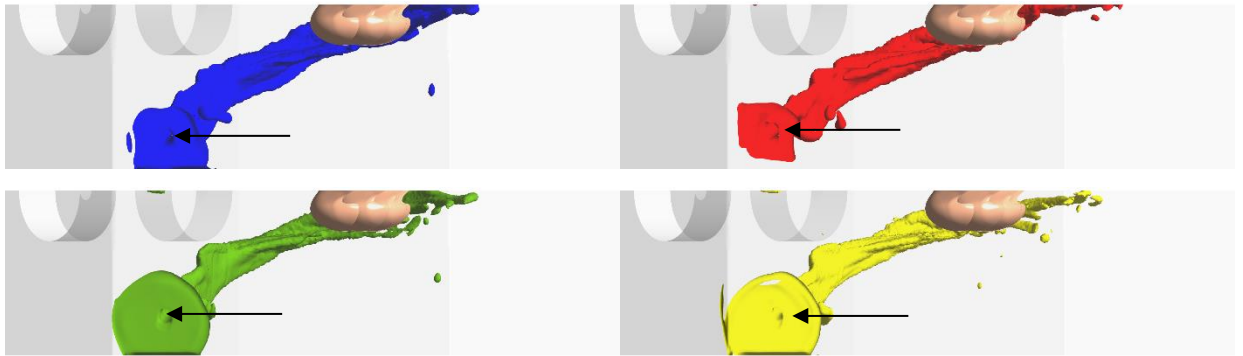


Fig. 3-37 Impact of the water sheet on the roof of the casing with coarse (blue), medium (red), fine (green) and extra fine (yellow) grids (snapshot at 200° rotation)

3.4.4 Estimating Efficiency Loss due to Casing

The method of determining mesh and timestep independence is based upon measuring the torque of the runner developed by the water jet and then using this to work out the efficiency. However, in order to measure the effect on efficiency from the splash water interference the simulation should be run for several runner rotations to establish the flow field within the casing. As a standalone test case, the 18 – bucket runner simulation, described in section 3.3.1.3, was run for four full runner revolutions, the torque plots for the first and second bucket have been modelled for the four phases, shown in Fig. 3-38.

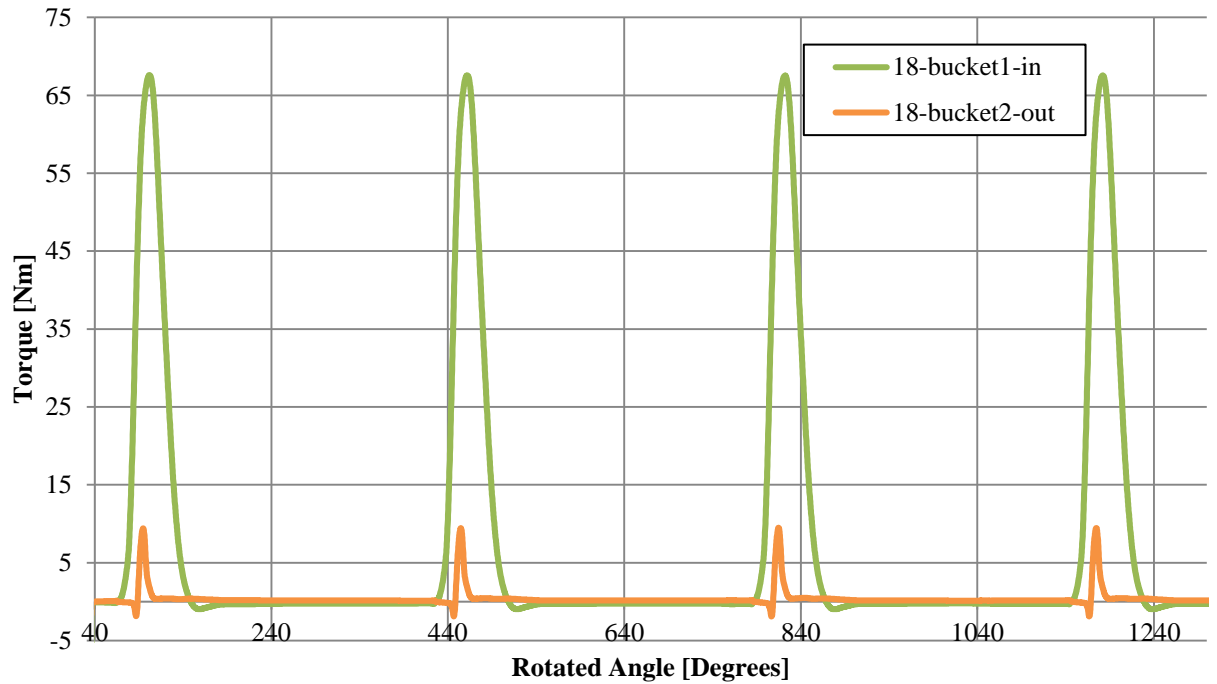


Fig. 3-38 Comparing the torque curves for bucket 1 and 2 during four rotations

As the results indicate the predicted torque experienced on the first two buckets are very similar for the four rotations. This suggests that at the current mesh resolution the splash water is not captured with enough detail to contribute to any significant interference with the runner and therefore influence to generated torque, which would show up after two revolutions when there is a considerable volume of water in the casing.

3.5 Correlating CFD Post Processing with Experiments

In 3.5.1 an attempt is made to correspond the critical flow patterns that appear with experimentally obtained images in order to validate the CFD model from a visual perspective. Overall the correlation is good, though the CFD model is limited in how it actually depicts the combination free surface, dispersed water sheets, and droplets as distinct media, which has been previously discussed.

3.5.1 Visual Comparison of Results

The use of advanced image techniques such as LDA and PIV to validate CFD results has been widely documented in the literature [105] [106]. From the PIV data, the mean velocity, turbulent kinetic energy, Reynolds stresses and dissipation rate can all be extracted from the snapshots of instantaneous velocity field. Despite the availability of PIV and similar techniques the CFD results within this study are to be used as a purely visual tool in order to provide detailed information related to the direction of the water flow and not necessarily the velocity, hence the

decision to compare the CFD results with visual snapshots obtained from the experimental test rig at NTUA.

Since the initial CFD modelling has been carried out for upper jet only the visual comparison will be made against the experimental test for upper jet operation detailed in 5.1.2. Following this the model is then applied for lower jet operation. In Fig. 3-40 it has been identified that there are three main portions of flow that offer visual comparison to the CFD results.

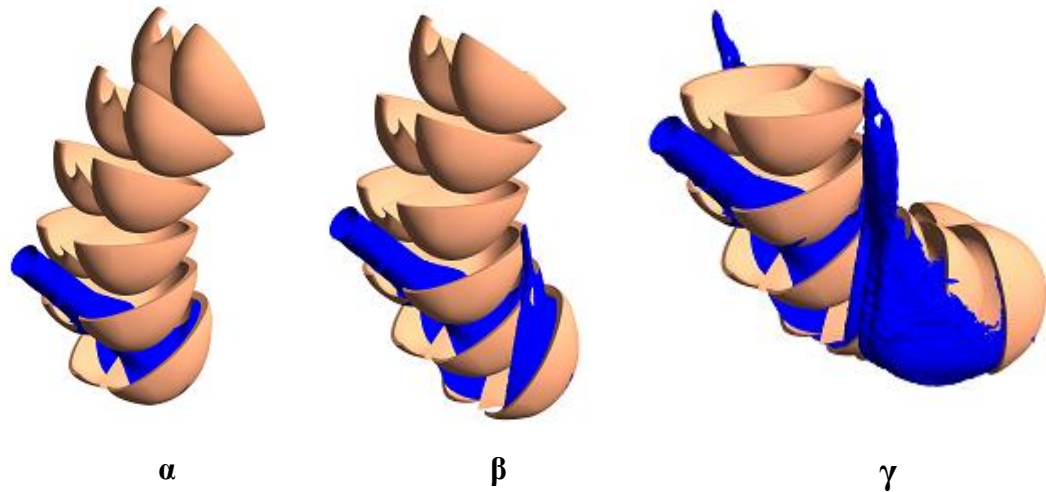


Fig. 3-39 Flow sequence of water leaving the bucket

The first, α , is the water that leaves closer to the root and along the sides of the bucket in the first 40° of rotation; this is shown in the first snapshot of the sequence. However not all of the flow can leave the bucket in this first initial stage, this flow can be seen in the right hand side of top right hand quarter of Fig. 3-40 and leaves more towards the cut-out. This flow still has a remaining portion of axial kinetic energy and makes its way towards the front face of the casing, as identified as the second main portion of flow, β . The third main portion, γ , identified is the last residual 20% of flow that remains in the bucket after at least 90° (i.e. the time period of the energy exchange for a single bucket in the torque graph in Fig. 3-33) of rotation; this is mainly visible as a fine spray mist in the experimental visualisation that travels towards the symmetry plane as a result of high radial but low axial kinetic energy. Once the water has impacted the front face of the casing it dissipates much of its remaining kinetic energy and the major force is now gravitational, it spreads a short distance before falling into the tailrace below, however on the side closest to the injectors this flow tends to recirculate and accumulate in the top left hand side of the casing, where interference with the water jet leaving the injectors occurs.

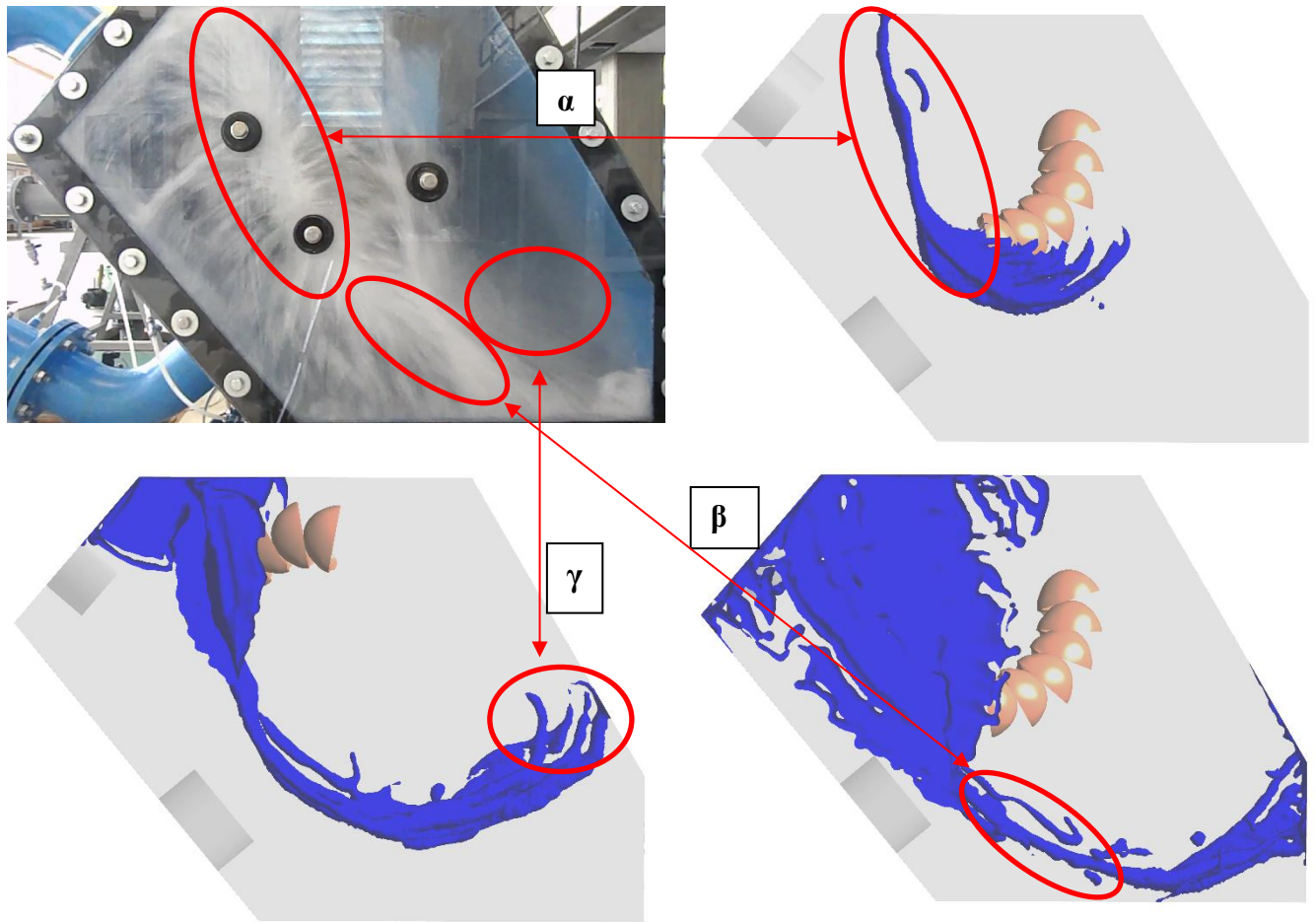


Fig. 3-40 Upper Jet Experimental and 1% water VF plot comparison for 6-bucket coarse mesh at 200°, 360°, 560° rotations at BEP of 946 rpm

3.5.1.1 Visual Comparison at different Rotational Speeds

Further analysis of the flow patterns described in section 3.5.1 will be carried out in Chapter 4 to aid understanding of how the casing design interacts with the flow and subsequently the impact this may have on splash water returning onto the runner or jet.

The simulations described so far have been at BEP of the turbine, however experimental testing will be carried out at different rotational speeds and flow rates, therefore as a further validation by means of visual inspection, two further simulations have also been carried out at different rotational speeds, one slower and one faster than the BEP and the flow patterns on the front casing wall have been compared with the CFD results. Fig. 3-41 illustrates the comparison between experiments and CFD by considering three snapshots reflecting 200°, 360°, 560° rotations at a rotational speed of 847 rpm.

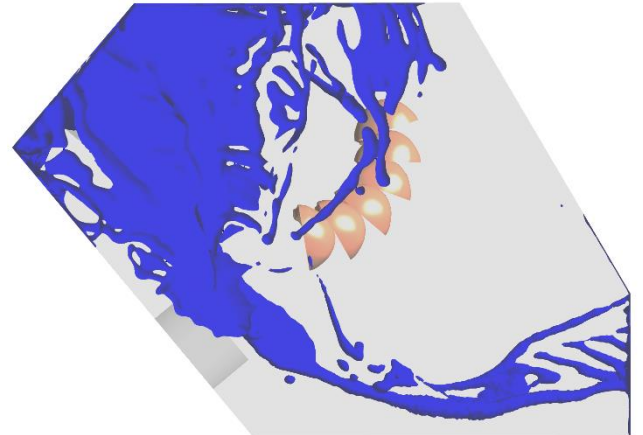
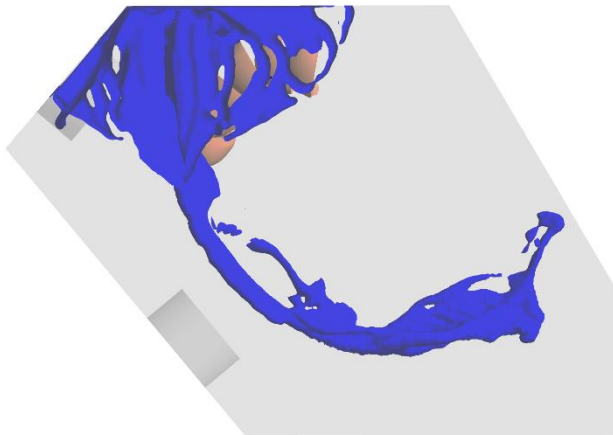
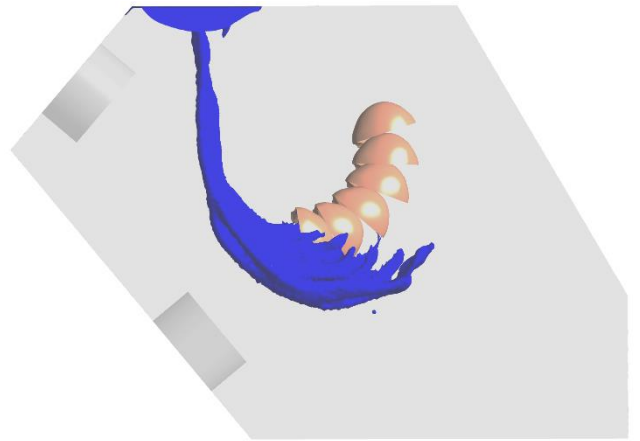
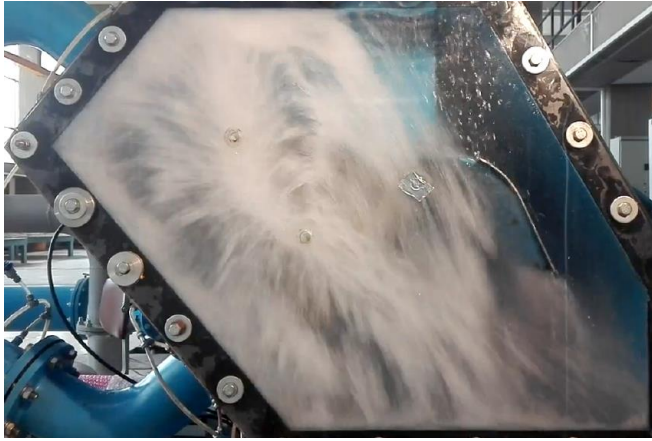


Fig. 3-41 Upper Jet Experimental and 1% water VF plot comparison for 6-bucket coarse mesh at 200°, 360°, 560° rotations at 847 rpm

Similarly, this is shown in Fig. 3-42 for 1040 rpm.

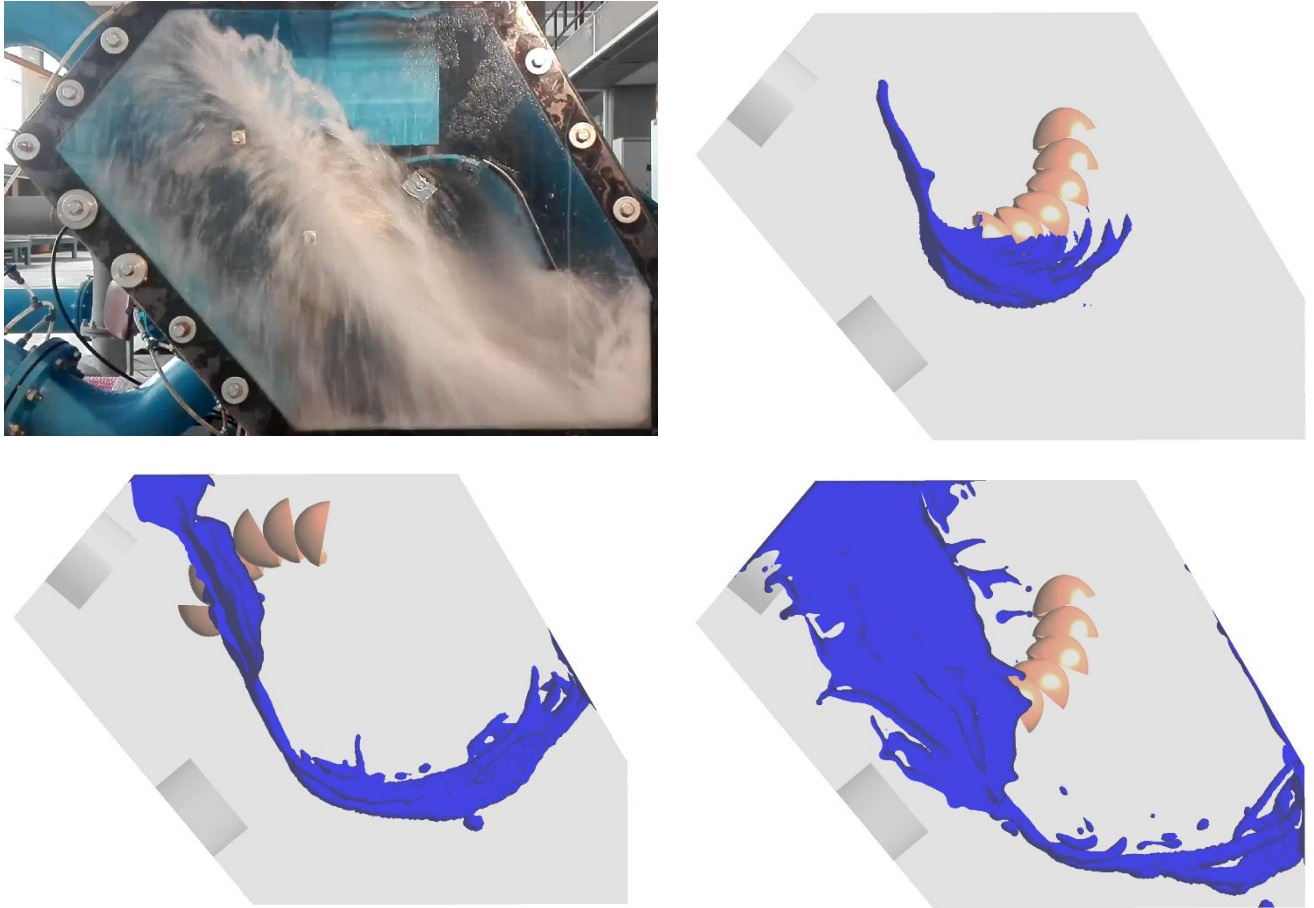


Fig. 3-42 Upper Jet Experimental and 1% water VF plot comparison for 6-bucket coarse mesh at 200°, 360°, 560° rotations at 1040 rpm

3.6 Summary of Pelton turbine casing CFD Modelling

This chapter has presented the CFD model that will be used to analyse the flow in the Pelton turbine and the general principles behind the modelling techniques. In addition, where possible, the assumptions have been discussed, justified and attempts to quantify the limitations are introduced. The creation of the modelling domains, meshes, definition of the solver physics and general setup of the simulation as well as the post-processing of the results with specific regard to the casing flow has also been discussed in detail.

The question that perplexes the author is, how might the casing simulations be validated against experiments beyond considering the calculation of bucket torque alone? Since it has already been described, there is a discontinuity of velocity across the interface in as much as the mesh in non-conformal and different frames of references are used for the two domain. This would make matching the velocity taken by PIV measurements or otherwise in a 3D case very difficult. One possibility is to correlate the obtained value of pressure on the casing walls from the CFD model to experimental measurements of force on the wall. However, this relies on the water

sheets characterising as close to reality as possible, which is unfeasible and such in any model the water sheets are always going to be representative rather than accurate. Unfortunately, the structure of the water (as droplets or sheets or mist or splashing) predicted by the CFD model is always going to be different from real life. In summary, it is challenging to achieve entirely mesh independent results since a much finer mesh than is currently used would be required, which is unfeasible with current computers available to the author.

In the absence of a true like for like comparison of the velocity of the flow and verification of exact location of the water in the casing based on pressure force, it would seem appropriate to select modelling methods, which solve in a reasonable timescale. Hence opting for the coarse mesh simulation, while being fully aware of the errors that can be introduced by lower order methods, poor mesh and insufficient temporal discretisation. Surface tension has been modelled in this chapter, however strictly speaking the volume of water present it can be assumed that this will over compensate for the surface tension force, which in reality is very small compared to the inertial forces. Moreover, modelling of turbulence using a number of two-equation RANS models has been shown to have minimal effect on the calculated torque, despite inviscid methods being suggested by other researcher. In spite of this turbulence will be applied to all future simulations.

Throughout this chapter the relative numerical errors based on the assumptions are given in Table 3-9 below¹⁵. The total numerical error calculated using the root-sum-square method is 0.97%. It should be noted, however, that there could be further sources of error not included, such as surface roughness. There could also be additional errors arising from the turbulence model used.

Source of Error	Numerical Error Band δ [%]
Timestep	0.50
Turbulence Modelling	0.47
Periodicity	0.12
Domain Discretisation (Mesh)	0.68
Total (Root-Sum-Square)	0.97

Table 3-9 Known relative numerical error band introduced by various assumptions

¹⁵ The errors are listed in the relevant sections, for example the timestep error is found as the difference between the normalised efficiency of timestep used in the study (0.2 deg) and the smallest timestep considered (0.1 deg), which equates to $100\% - 99.503\% = 0.5\%$

4 CFD Analysis of Pelton Casing Designs

In this chapter the Gilkes twin jet horizontal axis Pelton turbine, complete with the Z120 bucket type runner, depicted in Fig. 4-1, will be analysed in further detail using the CFD model developed in Chapter 3.

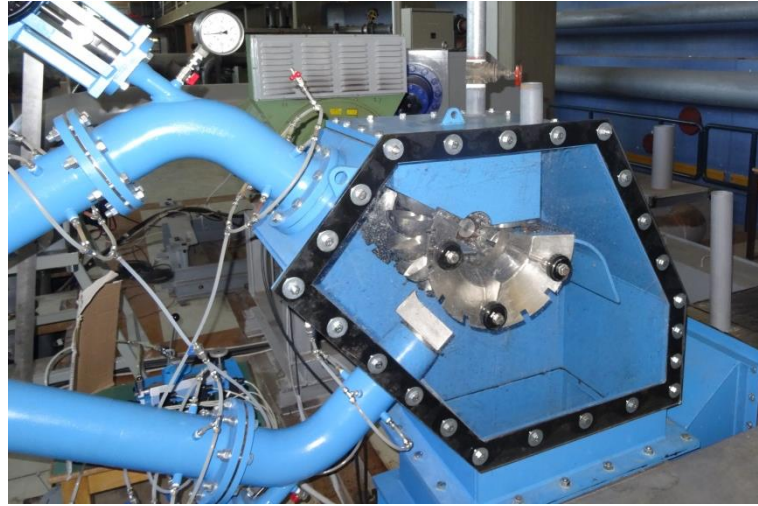


Fig. 4-1 Gilkes twin jet horizontal axis Pelton turbine

As highlighted in Fig. 4-1 and further detailed in the CAD and internal view shown in Fig. 4-2 and Fig. 4-3, the Gilkes Pelton turbine includes several shrouds and baffle plates. The purpose of these are to direct spray water away from the buckets and to avoid further inference with the runner and injectors.

At the start of the project the exact role of these shrouds and baffles was unknown and their influence on the efficiency has not been previously documented, therefore a systematic approach was taken whereby the addition of the individual components can be evaluated.

Following this, the CFD model was then applied to a significantly reduced casing width in phase 2.

Experimental testing of these different configurations will be provided in the following Chapter 5.

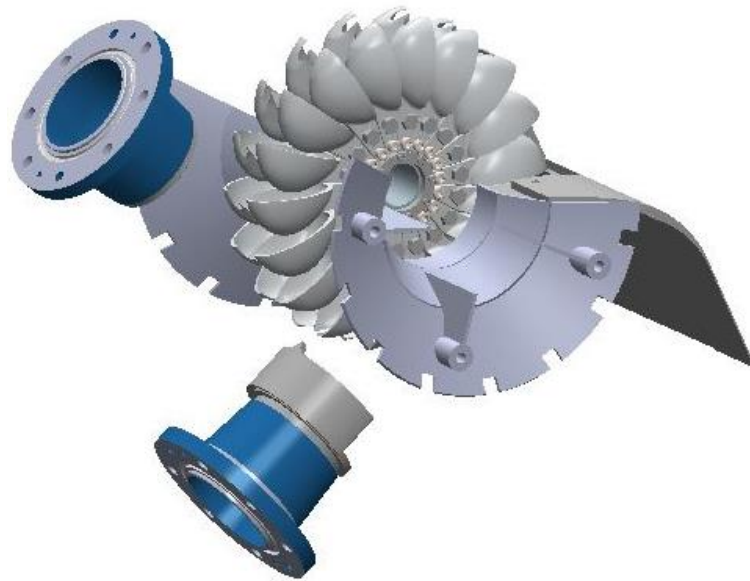


Fig. 4-2 CAD of internal view of the Gilkes Pelton turbine with baffle plates

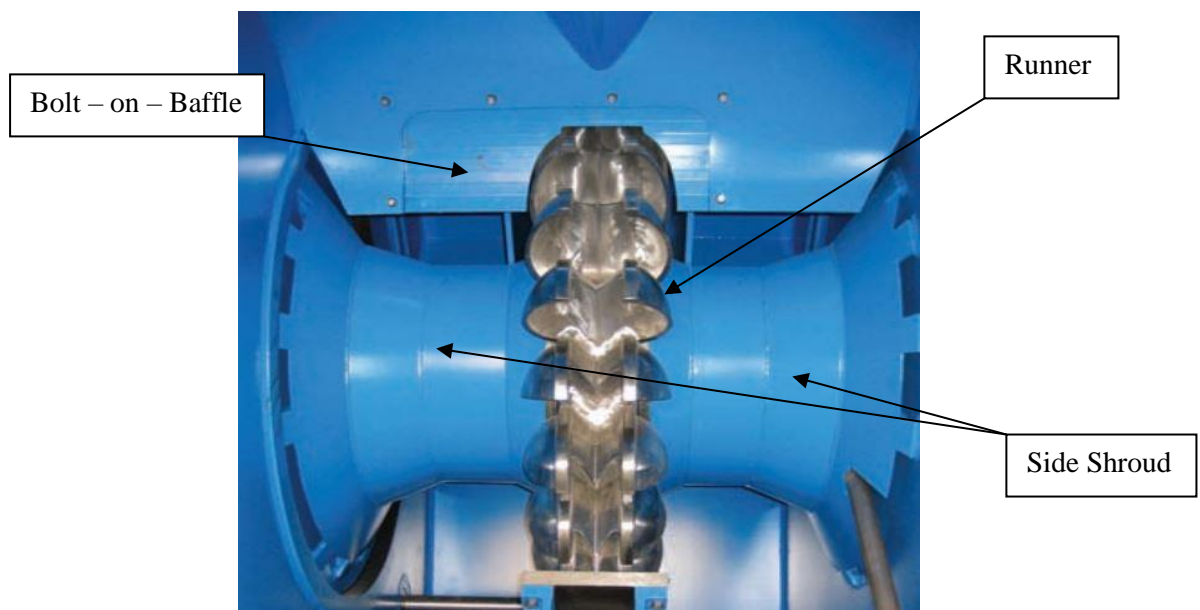


Fig. 4-3 Internal view of the Gilkes Pelton turbine with baffle plates

The investigation follows the standard CFD process developed in Chapter 3, namely;

1. Geometry creation
2. Mesh generation
3. FLUENT solve
4. Post processing

All simulations are run using the coarse 6-bucket runner mesh described in section 3.4. The new casing meshes, with the inclusion of shrouds and baffles, are generated with the same body, surface and edge element sizing applied and with 5 inflation layers around wall boundaries.

4.1 Phase 1 - Pelton Shroud and Baffle Testing

In this section the CFD model will be used to visualise the flow conditions within the casing for a number of different configurations as per the geometry depicted in Fig. 4-2. In the first instance it will be used to carry out further analyses of domain described in section 3.2.1, known henceforth as the ‘naked case’.

4.1.1 The Naked Case

The Naked Case, shown in Fig. 4-4 is the domain described in Chapter 3 and as the name implies is completely absent of shrouds or baffles. This will serve as the benchmark and provide further understanding into the flow phenomena and offer insight into the specific flow conditions that lead to optimal efficiency.

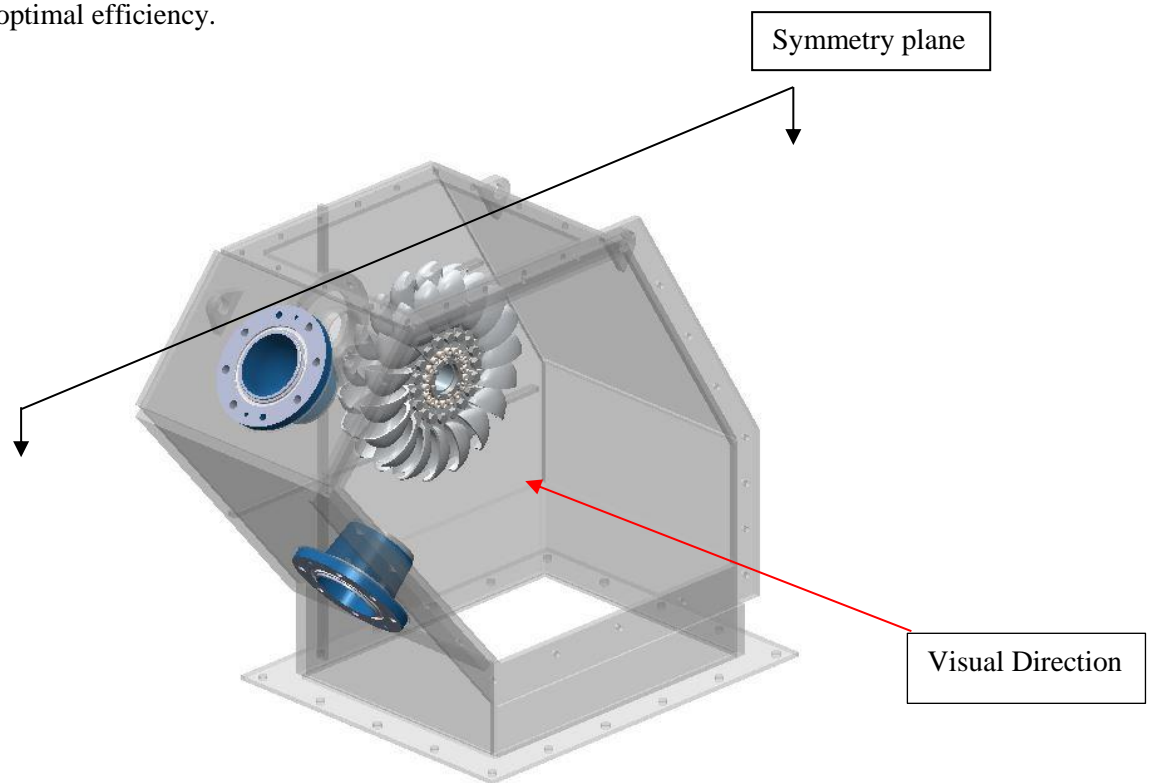


Fig. 4-4 The Naked Case

A more detailed description of the flow sequence will be outlined in 4.1.1.1.

4.1.1.1 Further Analysis of the Flow Sequence within the Casing – Upper Jet

When the time came finally to begin post processing the CFD results a number of decisions had to be made about the best way to visualise the flow and how it subsequently interacts with the casing. Since, the flow is inherently transient and time dependant it is often difficult to get a sense of movement from static images, so in some cases the images have been repeated using different visualisation strategies for further clarity. As previously stated the following figures plot an isosurface of 1% water volume fraction, which is not wholly realistic but does give an indication of where the water appears within the casing.

The following snapshots show the flow sequence of the water leaving the runner for upper jet operation for the naked case at the BEP operation. The first snapshots is taken at 100° rotation, shown in Fig. 4-5, which corresponds to the final portion of the simulation sequence described in section 3.2.5 (the red arrow indicates jet location and direction). The snapshots are then shown from 200° to 480°, representing a total simulation time of 0.083 s.

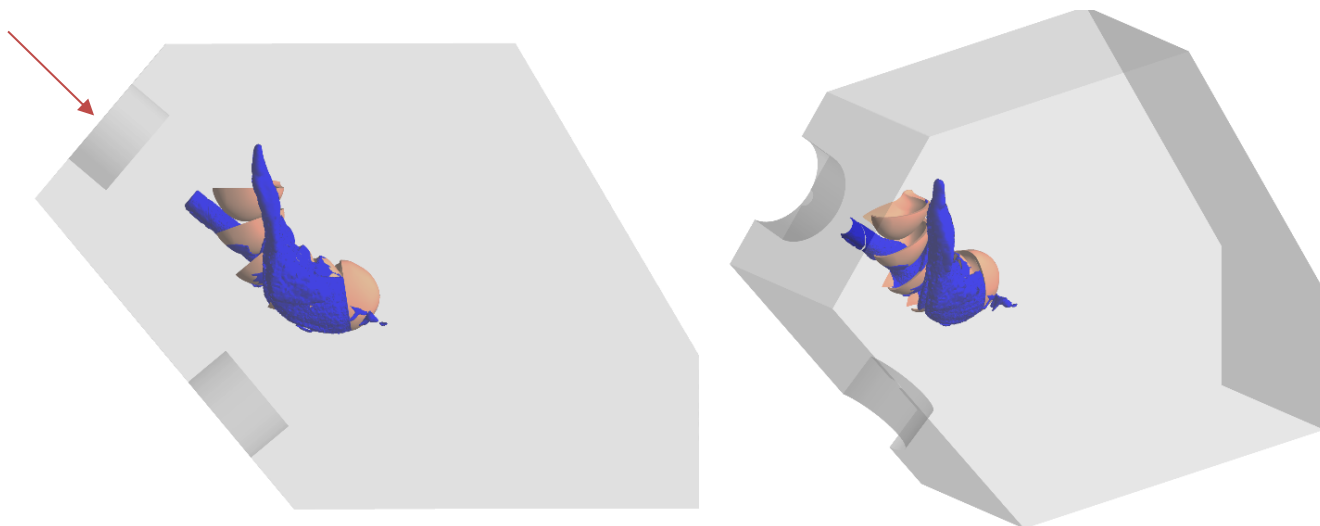


Fig. 4-5 Upper jet: casing flow for 100° rotation

The shape of the flow in relation to the casing depends mainly on the injector in operation. Thus, for the operation of the upper injector the flow after interacting with the rotor is diverted perpendicular to an area about an almost vertical line, which is slightly to the left of the shaft. However, part of the flow is driven upward and after impact on the roof of the casing it is reflected towards the runner area and injectors, causing a reduction in efficiency. As it can be observed, the flow after the interaction with the runner exits approximately parallel to the axis of the rotor, i.e., without significant twisting. It is obvious that this undesirable behaviour becomes more intense as the flow rate of the hydro turbine increases.

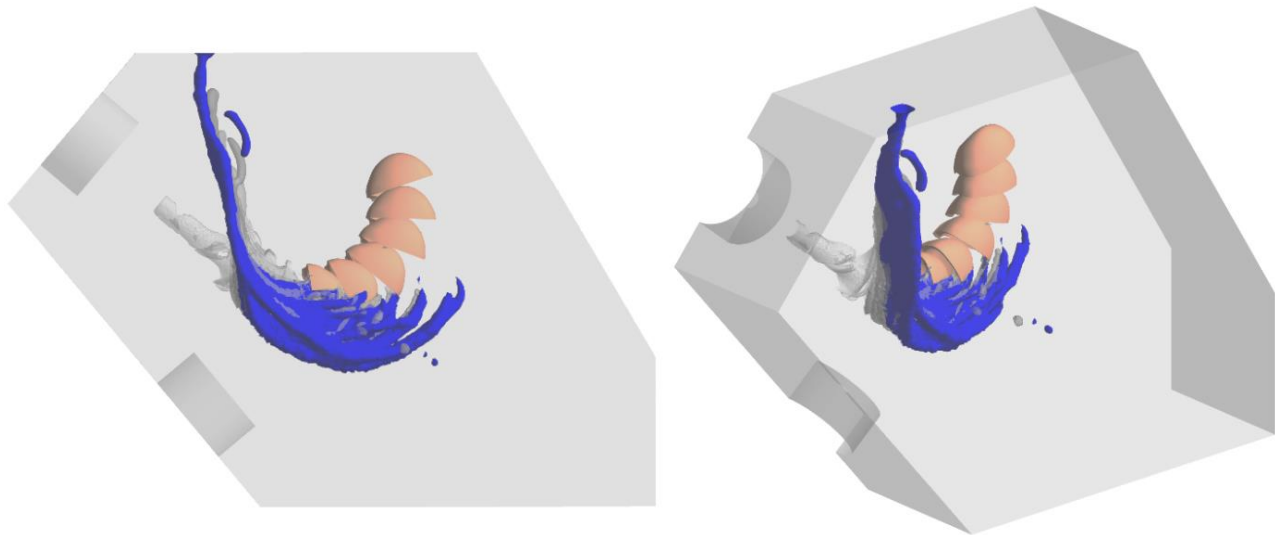


Fig. 4-6 Upper jet: casing flow at 200° rotation

It is shown in Fig. 4-6 that at 200° rotation, the water leaving the runner begins to interact with the roof of the casing. The point at which it interacts is at an axial distance, approximately 0.2 m from the symmetry plane of the runner. Based on the previous time frames, as shown in the grey volume fraction plots the water appears as an almost vertical sheet and the characteristic shape is due to the merging of the flow leaving the successive buckets closest to the root of the bucket.

Based on the corresponding velocity triangle, shown in Fig. 4-7 it is evident that the water has high relative components and small axial component due to the small deviation angle at this point of the bucket, hence it reaching the roof, a distance of approximately compared to the 0.2 m axial distance. Also, the remaining part of the water leaves the runner relatively low below the plane of the shaft, leading it to be directed mainly towards the tailrace and a portion of this to be directed towards the right hand side of the casing.

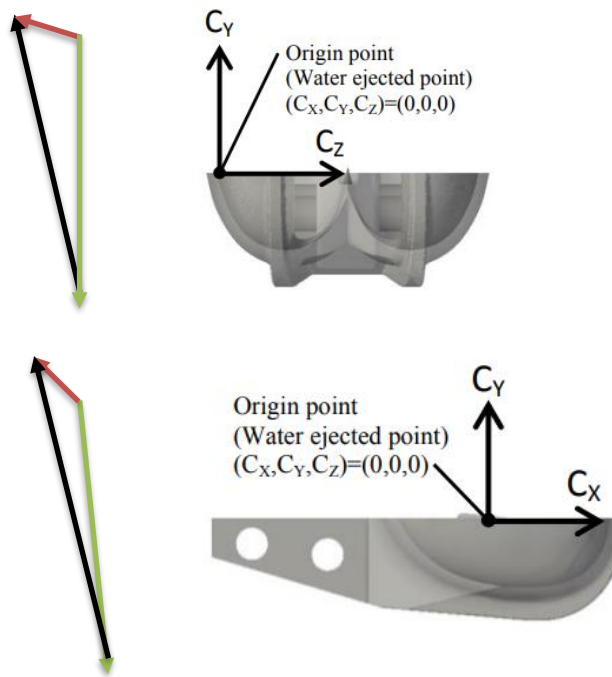


Fig. 4-7 Velocity triangle at maximum torque point from centre of bucket for axial and radial views U (green), C_2 (red), and W_2 (black) adapted from [107]

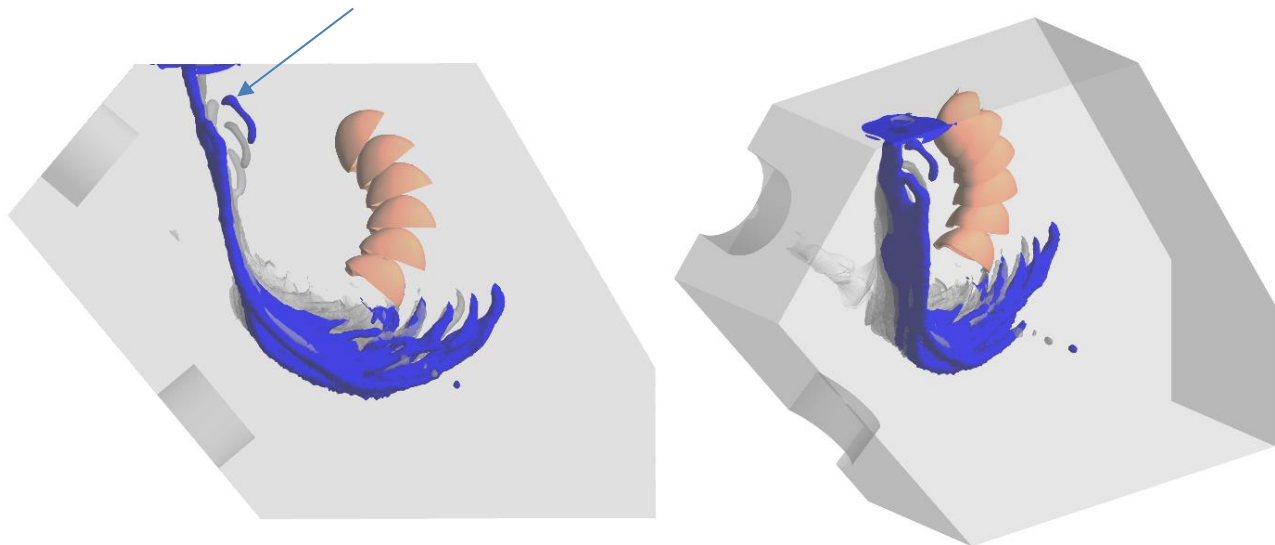


Fig. 4-8 Upper jet: casing flow at 240° rotation

The small amount of water that has broken away from the main portion of the water sheet, indicated by the arrow in Fig. 4-8, is due lack of interaction of the flow from the first bucket with a preceding bucket, this is largely a cosmetic feature and can therefore be ignored.

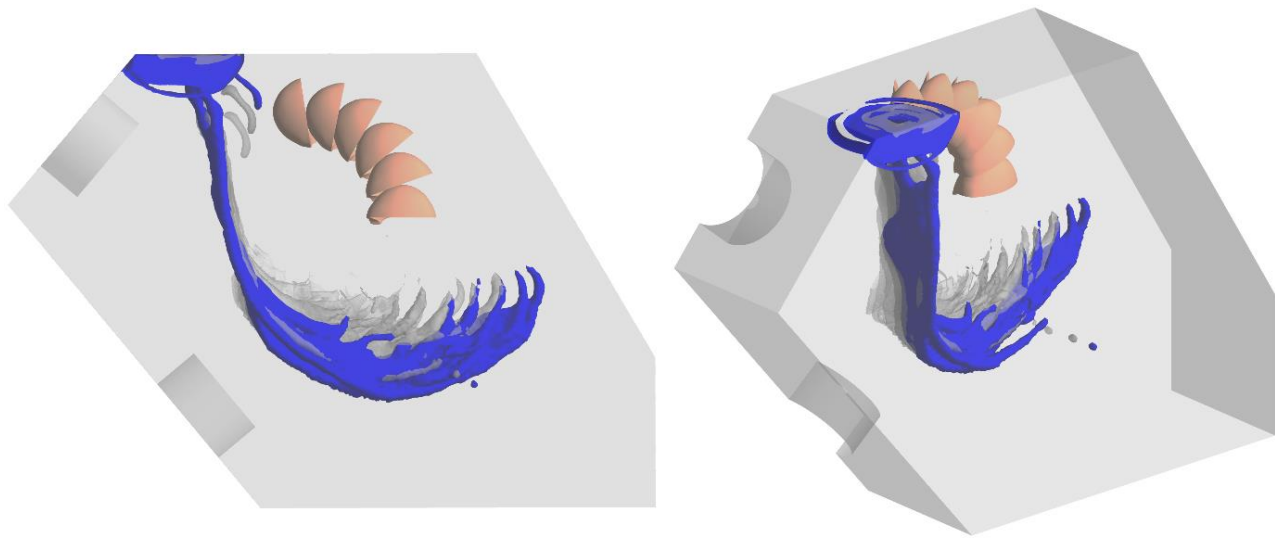


Fig. 4-9 Upper jet: casing flow at 280° rotation

It can be observed that by 280° (Fig. 4-9) rotation there is small portion of water, which has started to collect in the front top left corner of the casing; however, the majority of water has not yet made impact with the front face of the casing.

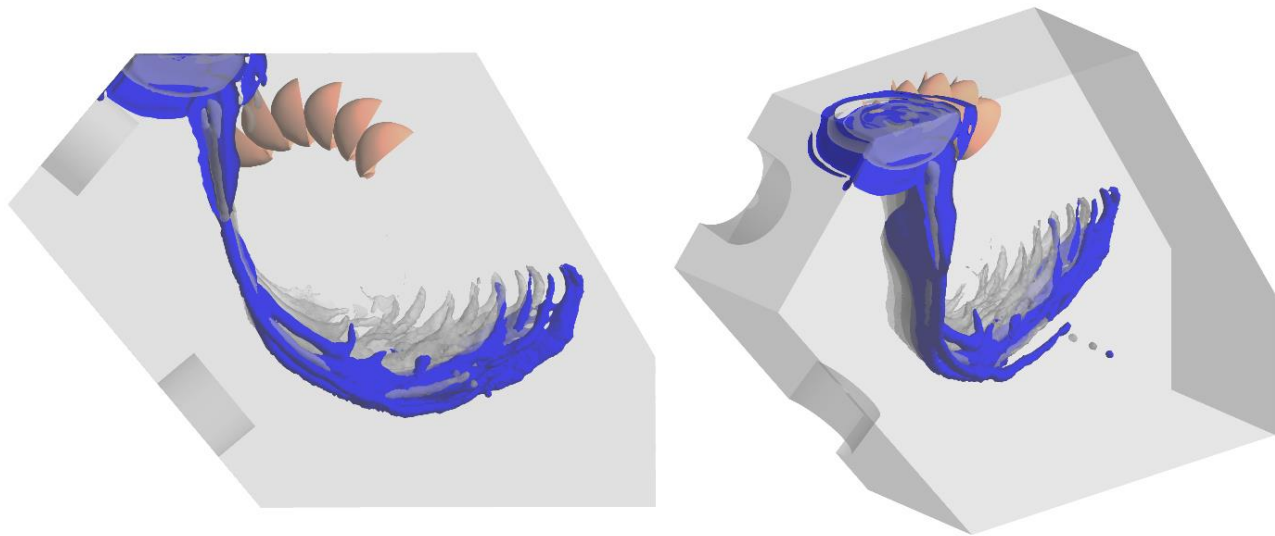


Fig. 4-10 Upper jet: casing flow at 320° rotation

By 320° (Fig. 4-10), the vertical water sheet has reached the front face of the casing wall and due to high inertial energy will tend to be guided by the casing walls rather than generating significant splashing. This is shown more clearly by observing how the water spreads along the wall surface as depicted in Fig. 4-12, which plots successive contours of water volume fraction for various rotated angles.

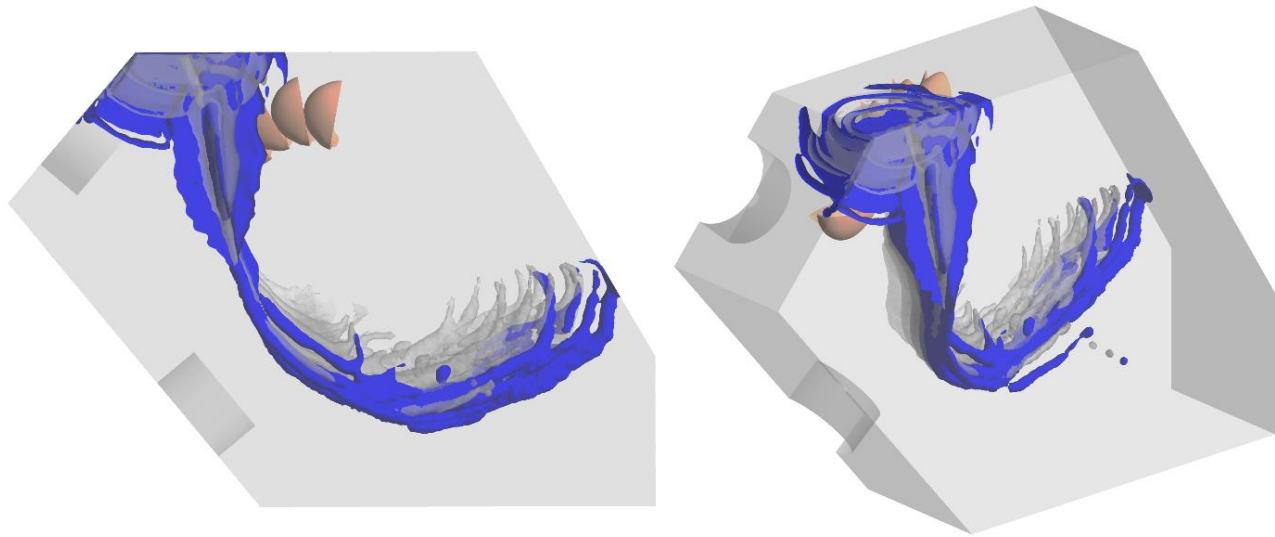
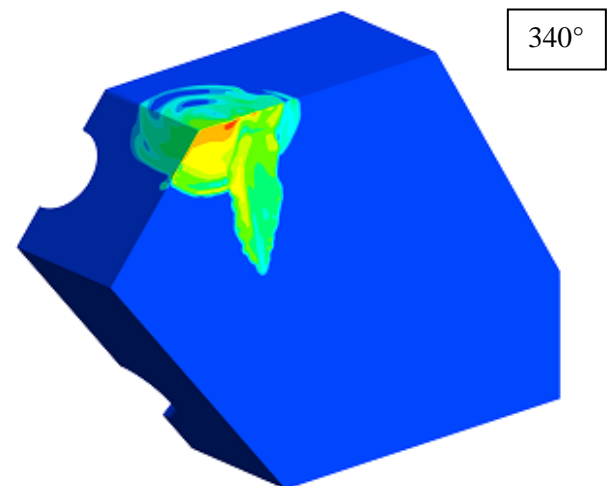
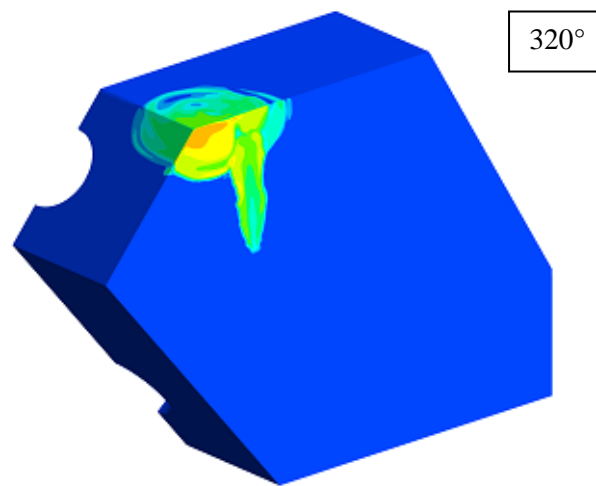
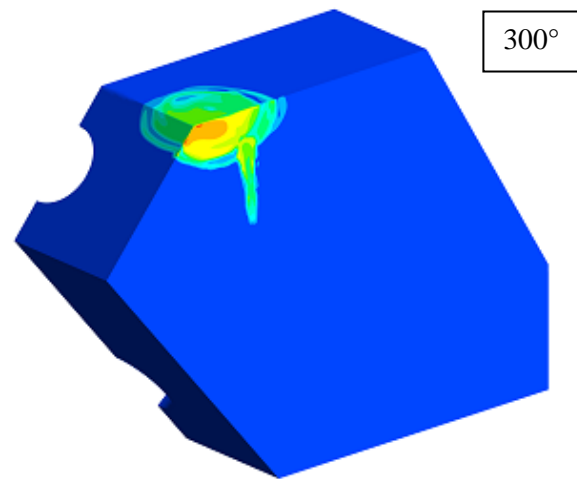
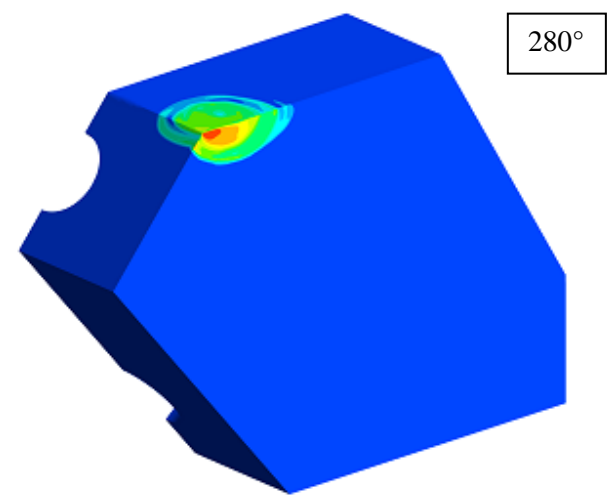
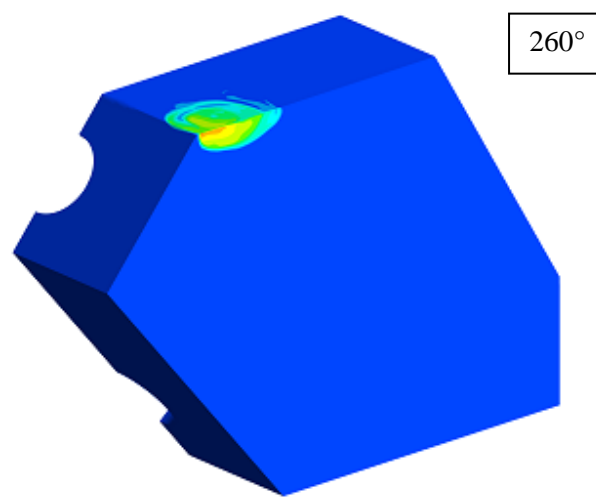
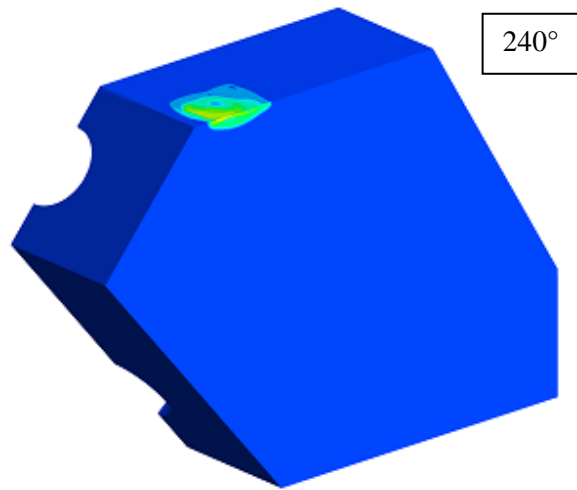


Fig. 4-11 Upper jet: casing flow at 360° rotation

By 360° (Fig. 4-11), the water, which leaves the bucket in the last part of the cycle close to the cut-out, has reached the right hand wall of the casing. In reality as shown in Fig. 3-40. This is in fact a very fine mist, which is made up of small droplets that are ejected from the bucket due to the centrifugal force.



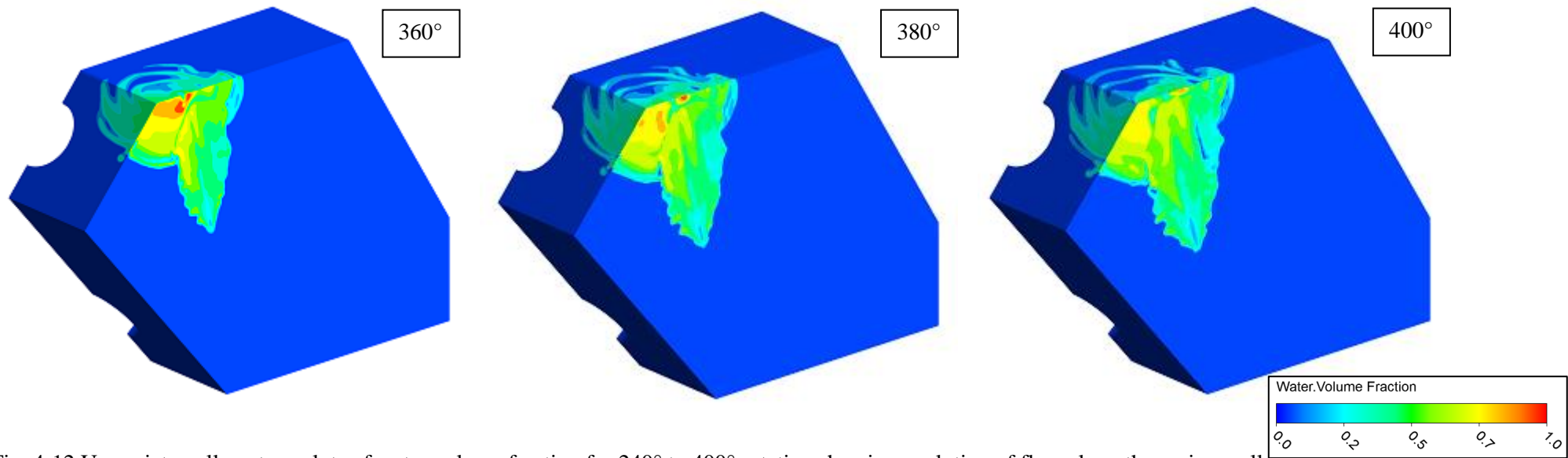


Fig. 4-12 Upper jet: wall contour plots of water volume fraction for 240° to 400° rotation showing evolution of flow along the casing walls

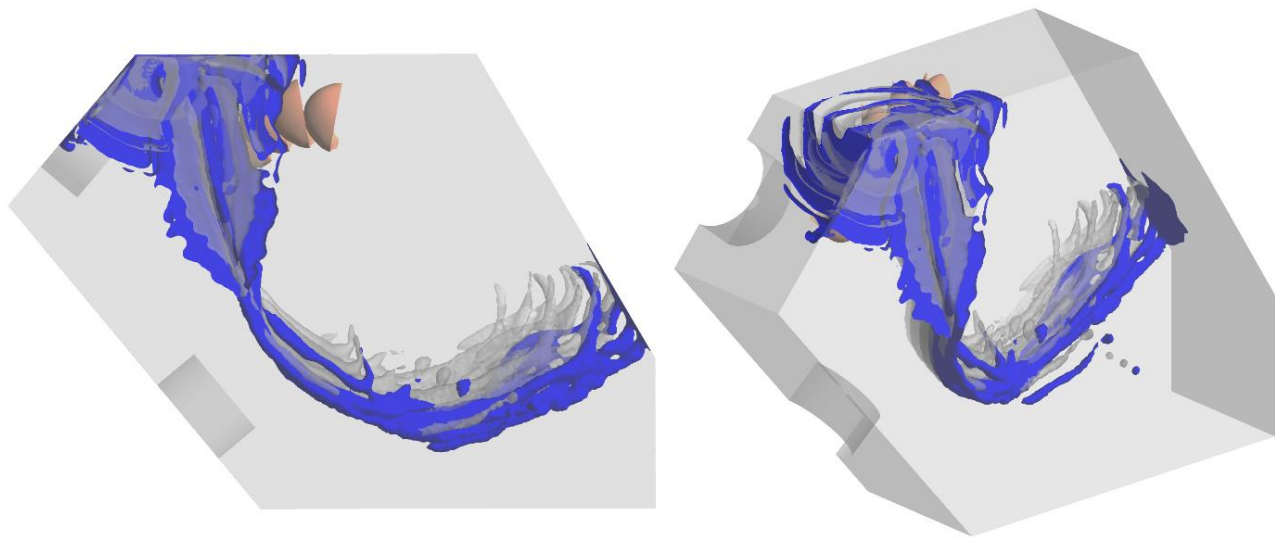


Fig. 4-13 Upper jet: casing flow at 400° rotation

By 400° (Fig. 4-13), a significant amount of water is collecting in the front top left hand corner of the casing. Some of this water is spreading along the roof and sidewalls of the casing and ‘fingers’ start appearing, which show the interaction of the water sheets from the individual buckets in the simulation sequence.

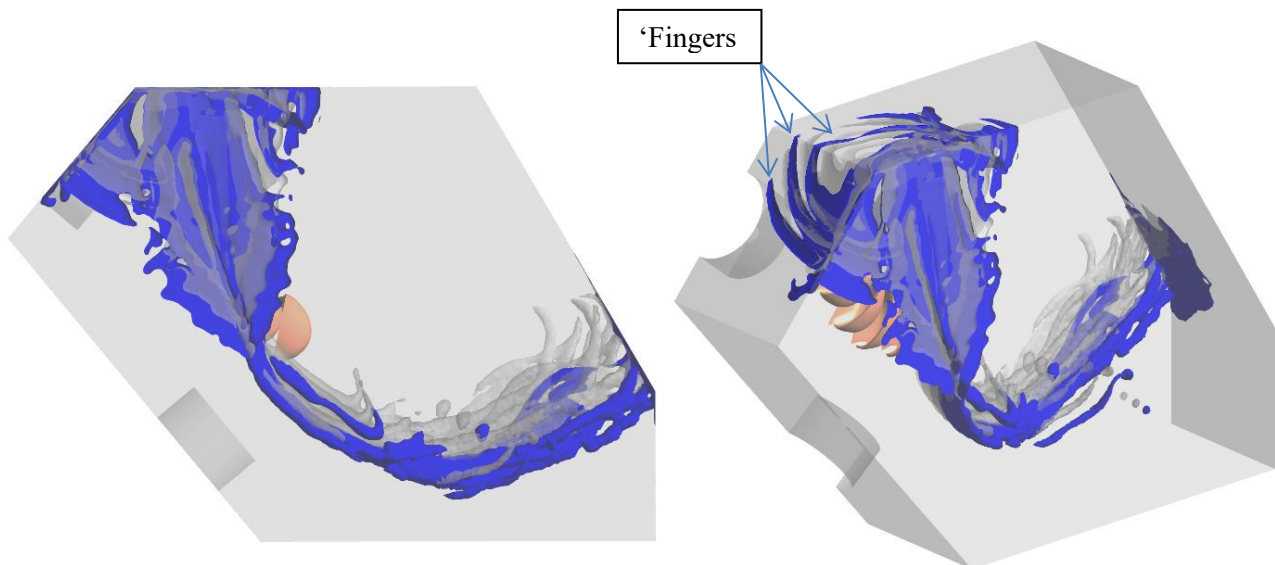


Fig. 4-14 Upper jet: casing flow at 440° rotation

By approximately 440° (Fig. 4-14) rotation the water has dissipated much of its kinetic energy, hence the slow movement from thereafter. What is also evident, is that the water collecting in the top left hand corner of the casing is interacting with the nozzles.

Since also that the volume fraction plots smear out the water in comparison to the video footage an attempt has been made to freeze the flow, Fig. 4-15 shows the vectors indicating both the

velocity magnitude and direction of the flow for the snapshot at 440° rotation. The size of the vector arrows indicates the absolute magnitude of velocity (the velocity has been limited to 8 m/s, to indicate more clearly the differences in the area closer to the nozzles, however the velocity of the water closer to the right hand side of the casing is higher).

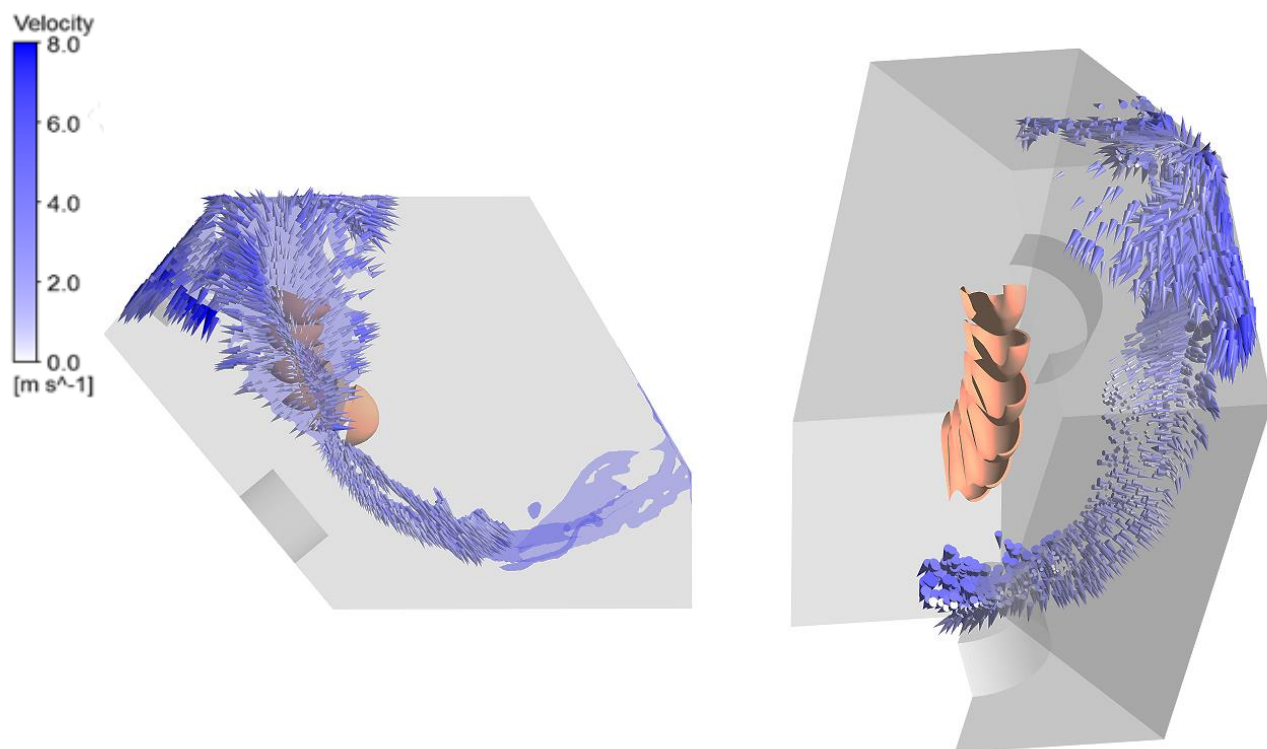


Fig. 4-15 Velocity vectors showing casing flow at 440° rotation

These plots indicate the necessary role of the jet shroud to deflect the droplets and protect the quality of the jet.

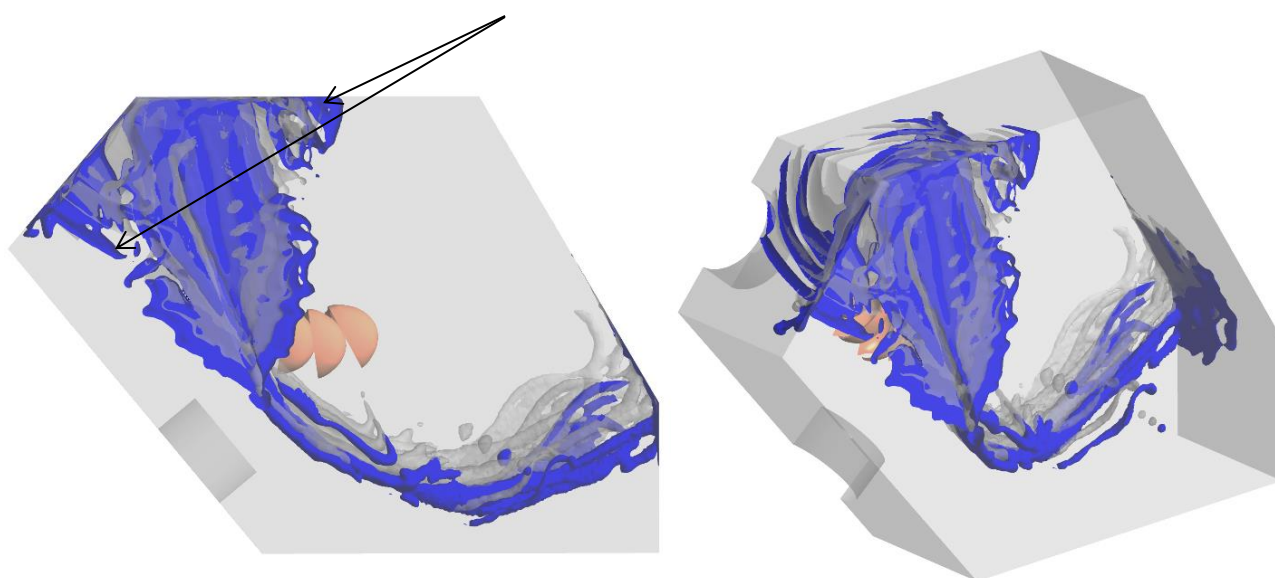


Fig. 4-16 Upper jet: casing flow at 480° rotation

By 480°, shown in Fig. 4-16 much of the flow is now largely gravity dominant, since as soon as there is an impact of the water sheets on a solid obstacle or when there is an intersection of one water sheet with another one, kinetic energy is dissipated and after some time gravity will drive the flow. This is now evident by the water ligaments, which have broken away from the main portion of the flow, indicated by the arrows.

Though the volume fraction plots have been highlighted from 200° – 480° degrees, it is expected that the plots after some time post the splash water interaction with the casing walls will not be entirely realistic. This is due to the fact that the water from the subsequent buckets (i.e. the final 12 buckets) in addition to the continuous nature of the water supply will interact with the existing flow in the casing.

4.1.1.2 Further Analysis of the Flow Sequence within the Casing – Lower Jet

In the case of lower injector operation only, the flow after interacting with the rotor is deflected in an area around an almost horizontal line which is just below the axis of the runner, as shown for the snapshot taken at 100° rotation in Fig. 4-17 (the red arrow indicates location and direction of water jet). However, unlike the case of the upper injector, the water direction has a small downward angle, and as a result, the flow tends to be directed towards the tailrace. Furthermore, the flow leaving the cut out region towards the end of the bucket cycle as seen towards the right has mainly vertical velocity components and most of the flow subsequently will be driven onto the runner by the interaction with the top right hand corner of the casing.

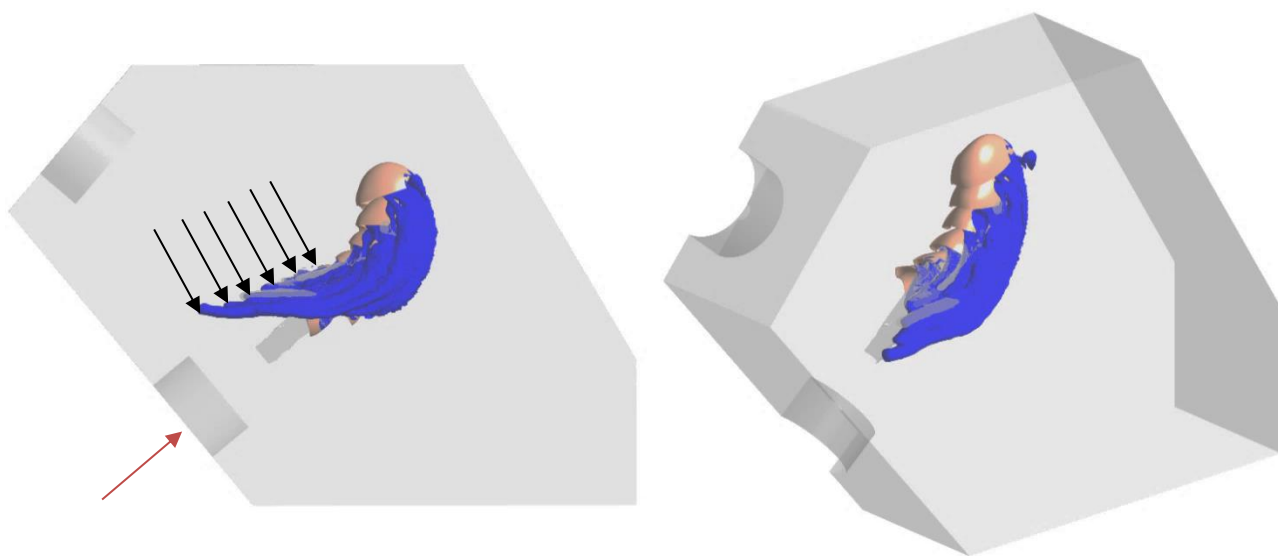


Fig. 4-17 Lower jet: casing flow for 100° rotation

By 100°, the water sheets that leave close to the root of the buckets (as described in Fig. 3-39 α) are clearly visible, as highlighted by the six black arrows in Fig. 4-17, these water sheets have velocity components in both the direction of the shaft and opposite to the jet.

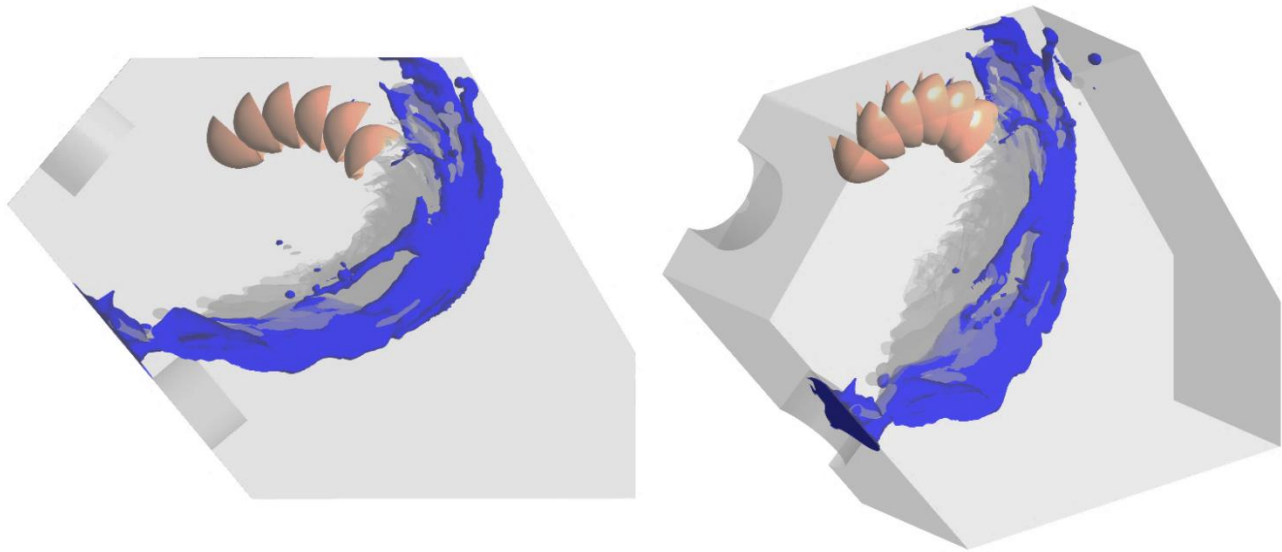


Fig. 4-18 Lower jet: casing flow at 240° rotation

By 240° (Fig. 4-18) rotation the water has made impact with the side wall in the region of the lower nozzle and has started to spread around the front face and the side wall. Furthermore, a large amount of water is starting to recirculate around the roof of the casing above the runner.

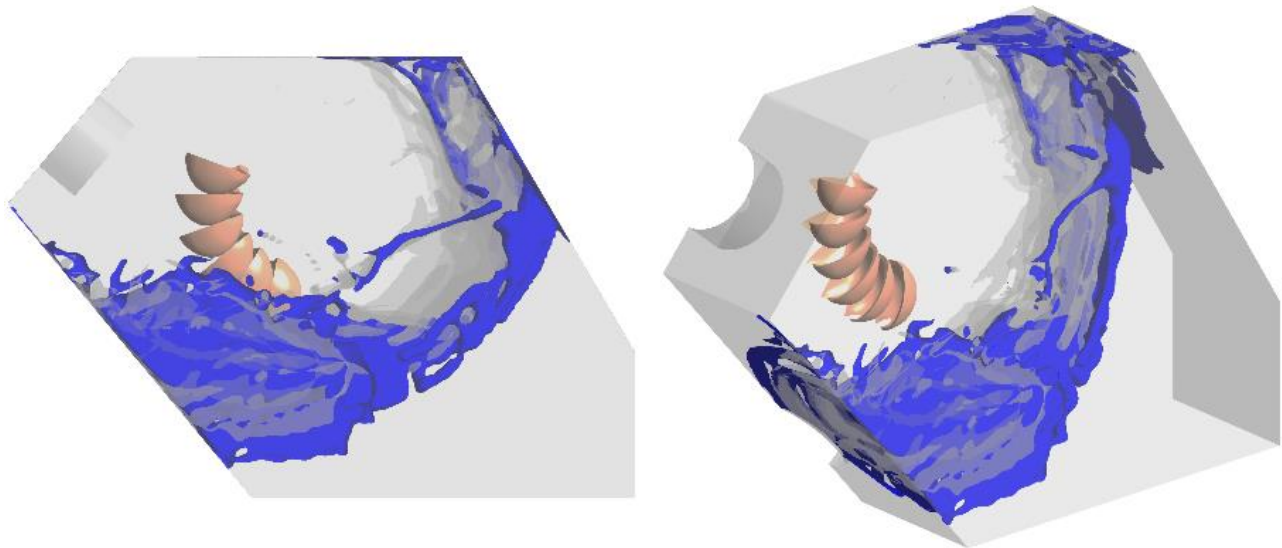
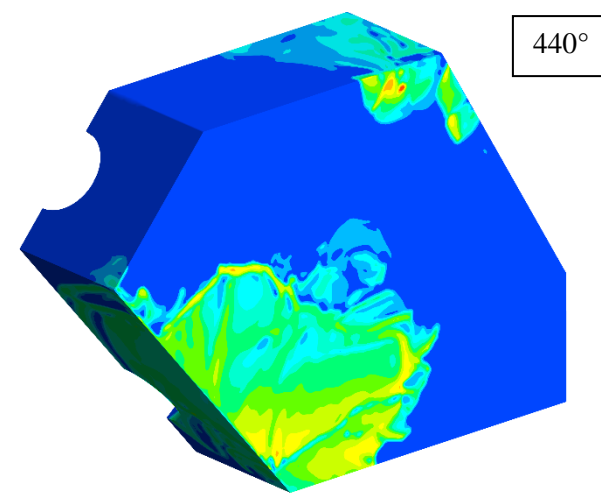
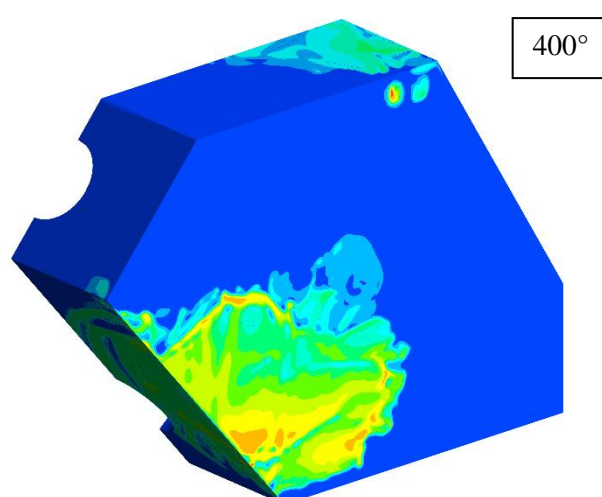
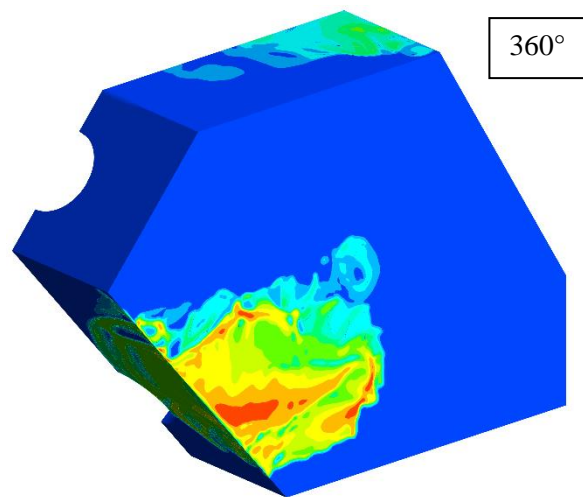
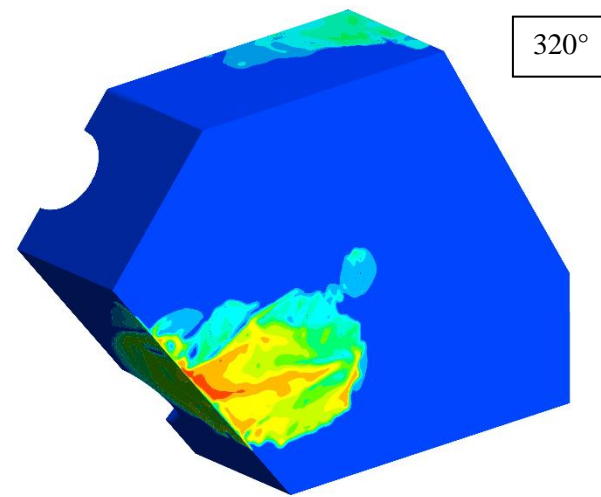
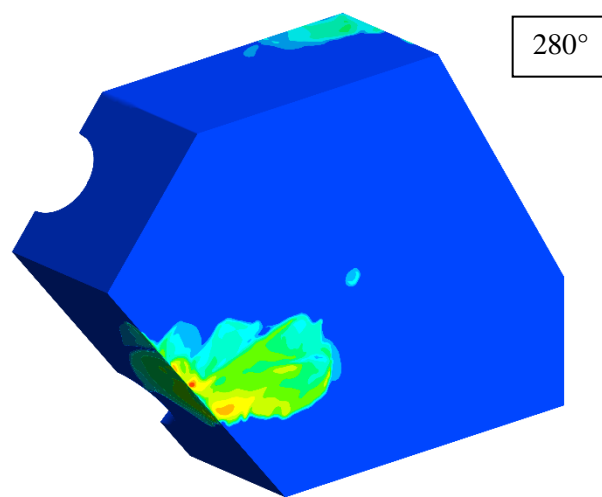
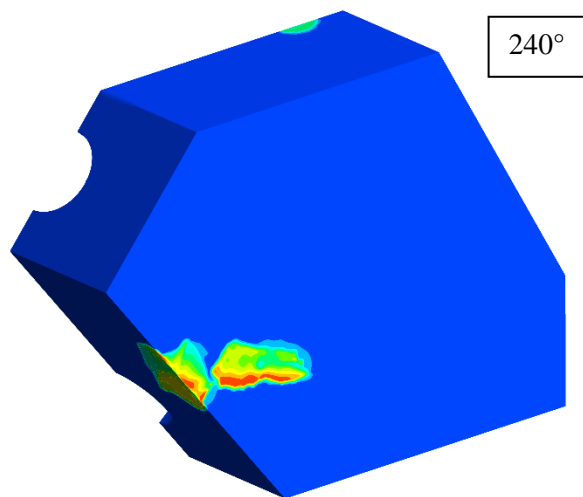


Fig. 4-19 Lower jet: casing flow at 360° rotation

By 360° (Fig. 4-19) rotation a large portion of the water in the top right hand side of the casing has started to make its way towards the front face, likewise the water has significantly spread

across the front face of the casing and it is anticipated that there will be interference with the lower jet by this point. The spreading is shown more clearly by observing how the water spreads along the wall surface as depicted in Fig. 4-20, which plots successive contours of water volume fraction for various rotated angles.



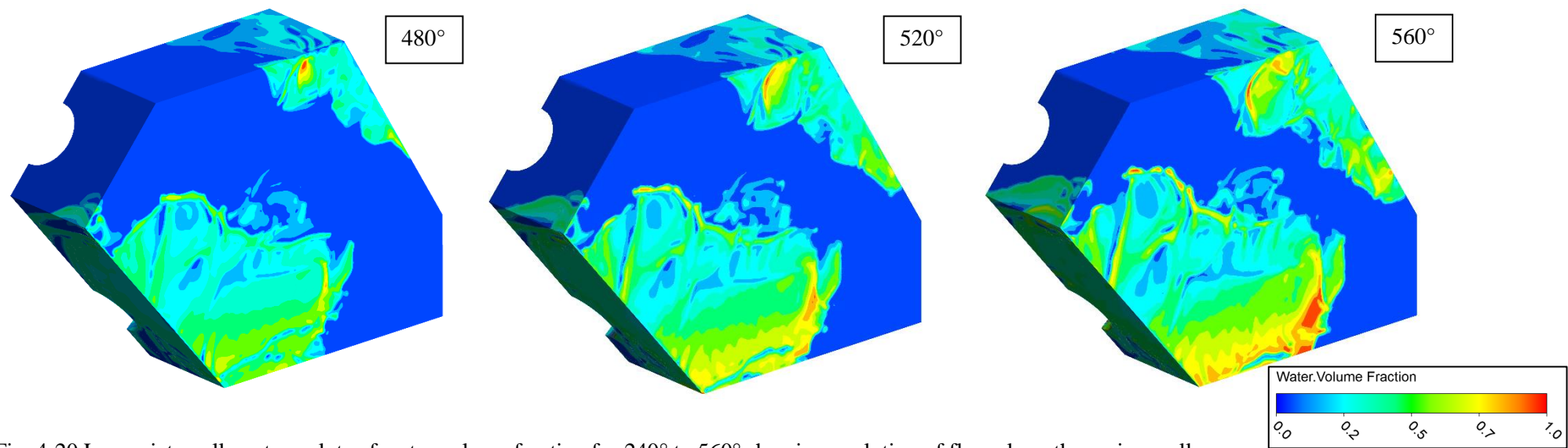


Fig. 4-20 Lower jet: wall contour plots of water volume fraction for 240° to 560° showing evolution of flow along the casing walls

4.1.2 The Role of the Bolt on Baffle

From observations of the lower jet in the absence of shrouds and baffles the water is allowed to circulate around the casing and it can be noted from the velocity vectors that this collects in the top left hand corner before falling onto the runner, as highlighted in the previous section. In order to combat this problem and remove the water from the roof of the casing a curved baffle (BAF) that sits around the runner was added to the naked case, this is shown in Fig. 4-21. Indeed, Nechleba [5] noted that the inclusion of a ‘scraper’ ensures a reduction in the ventilation losses, however it also serves the purpose of preventing the formation of backwater in the roof of the casing.

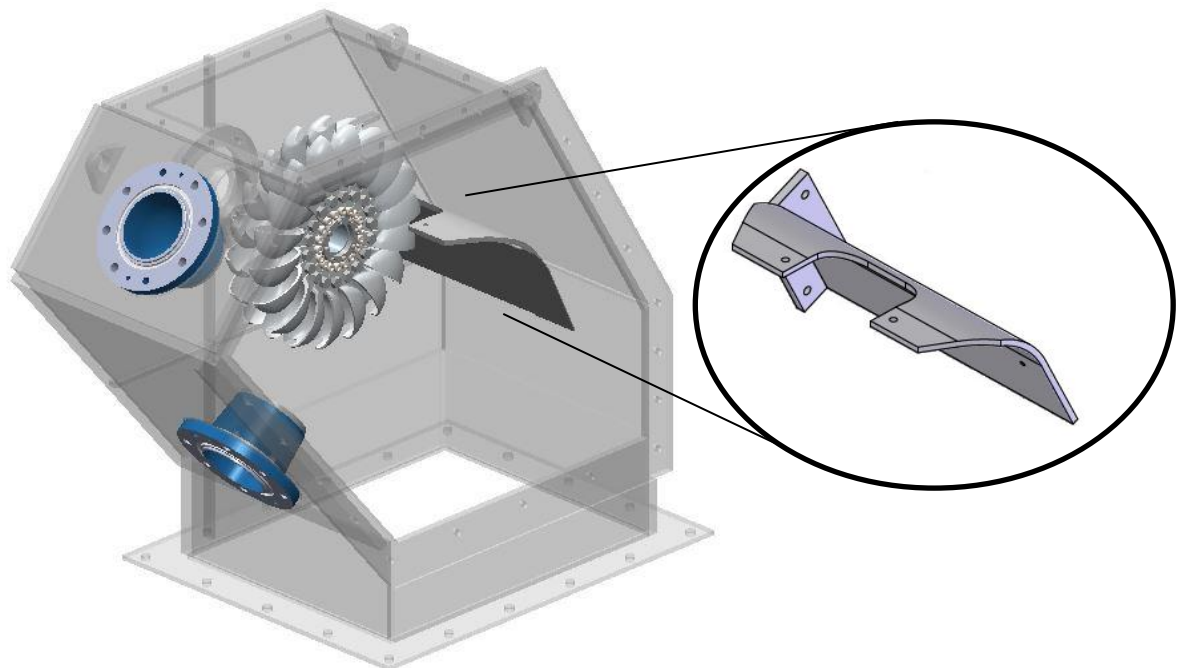


Fig. 4-21 The Bolt on Baffle in-situ within the casing

Further analysis shows that the clearance between the runner and the BAF is very important and consequently a closing plate was secured to the BAF, reducing the gap to a maximum distance of 2 mm. The specific role of the closing plate is demonstrated in the following Fig., comparing to the case with just the BAF installed it is demonstrated that the closing plate is responsible for the reduction in the leakage through the clearance, which is created by reduced suction in the narrow gap.

The position of the lower jet will always be an issue for horizontal axis machines since it is obvious that water flowing out of the bucket throughout the entire cycle tends to create a continual flow in the direction of turbine rotation which severely impacts on the right hand side of the casing. For this reason, the lower jet is more subject to efficiency differences as a direct

result of the splash water interference with the casing. The water flowing up the side wall is reflected at the nozzle-side end wall and falls back into the runner in a narrowly defined area. Contrastingly, the upper jet benefits from its relative position, ensuring that the water leaving the runner has far more space to move around before interacting with the casing and as a result the effect will be reduced due to the increased dissipation of kinetic energy prior to impact. Therefore, the CFD results documented below will focus on the lower jet only.

The BAF and closing plate ensure that the water from the lower jet on the right of the shaft is deflected by the curved shape downwards and into the tailrace with minimal further interference. However, a small portion of the flow passes between the BAF and the runner, and after impacting the BAF wall as shown in Fig. 4-25, it is deflected toward the injector side and returns to the region of the runner. Similarly, the section on the left of the runner is deflected to the left toward the injector area, resulting in a significant amount of water affecting the jet. It is noted that, as shown by the comparison of Fig. 4-25 and Fig. 4-19 in the case of the lower injector, the amount of flow remaining in the casing is smaller as a result of the BAF and the geometric position as the localised water is closer to the tail race.

As it transpires, the BAF diverts much of the flow to the tailrace in the case of lower injector operation. But in the case of the upper injector they have a negligible role as the flow is generally moved into the casing resulting in a small portion of the flow deflected to the right and above the runner impinging on the top of the fins and directing to the rotor space at the opposite speed of the rotation of the runner. This phenomenon is also noticeably weaker in the case of lower injector operation for large flow rates. It is also noted that a significant disadvantage is that the BAF does not interact at all with the flow which, after impacting the side walls of the shell, is driven upward and impinges on the roof and causes considerable losses.

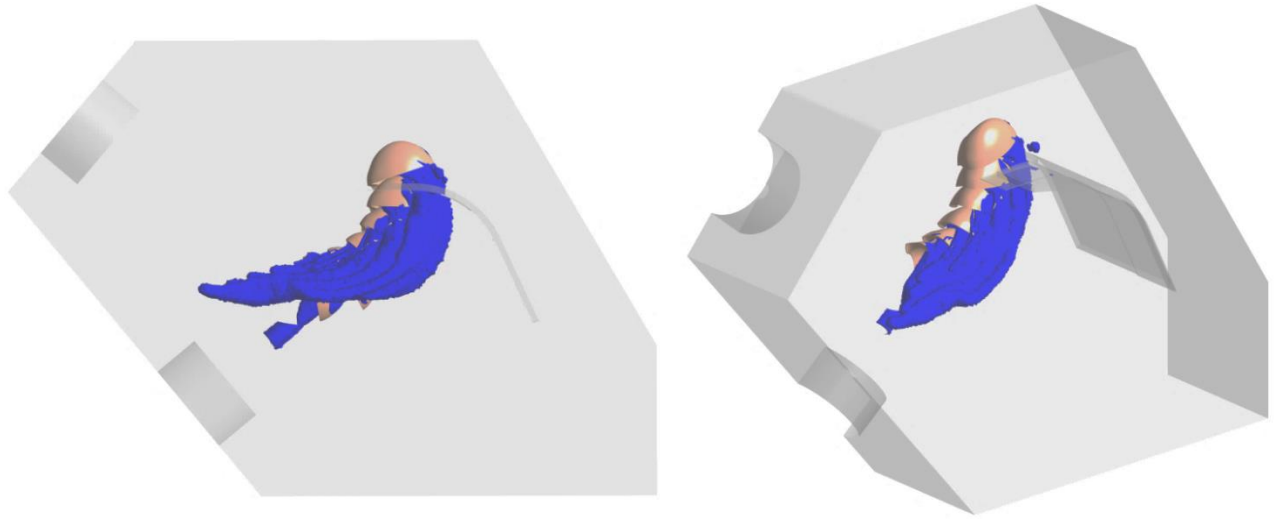


Fig. 4-22 Lower jet with the BAF and SP: casing flow at 100° rotation

From Fig. 4-22 it can be observed that there is a similar pattern compared to the naked case lower jet operation as shown in Fig. 4-17 of the six water sheets leaving close to the root of the buckets. Moreover, the water that leaves close to the cut-out (as described in Fig. 3-39 γ) has started to appear in the roof of the casing above the BAF plate.

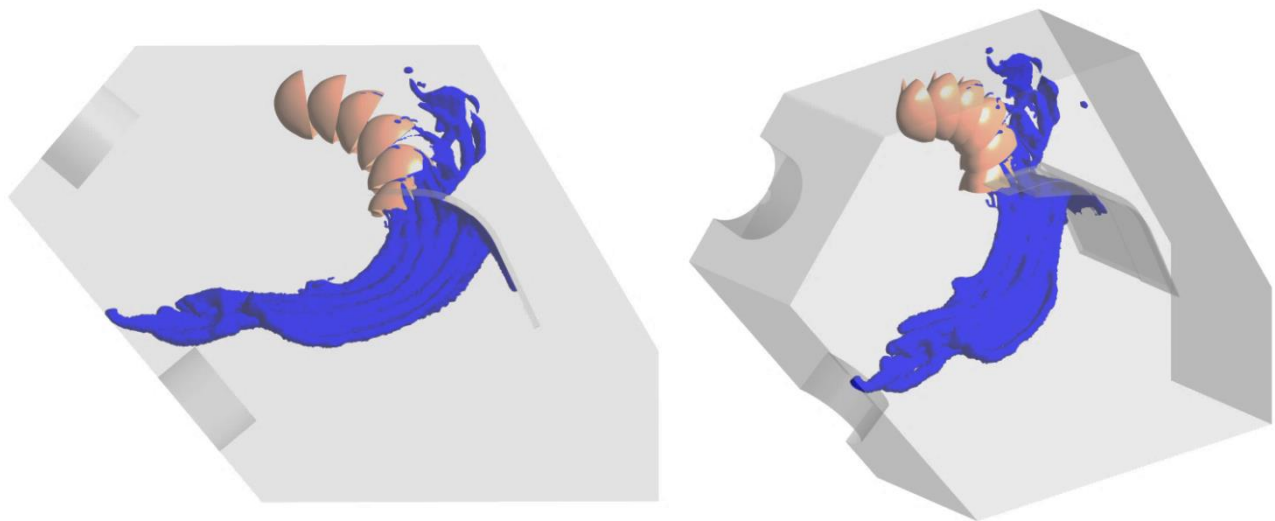


Fig. 4-23 Lower jet with the BAF and SP: casing flow at 200° rotation

By 200° (Fig. 4-23) rotation almost all six of the buckets have now passed the BAF plate, the water which leaves along the lip of the bucket (as described in Fig. 3-39 β), which would in the naked case leave the bucket in an anticlockwise rotation before impacting the top right hand side of the casing is now being diverted downwards towards the tailrace by the curvature of the BAF plate. The small portion of water that remains in the bucket beyond the BAF plate (also shown in Fig. 4-22) can be seen to enter the roof of the casing in as distinct sheets of water.

This flow will in reality most likely be fine mist and droplets as the small clearance between the BAF and the buckets will cause atomisation of any bulk flow that may be in this region.

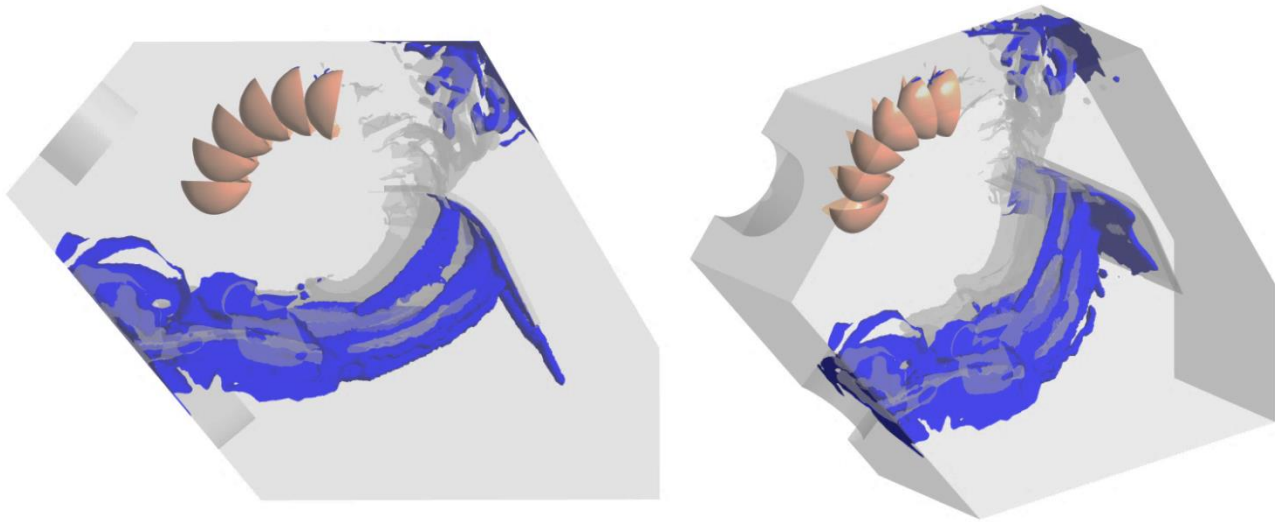


Fig. 4-24 Lower jet with the BAF and SP: casing flow at 280° rotation

By 280° (Fig. 4-24) the water that has impacted the BAF is already experiencing a considerable deflection towards the tailrace. In addition the water that has managed to pass beyond the BAF has now accumulated in the top right hand corner of the casing and is being directed towards the front face of the casing.

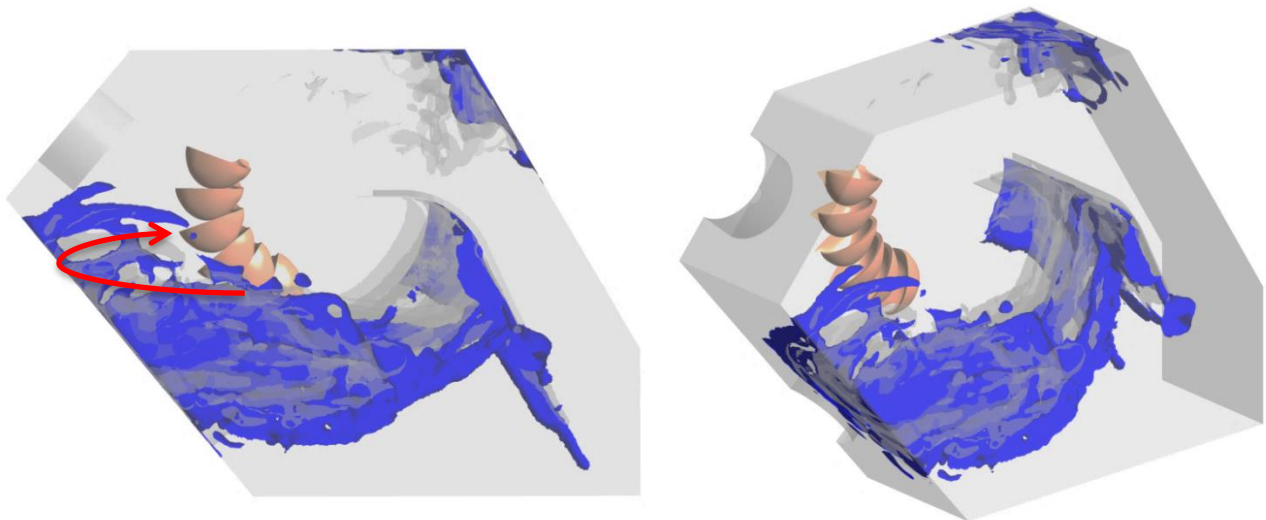


Fig. 4-25 Lower jet with the BAF and SP: casing flow at 360° rotation

The water that has travelled towards the left hand side wall of the casing is now being reflected back towards the runner and along the front face of the casing, as shown by the arrows in Fig.

4-25. This is more pronounced in the case with BAF as opposed to the naked case, shown in Fig. 4-19.

The snapshots shown in Fig. 4-22 to Fig. 4-25 indicate the positive role of the BAF and SP for lower jet operation in ensuring that splash water interaction with the runner is minimised as much as possible by ensuring that the water path into the roof of the casing is restricted. The curved shape of the BAF means that water is collected and directed towards the tailrace with little to no splashback.

4.1.3 The Role of the Side Shroud

The most interesting feature of the Gilkes Pelton design is the addition of Side Shrouds (SS) on the side walls of the casing. The shrouds are truncated cones, with the smaller radius being the same as the inner radius of the buckets, shown in Fig. 4-26. It was not known from the outset of the project where the design of the SS originated or its role in directing the spray water away from the critical components. It is possible that the design evolved from more traditional casing arrangements, where there is a split above the axis of the runner, with a very small (several mm) clearance between the side and outer radius of the buckets and a large domed shape casing below the axis of the runner, as shown in Fig. 4-27.

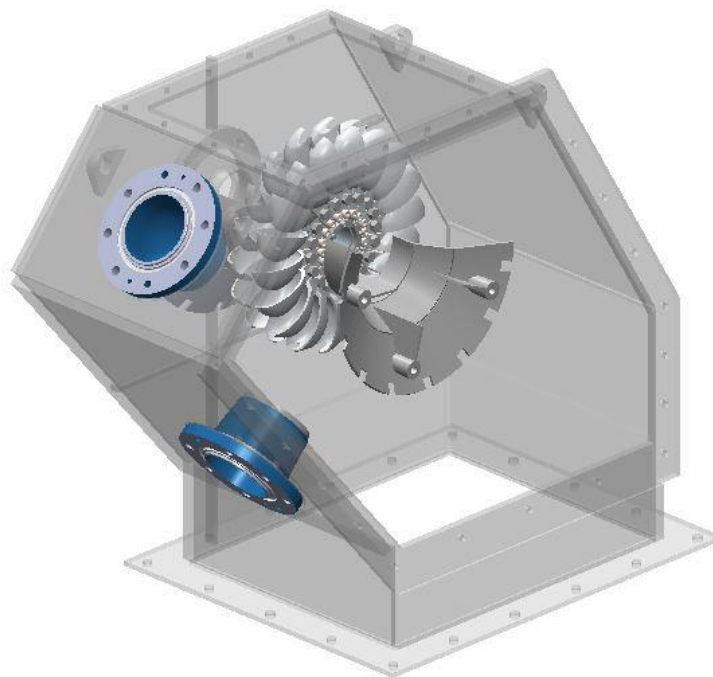


Fig. 4-26 The Side Shroud in-situ within the casing

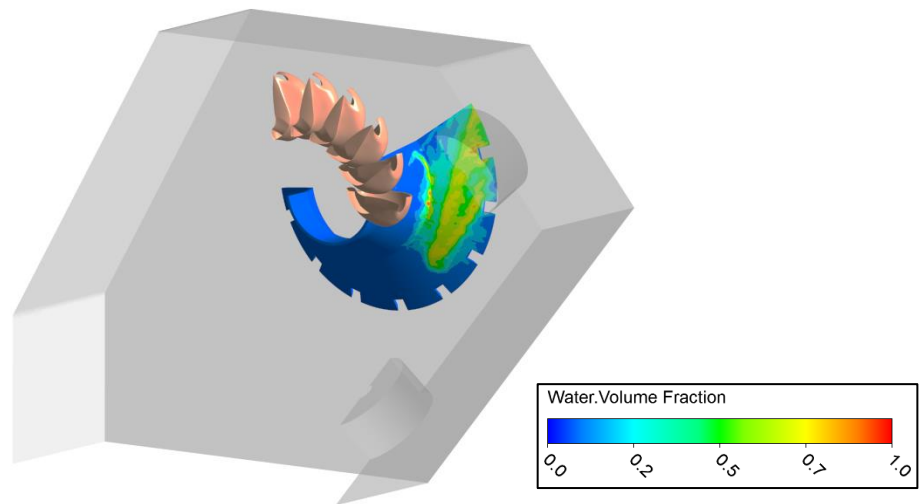


Fig. 4-29 Upper jet with the SS: volume fraction contour plot at 360° rotation

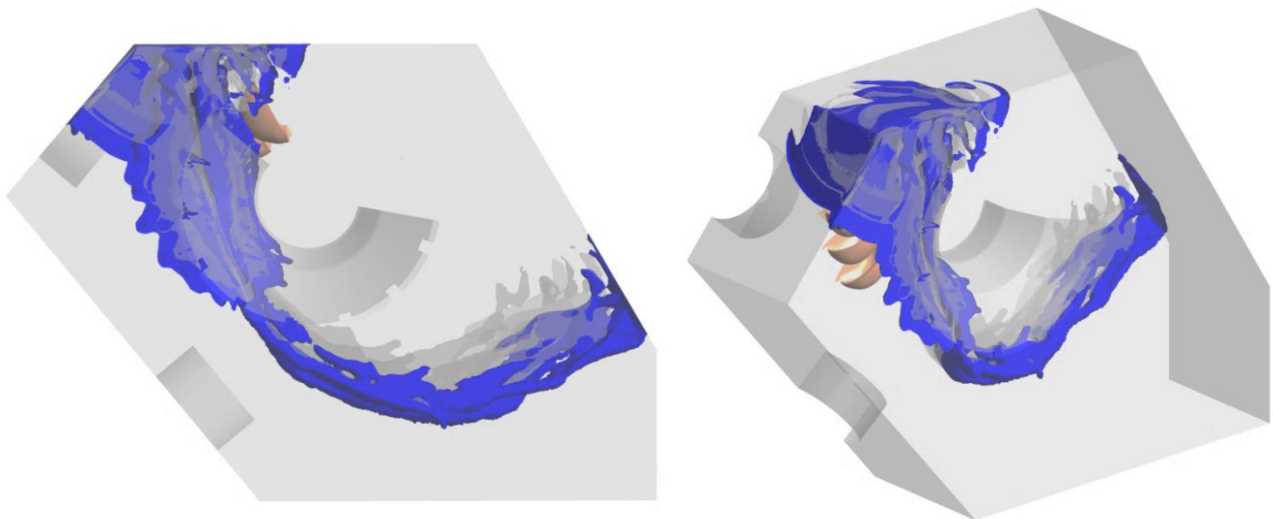


Fig. 4-30 Upper jet with the SS: casing flow at 400° rotation

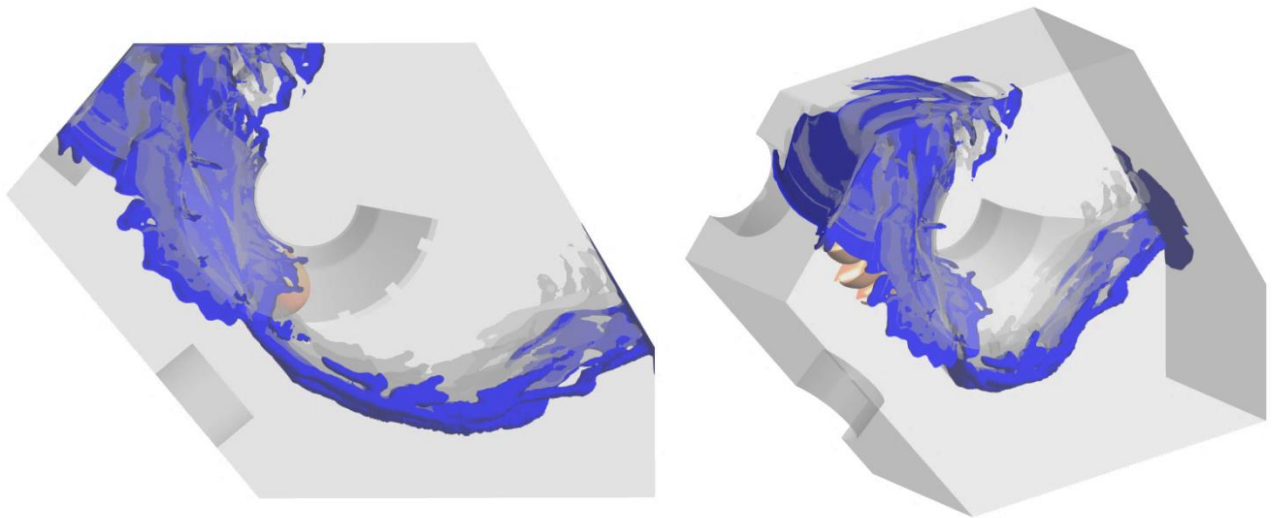


Fig. 4-31 Upper jet with the SS: casing flow at 440° rotation

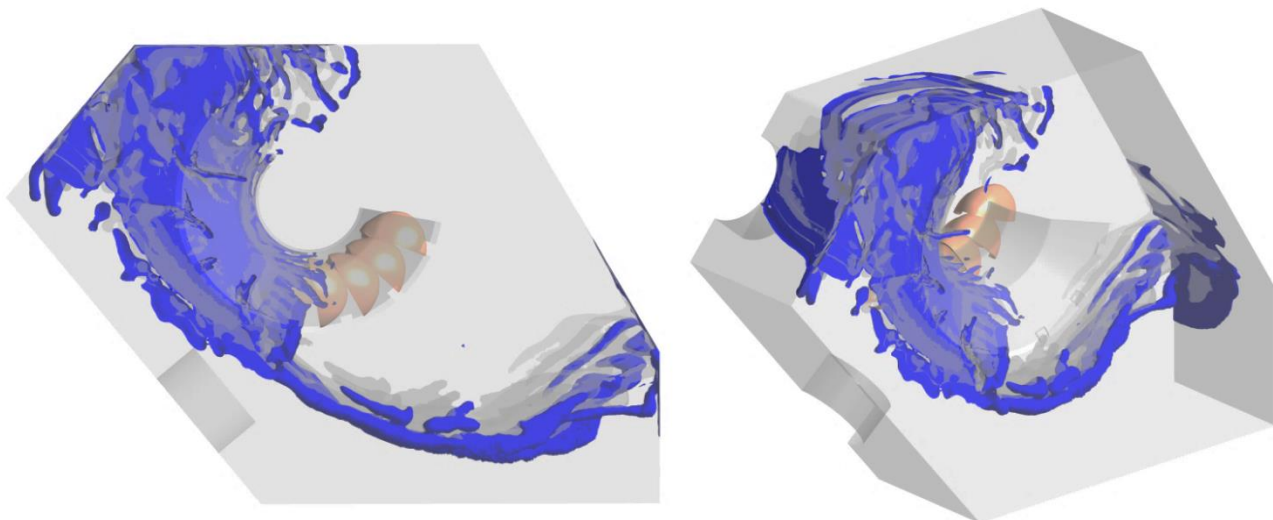


Fig. 4-32 Upper jet with the SS: casing flow at 480° rotation

Very little can be said about the role of the SS by simply observing how the flow develops from the snapshots shown in Fig. 4-28 to Fig. 4-32. As the contour plot in Fig. 4-29 indicates, the vertical water sheet makes contact with the SS, however since the SS has a curved shape this inherently imparts a rotational velocity component, which can be observed in the slight change of the velocity vectors, shown in Fig. 4-33 highlighted in the red circle. This additional velocity component will impart to the water

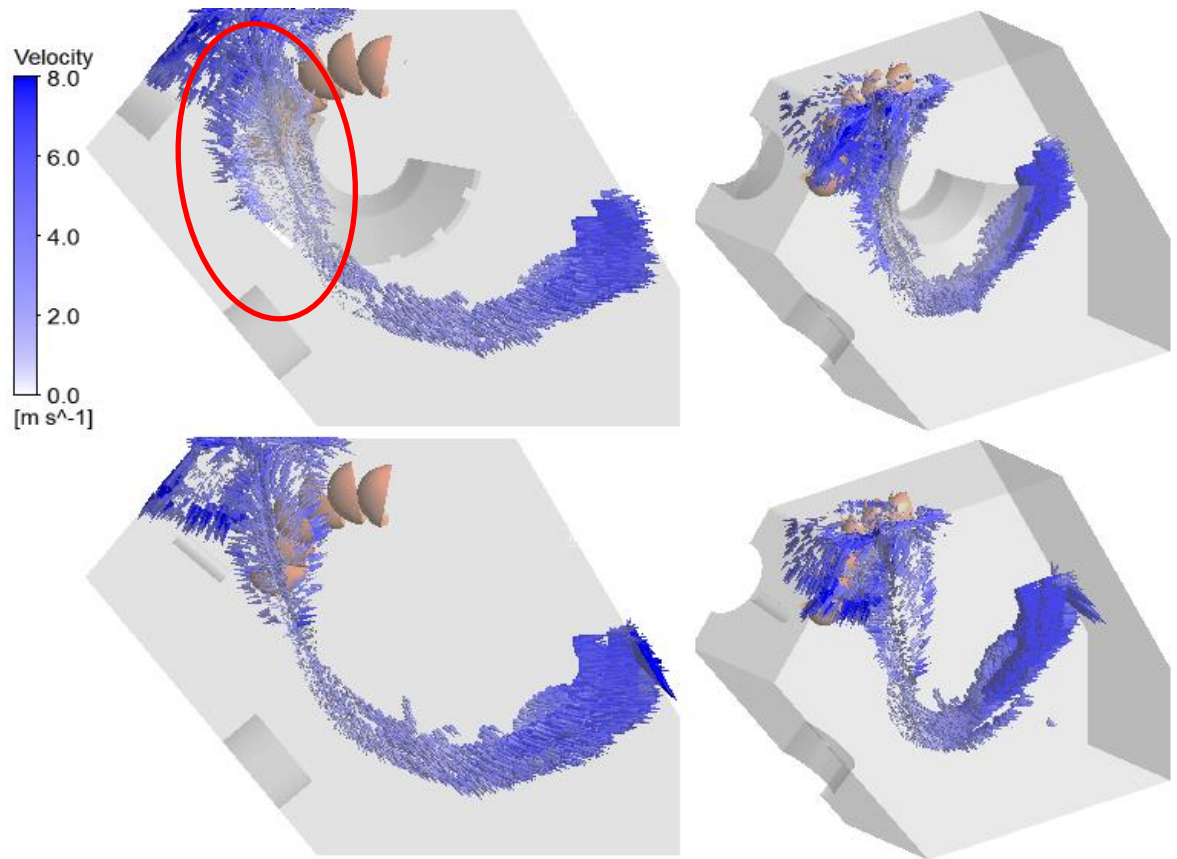


Fig. 4-33 Velocity vector comparison between SS and naked case at 360° rotation

It is interesting that the SS have been retained in the casing as the simulations have shown that they could potentially contribute to increasing the splash water interaction with the injectors and runner, since the curved shape particularly on the nozzle side means that the water has a larger velocity component in the axial direction.

4.2 Phase 2 – Analysis of Pelton Casing Width

In this section, the CFD model will be used to visualise the flow conditions within a casing of significantly reduced width of 240 mm, which corresponds to twice the bucket width. As documented in the literature in section 2.6.3, there are some general rule of thumb suggestions that relate the size of the casing to bucket width or jet diameter, however these are guidelines and relate to casing designs, which look very different to the present Gilkes arrangement. The rationale for the width testing is therefore to offer some more practical relationships between width and efficiency and to as far as possible offer some cost savings by simplifying or reducing the standard casing size.

4.2.1 Further Analysis of the Flow Sequence within the Casing – Upper Jet

The following snapshots show the flow sequence of the water leaving the runner for upper jet operation for the 240 mm wide case at the BEP operation. The snapshots are shown from 240° to 480°, in Fig. 4-34 - representing a total simulation time of 0.083 s.

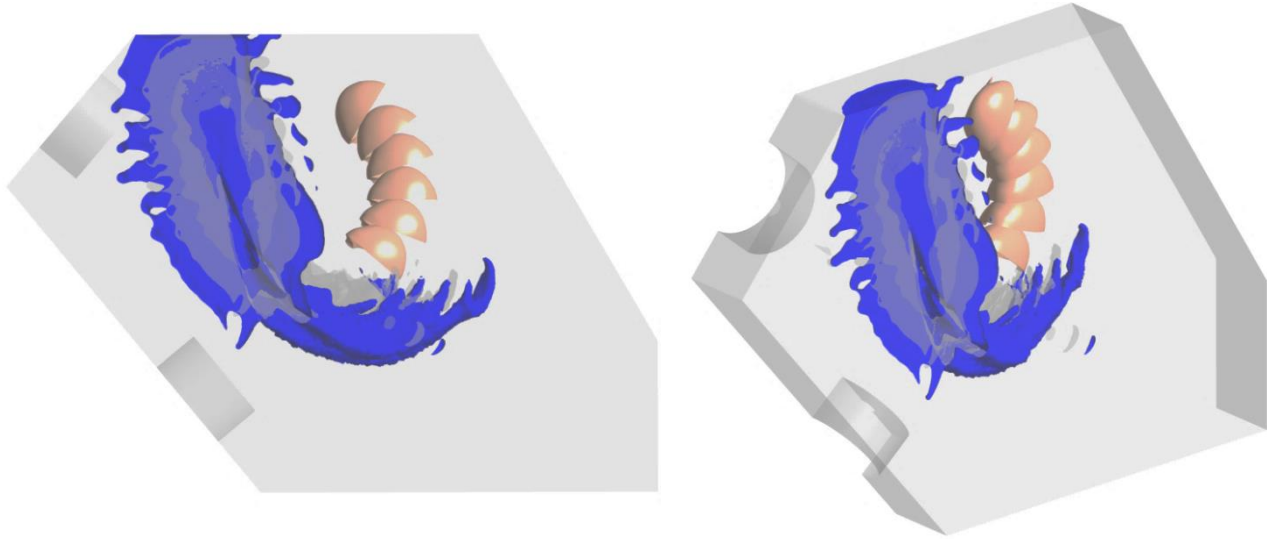


Fig. 4-34 Reduced width upper jet: casing flow at 240° rotation

What is apparent here is that by 240° rotation (Fig. 4-34), the main water sheet has already made impact with the front face of the casing and is beginning to spread along the roof and towards the upper injector. The water will have a higher kinetic energy, as indicated by the velocity vectors depicted in Fig. 4-35 with scale from 0 – 8 m/s, since there is less time for dissipation in the volume of the casing and for atomisation of the liquid sheets to take place.

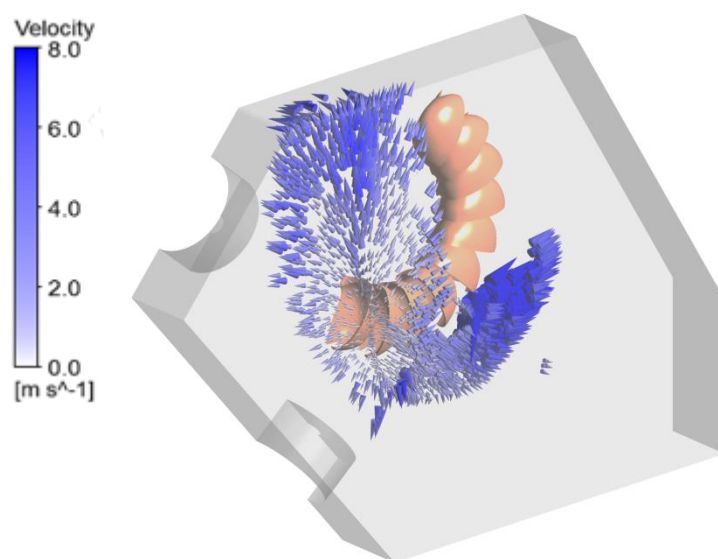


Fig. 4-35 Velocity vectors for 240 mm casing at 240° rotation

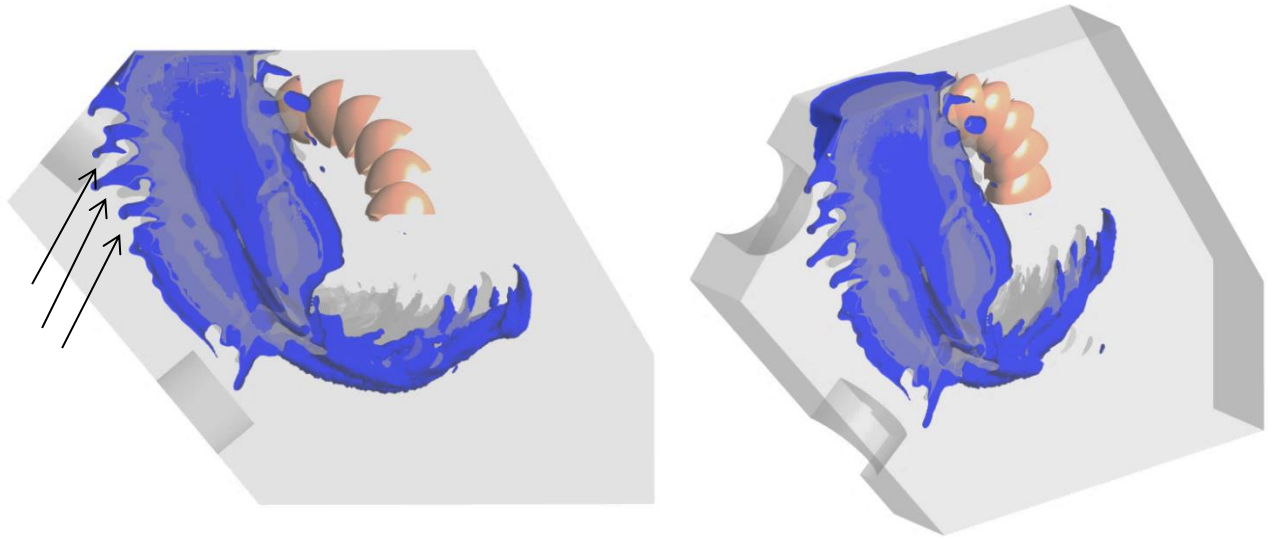


Fig. 4-36 Reduced width upper jet: casing flow at 280° rotation

By 280° (Fig. 4-36) rotation, large ligaments, indicated by the black arrows, are starting to appear separating from the main water sheet flow, highspeed photography of the experiments where the flow can be frozen in time show a similar pattern since this will be a result of the water leaving in discrete bundles from each successive bucket rather than a continuous water sheet as the isosurfaces imply. This will be more severe in the 240 mm case where the Weber number is slightly lower (since the characteristic length in this case is the width) contributing to larger droplet formation on impact with the casing walls.

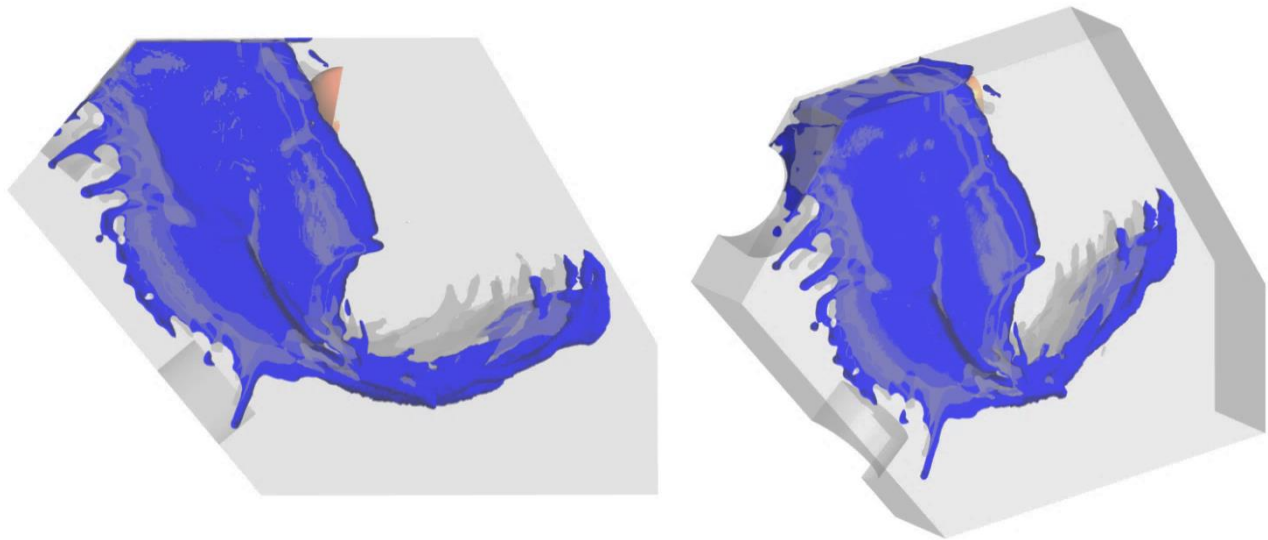


Fig. 4-37 Reduced width upper jet: casing flow at 360° rotation

By 360° (Fig. 4-37) rotation it can be observed that there is considerable spreading across the front face of the casing, furthermore there is significant accumulation of water in the roof of

the housing and some further interaction with the upper nozzle/injector. The velocity vector in Fig. 4-38 (ψ) shows how the water is forced along the roof of the casing in a direct line perpendicular to the plane of the runner and it anticipated that this will cause significant entrainment with the runner and subsequent degradation of performance.

Fig. 4-38 (σ) and Fig. 4-38 (ψ) compare the vector plots for the standard 520 mm casing width and 240 mm reduced casing width respectively for upper jet operation at the same timestep. What is apparent is that the water has considerably higher kinetic energy in the narrower casing at the point it makes contact with the wall and therefore shows noticeably more spreading across the surface. Furthermore, due to the reduced width the water experiences a choking effect when it impacts the top corner, leading to considerable interference and further entrainment with the runner, resulting in higher windage losses, highlighted by the red arrow.

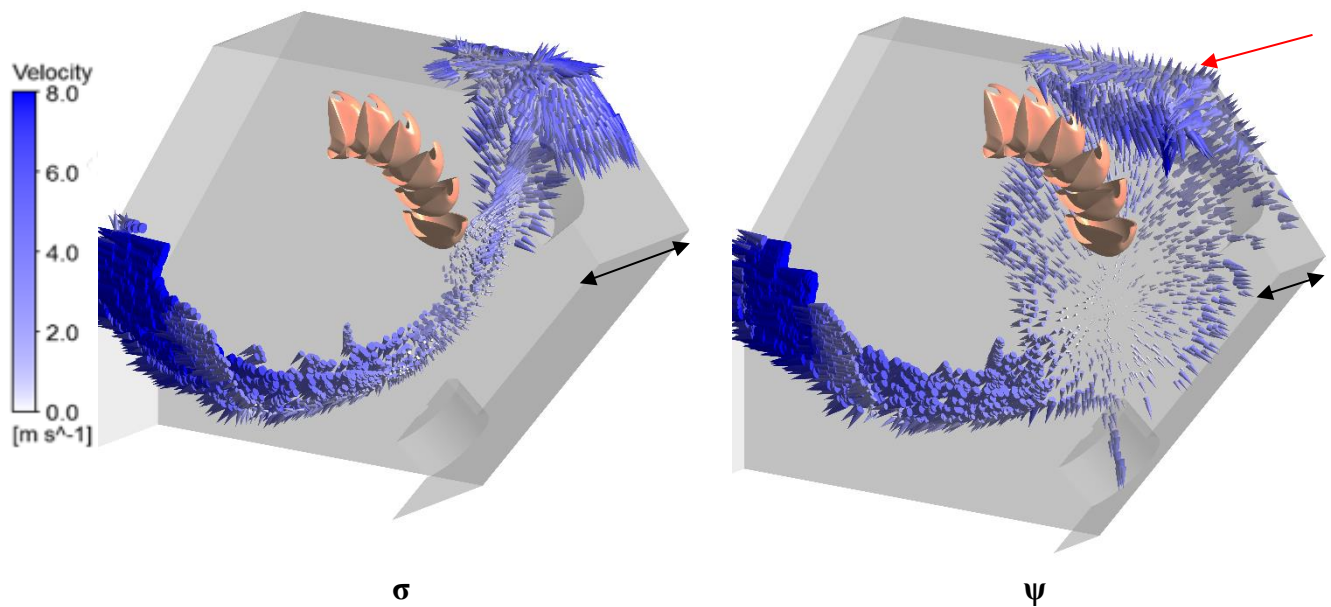


Fig. 4-38 Velocity vectors at 360° rotation comparing casing width (black arrows indicating relative width)

Similar to previous analysis of the naked case with width of 520 mm, described in section 4.1.1.1, the development of the flow in the casing can be observed by how the water spreads along the wall surface as depicted in Fig. 4-39, which plots successive contours of water volume fraction for various rotated angles.

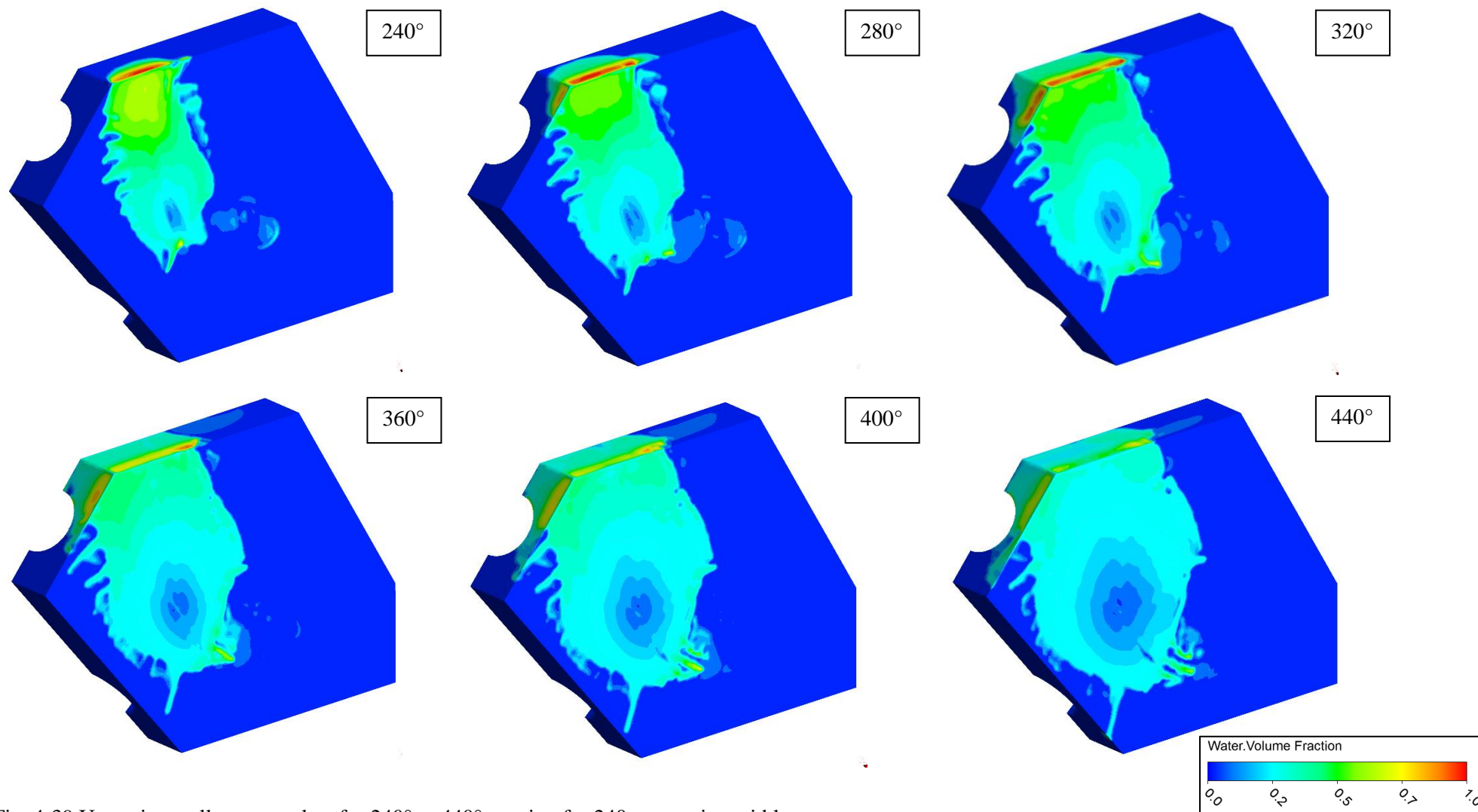


Fig. 4-39 Upper jet: wall contour plots for 240° to 440° rotation for 240 mm casing width

The CFD analysis of the 240 mm casing has shown that at these extreme cases the efficiency of the turbine is likely to be greatly affected by the splash water.

4.3 Summary of CFD analysis of Pelton Casing Design

The numerical analysis in this chapter represents the first time, to the authors knowledge, that a mesh-based Eulerian CFD solver has been used to visualise the flow within a Pelton turbine. The analysis has been split into two – phases, where the first investigated the addition of the Bolt on Baffle and Side Shroud and the second phase visualised the flow in a casing with severely restricted width, namely 240 mm.

The CFD models can be used as a visualisation tool to provide an indicative qualitative assessment of the likely impact different geometries will have on hydraulic performance by interpreting the flow patterns and the subsequent influence of the splash water on the injectors and runner. For this reason experimental testing to obtain measurable efficiency data will be carried out in the following Chapter 5.

Further analysis of this method will be presented in Chapter 8, where the CFD tools will be applied to a second case study, a test rig designed and developed by the author and established at Lancaster University. This second case study will highlight the versatility of these numerical tools, where the design of additional inserts will be explicated.

5 Experimental Testing of Pelton Turbine Casings

This chapter describes the experimental testing of the Gilkes twin jet horizontal axis Pelton turbine. The testing was carried out at the Laboratory of Hydraulic Machines, National Technical University of Athens (NTUA) according to IEC 60193 testing standards. The testing can be divided into two phases:

Phase 1: Systematic testing of casing baffle inserts

Phase 2: Testing of the most efficient configuration from Phase 1 with different casing widths

In the following chapter the results will be compared against the CFD analysis carried out in Chapter 4. This chapter will later form the framework that examines the use of and also the development of the Lancaster University Pelton test rig, which investigates the effect of different casing design parameters in a broader context with the provision for more detailed visual documentation.

5.1 Phase 1 - Pelton Shroud and Baffle Testing

5.1.1 Technical Program

A number of the various components that have been outlined in Chapter 5 were constructed and the experimental results obtained in this chapter were carried out using the Pelton test rig at NTUA, shown in Fig. 5-1. The test rig consists of a high head adjustable speed multistage pump of nominal operation point $Q=290 \text{ m}^3/\text{hr}$, $H=130 \text{ mWG}^{16}$, coupled via a hydraulic coupler to a 200 kW induction motor is used to feed the model turbine, pumping from the 320 m^3 main reservoir of the lab. The tests were carried out using the twin jet Z120 Pelton manufactured by Gilkes, which was coupled to a 75kW DC generator with continuous speed regulation.

¹⁶ mWG – meters of water column (gauge) = 127.4 m


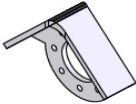

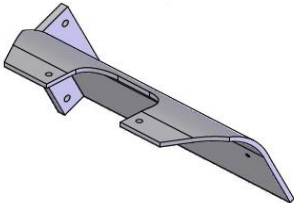


Fig. 5-1 Pelton testing facility at NTUA

Testing and calibration of all the sensors was carried out according to testing standard IEC 60193:1999 [108].

5.1.2 Program of Tests

An outline of the testing programme carried out is given in Table 5-1, highlighting the different casing components used.

Test #	Components	
Test A	Naked Case	
Test B	+Jet Shroud design 1 (JS1)	
Test C	+Jet Shroud design 2 (JS2)	
Test D	+JS1 + Bolt on Baffle (BAF)	

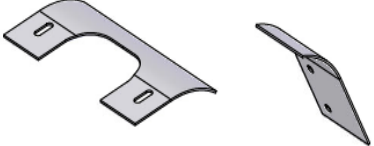
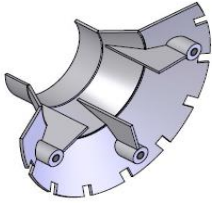
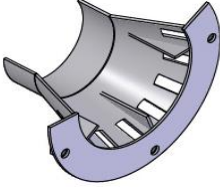
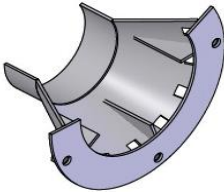
Test E	+JS1 + BAF + Sealing Plates (SP)	
Test F	+JS1 + BAF + SP + Side Shroud design 1	
Test G	+JS1 + BAF + SP + Side Shroud design 2	
Test H	+JS1 + BAF + SP + Side Shroud design 3	

Table 5-1 Program of experimental tests carried out indicating components used

5.1.3 Characteristic Equations

The quasi non-dimensionalised characteristic equations used to define rotational speed (5.1) and flow rate (5.2), in addition to those used to define output power (5.3), input power (5.4) and efficiency (5.5) are given below. The pitch circle diameter of the Z120 runner used in the testing was 320 mm.

$$n_{11} = \frac{n \times D}{\sqrt{H}} \quad (5.1)$$

$$Q_{11k} = \frac{Q/N_j}{B^2 \times \sqrt{H}} \quad (5.2)$$

$$P_{out} = M\omega \quad (5.3)$$

$$P_{in} = \rho g H Q \quad (5.4)$$

$$\eta = \frac{P_{out}}{P_{in}} \quad (5.5)$$

Where n_{11} is the unit speed, Q_{11k} is the unit flow rate, D is the pitch circle diameter and B the bucket width, n is the rotational speed of the runner, H is the net head, Q is the flow rate, N_j is

the number of jets, M is the torque measured on the turbine shaft, ρ is the density of water and g is the acceleration due to gravity. ρ and g were calculated according to the tables provided in the testing standards IEC60193:1999 [108].

5.1.4 Test Points

Despite the CFD model being analysed at the BEP of the turbine the measurements for tests A – H were made over a series of 13 points each for upper, lower and twin jet operation, as defined in Fig. 5-2, with the BEP highlighted as the red diamond. Control points are taken at the beginning, between and after each test in the order of upper, lower and twin jet respectively. There are a total of 6 control points per test at $n_{11} = 39$, $Q_{11k} = 0.15$.

Each operating point is run for a period of 90 seconds and data is recorded from the sensors at a rate of 2 Hz. A total of 180 readings were obtained for each operating point, through the first 60 are disregarded, this is in order to ensure steady state conditions and minimise the random uncertainties, while care has also been taken to remove any outliers.

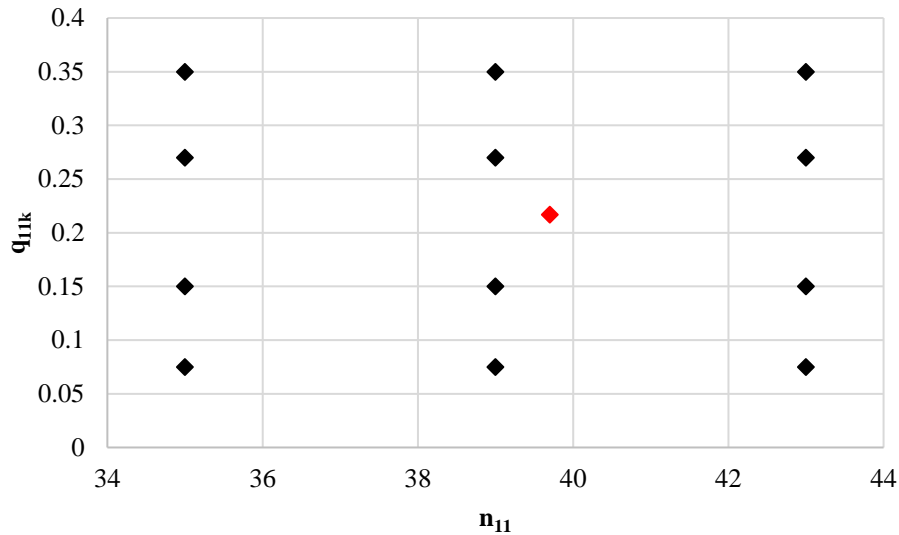


Fig. 5-2 Test points under consideration with BEP indicated as the red diamond

5.1.5 Test Procedure

The tests conducted all followed the established procedure, starting first with turning on all the instruments to allow a preheat of at least 30 minutes prior to taking measurements. Before starting the pump the following should take place:

1. Ensure that both nozzles are open and set the spear position to an arbitrary distance, normally 15 mm;
2. Start up the brake at low rotational speeds;
3. Turn on the pump cooling water;

4. Start up the pump;
5. Increase the speed of the pump and the brake simultaneously and set it to produce the required head for measurements and to the control point respectively.

Once a sufficient time for preheat has passed measurements of the test point can begin following this the test points can be completed;

1. Increase the turbine rotational speed to the required value;
2. Allow sufficient time for the flow conditions to be stabilised (10-20 seconds should be adequate);
3. Obtain measurements continuously for at least 60 seconds;
4. Increase the speed of the turbine;
5. Repeat steps 2-4;
6. Once the full range of speed has been obtained, change the spear position;
7. Adjust the pump rotational speed to maintain the head constant;
8. Repeat steps 2-7.

This method was chosen as it encourages stable operating conditions between measurements allows the procedure to be completed efficiently.

The spear position associated with the required flow rate is listed in Table 5-2 below.

	Nozzle Opening [mm]		
	Upper	Lower	Both
0.075	4.25	4.5	4.25
0.15	8.75	8.75	8.75
0.217	13.5	13.75	12.25
0.27	17.25	17.5	17.25
0.35	25.5	26	25.5

Table 5-2 Spear position and associated flow rates

5.1.6 Normalised Efficiency

For Phase 1 and Phase 2 testing, the presented efficiencies have been normalised for commercial reasons, whereby all of the efficiencies in this chapter are expressed as a percentage of the peak efficiency of the turbine during twin jet operation, shown in equation (5.6). Where η_0 is the efficiency of the test point.

$$\eta = \frac{\eta_0}{\eta_{Max}} \quad (5.6)$$

5.1.7 Uncertainty Analysis

Based on the most recent calibrations the systematic uncertainty for each instrument used during this testing is given in Table 5-3.

Instrument	Detail	Systematic Uncertainty
Pressure Transducer (H)	ESI Technology, model: Ellison-Pr3200	$\pm 0.3\%$
Flow meter (Q)	ABB, model: DE41F	$\pm 0.5\%$
Torque meter (M)	Datum Electronics, model: M425	$\pm 0.1\%$
Speed Sensor (n)	Efectron, model: GA3005-ANKG	$\pm 0.05\%$

Table 5-3 Systematic error of each instrument

When determining the uncertainty the calibration error for each instrument becomes the systematic uncertainty. The total systematic uncertainty for the hydraulic efficiency, δ_S , can be calculated using equation (5.7)

$$\delta_S = \sqrt{\delta_H^2 + \delta_Q^2 + \delta_M^2 + \delta_n^2} \quad (5.7)$$

The total systematic uncertainty in the efficiency, η , was calculated as $\pm 0.6\%$.

During the experimental testing repeat measurements at a single operating points, known as the control points, were recorded. These were then used to determine the random uncertainty according to the procedure defined in Annex L of the International Standard, IEC 60193, which covers these experimental tests [108]. Table 5-4 outlines the control points, where the efficiency values have been normalised according to 5.1.6.

The standard deviation, s_y , is calculated as 0.0006719 using equation (5.8) below.

$$s_y = \sqrt{\frac{1}{n-1} \sum_{i=1}^n (\bar{Y} - Y_i)^2} \quad (5.8)$$

The random uncertainty associated with the mean value at the 95% confidence level, using the Student's T distribution, is given by equation (5.9).

$$s_r = \frac{t \cdot s_y}{\sqrt{n}} \quad (5.9)$$

Where t is the Student's T factor and can be approximated using equation (5.10).

$$t = 1.96 + \frac{2.36}{n-1} + \frac{3.2}{(n-1)^2} + \frac{5.2}{(n-1)^{3.84}} \quad (5.10)$$

The total random uncertainty, δ_R at 95% confidence was calculated using this method as $\pm 0.033\%$.

#	Y_i	$\bar{Y} - Y_i$	$(\bar{Y} - Y_i)^2$
1	0.999009	0.000991	9.81E-07
2	1.00188	-0.00188	3.53E-06
3	0.99949	0.00051	2.6E-07
4	1.000225	-0.00022	5.05E-08
5	1.000777	-0.00078	6.03E-07
6	0.999434	0.000566	3.21E-07
7	0.999242	0.000758	5.75E-07
8	0.999698	0.000302	9.13E-08
9	1.000626	-0.00063	3.92E-07
10	0.999844	0.000156	2.42E-08
11	1.000302	-0.0003	9.15E-08
12	0.99988	0.00012	1.43E-08
13	0.999242	0.000758	5.75E-07
14	0.999698	0.000302	9.13E-08
15	1.000626	-0.00063	3.92E-07
16	0.999844	0.000156	2.42E-08
17	1.000302	-0.0003	9.15E-08
18	0.99988	0.00012	1.43E-08
	$\bar{Y} = 1$		$\Sigma = 8.12728E-06$

Table 5-4 Normalised control points used for uncertainty analysis

The total uncertainty, δ_t , was calculated as $\pm 0.6009\%$ using equation (5.11) below.

$$\delta_t = \sqrt{\delta_S^2 + \delta_R^2} \quad (5.11)$$

The total uncertainty for the experimental testing using the Pelton test rig was acceptable for the purpose of this research, since when comparing the testing of the different designs the systematic uncertainty can be cancelled out and it is only the random uncertainty which determines the error bars in the calculations. Moreover, the random uncertainty falls below the acceptable limit of 0.1% as suggested in IEC 60193:1999 [108].

5.1.8 Phase 1 Test Results Analysis and Discussion

General description of the trend curves Q_{11k} v normalised η for fixed speeds are as follows:

For twin jet operation a consistent pattern emerges for lower specific speeds of $n_{11} = 35$ rpm, the efficiency is generally close to that of $n_{11} = 39$ rpm at high or low specific flow rates away

from the BEP, however as the flow rate approaches the BEP the efficiency remains fairly steady, rising to a peak of 97.26% in test B.

In contrast to this for higher specific speeds, i.e. $n_{11} = 43$ rpm, the opposite is true, that at high or low specific flow rates away from the BEP and for almost all cases in fact the efficiency is the lowest, with a minimum efficiency of 89.81% for test A. As the flow moves towards the BEP, the efficiency rises steeply and overtakes $n_{11} = 35$ rpm at a specific flow rate of $Q_{11k} = 0.15$, achieving a peak efficiency of 98.09% for test E, before falling successively at each test point.

For specific speeds close to the BEP, i.e. $n_{11} = 39$ rpm, the efficiency remains the highest for all specific flow rates, rising and falling steadily as it approaches and moves away from the BEP respectively. The graphs tend to be rather flat between $Q_{11k} = 0.15 - 0.27$, either side of the BEP, however it is anticipated that in reality this is a smooth curve approaching a peak at $n_{11} = 39.7$ rpm, $Q_{11k} = 0.22$, which would be demonstrated with a greater number of test points.

To illustrate this included are the typical Q_{11k} v efficiency graphs of test E for upper, lower and twin jet operation, as shown in Fig. 5-3, Fig. 5-4 and Fig. 5-5 respectively.

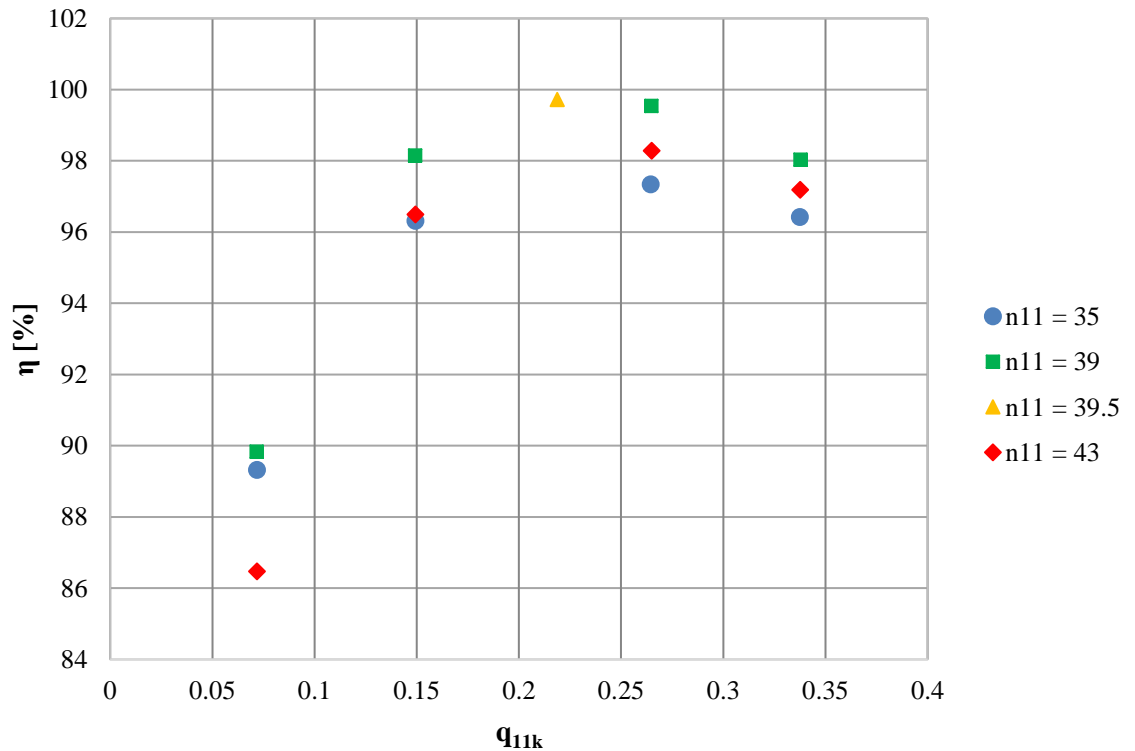


Fig. 5-3 Test E upper jet Q_{11k} plotted against efficiency for constant unit speeds

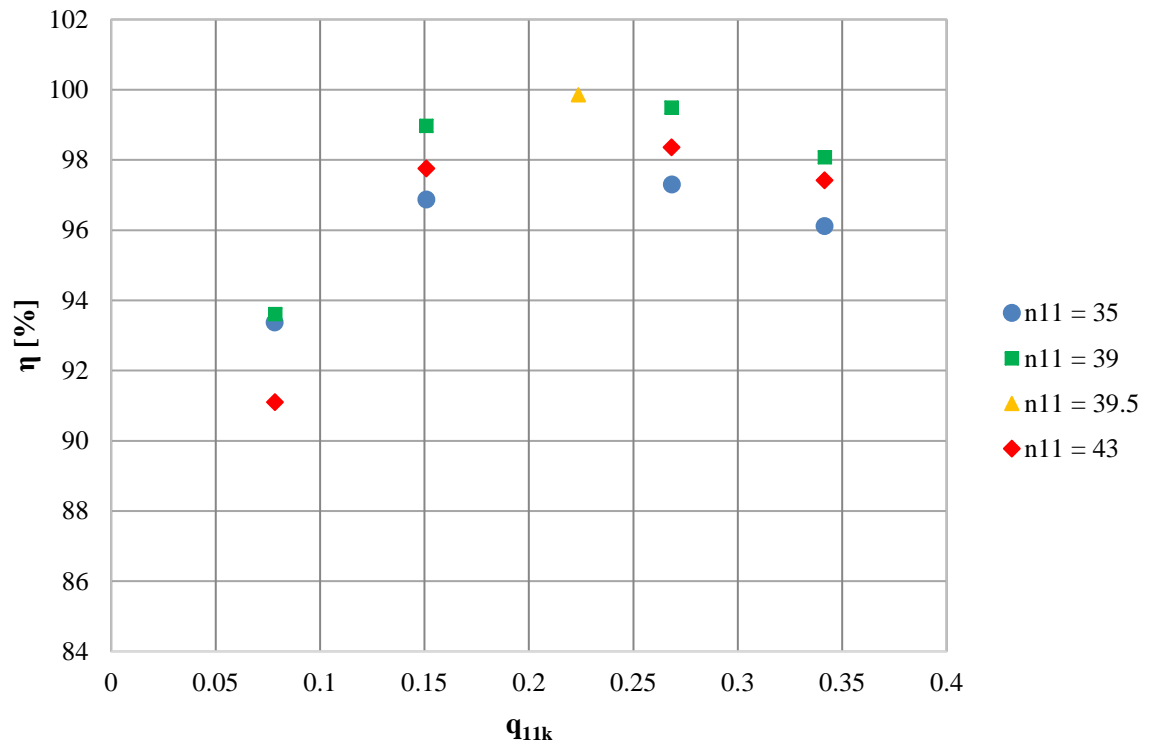


Fig. 5-4 Test E lower jet Q_{11k} plotted against efficiency for constant unit speeds

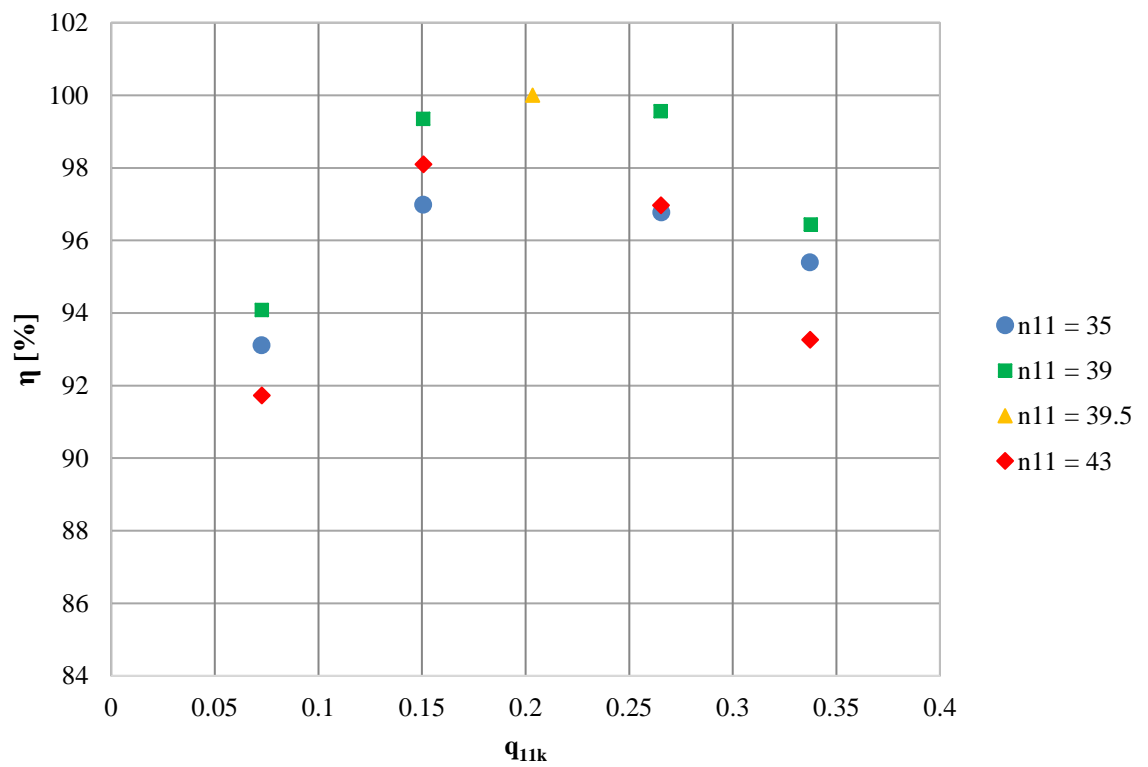


Fig. 5-5 Test E twin jet Q_{11k} plotted against efficiency for constant unit speeds

For upper jet alone the graphs show a consistent trend with efficiency rising as the specific flow rate increases towards the BEP with peak efficiency occurring at the BEP and then remaining steady as the flow rate continues to increase. As with twin jet operation, for specific speeds close to the BEP, i.e. $n_{11} = 39$ rpm, the efficiency is the highest across the full range of specific flow rates. At low specific flow rates, the efficiency of $n_{11} = 43$ rpm is lower than $n_{11} = 35$ rpm, however by $Q_{11} = 0.15$ the efficiency of higher specific speeds has over taken $n_{11} = 35$ rpm and remains consistently higher across the operating range.

For lower jet operation the trends are very similar to upper jet operation.

It is shown in Fig. 5-6 that the BEP of twin jet operation is highly dependent on the configuration of the casing components and the highest value occurred during test E. The lowest efficiency occurs during test A, the naked case, at 99.41%. This is improved by the addition of the jet shrouds (design 1 and 2) to 99.93% and 99.96% in tests B and C respectively. The addition of the baffle plate is negligible in test D, however the baffle plate and baffle closing plates in test E do seem to improve the efficiency and combine to give the overall best efficiency configuration. The addition of the side shrouds contributes detrimentally to the overall BEP's, with efficiencies of 99.77%, 99.61% and 99.62% in tests F, G and H respectively. The overall range of efficiency from highest to lowest BEP is 0.5%.

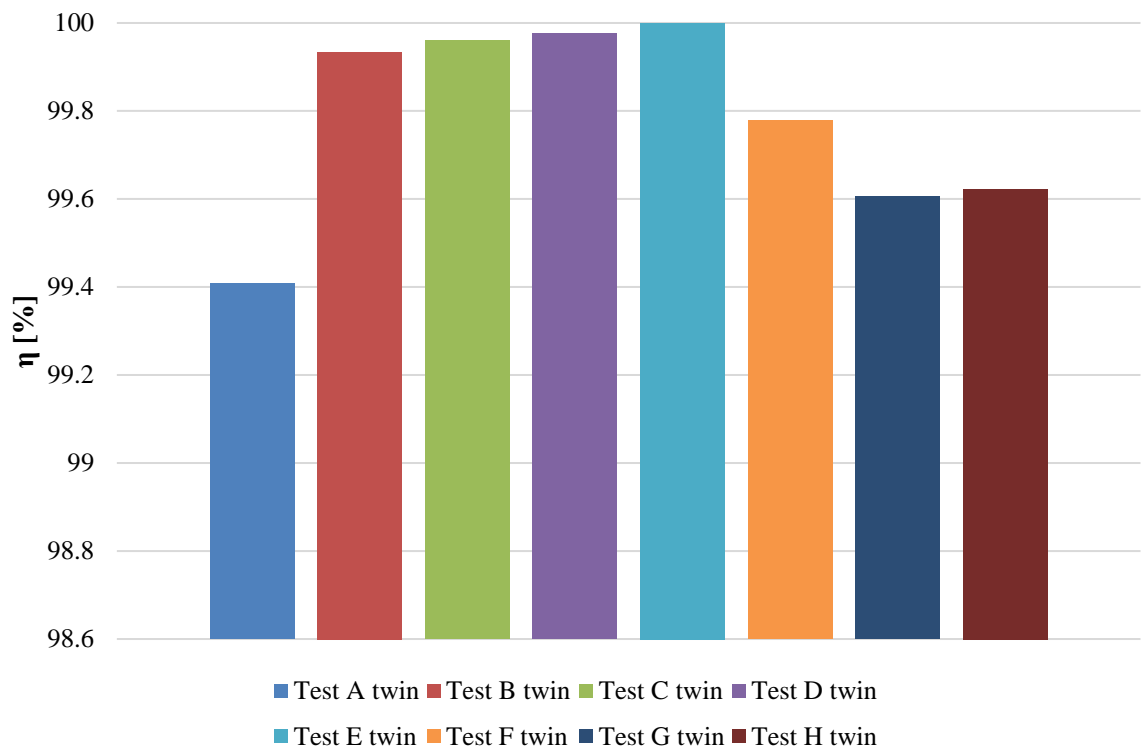


Fig. 5-6 Experimental test results A – H at the BEP for twin jet operation

The best efficiency point for lower jet also occurred during test E achieving 99.85%, shown in Fig. 5-7. It can be observed that the lower jet is considerably influenced by the casing configuration and that at operating conditions close to the BEP the performance of the lower jet is significantly inferior to the upper jet apart from in test E.

Similarly the BEP for upper jet operation is affected by the casing components configuration and the highest value is observed to be 99.74% occurred during test C, shown in Fig. 5-8.

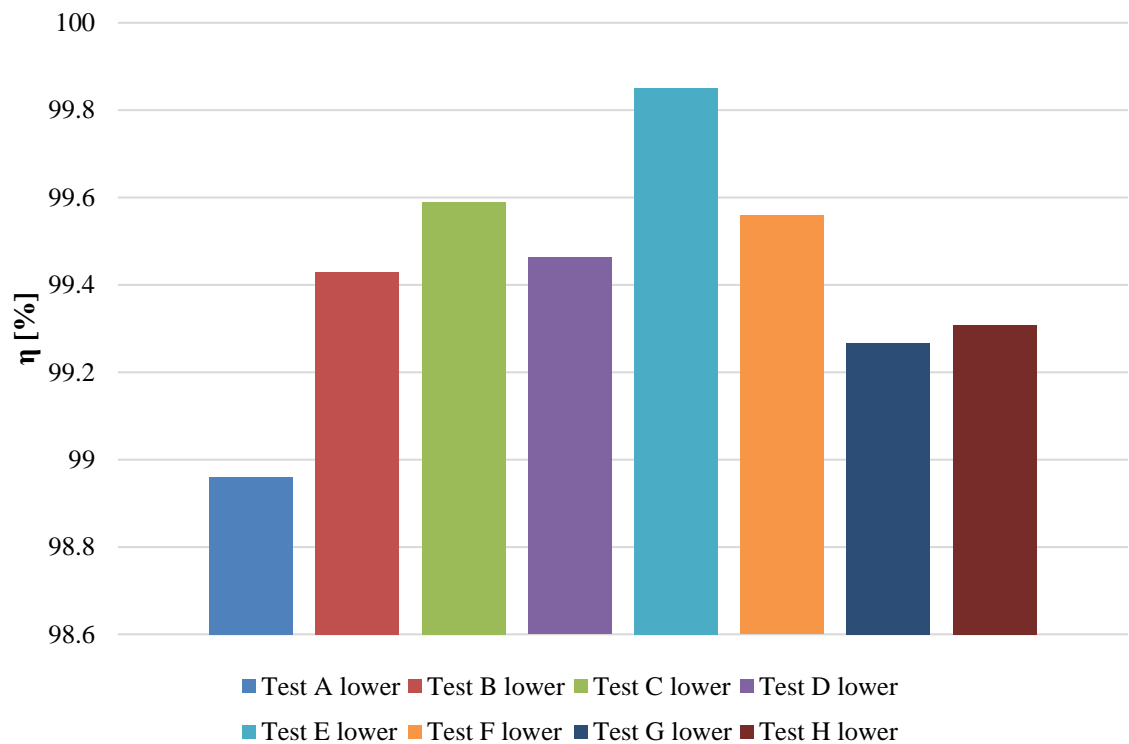


Fig. 5-7 Experimental test results A – H at the BEP for lower jet operation

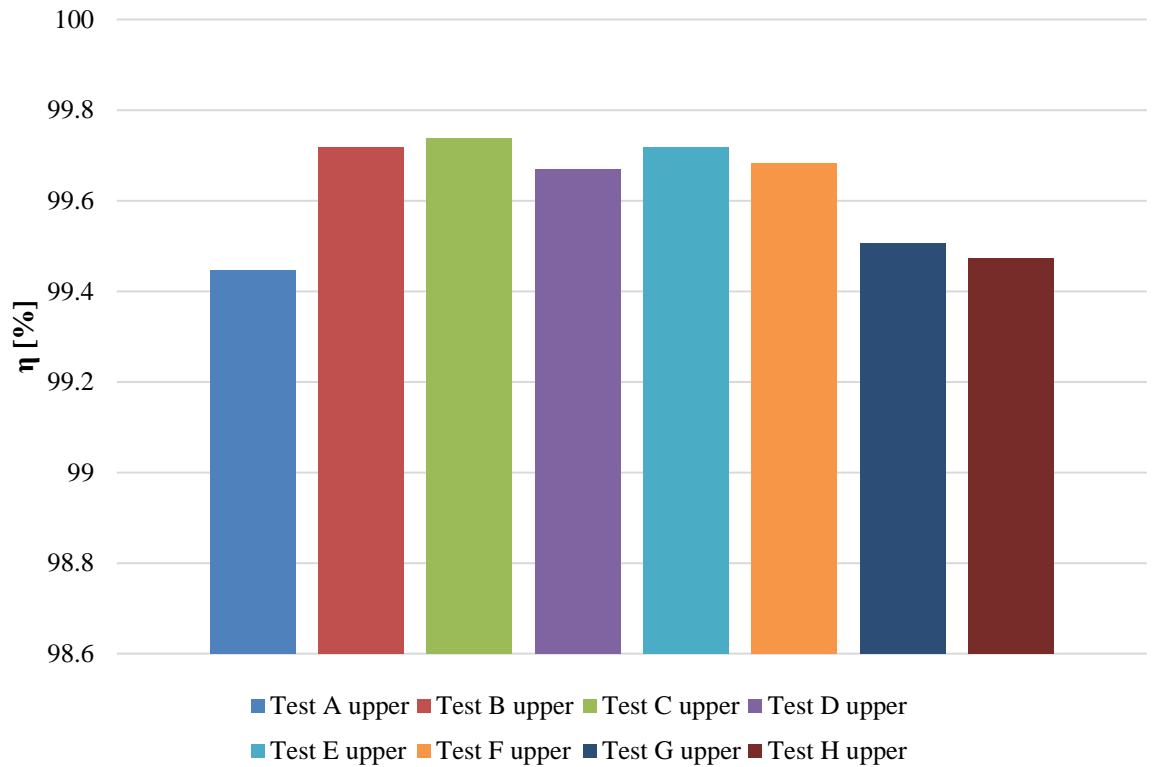


Fig. 5-8 Experimental test results A – H at the BEP for upper jet operation

For upper jet it is expected that the efficiencies for test B - E should be almost identical and therefore to a certain degree of confidence the 0.04% drop in efficiency for test 31 can be assigned to experimental/measurement error. Fig. 5-9 shows the upper and lower error band centred on the average for BEP results for upper jet, showing that all results lie on or within this region. The graphs for tests F - H do however show a slight decrease across the range of speeds and flows, which is to be expected with the addition of the side shrouds. It is interesting to notice that the trend for upper jet is almost identical for all tests conditions despite the addition of the baffle and side shrouds and that even the addition of the dummy deflector in test B improves the efficiency by 0.24%.

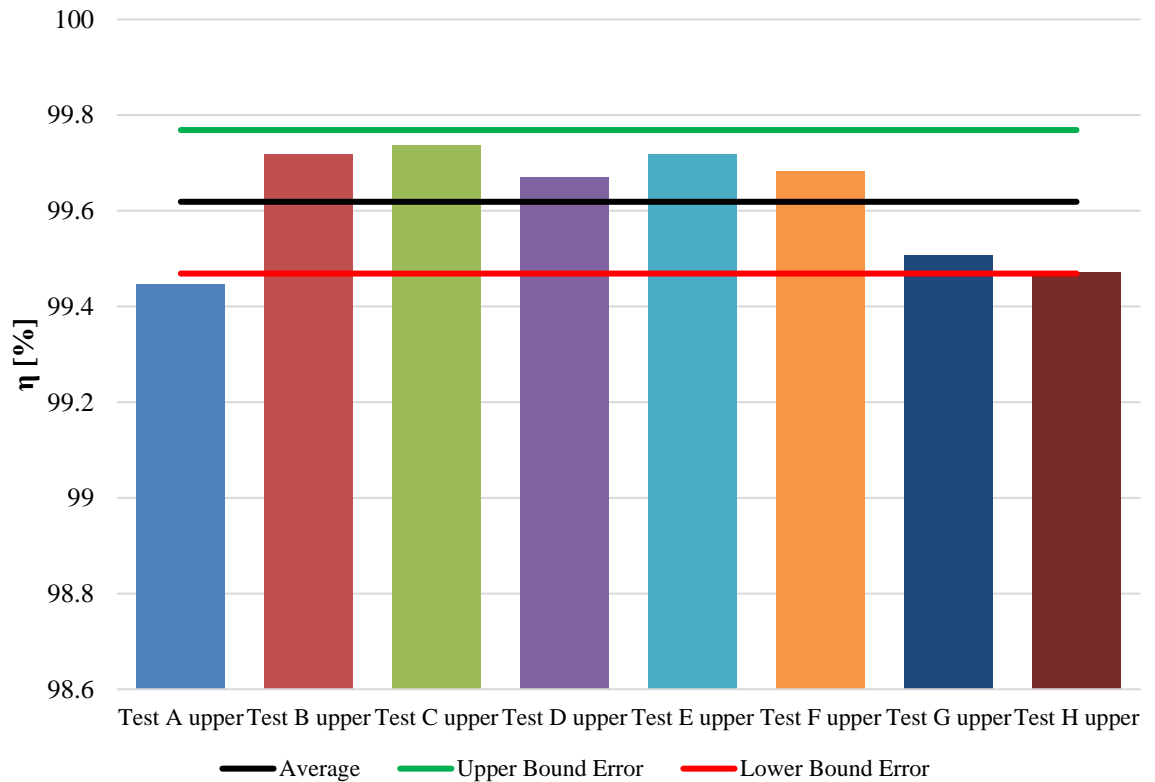


Fig. 5-9 Experimental test results A – H at the BEP for upper jet operation BEP error bars

Table 5-5 provides an overview of the highest efficiencies achieved for single jet (lower and upper) and twin jet combination and during which tests these were indicated. A more indicative observation of the difference between single jet and twin jet performance can be seen in graphs of Q_{ilk} plotted against efficiency for constant unit speeds in this case $n_{11} = 39$ rpm, as shown in Fig. 5-10, Fig. 5-11 and Fig. 5-12.

$n_{11} = 35$		
Lower	97.30%	Test E
Upper	97.34%	Test E
Twin	97.26%	Test B
$n_{11} = 39$		
Lower	99.41%	Test E
Upper	99.62%	Test C
Twin	99.56%	Test E
$n_{11} = 39.5$		
Lower	99.85%	Test E
Upper	99.73%	Test C
Twin	100.0%	Test E

$n_{11} = 43$		
Lower	98.36%	Test E
Upper	98.27%	Test G
Twin	98.10%	Test E

Table 5-5 Test efficiencies

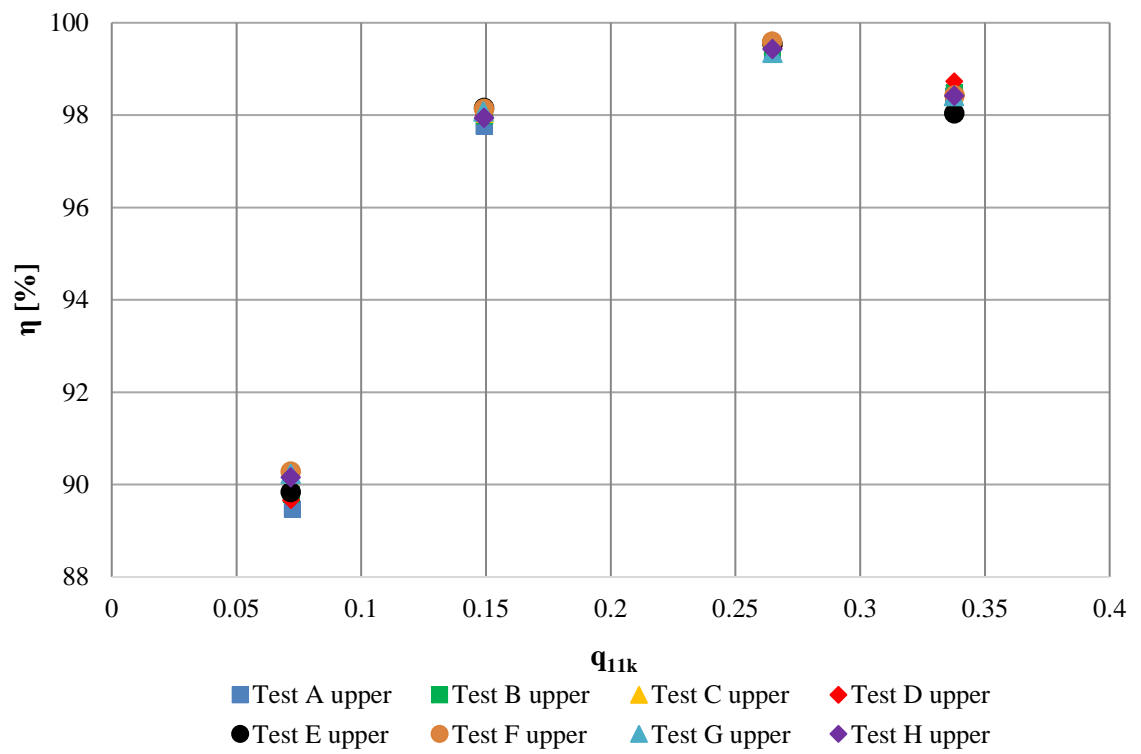


Fig. 5-10 Experimental test results A – H at $n_{11} = 39$ for upper jet operation

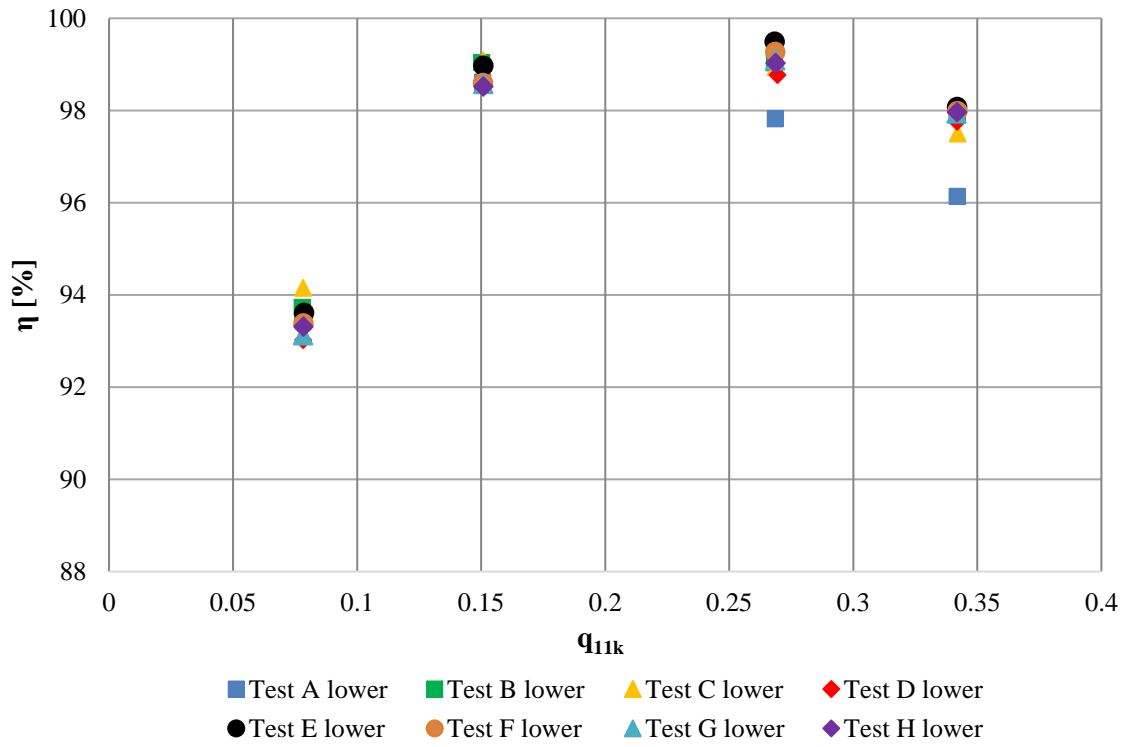


Fig. 5-11 Experimental test results A – H at $n_{II} = 39$ for lower jet operation

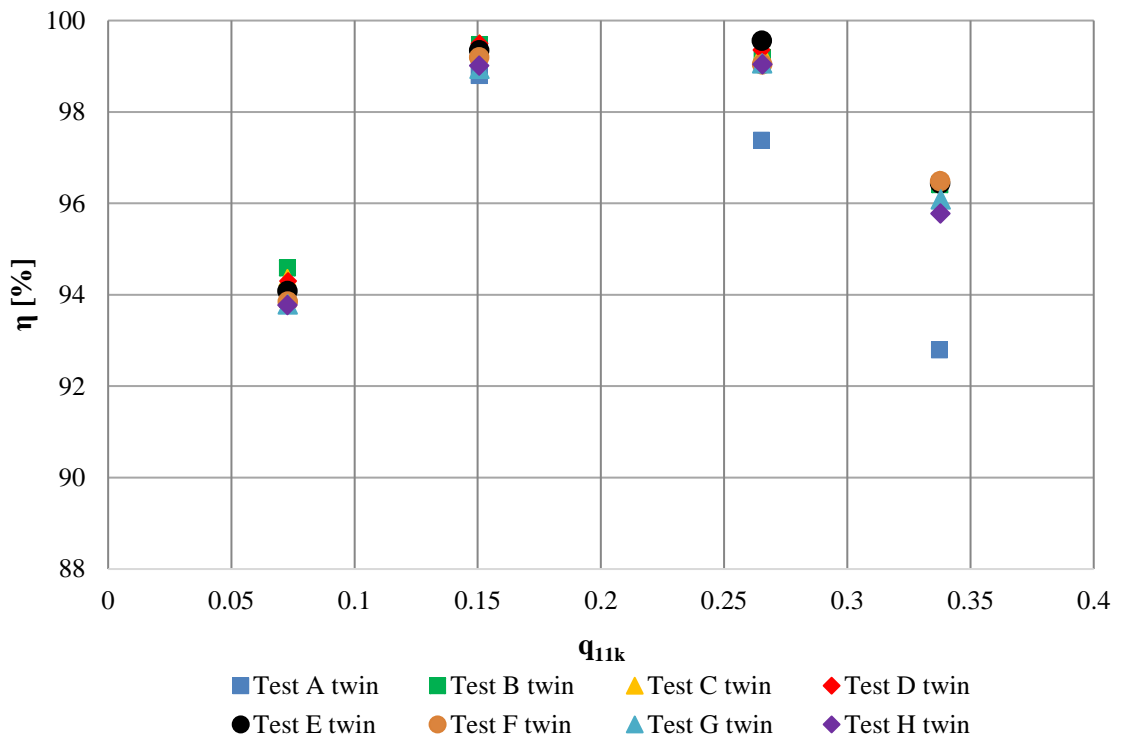


Fig. 5-12 Experimental test results A – H at $n_{II} = 39$ for twin jet operation

Comparing the graphs of lower and upper jet, at the same axis scale, there is a marked difference in efficiency at low Q_{ilk} values and this is evident across the whole range of specific speeds, with the upper jet considerably lower, in the case of test E at specific speed = 39 rpm, the upper jet achieved 89.84% and the lower jet 93.61%, a difference of 3.77%. However, for higher flows $Q_{ilk} = 0.34$ the efficiency ranges for upper and lower jet are much closer with upper jet average = 96.22% and lower jet 95.99%. It can be argued that for higher flows, the jet diameter is larger therefore any disturbance to the jet profile, leading to losses, as a percentage of the overall jet diameter will be smaller, however this does not account for the fact that there are differences between the two jets.

In cases for specific speeds away from the BEP, for upper jet operation alone the side shrouds seems to be effective, however it is random as to which design provides the optimum performance, i.e. $n_{II} = 35$ rpm uses the SS1 and $n_{II} = 43$ rpm the SS2.

The lower nozzle benefits from the addition of the jet shroud, however in the naked case test the efficiency is only improved by 0.3% by the addition from 90% in test A and 93% in test B, therefore the difference between the two jets must be as a result of something else.

The difference between the two jets can be explained as an effect of the geometry of the turbine, both upper and lower jets are supplied by similar pipe lengths with 90° bends, however the upper jet will experience a greater head loss due to the fact that the upper jet acts against gravity away from the centreline of the bifurcator. Table 5-6 shows the average pressures measured during test E for the corresponding sensors shown in Fig. 5-13, and it can be observed that there is a measurable pressure drop associated with sensor 5 in comparison to 3, leading to observable losses emerging as lower measured efficiencies, which are more pronounced at low flow rates¹⁷.

¹⁷ Moreover, it can be postulated that this is a direct result of the design of the pipework layout and the consequence that this has on the jet – runner interaction. Based on the literature in 2.6.1 it is known that that the design of the pipework will result in a jet separation on the underside of the jet. This will be further analysed by CFD simulation in Chapter 8 where a noticeable bead is formed. It could be expected that during the jet cut in process (and due to the Coanda effect already described) that this bead will become detached from the main flow resulting in a smaller overall energy exchange to the runner. For the case of the lower jet, the bead will be on the topside of the jet and therefore the jet will remain largely intact during the cut in process.

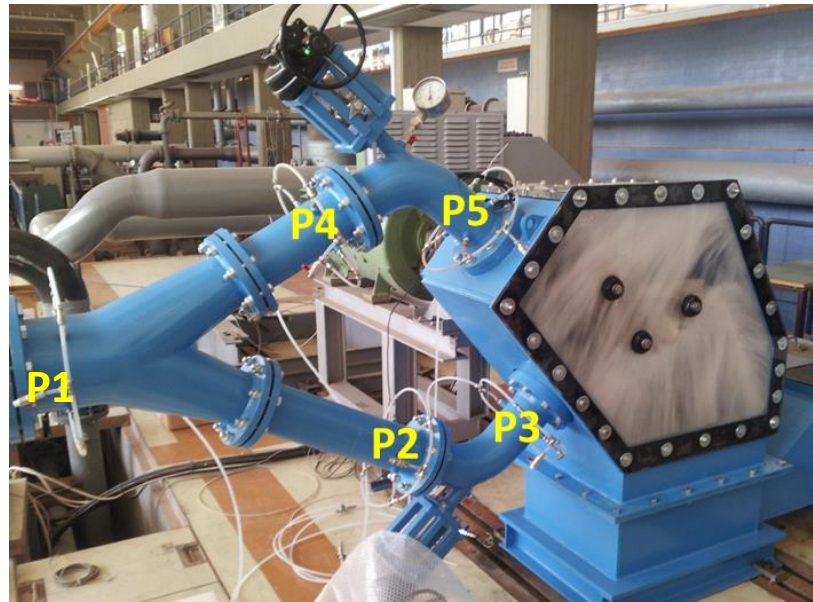


Fig. 5-13 Location of pressure transducers in the NTUA test rig

	Pressure Reading [V]		
	P1	P3	P5
0.075	6.847	4.441	4.223
0.15	6.827	4.398	4.210
0.217	6.824	4.395	4.205
0.27	6.833	4.394	4.206
0.35	6.846	4.394	4.206

Table 5-6 Pressure sensor readings test E twin jet operation

Another reason, for the difference in upper and lower jet efficiency could be a result of construction, and further analysis of this will be carried out in Chapter 8, where CFD simulations of the full 3D injectors will be carried out.

5.2 Phase 1 Comparison with CFD

The following section will provide a short commentary on the salience of CFD as a visualisation tool, since it is often thought that this is unreliable and can sometimes be misleading. The observations made in the previous chapter 4 offered some practical guidance on the effect that the various casing inserts have on the flow and how this might affect efficiency, however this impression expressed in words cannot be precise, nor is theoretically significant. Nevertheless, attempts have been made to compare the CFD results against photographs taken during the experimental measurements (taken through a single Perspex window on the front face of the casing) and comments on the validity of this method will be provided.

5.2.1 Flow Visualisation

Snapshots for various tests for upper jet, lower jet and twin jet operation at the BEP are shown in Fig. 5-14.

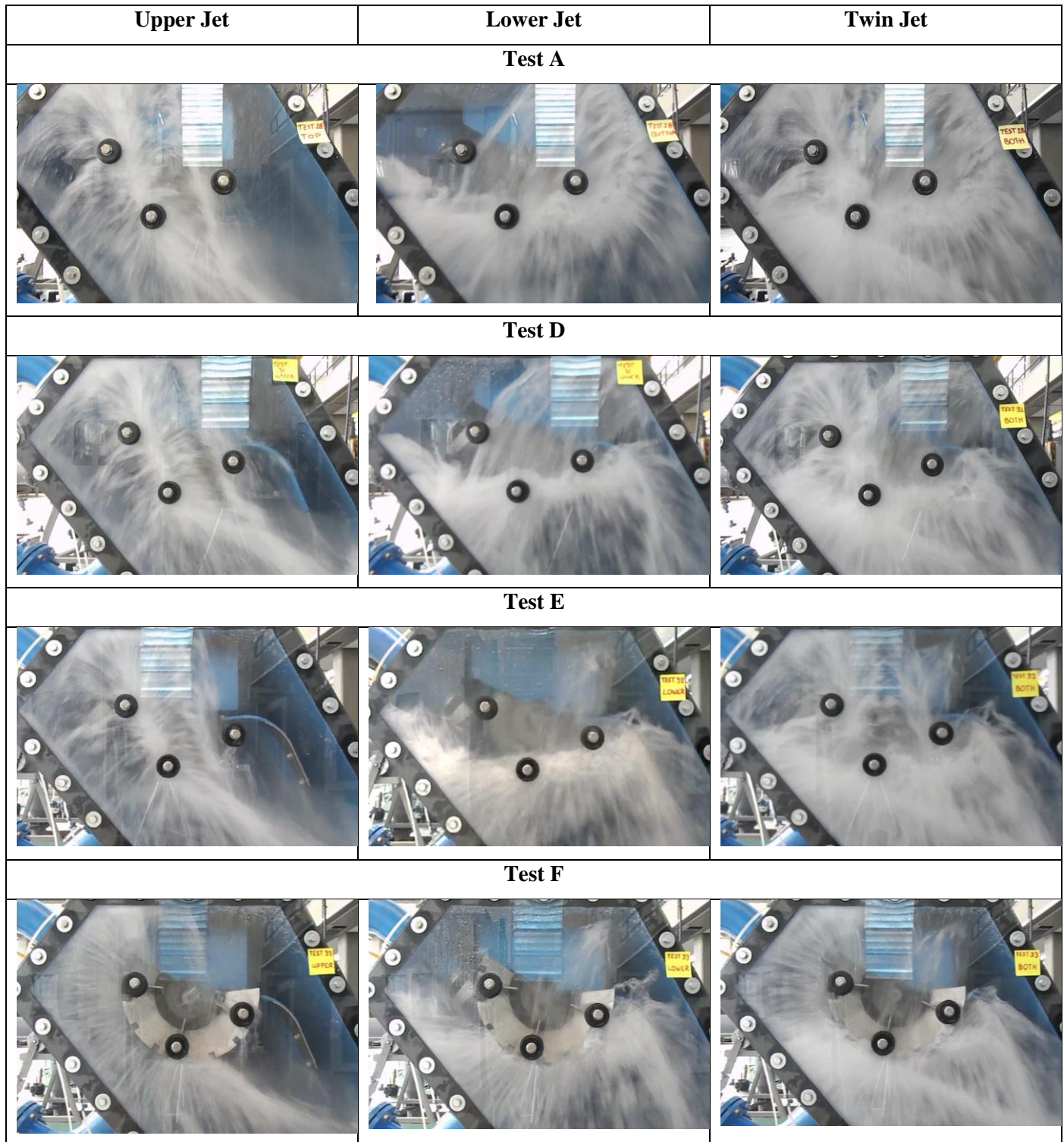


Fig. 5-14 Snapshots of experimental operation at BEP for upper, lower and twin jet measurements

Some further analysis and comparison between the photographs taken during the experimental testing and the CFD simulations, which have already been described will be outlined in the following sections.

5.2.2 The Naked Case – Test A

For post processing purposes, an isosurface of 1% water is initially calculated. Since this is not physically realistic velocity vectors are plotted on the isosurface, coloured by magnitude (i.e. red high velocity and blue low velocity). Fig. 5-15 shows a representative plot for the upper jet and is compared against a photograph of the experimental setup for the same operating point in Fig. 5-16. Identical black lines are overlaid in both Fig. 5-15 and Fig. 5-16, demonstrating good correlation of the CFD with the experimental result as both the direction and general shape of the water sheet as it impacts the front wall are captured. However, since it is only a snapshot it does not show the fully developed flow in the casing.

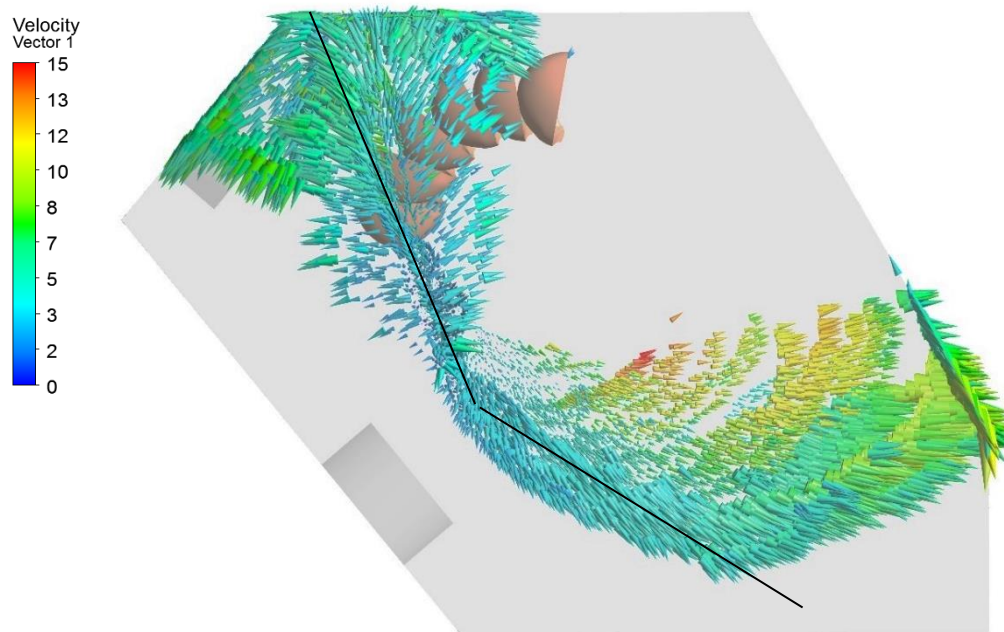


Fig. 5-15 CFD velocity vectors upper jet

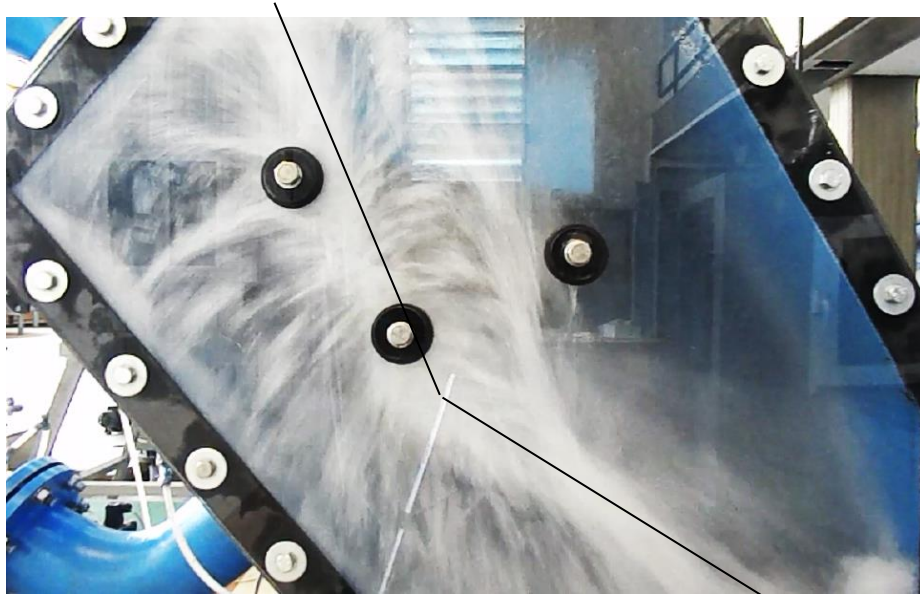


Fig. 5-16 Experimental flow visualisation upper jet

Similar to the upper jet comparison, Fig. 5-17 shows the representative plot for the lower jet and is compared against a photograph of the experimental setup for the same operating point in Fig. 5-18.

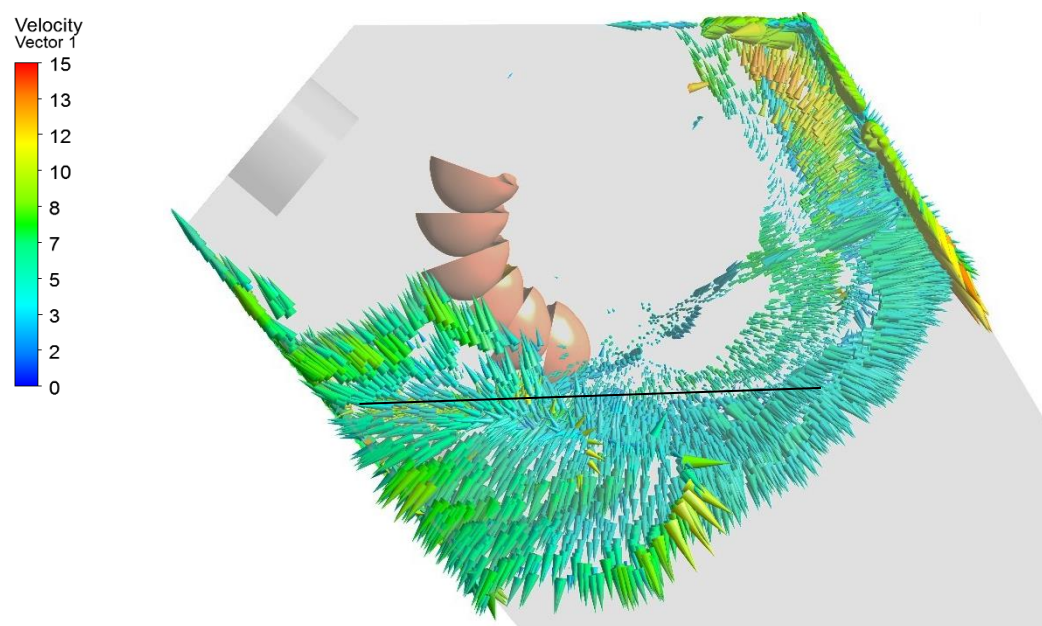


Fig. 5-17 CFD velocity vectors lower jet

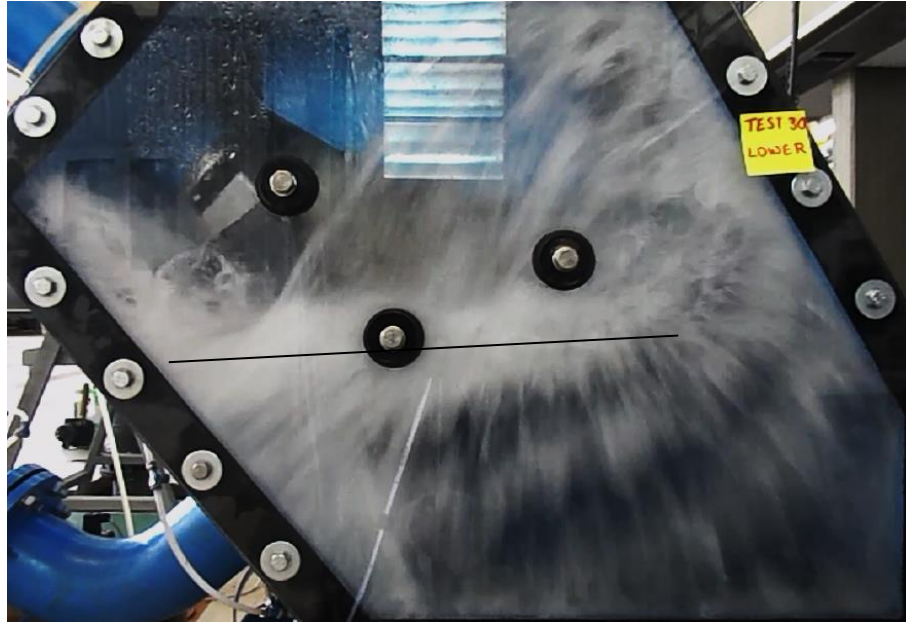


Fig. 5-18 Experimental flow visualisation lower jet

In the absence of shrouds or baffles the water is allowed to circulate around the casing. It can be noted from the velocity vectors in Fig. 5-19(δ) that the water in the top left hand corner of the casing is directed towards the symmetry plane, eventually falling onto the injector and jet. Likewise, in Fig. 5-19 (ε), the water from the lower jet circulates in the top right hand corner before falling onto the runner. The obvious conclusion of this was to ensure that the jets are shrouded as much as possible to ensure that the quality is not hindered by the splash water interference. Indeed the experimental results for test B show that the inclusion of the jet shroud improves the efficiency by for the upper jet and lower jet respectively at the BEP. Furthermore the lower jet suffers most from water entering the roof of the casing and a curved baffle can be placed around the runner to inhibit this water, as recommended in [5].

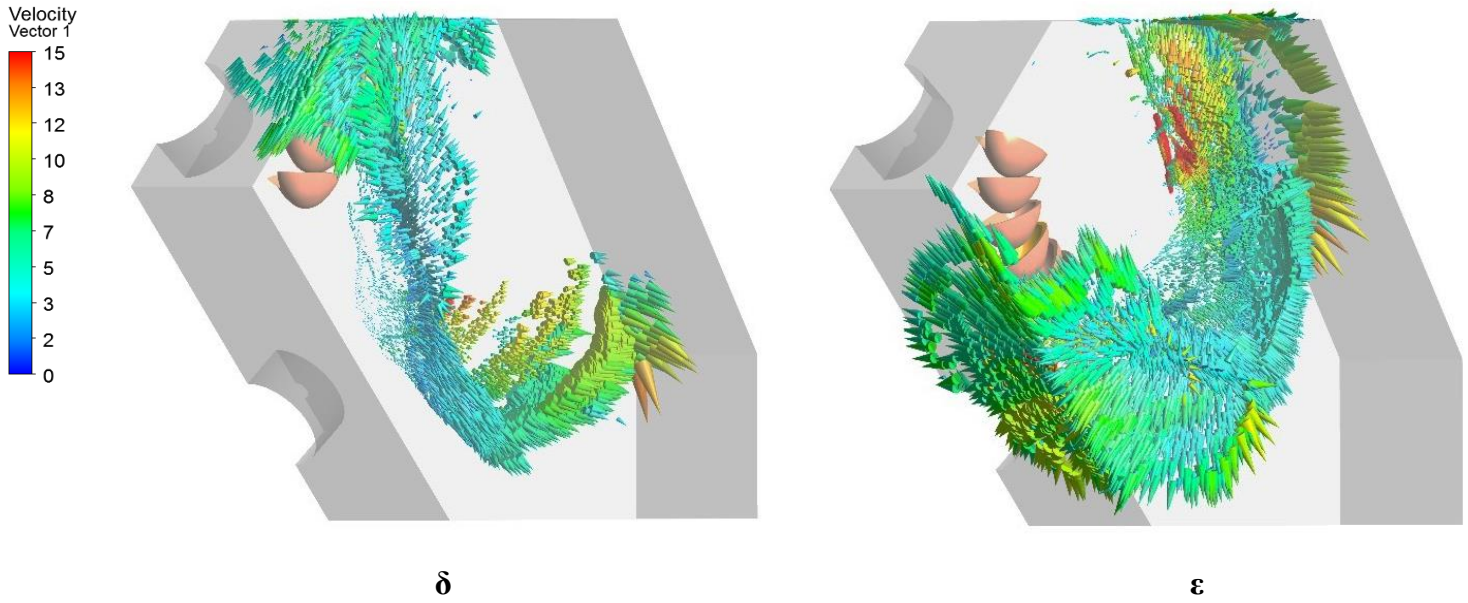


Fig. 5-19 Comparison of velocity vectors for upper and lower injector in the naked case

5.2.3 The Role of the Bolt on Baffle

In Fig. 5-20 efficiency curves for the unit speed, $n_{II} = 39$, are plotted against a range of non-dimensional flow rate, Q_{II} , for both the upper jet and lower jet, with and without shrouding, normalised against the lower jet with shrouding, indicating the positive improvement of their installation, particularly at higher flow rates for the lower jet. While it is not yet possible to make a quantitative prediction of the efficiency of a full Pelton turbine using the simulation described, it has nevertheless been shown by observations of the flow in the casing how baffles and shrouding can be added with positive effect. Since the addition of the curved baffle has very little influence on the flow for the upper jet, the corresponding photograph from experiment is shown for lower jet only in Fig. 5-21 and a comparative photograph and CFD visual shown in Fig. 5-23.

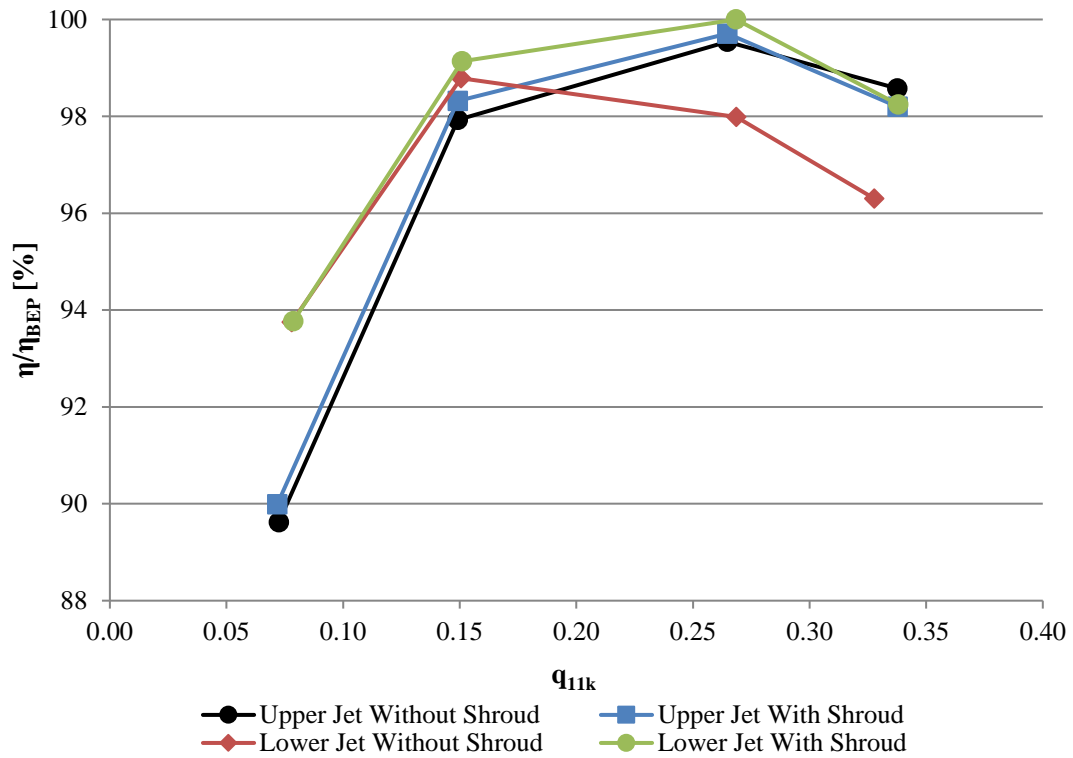


Fig. 5-20 Comparison of experimental results for upper and lower injector with and without the BAF and SP

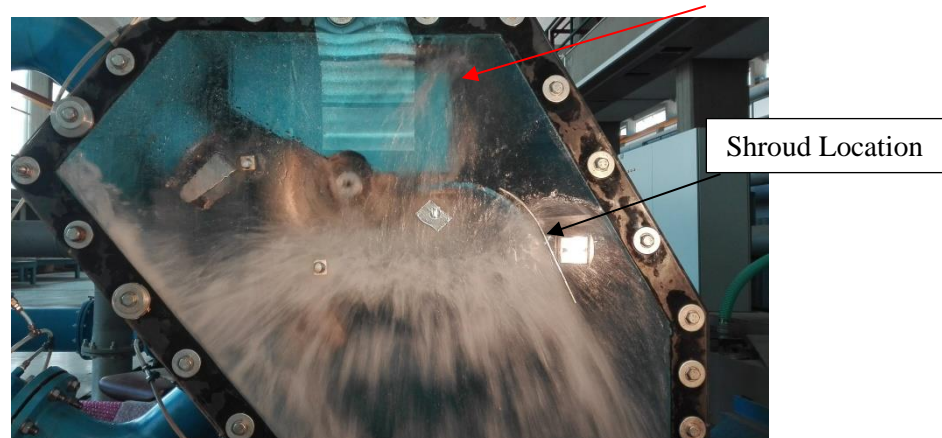


Fig. 5-21 Lower jet with BAF and SP

The exact role of the sealing plate in removing as much water as possible from the roof of the casing can be observed by comparing the two snapshots from test D and E as shown in Fig. 5-22.

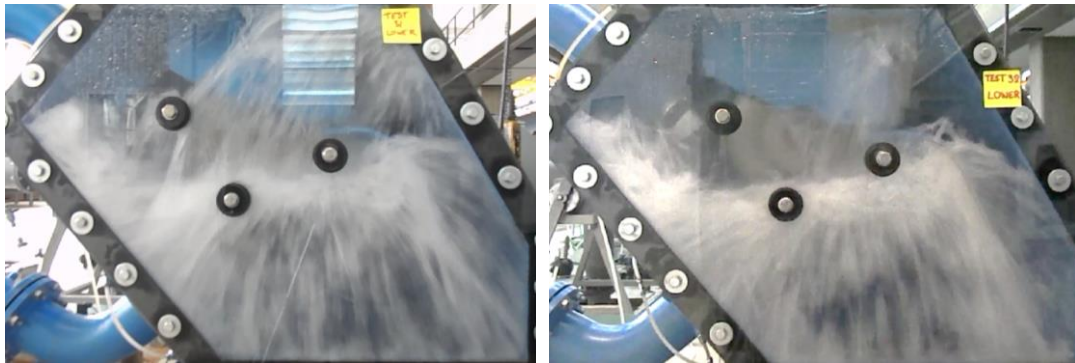


Fig. 5-22 Comparing snapshots taken during experimental testing of D (left) and E (right)

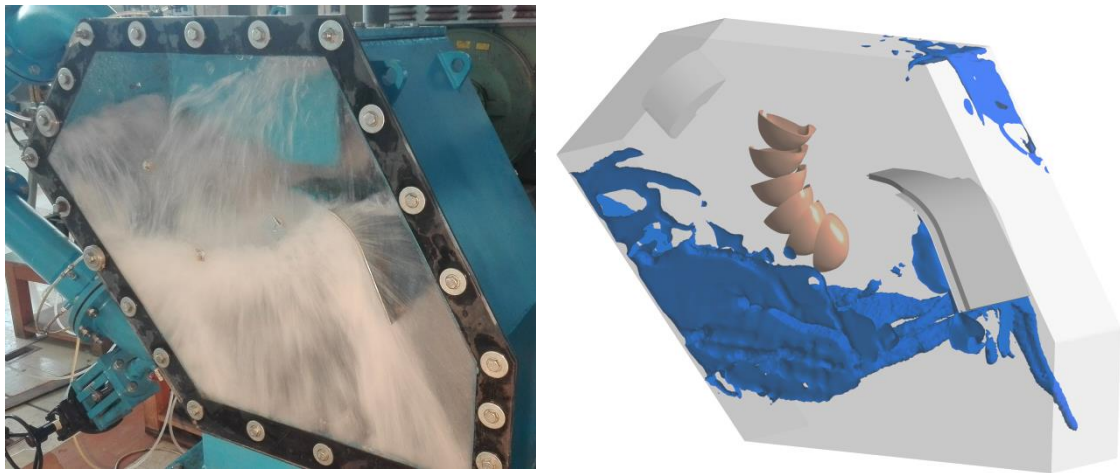


Fig. 5-23 Comparing CFD and experiment with the BAF and SP for lower jet operation

A small portion of flow still enters the roof of the casing, indicated by the red arrow. Therefore, the clearance between the baffle and the runner must be as small as possible to minimise the leakage through the clearance, which is created by the suction in the narrow gap which in turn leads to windage losses.

Furthermore, there was a second opportunity during later testing to take some additional photographs with a camera with a much faster shutter speed, this

5.2.4 The Role of the Side Shroud

Looking at the photographs in Fig. 5-24 and Fig. 5-25 of upper and lower jet at low flow rates, there is more splashing around the upper jet in the left hand corner of the casing, which is not evident around the lower jet. Arguably, the shape of the casing walls has a greater impact on the upper jet where they are in closer proximity to the runner, the centrifugal force causes the water to be forced out of the bucket in an anticlockwise direction impacting on the left and top walls of the casing, before being recirculated and impacting on the jet and the runner.

From observation, the effect of the addition of the side shroud is clear, Fig. 5-24 demonstrates to some extent why the side shrouds have a negative effect on performance, as water from the upper jet hits the shroud it is directed along the front case and follows the course of the casing, before hitting the jet housing from the side, the water causes splashing and gathers in the upper left hand side causing a choking of the flow and subsequent losses arise.

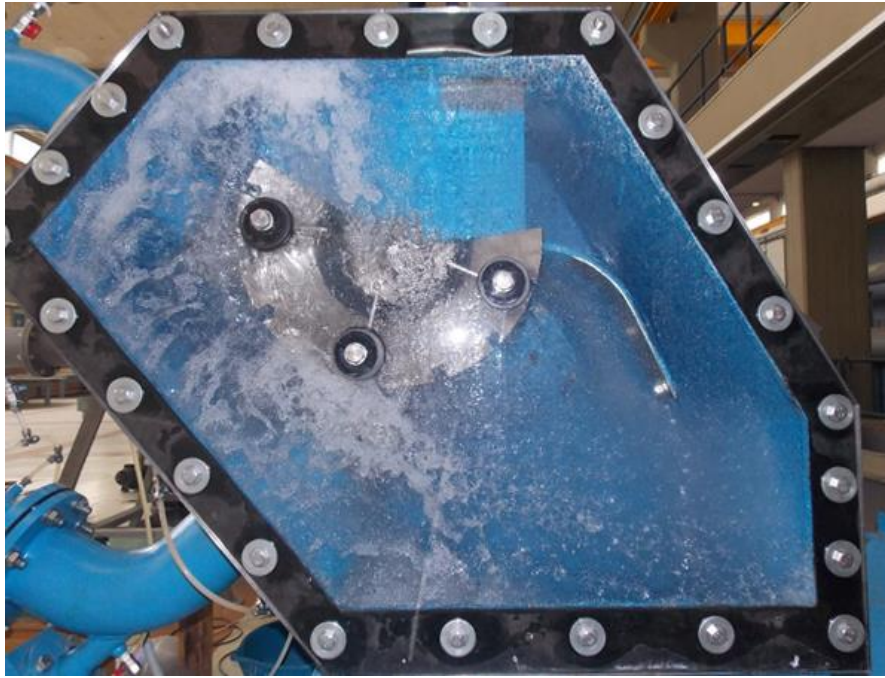


Fig. 5-24 Experimental photograph of test F at BEP for upper jet operation

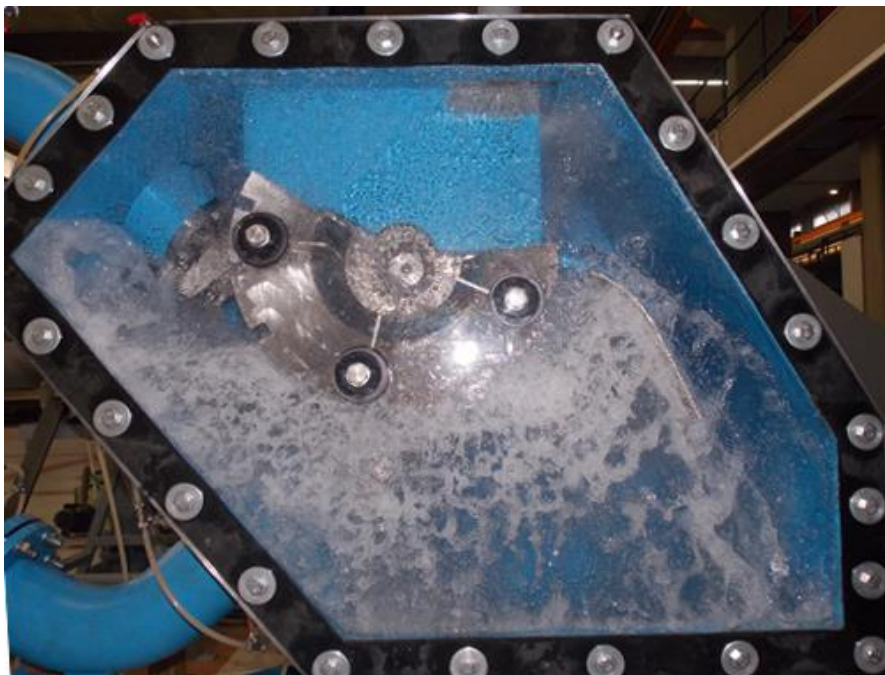


Fig. 5-25 Experimental photograph of test F at BEP for lower jet operation

5.2.5 Summary of Phase 1 testing

The Phase 1 testing results demonstrate that in some setups the path of the water leaving the runner can be diverted to have a positive effect on efficiency, test E, and in other cases a negative effect, test F, G and H. The most efficient arrangement of internal baffles was found to be those used in test E. The overall contribution of the Bolt on Baffle and Sealing Plates in test E saw a modest improvement in efficiency of 0.52% in the best case.

In conclusion, it has been determined that the Side Shrouds negatively impact the performance of the turbine in the test operating region, further analysis would be required in order to determine at which point the side shrouds become beneficial, if at all. Since no prior data is available one has to assume that their addition may have been for a very specific project, where perhaps the turbine was operating at a higher specific speed than optimum and the SS was included to minimise interference with the lower jet. Despite lack of evidence it is however recommended that they not be included in any future Pelton installations, leading to a substantial cost saving, since they are a complex component to manufacture.

5.3 Phase 2 - Pelton Width Testing

5.3.1 Technical Program

A number of various components were constructed and were used in the previously installed test rig in the NTUA laboratory, these include 4 panels and a number of spacers in order to reduce the width of the side walls of the panels from the original width of 520 mm to 420mm, 350 mm and 240 mm.

5.3.2 Program of Tests

An outline of the testing programme carried out is given in Table 5-7 below.

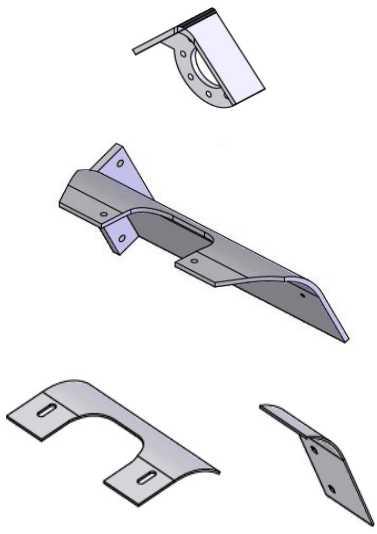
Test #	Width	Components	
Test J	420 mm	+JS1 + BAF + SP	
Test K	350 mm		
Test L	240 mm		

Table 5-7 Experimental width testing program indicating components

The spacers and panels as set up for the 240 mm casing are shown in Fig. 5-26.

The measurements for tests J - L were made over a series of 16 points each for upper, lower and twin jet operation, as defined in Fig. 5-27. Control points are taken at the beginning, between and after each test in the order of upper, lower and twin jet respectively. There are a total of 6 control points per test at $n_{II} = 39$, $Q_{IIk} = 0.15$.

A total of 180 readings were obtained for each operating point, though the first 60 are disregarded, this is in order to ensure steady state conditions and minimise the random uncertainties, while care has also been taken to remove any outliers.

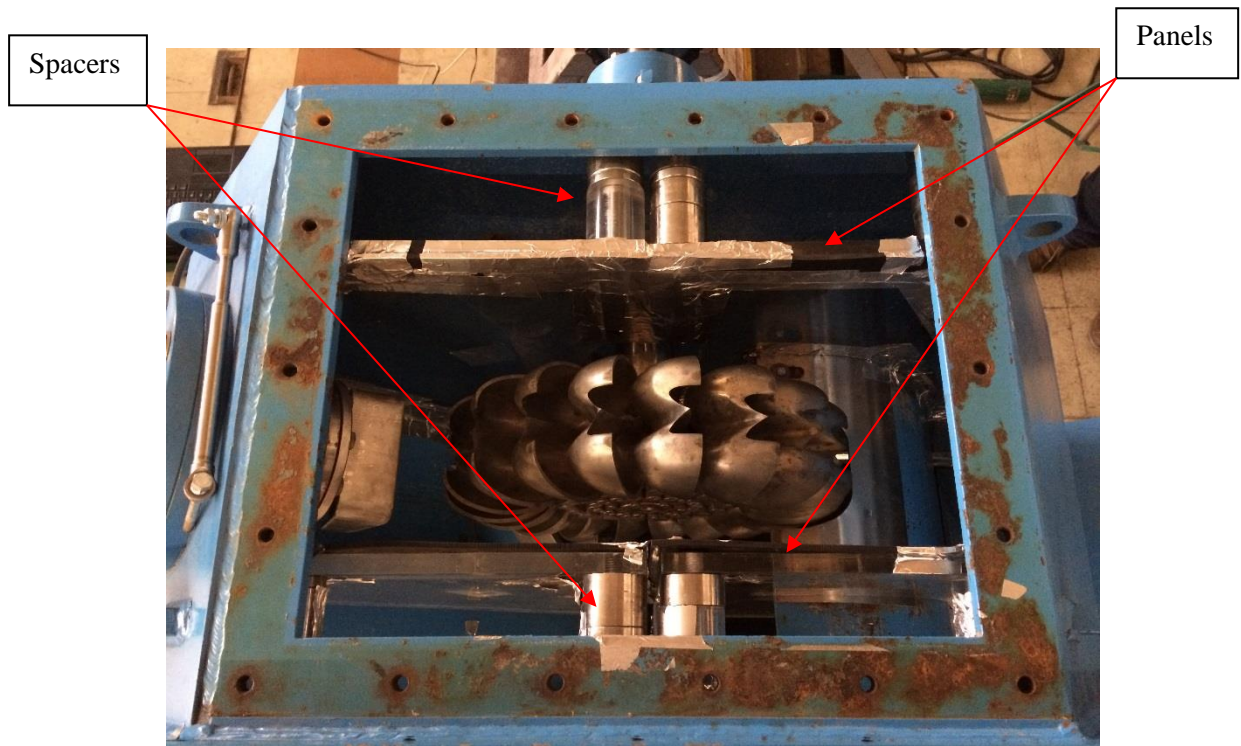


Fig. 5-26 Test rig with components assembled for 240 mm width testing

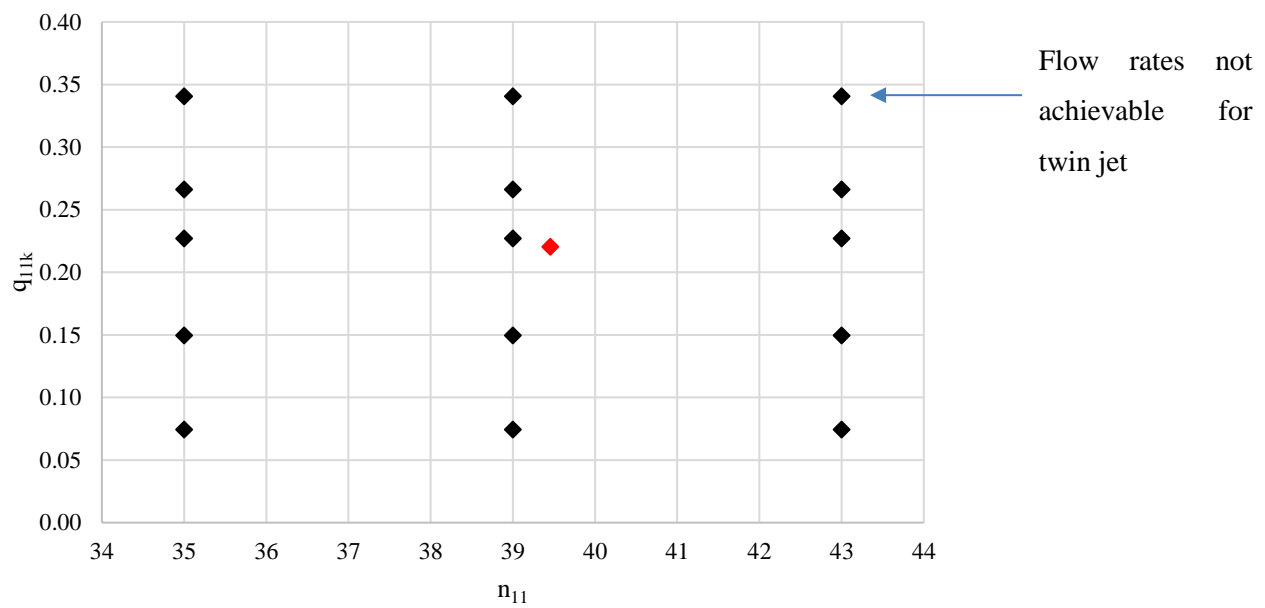


Fig. 5-27 Test points under consideration with BEP indicated as the red diamond

The spear position associated with the required flow rate is listed in Table 5-8 below.

	Nozzle Opening [mm]		
	Upper	Lower	Both
0.075	4.25	4.25	4.25
0.15	8.75	8.75	8.75
0.22	13.5	13.5	13.5
0.227	14	14	14
0.266	17.25	17.25	17.25
0.342	26.25	26.25	N/A

Table 5-8 Spear position and associated flow rates

5.3.3 Phase 2 Results Analysis and Discussion

The graphs of test J (420 mm casing) for upper, lower and twin jet are displayed in Fig. 5-28, Fig. 5-29 and Fig. 5-30 respectively. Comparing the graphs for upper and lower jet the trend lines for constant n_{11} match closely to those presented in the previous section.

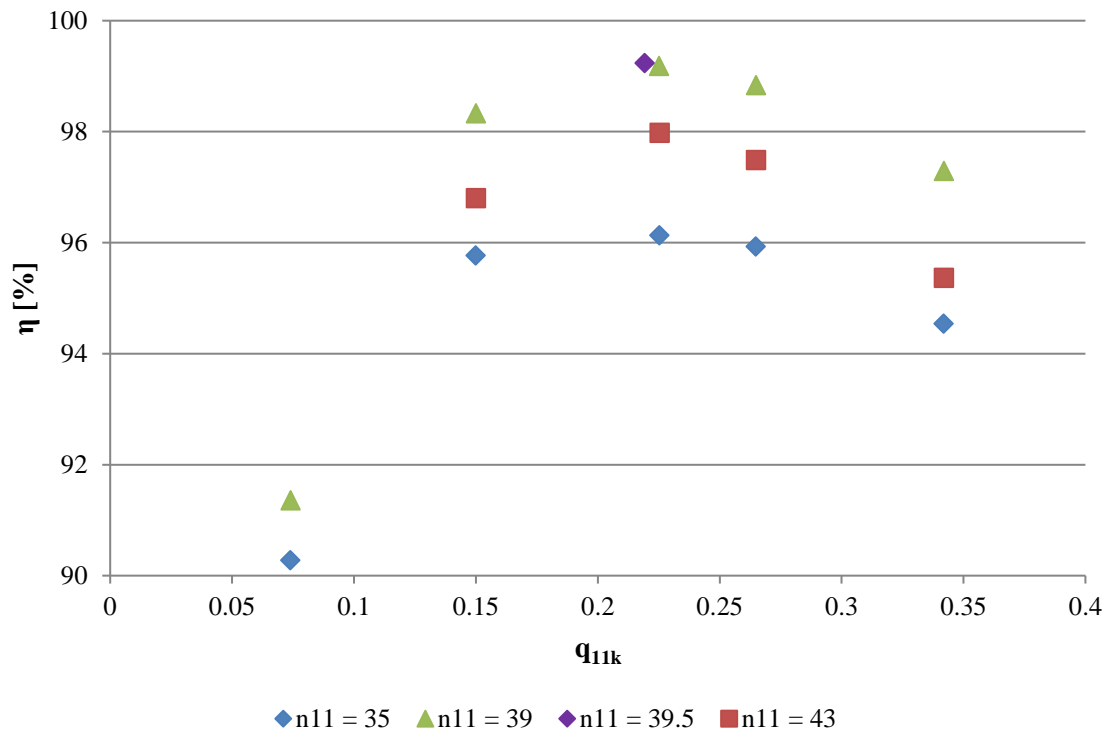


Fig. 5-28 Experimental Test J upper jet operation

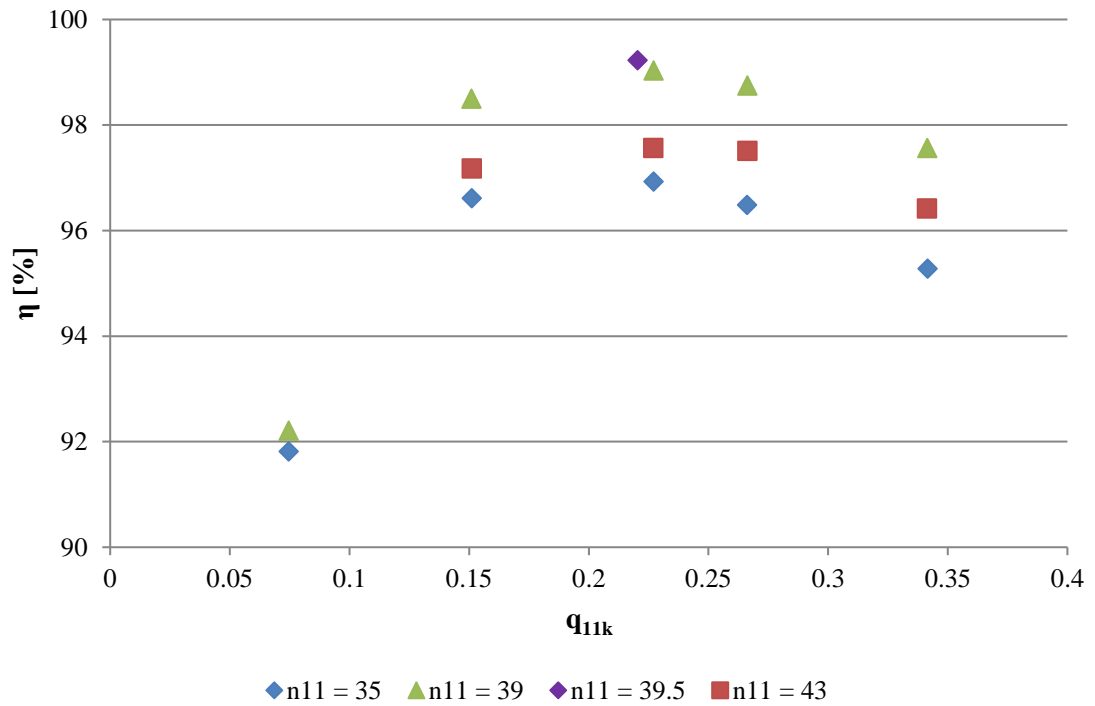


Fig. 5-29 Experimental Test J lower jet operation

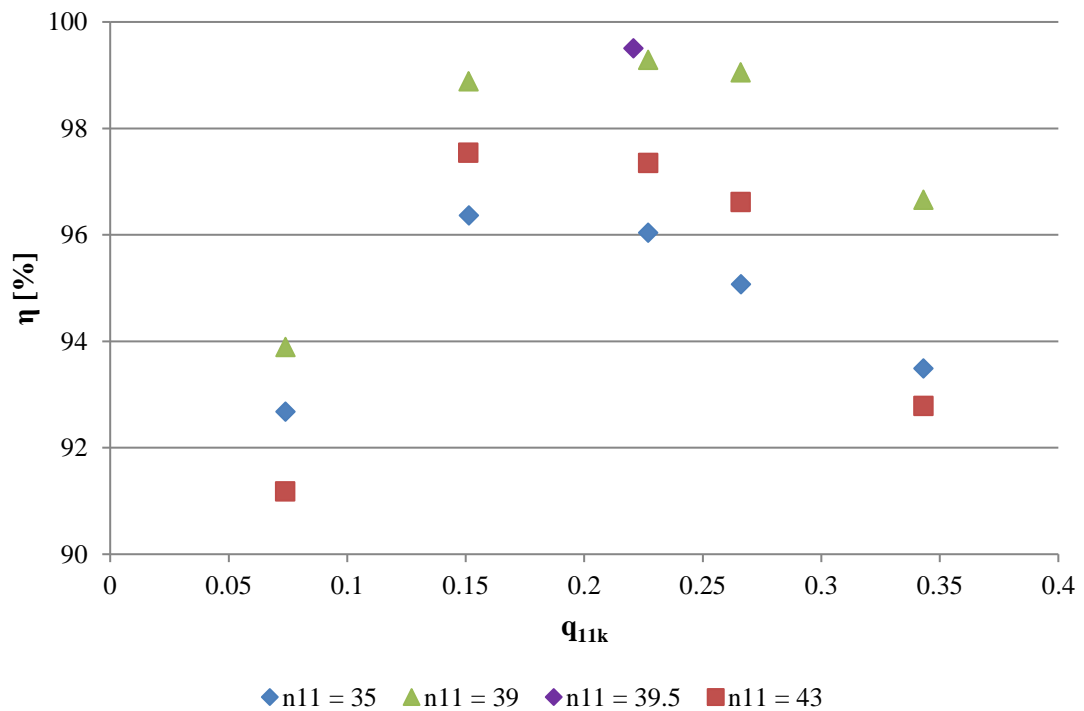


Fig. 5-30 Experimental Test J twin jet operation

As in previous analysis for twin jet operation a regular trend can be observed across all case width tests, namely that for speeds close to the BEP, i.e. $n_{11} = 39$ rpm, the efficiency remains

consistently higher across all flow rates. At the extreme flows away from the BEP, i.e. $Q_{11k} = 0.075$ and $Q_{11k} = 0.35$, $n_{11} = 43$ rpm is the lowest efficiency with $n_{11} = 35$ rpm being slightly higher, however for $Q_{11k} = 0.15$, 0.22 and 0.27 , $n_{11} = 43$ rpm produces a higher efficiency.

Likewise, for upper and lower jet operation, $n_{11} = 39$ rpm remains the highest efficiency across all tests, however $n_{11} = 43$ rpm is the lowest efficiency at the smallest flow rate of $Q_{11k} = 0.075$, but as flow rate increases $n_{11} = 43$ rpm overtakes the efficiency of $n_{11} = 35$ rpm and remains higher across all subsequent flow rates.

The graphs for $n_{11} = 39$, close to the design speed, comparing the measured efficiency for the different casing width for upper, lower and twin jet are shown in Fig. 5-31, Fig. 5-32 and Fig. 5-33 respectively. The results for the 520 mm casing tests are taken from test E, outlined in 0.

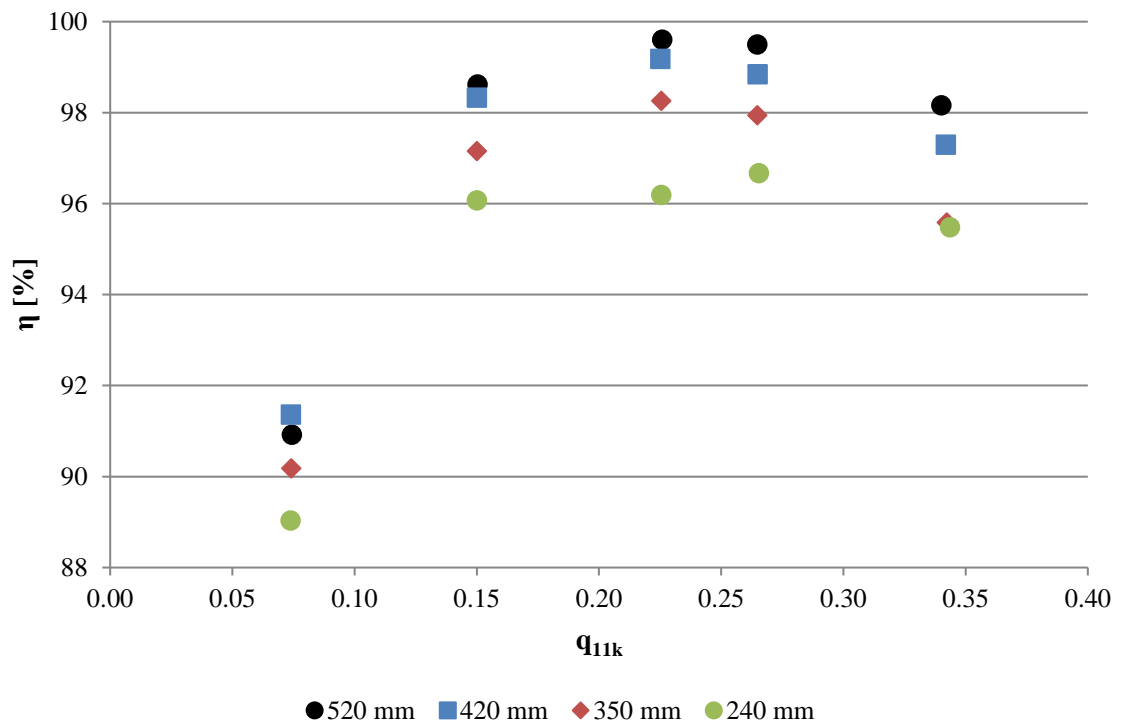


Fig. 5-31 Experimental results comparing casing widths at $n_{11} = 39$ for upper jet operation

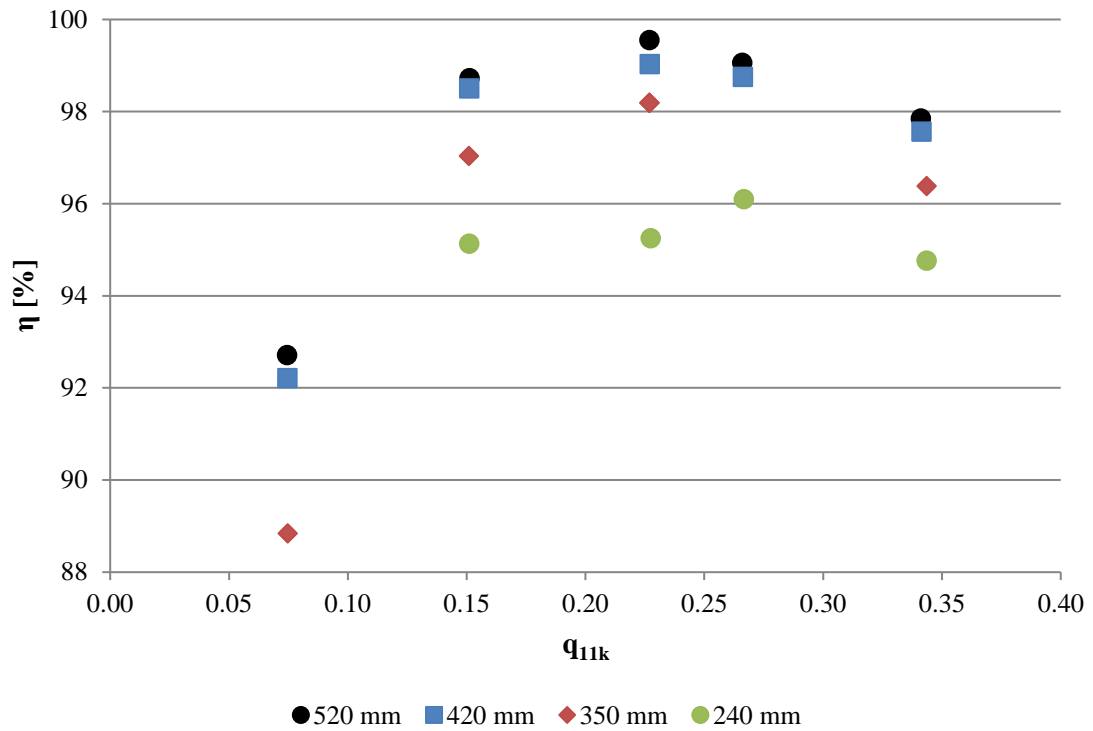


Fig. 5-32 Experimental results comparing casing widths at $n_{11} = 39$ for lower jet operation

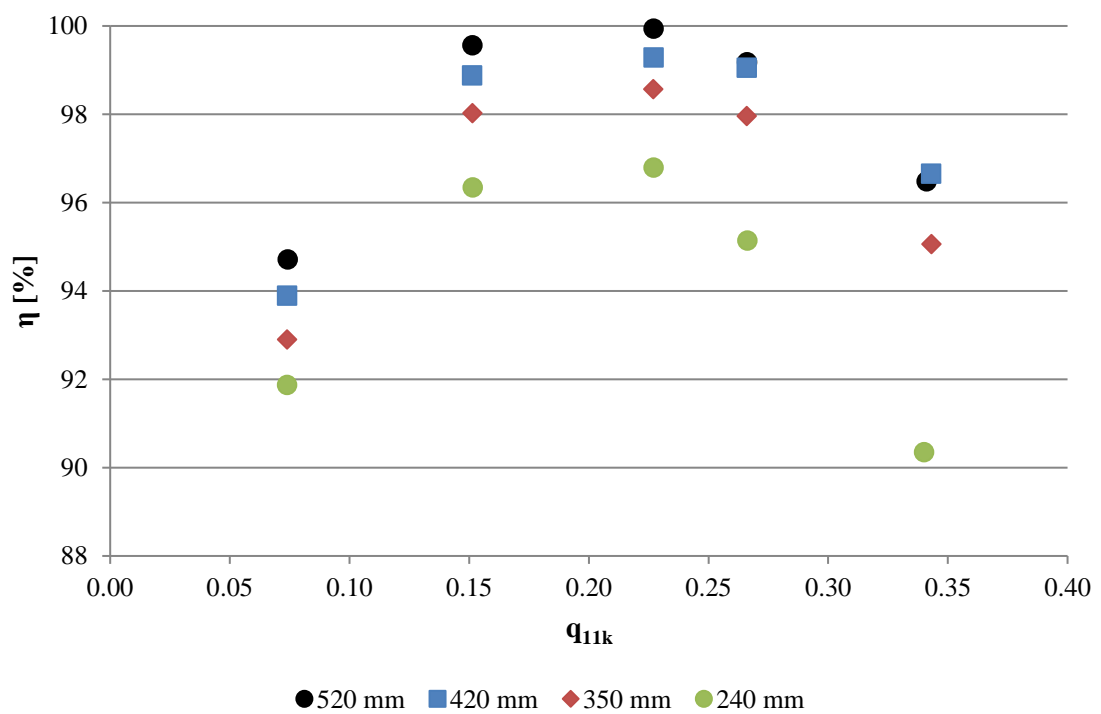


Fig. 5-33 Experimental results comparing casing widths at $n_{11} = 39$ for twin jet operation

The percentage decrease from 420 mm to 350 mm, 350 mm to 240 mm and 420 mm to 240 mm for the BEP upper, lower and twin jet is shown in Table 5-9. It is apparent that a bigger decrease

is experienced by the lower jet, though this may be spurious as demonstrated by the possible anomalous result for upper jet at 240 mm as shown in Fig. 5-34.

	420 to 350	350 to 240	420 to 240
Upper Jet	0.93%	1.06%	1.99%
Lower Jet	0.97%	1.62%	2.59%
Twin Jet	0.73%	1.56%	2.29%

Table 5-9 Percentage decrease in efficiency across test cases

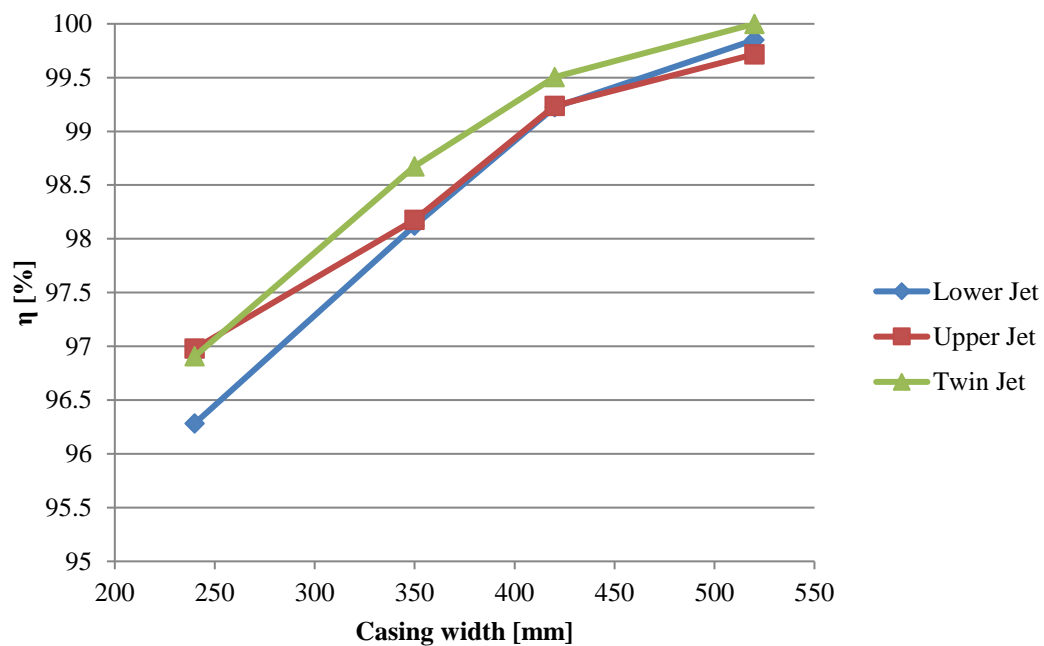


Fig. 5-34 Effect of changing casing width on efficiency at the BEP

It is anticipated that the efficiency at 240 mm for the upper jet will likely be similar to the lower jet and this is likely due to experimental error (a small amount of flow was observed to leak through the panel, which could affect results).

The general trend of decreasing efficiency with decreasing width is consistent with the theory, however the trend lines in Fig. 5-34 appear to be reaching a peak efficiency towards the 520 mm width and one might expect that on further widening of the casing the negative effect on efficiency will be minimised.

5.3.4 Summary of Phase 2 testing

The Phase 2 testing was carried out with the same internal baffles as used in test E, with spacers and side panels used to reduce the width of the casing. The results demonstrate a positive linear relationship between increasing casing width and efficiency, which correlates to theory.

From the current casing width of 520 mm to the narrowest testing, 240 mm, there was reduction of 3.3% in efficiency. Standard guidelines, as documented in the literature review, suggest a casing width based on this bucket and jet diameter of anything between 320 mm and 530 mm, which would correspond based on the twin jet results to 98.5% and 100.5% efficiency.

5.4 Summary of Experimental Testing

The experimental results of the Phase 1 and Phase 2 Pelton casing tests are compared and discussed in this chapter looking at the effectiveness of various casing baffle inserts and reducing casing width respectively.

On the whole, the overall influence of adding the baffles and shrouds is $\approx 0.5\%$, which is much smaller than the more significant decrease in efficiency of $\approx 3\%$ by halving the casing width.

Quantifying the exact role the casing plays is difficult. Even in the highest efficiency recorded the casing losses will not be negligible as shown in Fig. 5-6, Fig. 5-7 and Fig. 5-8 which compares the results of testing at the BEP of the turbine. Moreover, testing was carried out across a range of speeds and flows and therefore in these instances there is a more appreciable runner loss, hence at these points the differences between the different casings tested is much smaller, as demonstrated in Fig. 5-10, Fig. 5-11 and Fig. 5-12.

In general, all projects should include the jet shrouds (as in the case of test B, C) and the BAF (as in the case of test E) as together these resulted in the most efficient setup.

The Phase 2 testing indicated that the overall size of the casing is a much more important consideration and of course in the ideal scenario there would be no casing. It is recommended that the casing be made as large as possible, however plant size restrictions need to be taken into account. In the case of overhung bearing arrangement (as the test rig at NTUA), where there is only one bearing on the generator side it may be feasible to have different casing widths on either side of the runner, i.e. the generator side has a standard casing width and the opposite side is made wider. The current test rig is ≈ 4.4 bucket widths (≈ 17 jet diameters), which is slightly larger than the recommendations to be found in the literature; however it should be noted that these guidelines tend to be for casings where there is a split above the shaft axis and a very small enclosure sits around the upper half of the runner.

While it is important to minimise losses where possible, the positive effect of the addition of casing inserts must be weighed against the overall cost of manufacturing any additional baffles. Size restrictions may also be an important factor in smaller plants, assuming the same runner size one may conclude that a narrower casing with internal inserts would have the same efficiency as a wider casing without casing inserts, therefore Gilkes could offer two products based on different plant criteria without compromising the quoted efficiency. Wider casing also poses additional cost implications as it may not be possible to have an overhung Pelton as is the case on the NTUA test rig (i.e. only one bearing on the generator side). Different bearing arrangements will in turn, create a demand for a new frame size of generator. These changes would have significant impacts on the costs of the generator and overall cost of the plant.

Without further width testing it is not yet possible to ascertain the exact loss in efficiency due to casing and at what width the casing no longer has an influence, though it is anticipated it is beyond the current width and of course will vary with flow rate. From the flow observations at lower flow rates, the water appears to have little to no interference with the injector or backslash onto the runner, in effect mimicking a wider casing.

Another consideration is the $\approx 0.5\%$ difference between the upper and lower injector. Without further analysis of the injectors and the jet-runner interaction it is not yet possible at this point in time to determine whether this is more likely losses due to these phenomena or as a direct result of the casing design.

As a result, in Chapter 6, further 3D CFD analysis of the injector is carried out, including both the spear and nozzle and the guide vanes and pipework bend. The jet velocity profiles are then coupled to a 2-bucket runner simulation with very fine mesh (a further mesh independence study will be carried out) and used as an inlet boundary condition, these simulations enable a reasonable quantification of injector and runner losses. In Chapter 7 the mechanical losses of the test rig are estimated and together with the 3D injector simulations the losses due to the casing can be estimated by subtracting from the experimental test results.

6 Analysis of Flow through the Injectors

This motive for this chapter is twofold; first it is the result of a collaboration with researchers from Lancaster University and NTUA, the outcome of which is three conference papers and one journal paper and therefore represents a good portion of study time. Secondly, the lack of numerical or experimental data, which quantifies the energy loss as a result of the casing necessitates investigations into other Pelton turbine components in order to ascertain a reasonable estimate of casing loss by eliminating all of the other sources of losses.

Recent developments in CFD codes have meant that simulations of 3D Pelton injectors show good agreement with experimental data giving confidence in the reliability of the numerical results produced when simulating the complex phenomena as detailed in the literature review in section 2.6.1. There are some studies available where a selection of injector designs are modelled and compared using CFD or using a visual analysis. However, there is a lack of publications describing a thorough investigation of basic injector design parameters together with the importance they have on the performance of an injector. More recently, researchers from Lancaster University have applied two commercial CFD codes; ANSYS CFX and ANSYS Fluent to the parametric optimisation of a Pelton turbine injector using a 2D axisymmetric case [96]. The 2D CFD analysis has shown that injectors with noticeably steeper nozzle and spear angles, 110° and 70° respectively, attain a higher efficiency than the industry standard 80° and 55° . Since then this has been verified with experimental results [97], [109]. However, the response surfaces suggested that the optimum nozzle and spear angles could be even steeper. That is why, an additional case, a third design, Novel 2, with even steeper angles 150° and 90° is also investigated in this chapter. As these initial studies forms the basis of the work presented in this chapter a detailed explanation and analysis will be covered in the following section. Furthermore, this chapter presents an improved method of applying CFD to develop and improve the design of an impulse turbine injector further and offering some insight into the experimental results by simulating the interaction with the runner.

These three injector designs were manufactured for testing on the Pelton test rig at the Laboratory for Hydraulic Machines, NTUA.

6.1 Numerical Investigation

6.1.1 2D Axisymmetric Analysis & Optimisation

The influence of a number of geometric parameters were investigated using a Design of Experiments (DOE) study and in total 120 cases were simulated [98]. The most important design parameters according to the literature [5] have been identified as the needle tip angle, B,

nozzle angle, C, and needle width, D, outlined in Fig. 6-1, and as result it was decided that these will be the geometric parameters forming this study.

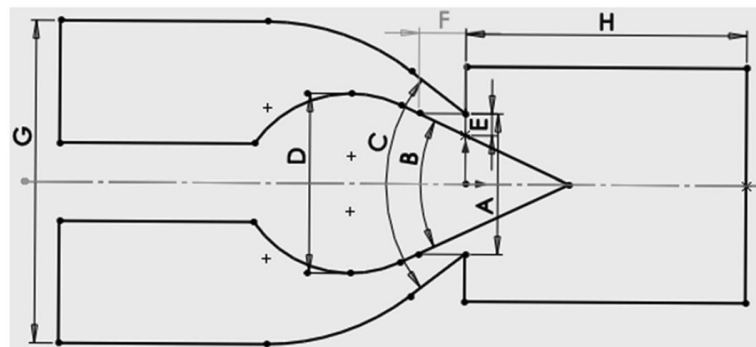


Fig. 6-1 Two dimensional injector geometry showing fixed and variable operational and geometric parameters [98]

The original DOE study explored nozzle angles ranging from $70^\circ - 110^\circ$ and spear angles of $30^\circ - 70^\circ$. The results indicated that the losses can be reduced with larger spear travel values since the restriction will be reduced [96]. Contrastingly, as the pressure head and spear width is increased the losses will be higher. More importantly, it highlights the importance of selecting nozzle and spear angles, which reduce the losses at lower flow rates, where the biggest resource for improvement lies. Moreover, the nozzle angle and spear angle must be analysed simultaneously as they are related to one another. It was anticipated that different spear travels will have an influence on optimum angles, however, it is not the spear travel but the flow rate which is important, and therefore the combinations of nozzle angles and spear angles were analysed over a range of four corresponding flow rates, two of which are presented in Fig. 6-2.

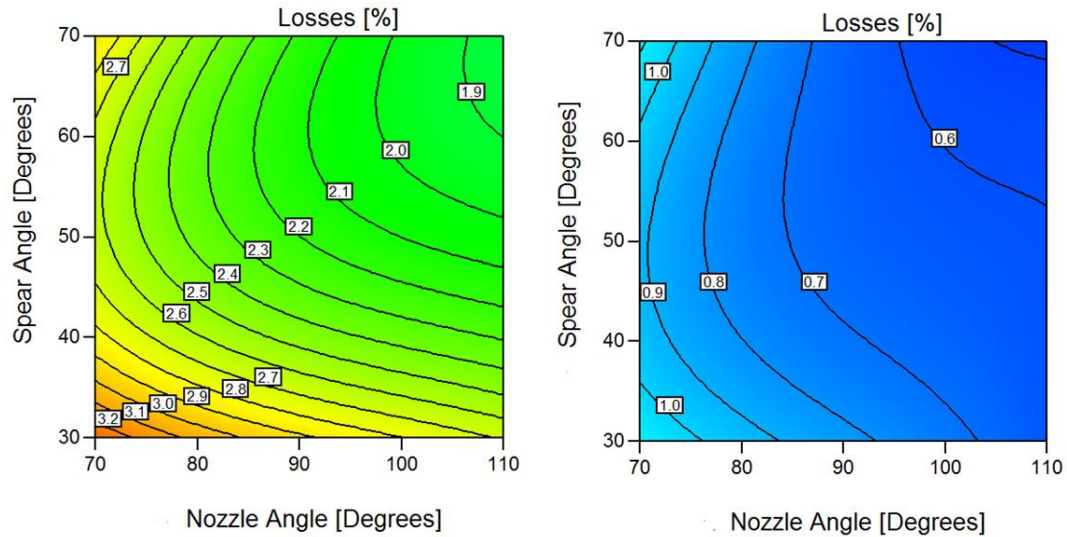


Fig. 6-2 Injector Loss contours for Nozzle and Spear Angles at $Q = 20 \text{ kg/s}$ (left) and 40 kg/s (right) [96].

In all four cases the lowest losses can be identified in the top right hand corner of Fig. 4, where the angles are the steepest combination studied, i.e. 110° for the nozzle and 70° for the needle tip. The research concluded that a potential 0.5% reduction in losses is possible incorporating the Novel 1 design (110° and 70° angles) instead of the Gilkes ‘Standard’ design, with angles 80° for the nozzle and 55° for the needle tip, which are close to the modern industry standard of 90° and 50° angles most frequently quoted in the available literature sources.

6.1.2 3D Analysis

The first two injector designs under analysis are the Standard design, and the Novel 1 design based on the outcome of the 2D CFD optimisation study defined in 6.1. The response surfaces in this study suggested that the optimum nozzle and spear angles may be even steeper and therefore an additional, third design, Novel 2, with even steeper angles of 150° and 90° also forms part of the study. The details of the injectors used in this study are tabulated in Table 6-1.

	Notation	Nozzle angle [°]	Spear tip angle [°]
Standard	80/55	80	55
Novel 1	110/70	110	70
Novel 2	150/90	150	90

Table 6-1 Details of the injector configurations

The 3D domain is more realistic than used in the previous 2D analysis and includes a single 60° pipework bend, the needle rod and three needle rod holding vanes, as shown in Fig. 6-3. In this

way, any differences in the design can be more fully demonstrated and the effects of the secondary velocities due to the upstream effects can be analysed. The nozzle opening diameter, A , and the injector diameter G , shown in Fig. 6-1, were fixed at 36 mm and 82.5 mm, respectively. The needle travel was therefore adjusted for the three injectors to correspond to the Best Efficiency Point flow rate condition of the tested Pelton turbine. The primary focus of this study is the injector losses and to identify where most energy is dissipated as the water escapes the injector into the air domain with atmospheric pressure. Equation (6.1) was used to calculate the losses that are accumulated between the inlet plane and any selected downstream reference plane.

$$L_{ref} = \left(1 - \frac{P_{ref}}{P_{in}}\right) \cdot 100\% \quad (6.1)$$

Where L_{ref} is the losses in the reference region, P_{in} is the power at the inlet plane and P_{ref} is the power at the reference plane.

The fluid power, P_{ref} , at any selected reference plane is calculated using equation (6.2).

$$P_{ref} = \int_A \left(p + \frac{\rho u^2}{2}\right) \cdot u \cdot dA = \sum_1^n p_i \cdot u_i \cdot A_i + \sum_1^n \frac{\rho u_i^2}{2} \cdot u_i \cdot A_i \quad (6.2)$$

The terms and variables for equation (6.2) are listed in Table 6-2. The two terms on the right side represent the fluid power due to static pressure (volume displacement energy) and to kinetic energy of the fluid, respectively. The injector hydraulic efficiency is calculated at a number of planes from the nozzle exit, which have set distances related to the nozzle diameter as shown in Fig. 6-3. The corresponding coordinate system is also indicated in Fig. 6-3, with gravity acting in the x direction.

Symbol	Name	Unit
p_i	Static (gauge) pressure	Pa
ρ_i	Fluid density	kg/m ³
u_i	Normal fluid velocity in each cell	m/s
i	Mesh cell	-
A	Area within the jet cross-section	m ²
n	Number of cells in A	-

Table 6-2 Units used in the equation (6.2)

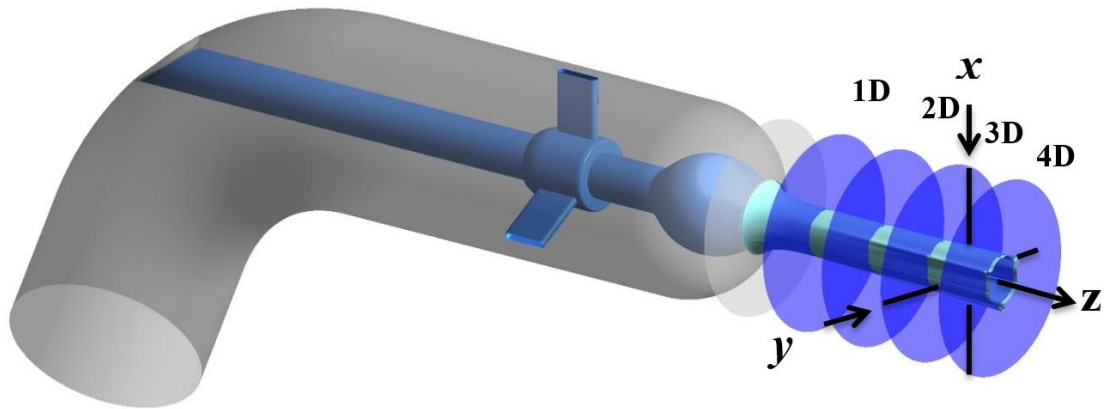


Fig. 6-3 3D injector simulation showing the planes used in the analysis

Based on the available literature, all CFD analyses reported herein were performed using the commercial ANSYS® FLUENT® package where all free surface flows are treated using the Volume of Fluid (VOF) method simulating two phases: water and air. The pressure and velocity were fully coupled using the pressure based Coupled scheme and second-order upwind spatial discretisation was adopted. Table 6-3 outlines the boundary condition types used in this study. The simulations were considered as steady state and a convergence target of an rms of 1×10^{-6} was chosen for the residuals of the momentum equations. For the turbulence closure, all CFD analyses used Menter's $k-\omega$ Shear Stress Transport (SST) model [90]. This choice was a result of an extensive investigation into different turbulence settings, found in [96], which concluded that $k-\omega$ SST was the most appropriate for free surface impulse turbine simulations and appear to deliver acceptable results.

Location	Boundary	FLUENT details	
Injector inlet	Inlet	Mass and momentum	Gauge pressure
		Turbulence option	$k-\omega$ SST
		Turbulence intensity	5%
		Turbulence viscosity ratio	10
Nozzle and spear surfaces	Wall	Mass and momentum	No slip wall
		Wall roughness	No slip condition
Injector outlet	Opening	Mass and momentum	Pressure outlet
		Turbulence option	$k-\omega$ SST
		Turbulence intensity	5%
		Turbulence viscosity ratio	10

Table 6-3 Details of the boundary conditions for injector simulations

The injectors were meshed using the ANSYS® Mesher tool and are of hybrid type consisting of a structured zone in the branch pipe and tetrahedral cells between the structured zone and far field boundaries, containing approximately 9 million elements per grid. The domain geometry was divided into blocks to assist the meshing process. Mesh refinement was employed in the centreline and outer surface of the jet; this was achieved by using the FLUENT mesh adaption algorithm, which refines any cells within the free surface. Inflation layers were placed on the spear and nozzle walls and the minimum wall spacing was such that the maximum values of the non-dimensionalised minimum wall distance y^+ are well below 1 for all three injector meshes. The surface mesh around the injector opening for the Standard design is shown in Fig. 6-4.

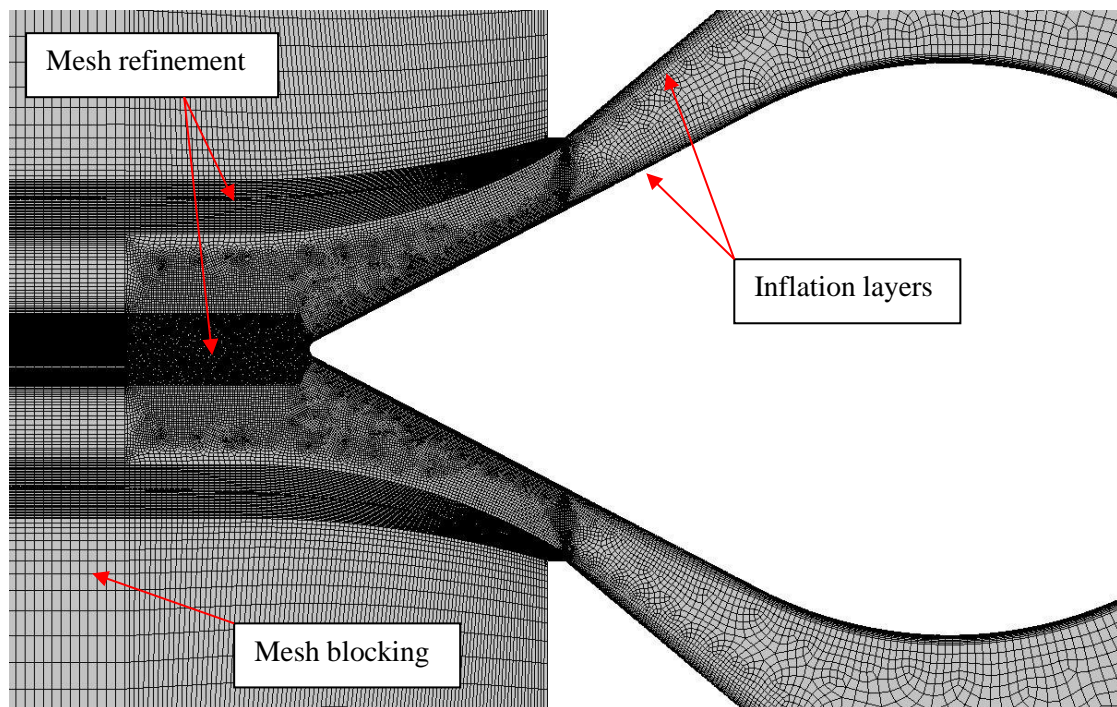


Fig. 6-4 3D mesh for Standard injector design showing spear and nozzle around the exit

All these simulations were performed at the best efficiency point conditions of the tested Pelton turbine operating at a test head of 60 m and the BEP flowrate, therefore the spear travel required to provide the flow rate of is shown in Table 6-4.

	Notation	Spear Travel [mm]
Standard	80/55	14.50
Novel 1	110/70	13.25
Novel 2	150/90	11.75

Table 6-4 Details of injector spear travel

The injector losses obtained from the three simulations are presented in Fig. 6-5 for various distances from the nozzle exit, indicating that Novel 2 design is 0.4% more efficient than the Novel 1, which is more efficient than the Standard design by some 0.18% at a distance of $z/D = 3$.

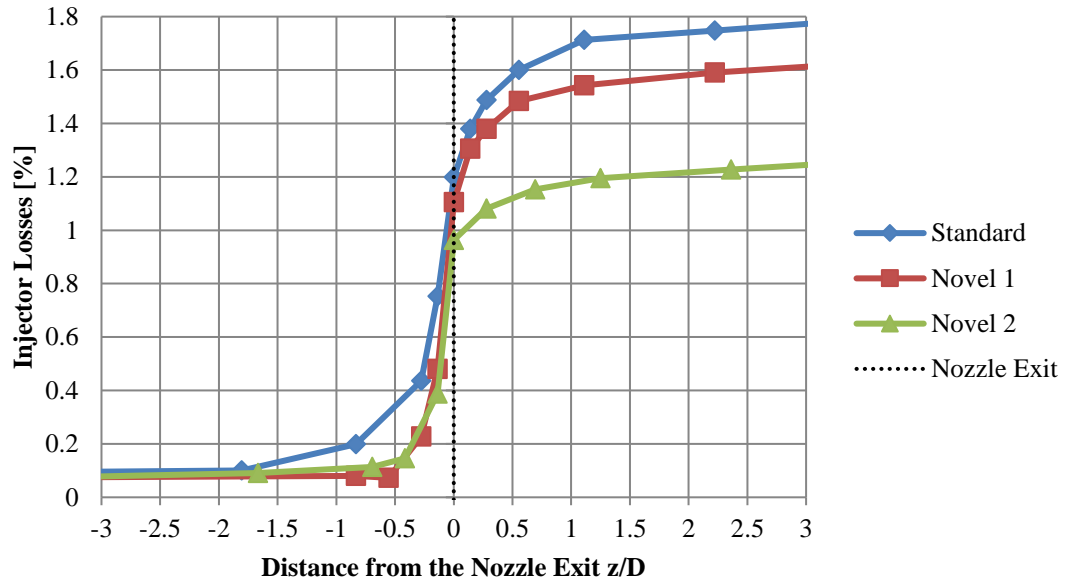


Fig. 6-5 3D Injector losses at different planes from nozzle exit

As the flow travels through the injector the hydraulic power at the aforementioned reference planes can be expressed as the sum of two components. The first is the power due to static pressure component and the second is the dynamic pressure (kinetic energy) component. Fig. 6-6 provides a graph of the power as a result of the two components at various distances from the nozzle exit. It can be observed that the fluid static pressure is progressively converted to dynamic pressure, and this mechanism lasts up to about $1.5 z/D$ downstream from the nozzle exit.

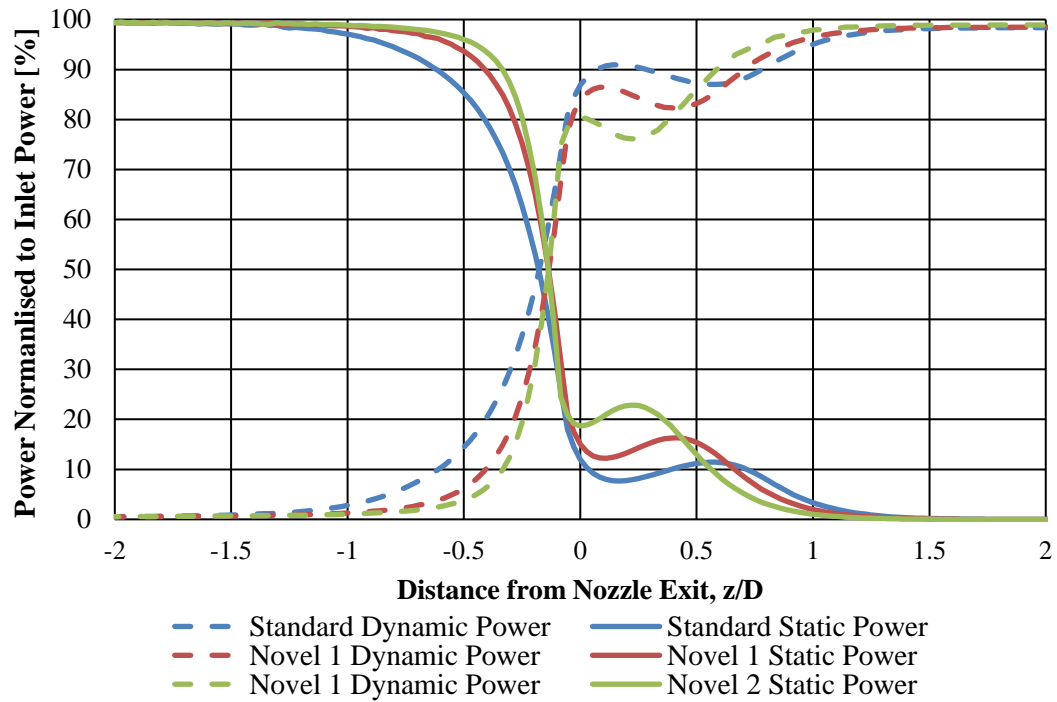


Fig. 6-6 Fluid power from conversion of static to dynamic pressure components for the three designs

It is evident from Fig. 6-6 that the conversion from static to dynamic power starts earlier in the Standard injector, at about $-1.5 z/D$, compared to about $-1 z/D$ in the Novel designs. Consequently, the flow in this region must be travelling at an increased velocity in the Standard injector, and hence the friction losses are higher. Conversely, the conversion occurs much more rapidly in the Novel 2 case, since the distance travelled between the widest point of the needle and the nozzle opening is shortest due to the steeper angle. Moreover, it can also be concluded that in the region right after the nozzle exit ($0 < z/D < 0.5$) there is a fluctuation in static and dynamic pressure components of fluid power. This is due to the conversion is happening backward and forward, as shown in Fig. 6-7 and Fig. 6-8. Firstly, the static pressure is converted into dynamic pressure as soon as the cross-section begins reducing and consequently there is still acceleration in the flow velocity. Then, towards the nozzle tip, the annular flow with radial velocity components converge at an angle causing some of the dynamic pressure to be converted back into static pressure, which is more pronounced in the Standard case. Due to the steeper convergence angle for the Novel designs the jet will contract faster, however there is also a greater flow separation at the needle tip, however this has a positive effect of shortening the re-laminarisation length. Finally, this static pressure is converted back into kinetic energy, leaving a free jet with zero manometric pressure travelling away from the injector at high velocity.

The three injector designs described were manufactured by Gilkes for experimental testing using the Pelton test rig at the Laboratory for Hydraulic Machines, National Technical University of Athens (NTUA), the details and results of this will be detailed in the following section 6.2.

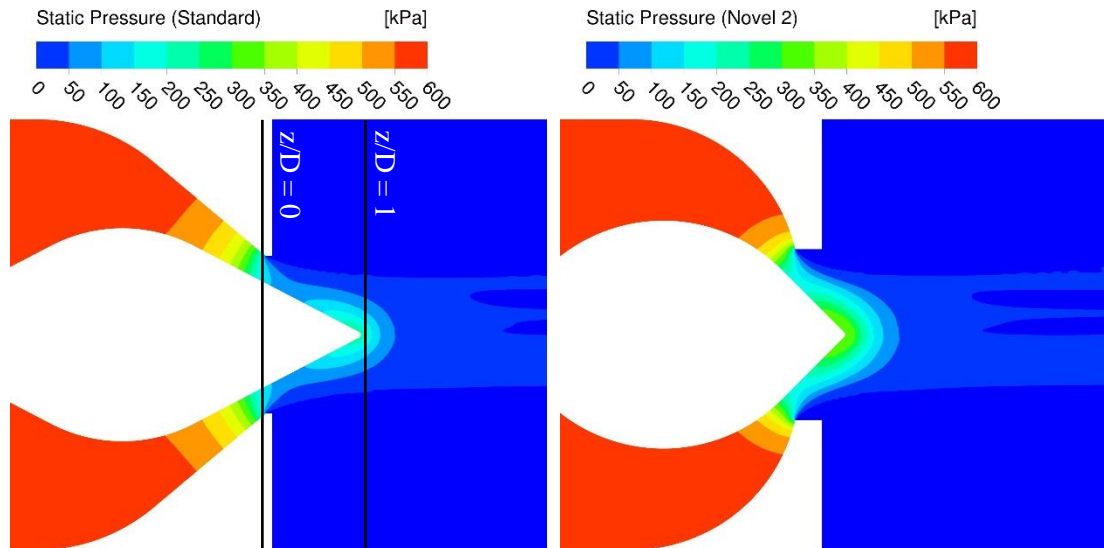


Fig. 6-7 Static pressure contours for Standard and Novel 2 designs

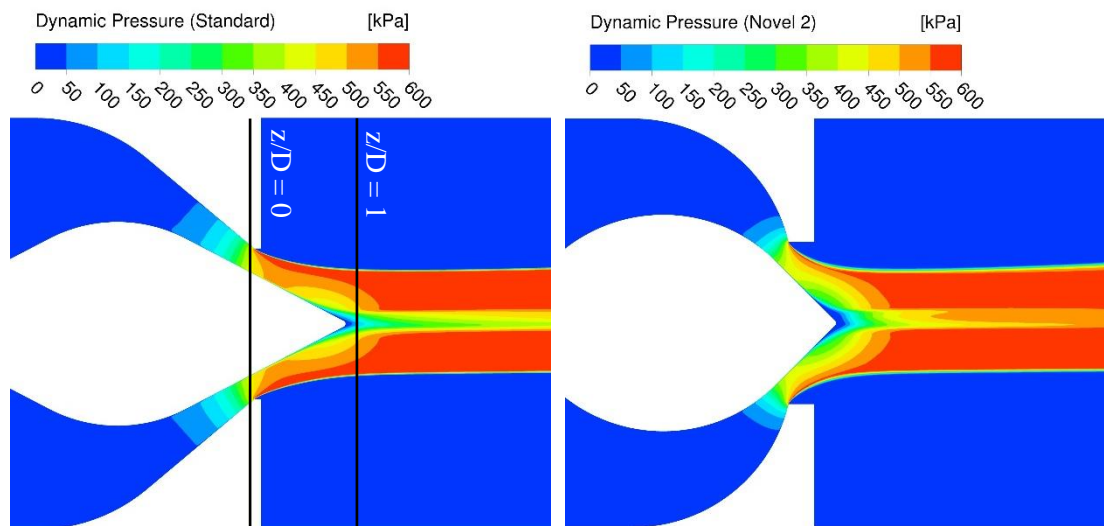


Fig. 6-8 Dynamic pressure contours for Standard and Novel 2 designs.

6.2 Experimental Investigation

The spears and nozzles used in these tests are shown in Fig. 6-9 and Fig. 6-10.

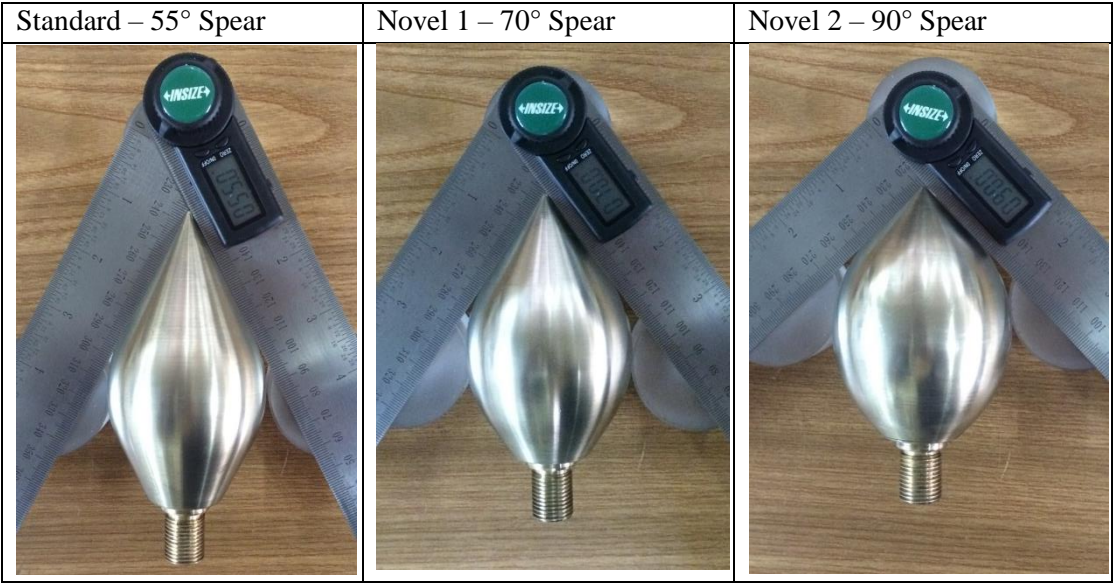


Fig. 6-9 Pelton spears used for experimental tests

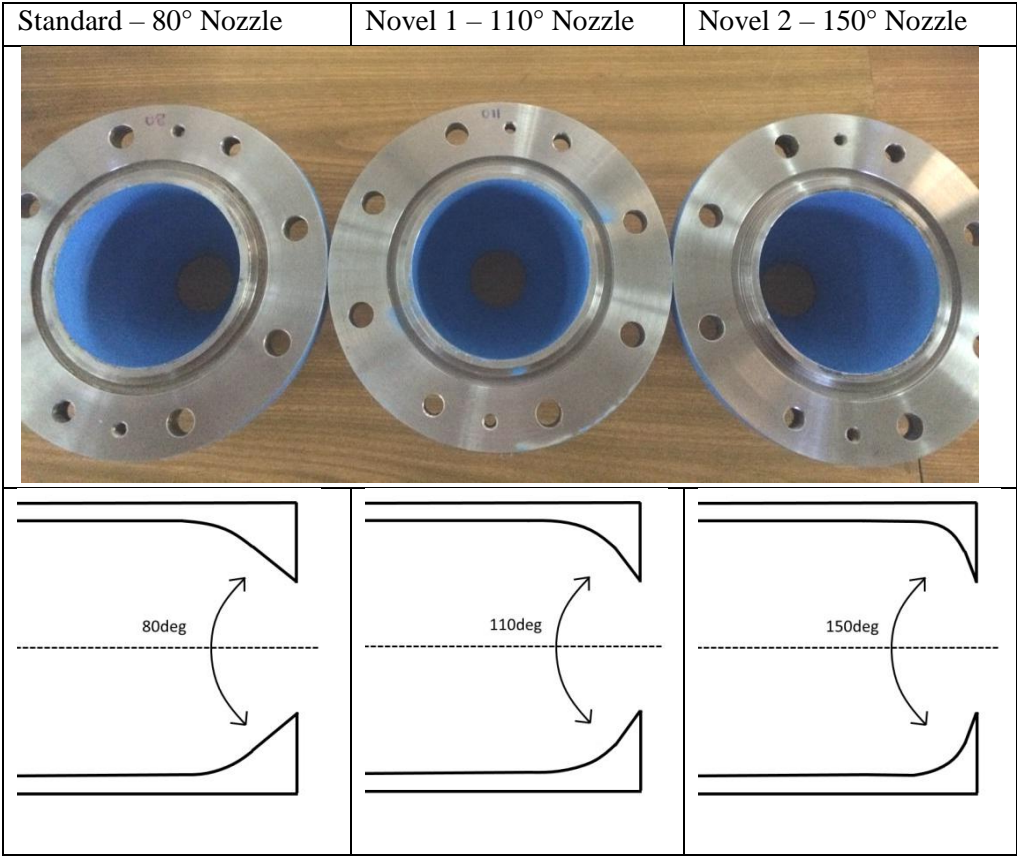


Fig. 6-10 Pelton nozzles used for experimental testing

6.2.1 Methodology

The injector tests considered herein were carried out at the Laboratory of Hydraulic Turbomachinery, National Technical University of Athens, using the Pelton turbine shown operating in Fig. 6-11. The turbine is fed by a multistage adjustable speed pump with nominal operation point $Q=290 \text{ m}^3/\text{h}$, $H=130 \text{ mWG}$, pumping from the laboratory reservoir of 320 m^3 volume. The tests were performed using the Gilkes twin jet Pelton with runner type ‘Z120’, which is coupled to a 75kW DC generator with continuous speed regulation.

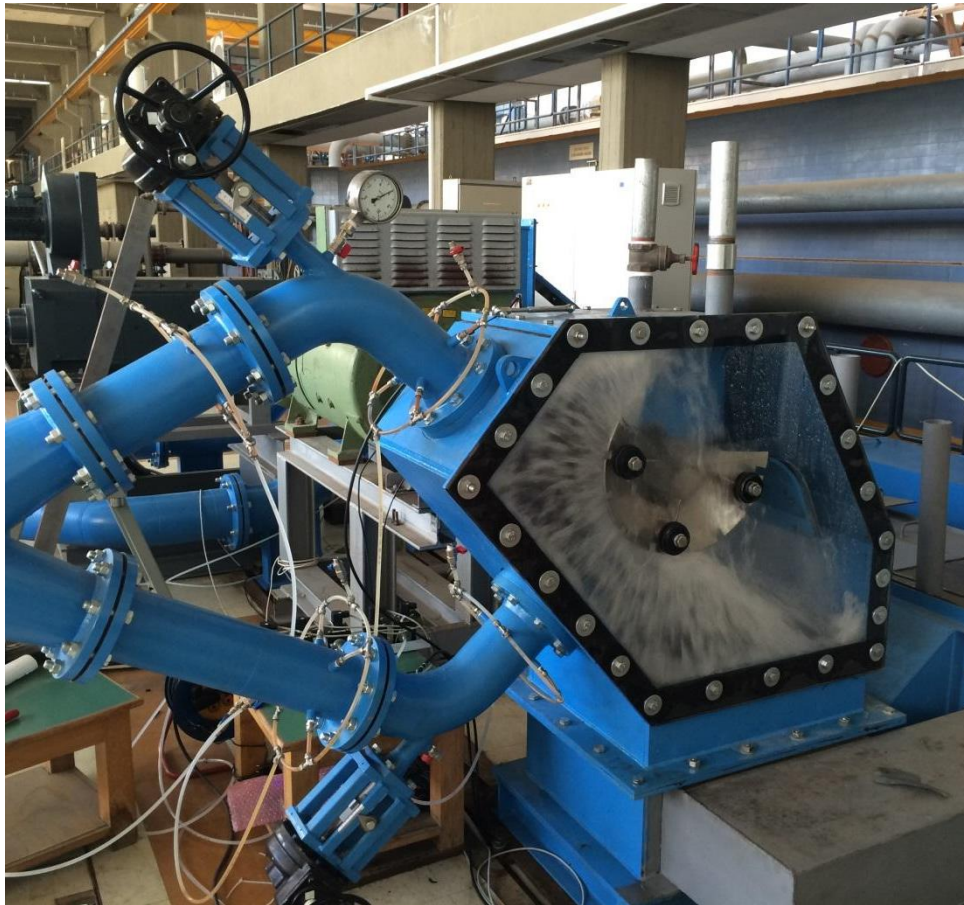


Fig. 6-11 Gilkes twin jet Pelton test rig in operation at NTUA

The test procedure and sensor calibration follow the methodology outlined in the IEC 60193 international standard. These standards provide general characteristic equations for unit speed and unit flow rate based on the diameter of a turbine. However, the minimum model size of Pelton turbine is specified in terms of bucket width rather than diameter suggesting that the bucket width is a key parameter representing a Pelton turbine. Therefore, following the same logic, unit flow rate definition was modified by [18] and used in [110] to allow a more generic comparison of Pelton runners. The unit flow rate specified to the bucket width and one jet allows comparison between different specific speed Pelton runners. These characteristic equations of turbine unit speed, n_{11} , and unit flow rate specified to the bucket width and one jet, Q_{11k} , are given in section 5.1.3. The results are presented for upper jet operation only.

Similar to the description given in section 5.1.7, the systematic uncertainty for each instrument used during this testing is given in Table 6-5, below. Model description is detailed in Table 5-3. The total systematic uncertainty in the efficiency, η , was calculated as $\pm 0.6\%$.

Instrument	Systematic Uncertainty
Pressure Transducer (H)	$\pm 0.3\%$
Flow meter (Q)	$\pm 0.5\%$
Torque meter (M)	$\pm 0.1\%$
Speed Sensor (n)	$\pm 0.05\%$

Table 6-5 Systematic error of each instrument

For each of the three injectors tested, a single operating point was recorded before, halfway through and after the test at rotational speed $n_{II} = 39$ and $n_{II} = 43$, therefore in total 18 points were recorded for each injector, these are known as the control points. The control points were then used to determine the random uncertainty according to the procedure defined in Annex L of the IEC 60193, which covers these experimental tests.

The random uncertainty in the efficiency, η , was calculated as $\pm 0.06\%$ at the 95% confidence interval.

Since the experiments are comparing the difference between the three injector designs the systematic uncertainty will be equivalent and can therefore be negated, as such it is the random uncertainty, $\pm 0.06\%$, which is considered important in this study.

6.2.1.1 Test Plan

The injector test plan can be seen in Fig. 6-12 below, showing the range of n_{II} and Q_{IIk} values which were tested. A total of 32 test points were measured excluding the control points. For each Q_{IIk} value, the head and flow rate is set by adjusting the spear travel and the speed of the pump. The rotational speed is then varied by adjusting the speed of the brake and n_{II} values are measured for each Q_{IIk} value. This is the approach suggested in the testing standards. For each test point, 180 readings are taken from the pressure, torque, flow and speed sensors over a period of 90 seconds. From these voltage readings, the pressure, flow rate, speed and torque can be calculated using the calibration curves for each instrument and used to determine the efficiency.

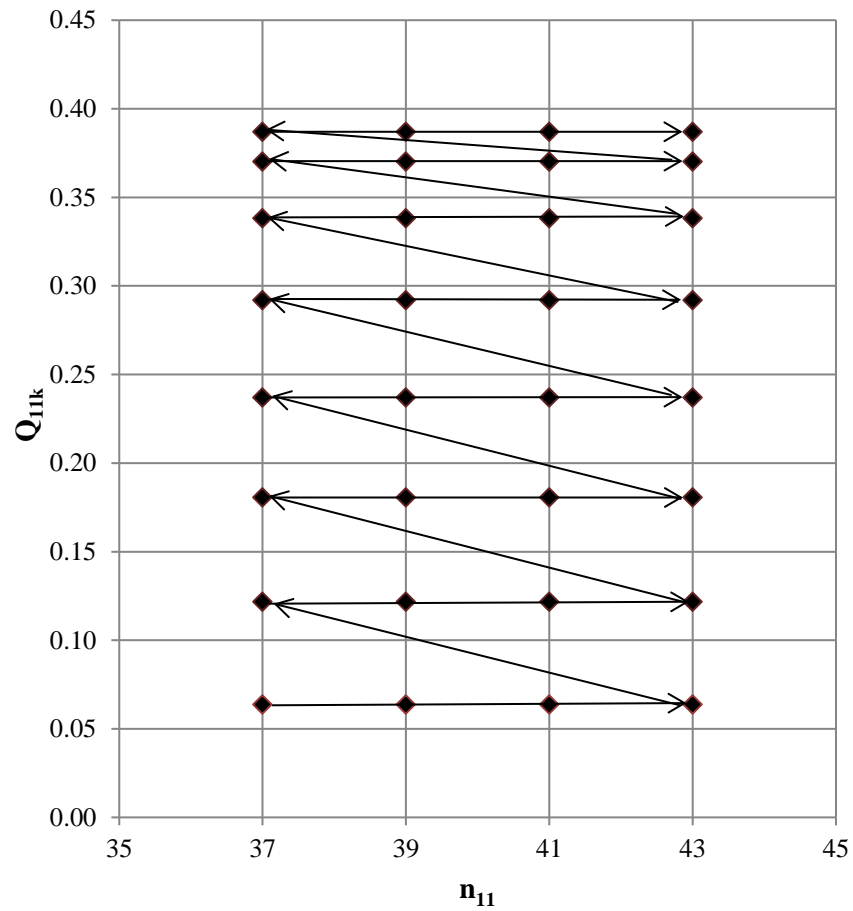


Fig. 6-12 Pelton injector test plan

6.2.1.2 Flow Curve Comparison

For the Novel designs with steeper angles the peak flowrate that can be delivered by the injector reduces, therefore the Novel injectors have been scaled up to correspond to the maximum flow rate delivered by the Standard injector. The respective nozzle diameters are detailed in Table 6-6, below.

Injector Design	Nozzle Angle	Spear Angle	Nozzle Diameter
	[deg]	[deg]	[mm]
Standard	80	55	46.9
Novel 1	110	70	48.9
Novel 2	150	90	50.9

Table 6-6 Pelton injector geometric details

The flow rate for each test point is plotted against the spear travel over the nozzle diameter (s/D_s) for each injector as shown in Fig. 6-13. The results show that although the maximum flow rates are not identical for each injector, they are within 1.6% of one another and the slight discrepancy is likely to be due to the precision of the spear positioning being limited to 0.25 mm.

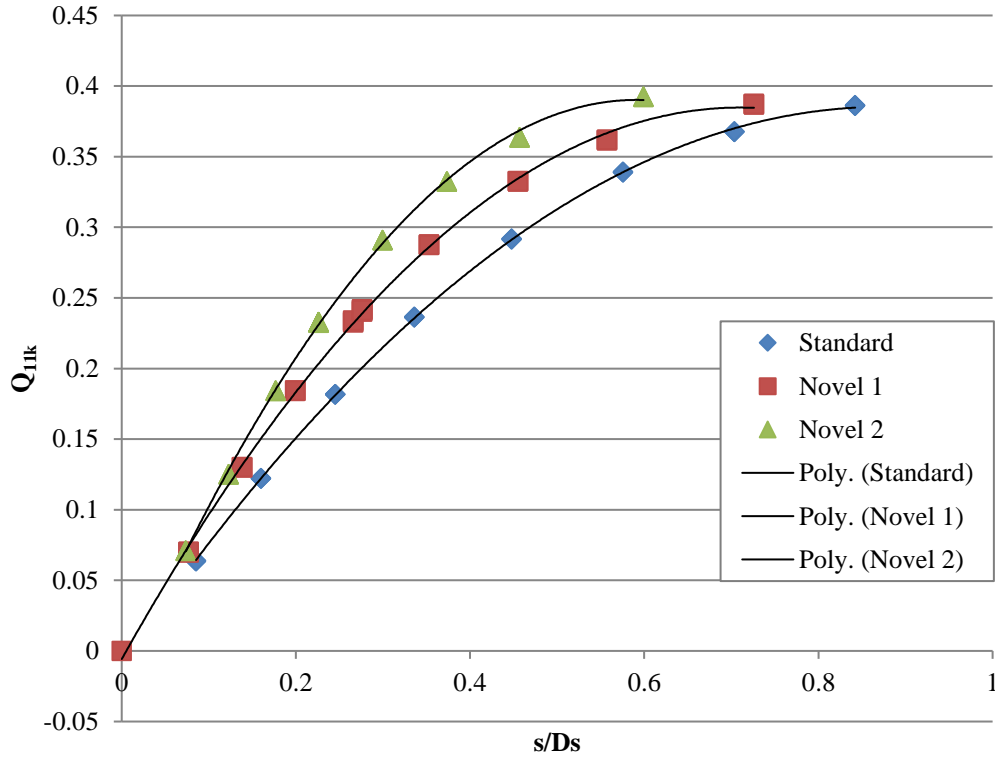


Fig. 6-13 Pelton injector flow curves comparison

6.3 Experimental Test Results

The efficiency curves for the upper jet are plotted against the Q_{1lk} for each unit speed n_{11} in Fig. 6-14 to Fig. 6-17. The highest measured efficiency has been used to normalise the results.

The graphs indicate the Novel designs perform better than the Standard design for the four speeds, however there is a more pronounced difference at lower flow rates. The gained efficiency increase is around 1% at the BEP for all tests. The results also show that out of the Novel 1 and Novel 2 injectors, the Novel 1 design performs slightly better (around 0.8% higher normalised efficiency at lower flow rates to 0.2% at higher flow rates, at the nominal speed $n_{11}=39$). Hence, the Novel 1 design achieves a 1.2% increase at the operating point corresponding to $Q_{1lk} = 0.234$ and $n_{11} = 39$, as shown in Fig. 6-15.

The gain in efficiency is reduced toward the maximum flow rate, where the viscous effects due to the injector geometry has the least impact on the performance [96] since the needles are fully retracted into the nozzles.

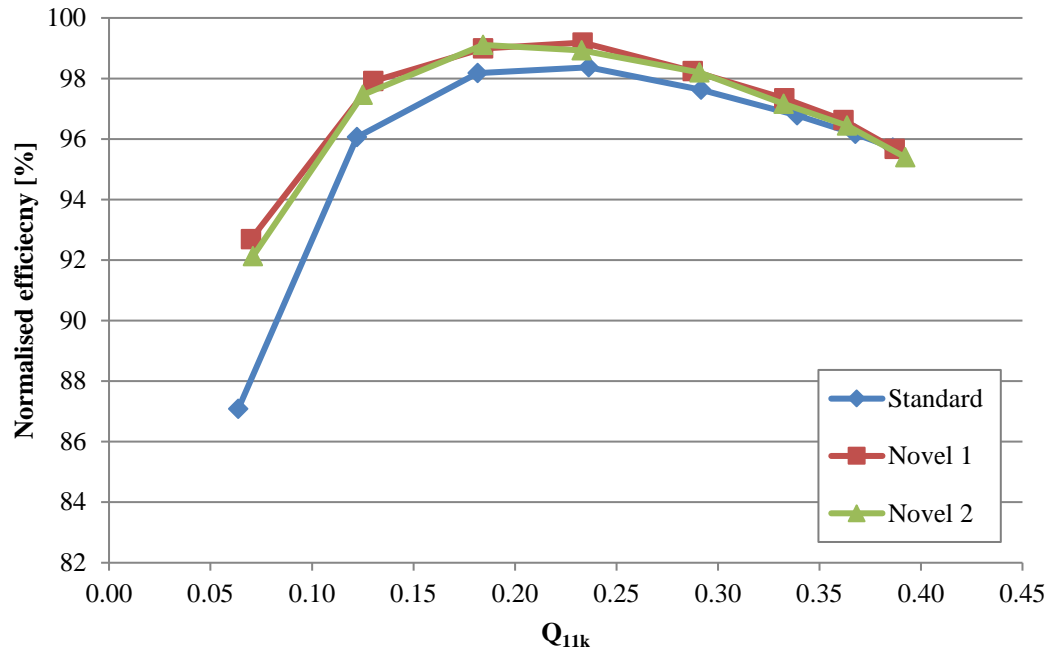


Fig. 6-14 Pelton efficiency curves for 80/55, 110/70 and 150/90 injectors at $n_{II}=37$

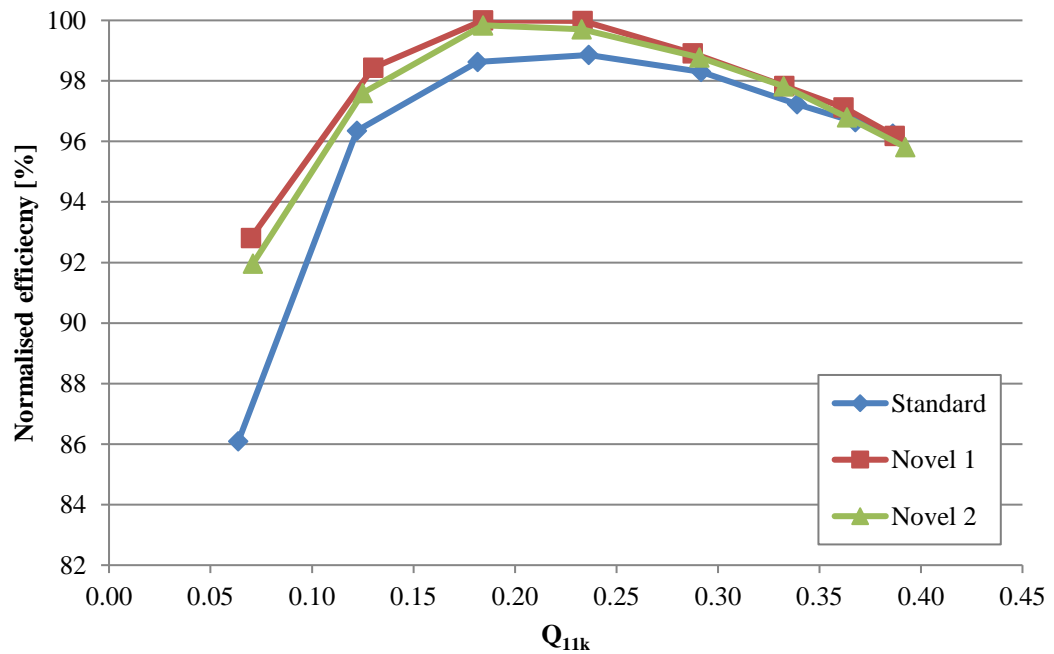


Fig. 6-15 Pelton efficiency curves for 80/55, 110/70 and 150/90 injectors at $n_{II}=39$

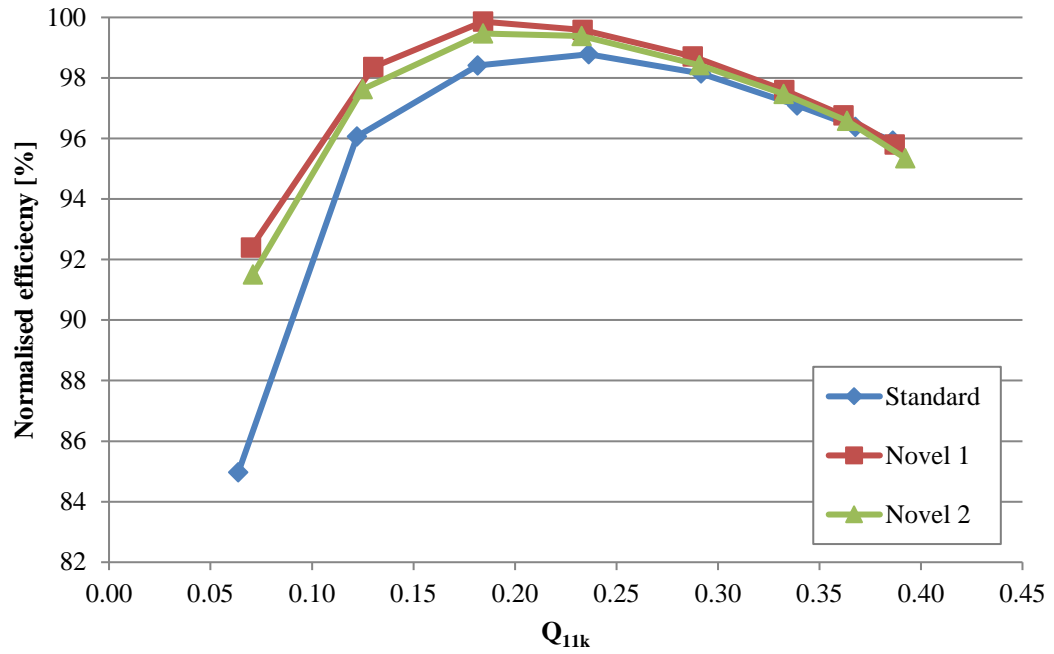


Fig. 6-16 Pelton efficiency curves for 80/55, 110/70 and 150/90 injectors at $n_{II}=41$

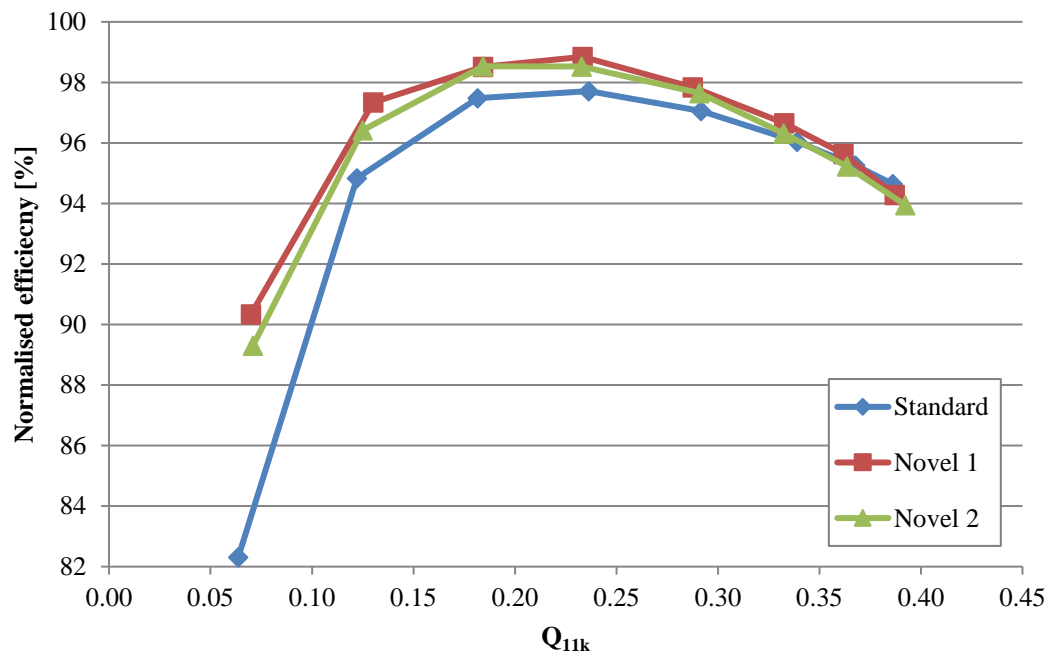


Fig. 6-17 Pelton efficiency curves for 80/55, 110/70 and 150/90 injectors at $n_{II}=43$

6.4 Numerical and Experimental Comparison

The experimental results indicate that there appears to be a cut-off point beyond which steeper angles are no longer optimal, which does not correlate with the 3D CFD simulations shown in Fig. 6-5. To address this the jet axial velocity profiles and the secondary flow pattern will be analysed in the following section.

6.4.1 Secondary Velocities in the Jet

The secondary velocities have been plotted on a number of cross sections through the free jet at distances $z/D = 1, 2, 3$ and 4 from the nozzle exit, the location of which is shown in Fig. 6-3. The highest secondary velocity magnitude represents approximately 3% of the axial jet velocity. The secondary velocities are responsible for the disturbances of the uniformity of the free surface. The pipe work bend creates two Dean Vortices¹⁸ one in the position above the needle rod and a smaller one below the needle rod, plotted before and after the guide vanes at a distance of $-8.75 z/D$ and $-3.5 z/D$ for the Standard jet in Fig. 6-18 and Fig. 6-19 respectively. These two main vortices interact with the guide vanes to form many smaller clockwise vortices, which remain in the fluid well beyond 4 jet diameter distance from the nozzle exit, as shown in Fig. 6-20. These vortices cause both jet deflection and smaller irregularities observed on the outer surface of the jet, which grow significantly. The most significant difference between the standard and Novel 1 and 2 design is the magnification of the bead formed at the bottom of the jet, corresponding to the inside pipework bend, and likewise disturbances which occur in the location corresponding to the guide vanes. In reality, it can be observed that this bead can be completely detached from the main portion of the jet, resulting in the formation of a sequence of water droplets, as shown in Fig. 6-21 at a flowrate of 0.12.

¹⁸ The Dean number is defined as $De = Re \sqrt{\frac{D}{2 R_C}}$

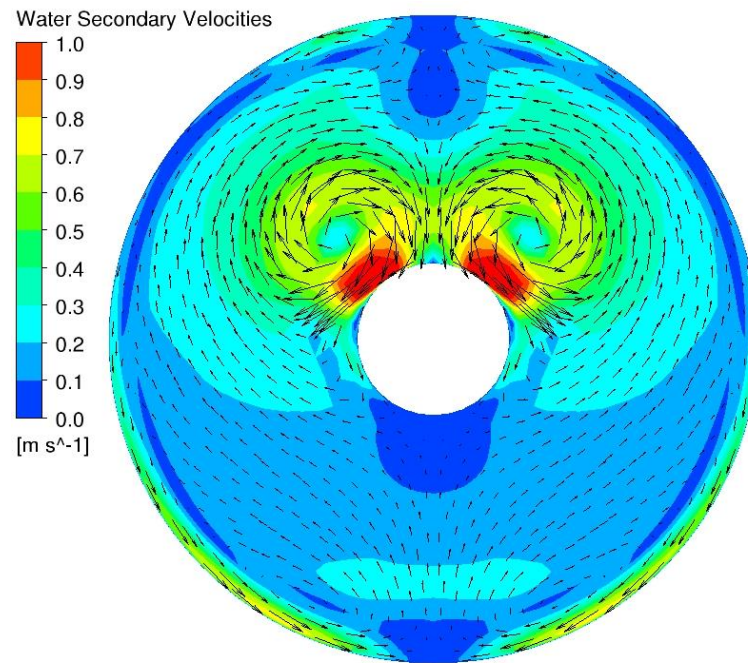


Fig. 6-18 Vector plot of secondary velocities in the flow before the guide vanes for the Standard jet

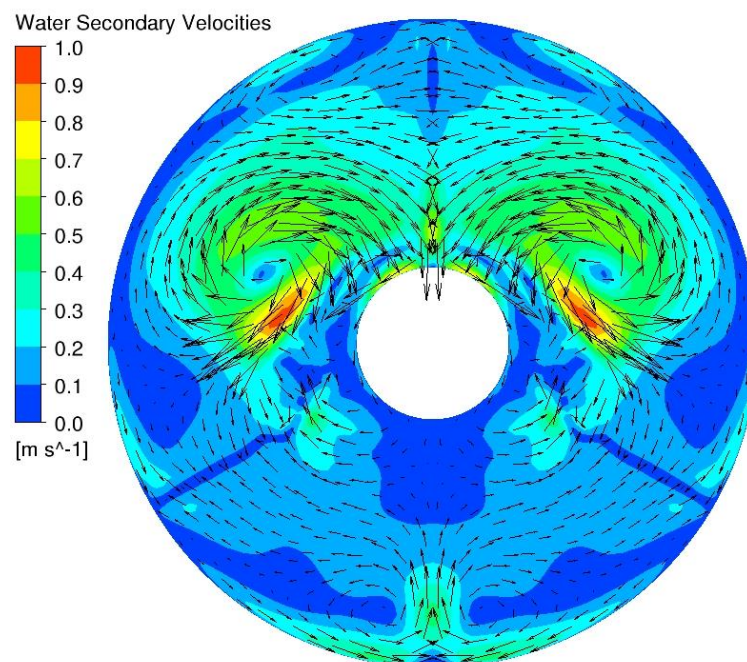


Fig. 6-19 Vector plot of secondary velocities in the flow after the guide vanes for the Standard jet

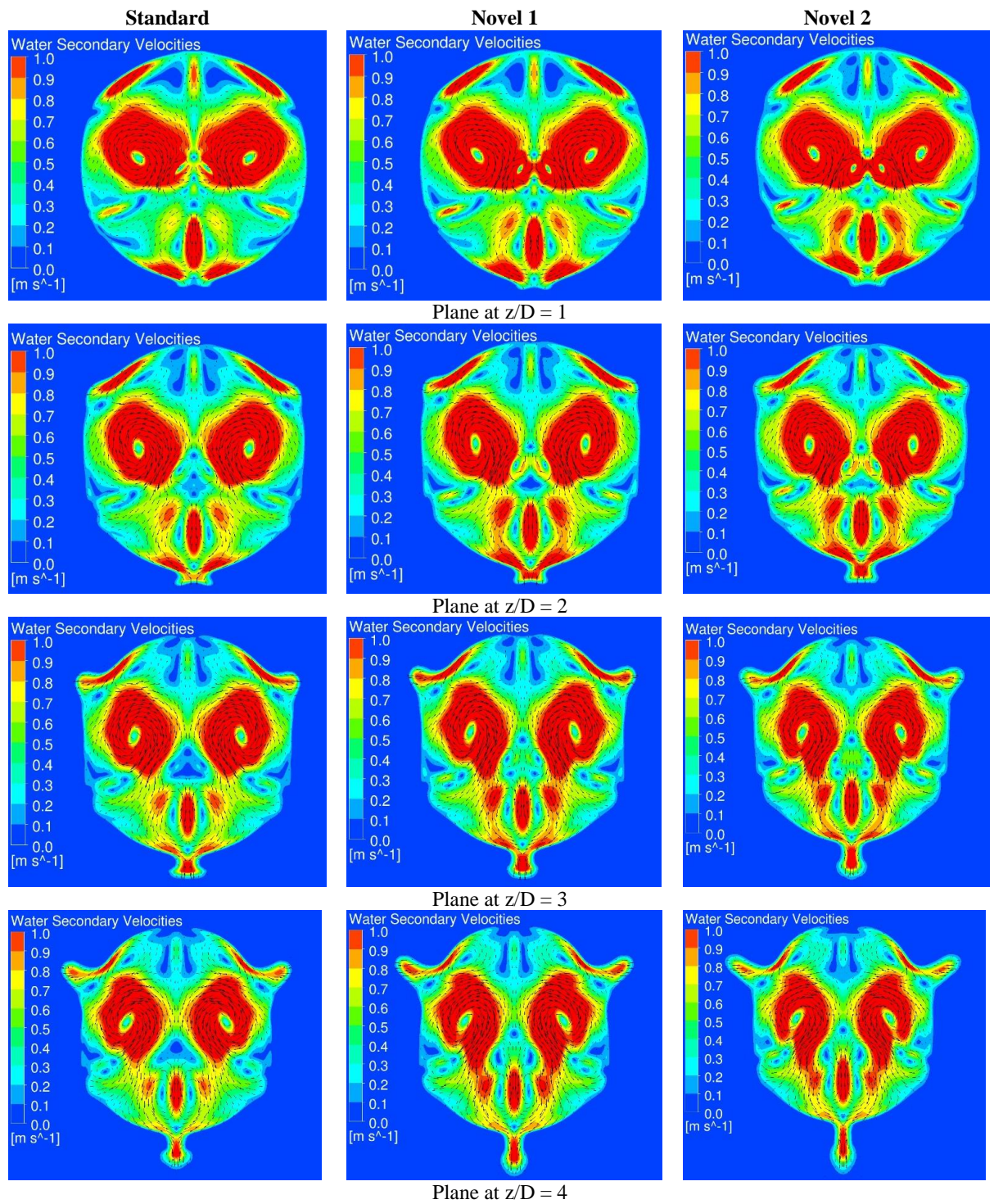


Fig. 6-20 Comparing the secondary velocity vectors at different planes from nozzle exit

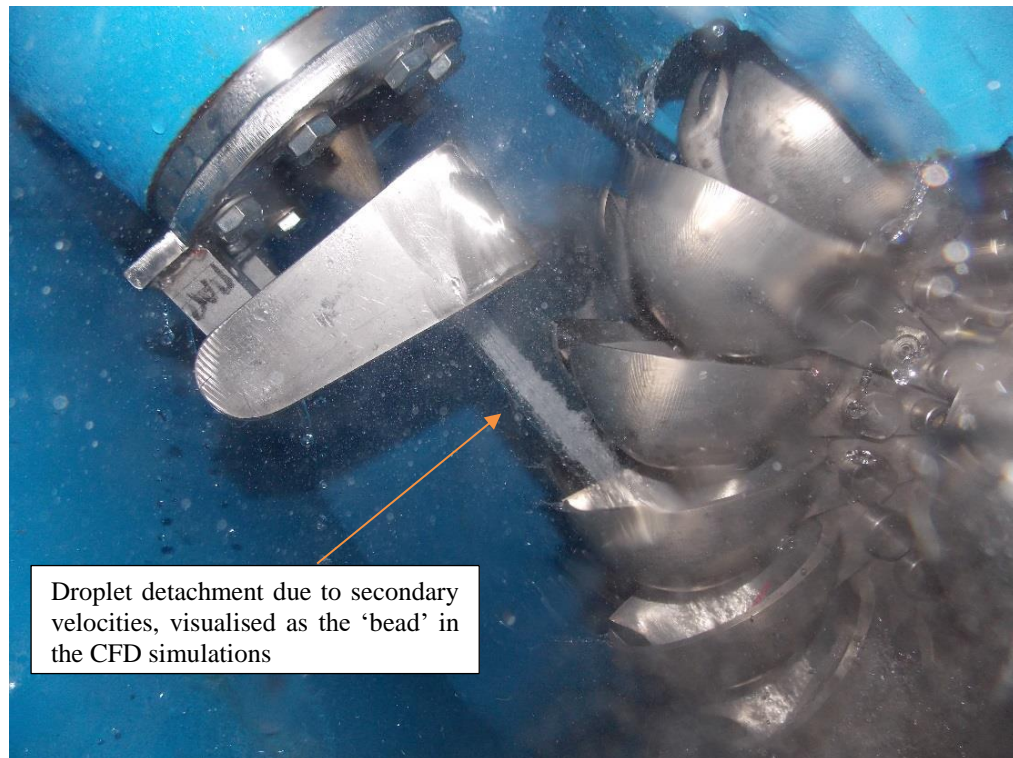


Fig. 6-21 Experimental observation of upper jet detachment

Further examination of the effect of the secondary velocities on the stability of the jet is shown in Fig. 6-22 and Fig. 6-23, which plot the profile of the velocity of the jet along the vertical, x , axis for the Standard and Novel designs at a distance of $z/D = 1$ and 4 from the nozzle exit respectively. While Fig. 6-24 compares the same velocity profiles along the horizontal, y , axis, as also with the corresponding 2D profile of the axisymmetric solution for the Standard design. It is observed that the profile in the horizontal direction is more symmetrical and corresponds more to the equivalent 2D case. In contrast, the profile in the vertical direction is asymmetrical, both in the region of the axis where the entire jet core is shifted downwards, and at the bottom of the jet, which is displaced downward, corresponding to the bead in the secondary velocity plots. The Dean vortices do not cause asymmetry in the free beam profile in the horizontal direction since they are symmetrical through the vertical plane of the injector.

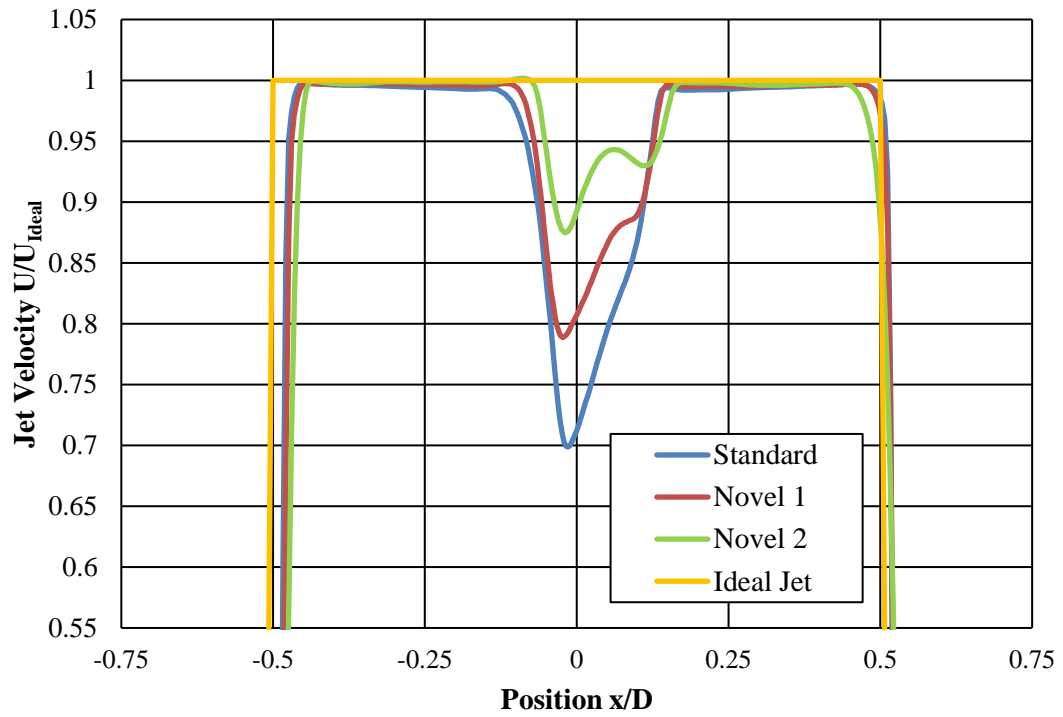


Fig. 6-22 Vertical velocity profile comparison for Standard and Novel injector designs at plane $z/D = 1$

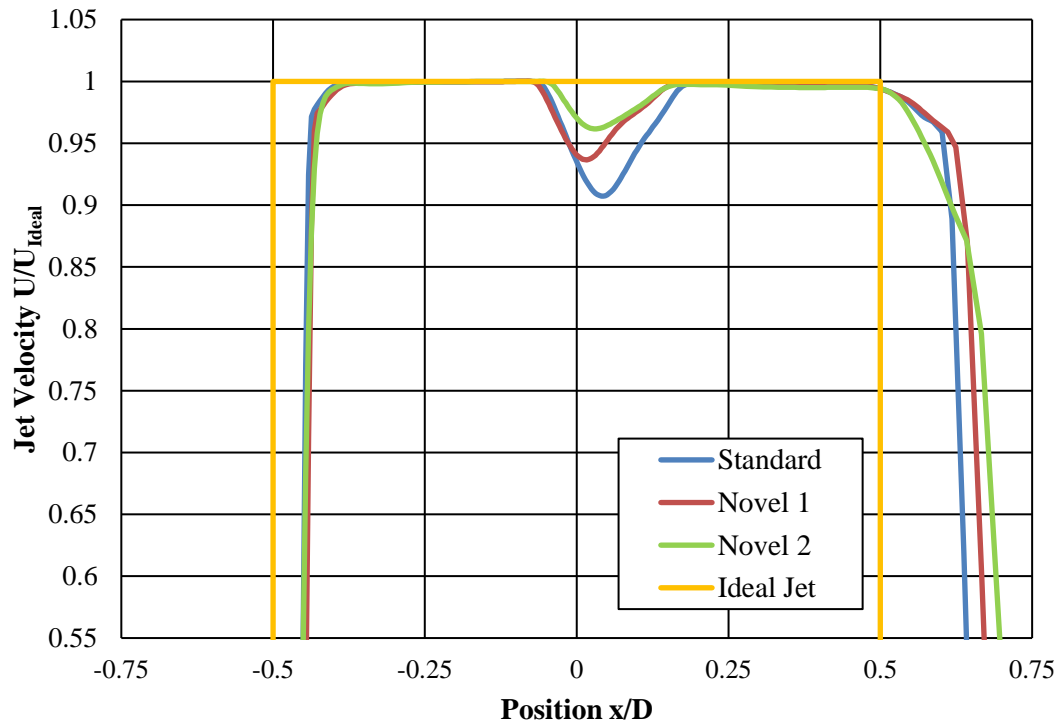


Fig. 6-23 Vertical velocity profile comparison for Standard and Novel injector designs at plane $z/D = 4$

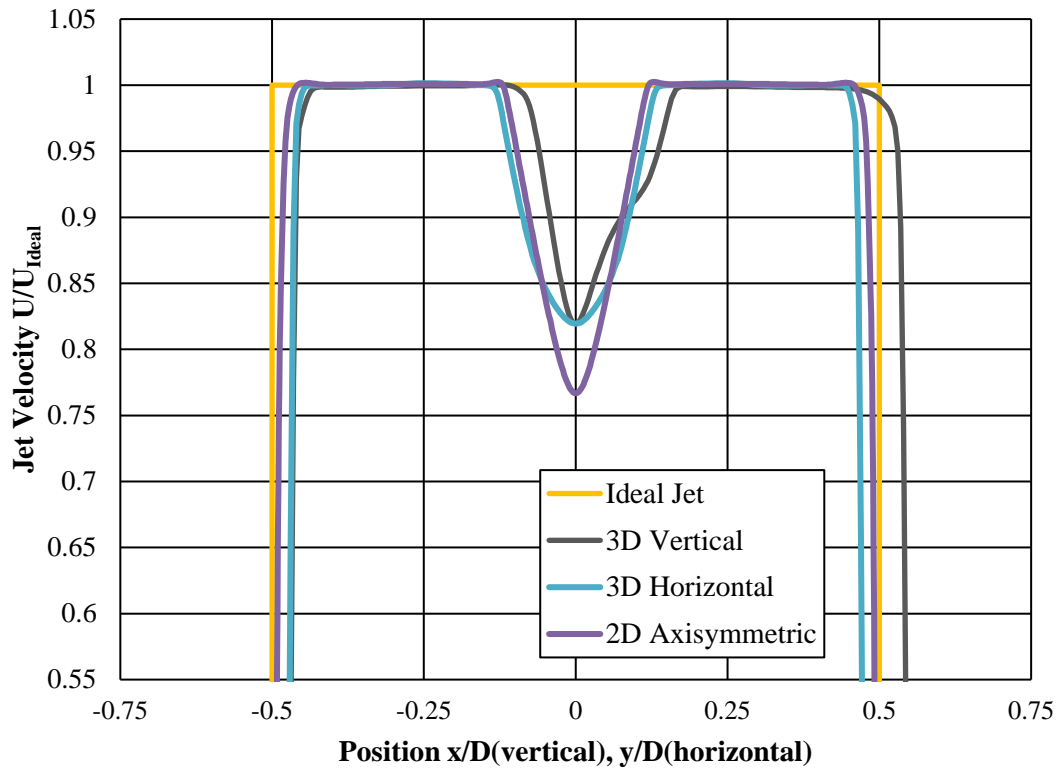


Fig. 6-24 Comparing the 3D vertical, 3D horizontal and 2D axisymmetric axial velocity profiles for the Standard injector design at plane $z/D = 2$

In all cases, the minimum velocity value at the centre of the jet axis appears higher in the 3D solution, probably due to numerical diffusion errors, which are smaller in the denser grid of the 2D modelling. Moreover, due to the existence of the secondary velocities the remaining part of the profiles resulting from the 3D solution is not as uniform as the equivalent of 2D solution. There is a slight shift in the jet core from the injector axis in the vertical 3D simulations, which is due to the secondary flow. Furthermore, the above-mentioned flow variations are less pronounced (lower axis velocity reduction) for the Novel designs, which could explain why the Novel designs perform better experimentally. However, while the steeper angled Novel designs provide more uniform velocity profile they also have higher secondary velocities. Since the Novel 1 design perform slightly higher than the Novel 2, at some point the negative effect of secondary velocities becomes larger than the positive effect of having more uniform velocity in the centre. This could be the reason why Novel 1 is more efficient experimentally but less efficient than Novel 2 in CFD injector results.

Chongji et al [111] demonstrated that at higher flow rates (i.e. longer spear stoke and thus a small spear distance beyond the nozzle opening) the jet vena contracta occurs much closer to

the opening and the jet disperses much more severely, particularly due to the bead formation on the side of the inner curvature of the bend. Therefore, the opposite of this will be true in the case of the Standard design, which has the largest spear distance beyond the nozzle exit resulting in a smaller bead formation. Moreover, due to the convergent nature of the nozzle, there is flow separation from the spear wall, which is experienced more significantly in the Novel cases immediately after the nozzle opening due to the steeper angles. This gives an indication as to why the vertical velocity profile is more uniform in the centre of the jet for the Novel cases, since as the spear distance is reduced the needle wall poses less frictional effect resulting in a more uniform axial velocity through the jet and a higher hydraulic efficiency of the injector in isolation, despite the jet dispersion.

In order to investigate this apparent difference between the CFD and the experimental results, further CFD results are presented in the following section 6.4.2, which analyses the influence of the nozzle and spear angle on the jet – runner interaction by considering four case studies. The first is an ideal jet, with uniform velocity profile and the following three will use the obtained velocity profiles from the three aforementioned injector designs.

6.4.2 Further Numerical Investigation of the Jet – Runner Interaction

In order to simplify the model and speed up convergence the numerical analysis can be broken down into two sub-simulations, the first highlighted in Fig. 6-25, consists of a single injector for each of the three nozzle and spear combinations. The geometry of interest includes the nozzle, spear, spear rod, three spear holding vanes and the 60° pipe bend. The second sub-simulation, highlighted in Fig. 6-26 consists of two domains, the stationary inlet and rotating runner, where only two (out of the full 18) buckets have been modelled. The two green circular planes in Fig. 6-25 and Fig. 6-26 represent 2 jet diameters distance from the nozzle exit and are the point at which the velocity profile representing the real jet is exported from the injector simulation and imported into the runner simulation in addition to the location at which the ideal jet boundary condition is defined. The boundary conditions for the runner simulation are detailed in Table 6-7.

Position	Type	FLUENT Boundary Conditions	
Inlet	Velocity Inlet	Momentum options	Real: components u, v, w and water volume fraction Ideal: Normal to boundary water volume fraction = 1
		Turbulence options	Real: components k and ω Ideal: turbulence intensity = 5% and turbulence viscosity ratio = 10
Buckets	Wall	Momentum option	No slip wall
		Wall roughness	Smooth wall (0 roughness height)
Interfaces and Openings	Pressure Outlet	Momentum option	Relative static pressure 0 Pa
		Turbulence intensity	5%
		Turbulence viscosity ratio	10

Table 6-7 Details of the boundary conditions for runner simulations

The runner analysis is a transient simulation and the rotation is modelled using a sliding mesh approach, with an interface defined between the stationary jet and runner domains. The meshes consist of swept hexahedral cells within the stationary jet and fully tetrahedral cells within the runner domain. Face sizing was used to match the element size across the interface in order to minimise numerical diffusion. In all meshes inflation layers were applied to the wall boundaries and the minimum wall distance was calculated in order to keep the y^+ value within the allowable limits of wall functions.

A preliminary timestep study was carried out and a conservative timestep of 3.52×10^{-5} sec was chosen, which corresponds to 0.2 degrees of runner rotation. A second-order backward Euler scheme is used for the transient terms and a second-order upwind for the spatial discretisation. The convergence criteria for each timestep was chosen to correspond to a rms value of 1×10^{-4} for the residuals of the momentum equations. In order to ensure minimal numerical diffusion a compressive scheme for the discretisation of the volume fraction equations was chosen and the surface tension model in FLUENT is the continuum surface force (CSF) model proposed by Brackbill et al [101].

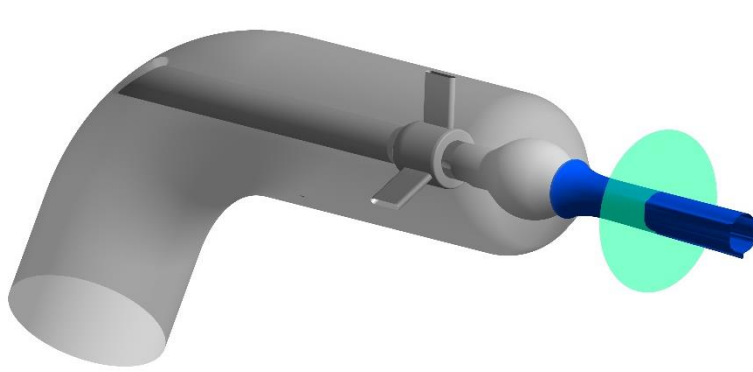


Fig. 6-25 3D injector simulation showing the plane used in the analysis

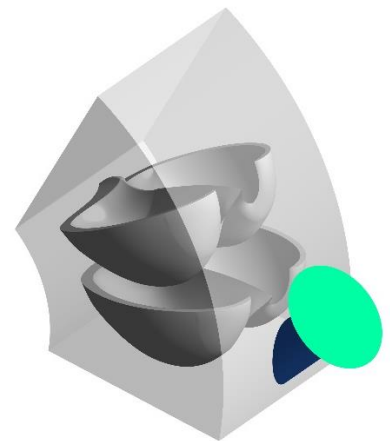


Fig. 6-26 3D runner simulation showing the corresponding plane used in the analysis

In order to investigate this apparent difference between injector losses and experimental efficiencies of the whole system the jet profiles were imported to the runner mesh, detailed in 6.4.2.1.

6.4.2.1 *Ideal and Real Jet Comparison on Runner Performance*

In FLUENT a moment monitor is defined to measure the torque, which writes out the final value of the moment for each timestep, this is defined for both the inside and outside surfaces (wall zones) of each bucket, highlighted for a representative bucket in Fig. 6-27.

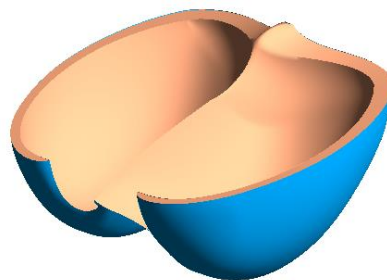


Fig. 6-27 Moment monitor wall zone definition – inside (orange) and outside (blue)

The torque is then numerically integrated using the trapezium rule to give the area under the total torque curve or the work done by a single bucket, the method for this has previously been detailed in 3.2.3.6. And the hydraulic efficiency of the runner, η_R , will be:

$$\eta_R = \frac{P_{out}}{P_{ref}} \quad (6.3)$$

Where P_{ref} is the hydraulic power of the incoming jet, which can be calculated using equation (6.2) at the respective inlet plane.

Similar to previous CFD analysis carried out in section 3.4.2, a Grid Convergence Index (GCI) study, as suggested by Roache [103], was carried out to investigate the discretisation errors introduced by the mesh with respect to the relative mesh refinement. The normalised efficiencies are indicated in Table 6-8 below, likewise the normalised efficiency with respect to normalised grid spacing is plotted in Fig. 6-28, where a zero mesh spacing is calculated as 100.79 %, which indicates that the fine mesh will provide mesh independent results.

	Grid Spacing Normalised	Element Count [million]	Efficiency (normalised to coarse mesh) [%]
Coarse	1.000	2.82	100
Med	0.694	6.19	100.68
Fine	0.482	13.9	100.79

Table 6-8 Mesh refinement study (2) results normalised to coarse grid

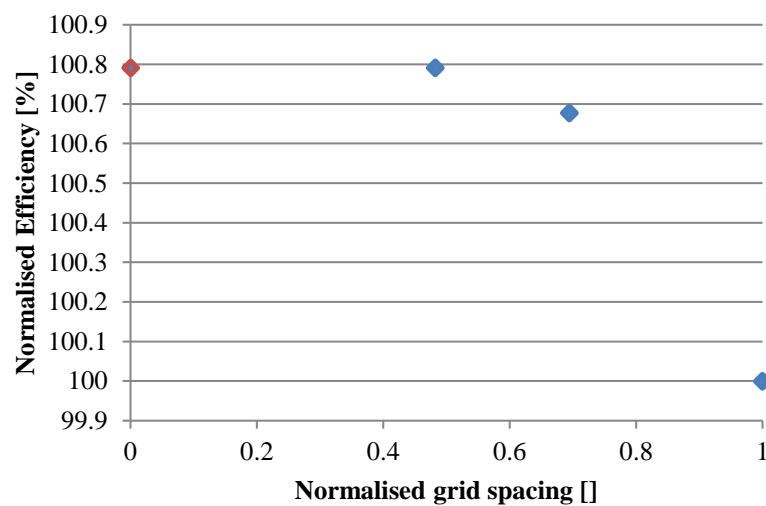


Fig. 6-28 Mesh refinement study results (2): efficiency with respect to grid spacing

The grid convergence indexes are given in Table 6-9 below.

Refinement Ratio	r	1.2
Order of Convergence	P_c	9.75513
Safety Factor	F_s	1.25
GCI for meshes 3 and 2	$GCI_{3,2}$	0.000288
GCI for meshes 2 and 1	$GCI_{2,1}$	0.001709
GCI for meshes 3 and 1	$GCI_{3,1}$	0.001995

Table 6-9 Mesh refinement study (2): Grid Conversion Indexes

The torque experienced on both inside and outside bucket surfaces for the four case studies are plotted in Fig. 6-29. Although all four configurations are characterised by the same periodic trend, the maximum positive torque obtained from the work due to the jet loading on the inside surface of the bucket is slightly different for the three designs, being always lower than the ideal, with Novel 1 efficiency being slightly higher than Novel 2 and Standard designs. The pressure coefficient distribution on the inside surface of bucket 1 for the ideal and Novel 1 configuration is shown in Fig. 6-30, where it can be identified that while the area of the peak pressure (red regions) for the ideal jet is slightly larger than the Novel 1 case, the overall shape of the pressure distribution is roughly comparable. This would explain why the general shape of the torque curves match, though with different relative magnitudes. It should be noted that the slight negative torque on the outside of the bucket (60° - 65° for bucket 2) is due to the negative pressure that is pulling the bucket, which arises during the jet cutting process as a result of the Coanda effect. This mechanism has been documented experimentally in [57].

Table 6-10 compares the numerically obtained efficiency with the experimental results, which has been normalised against the efficiency of the ideal jet case, this is shown graphically in Fig. 6-31. In the whole bucket cycle, the Novel 1 case was characterised by a greater energy exchange than the other real jet scenarios as reflected in the normalised efficiencies.

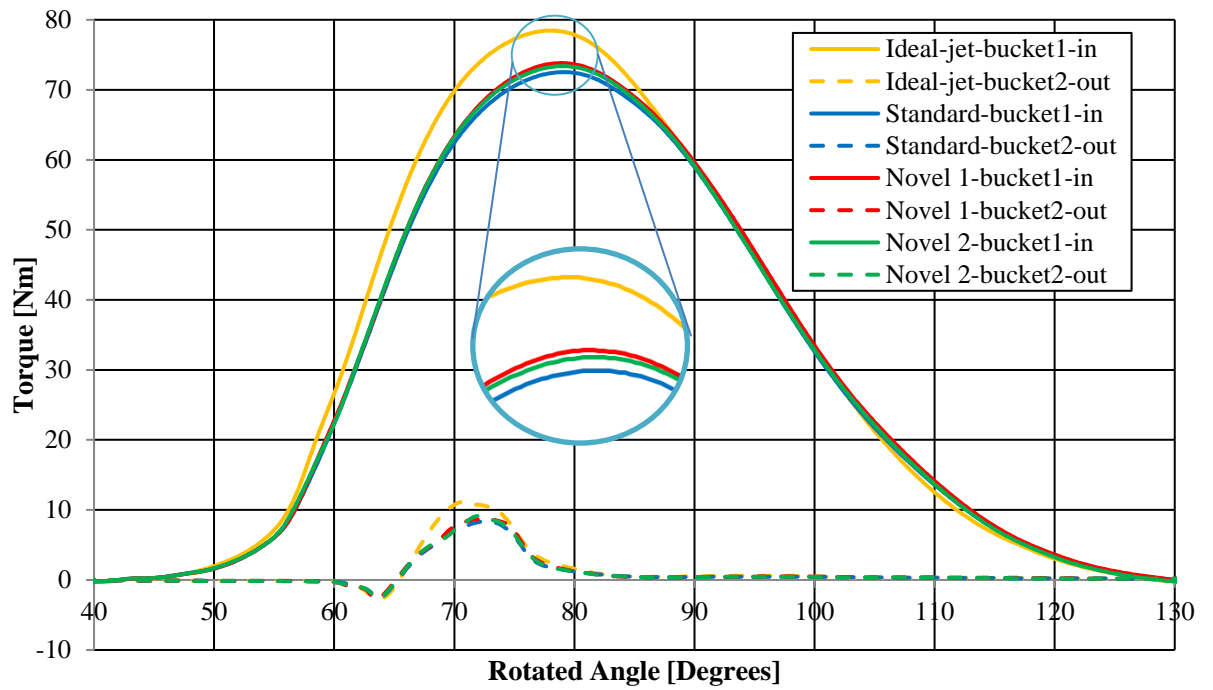


Fig. 6-29 Torque curves on the inside and outside of the bucket for 4 configurations

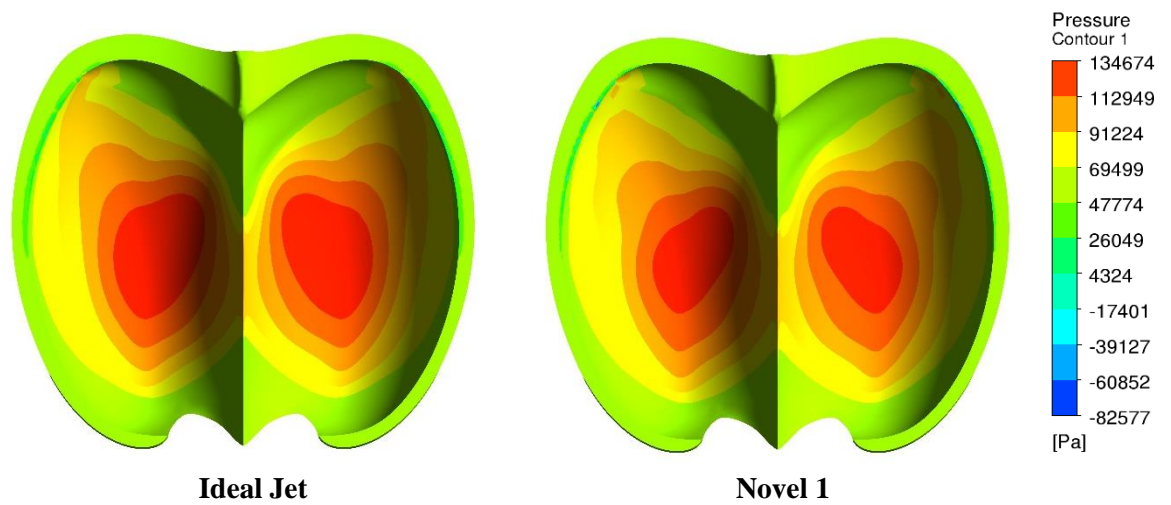


Fig. 6-30 Pressure coefficient distribution on the inside surface of bucket 1 at 80° rotation for two configurations

	Ideal Jet	Standard	Novel 1	Novel 2
Normalised CFD efficiency	100%	98.3%	99.8%	99.7%
Normalised experimental efficiency	N/A	96.9%	98.3%	98.1%

Table 6-10 Normalised efficiencies for the 4 case studies

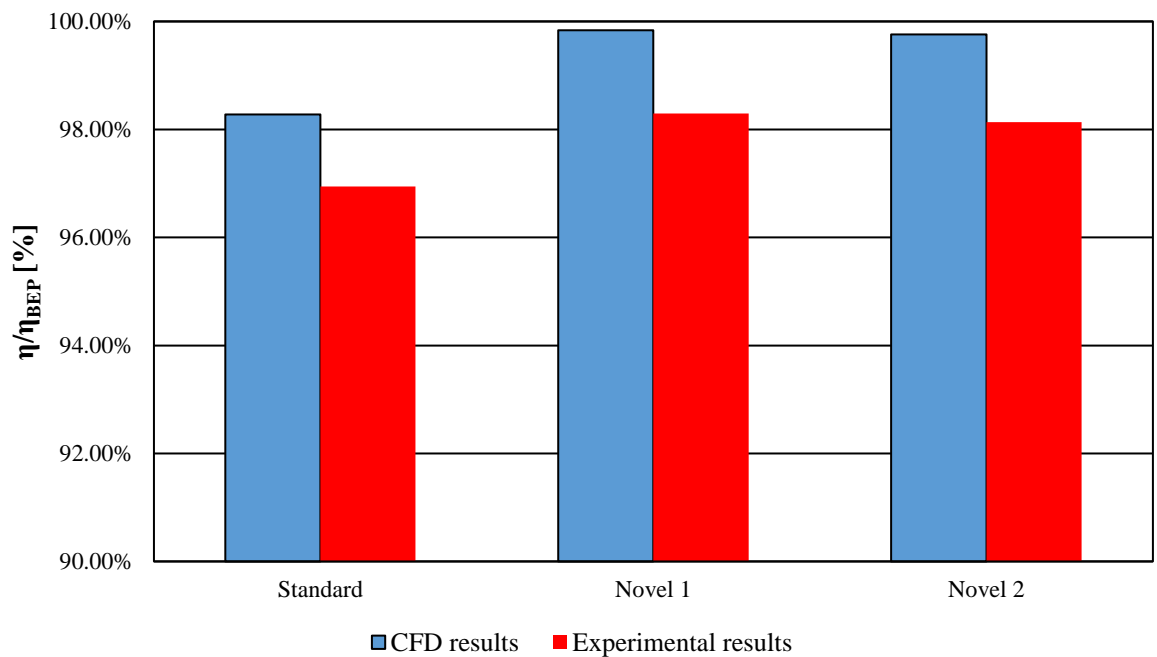


Fig. 6-31 Comparison of the CFD and experimentally obtained efficiency for the 3 real cases normalised to the ideal case

As it can be seen in Table 6-10, reporting the comparison between numerical and experimental data, the error in the calculation of the efficiency is around 1.5% for each case study, this is slightly lower than the error orders of other numerical analyses carried out on Pelton turbines [61] [58], [62], however typically the CFD will over predict efficiency. Further impact of the shape of the jet and the influence on performance can be investigated by inspecting the free surface isosurface plots at 20° degrees rotation, as highlighted in Fig. 6-32 to Fig. 6-34, for the Standard jet, Novel 1 and Novel 2 respectively. It can be observed that the aforementioned bead that develops as a result of the secondary velocities at the bottom of the jet enlarges as it moves closer to the bucket, and some of this is disturbed during the bucket cut-in process. Since the bead does not fully interact with the bucket as it extends beyond the splitter tip, the small amount

of available energy will be lost, resulting in a non-optimal jet runner interaction for the Novel 2 case, where the bead is the largest. Therefore, while in a standalone system the Novel 2 injector may experience the lowest losses, when coupled with a runner the secondary velocities and the effect these have on the overall shape of the jet play a more significant role within the jet-runner interaction and lead to a reduction in efficiency of the full Pelton turbine.

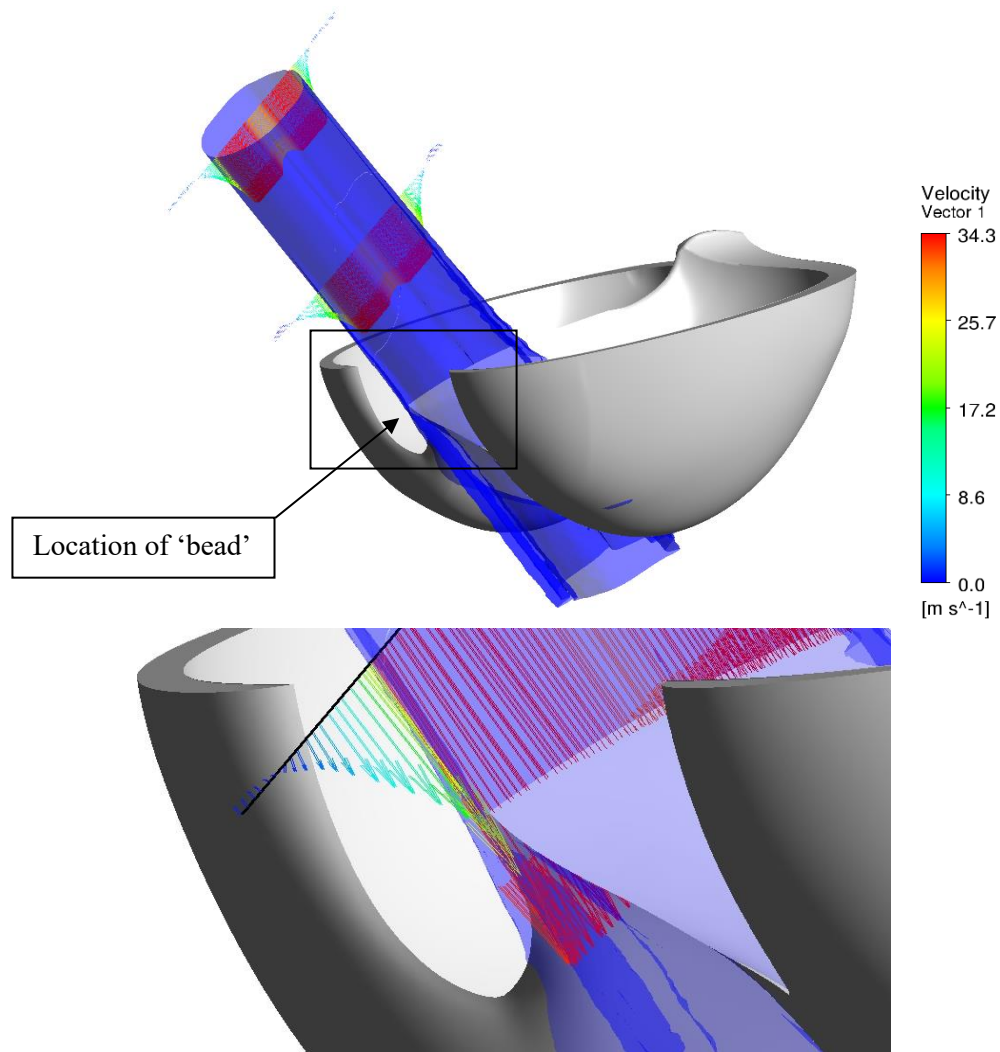


Fig. 6-32 Volume Fraction (free-surface) and vertical velocity vectors for Standard design

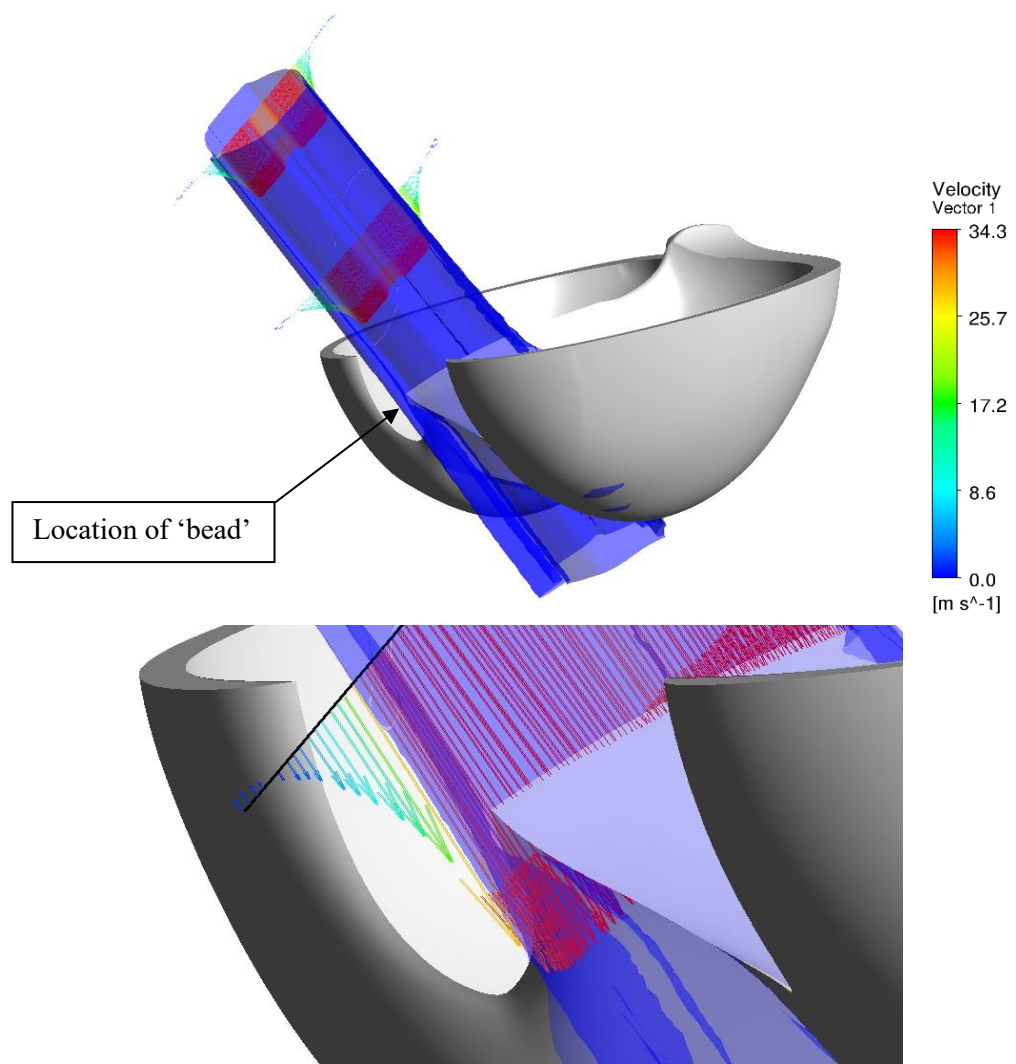


Fig. 6-33 Volume Fraction (free-surface) and vertical velocity vectors for Novel 1 design

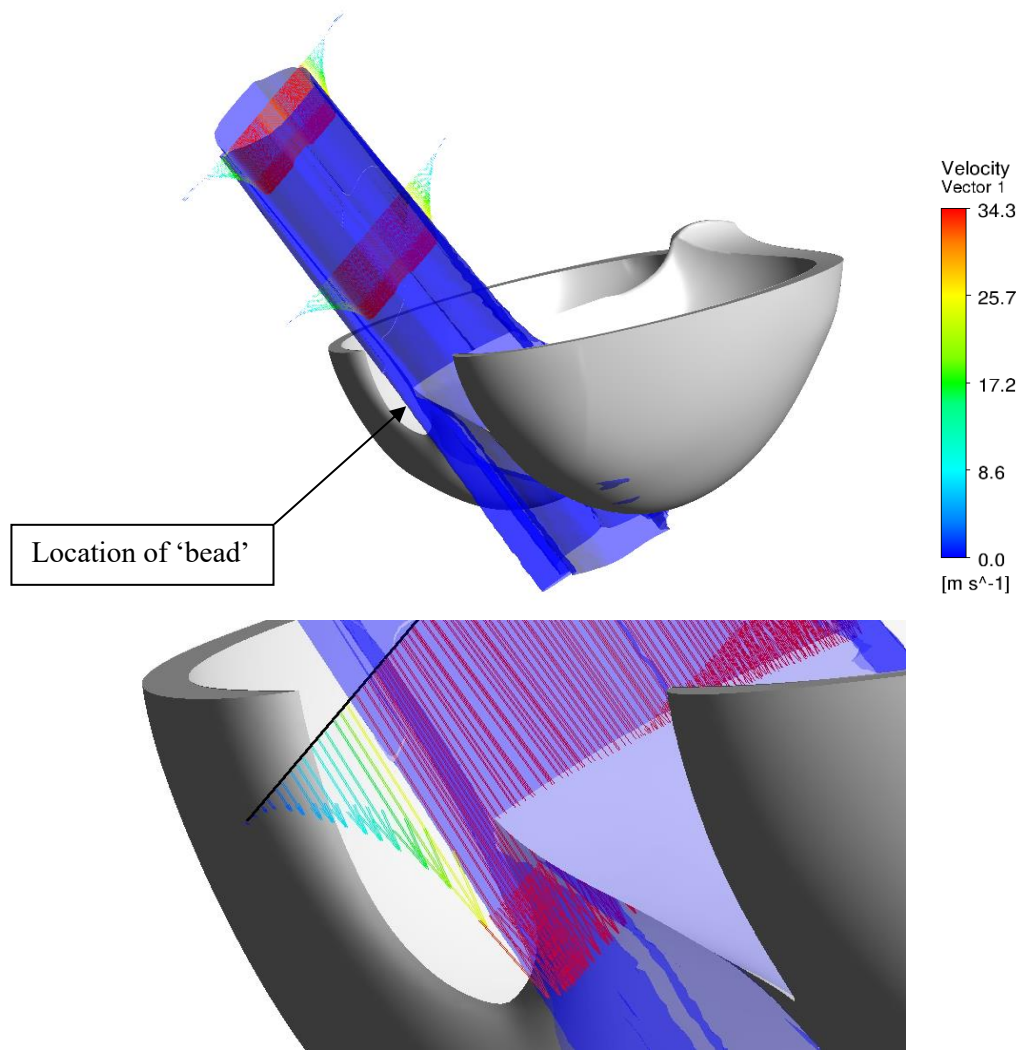


Fig. 6-34 Volume Fraction (free-surface) and vertical velocity vectors for Novel 2 design

Moreover, it could be postulated that since the remaining jet column and bead continues to travel until it impacts on the inner surface of the previous bucket, clearly visible in Fig. 6-32 - Fig. 6-34, which happens many jet diameters downstream the bead velocity will be further reduced due to the frictional effects of the surrounding air by this point. To investigate this the kinetic energy of the jet was calculated on a plane in red, as indicated in Fig. 6-35.

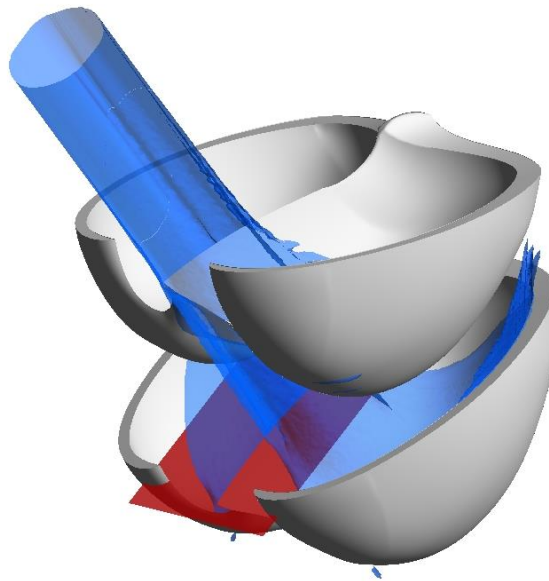


Fig. 6-35 Plane (red) indicating where remaining kinetic energy of the jet is calculated

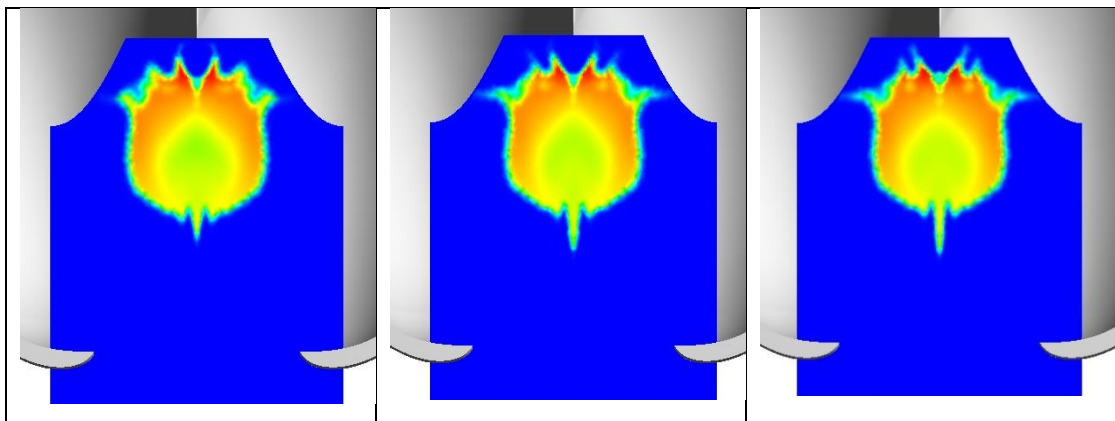


Fig. 6-36 Three contour plots showing the jet remaining after interaction with the first bucket, coloured by kinetic energy

Since, the jet column remaining after the first cut-in process continues to travel until it impacts on the inner surface of the previous bucket, which happens many jet diameters downstream it contributes to the overall torque experienced on the runner. Therefore, the sum of the kinetic energy (normalised to the Novel 1 case) on the plane is outlined in Table 6-11, indicating the Novel designs contribute a higher kinetic energy to the previous bucket, with the Novel 1 being slightly higher.

	Standard	Novel 1	Novel 2
Kinetic energy	97.5%	100%	97.8%

Table 6-11 Kinetic energy remaining in the jet after the first cut-in process

6.5 Conclusions of Injector Research

Following a detailed literature review of the research carried out on impulse turbine injectors it became apparent that there were few studies looking at the basic geometric design parameters of impulse turbine injectors and the impact they have on the hydraulic performance. A DOE study found that the nozzle and spear angles have the biggest impact on the injector losses and suggested an optimum design with nozzle and spear angles of 110° and 70° . This study was extended further to include even steeper angles of 150° and 90° respectively. Focussing initially on a 2D axisymmetric straight pipe case, the three injector designs were modelled in steady state with a mesh with much higher mesh independency. Following this the study was extended to include a full 3D case including the branch pipe and spear holding vanes.

The full 3D simulations reveal some important characteristics of the flow through the injector such as the development of secondary flows and symmetrical Dean vortices after the pipe bend, furthermore there is a number of smaller vortices generated as a result of the flow interaction with the needle rod holding vanes. They also reveal the role of the secondary velocities in the observed disturbances of the free jet surface. The increase of injector efficiency obtained by using steeper nozzle and spear valve angles can also be explained by the observed reduction of the non-symmetric jet structure characteristics, which includes the secondary velocity magnitude.

The verification of the efficiency of the stand-alone injector models is difficult to carry out in isolation as the performance of each injector design was measured by analysing the effect of the nozzle and spear geometry on the entire Pelton system in section 6.2. This means that the measured differences between the designs are not simply the differences between the losses through each injector but include the effect the jet has on the performance of the runner as well. More specifically the experimental results have been presented for the upper jet on the twin jet horizontal axis machine only. In order to investigate further the apparent difference between the prediction of efficiency for the injector system using CFD and that obtained experimentally, the injector model was verified by combining the injector results with a runner simulation which included the impact of the quality of the jet produced by each injector on the performance of the runner.

It has been demonstrated that a higher peak torque is experienced for the Novel cases with the highest peak torque on the inside of the bucket is experienced by the Novel 1 design and consequently results in a higher efficiency. The reason for this is that while the jet velocity may not be as uniform as the Novel 2 case, a more compact jet with less surface disturbance ensures a more optimal exchange of kinetic energy with the runner.

One can conclude that the effect of friction is by far the largest contributor to hydraulic loss within the injector and as the area of the wetted surface of the spears in Novel 1 and 2 design is significantly less than the Standard design this results in a more uniform velocity distribution. Furthermore, the protrusion of the spear beyond the opening (to achieve the same flow) is larger for the Standard design, meaning a much more turbulent interchange between the free surface and spear immediately after exiting the nozzle, hence a delayed vena contracta in the Standard designs resulting in higher losses in the jet.

It should also be noted that with the steeper angled designs, there is an increased likelihood of jet breakup and droplet formation. These high velocity water droplets are known to cause damage to the runner and could become problematic for very high head applications. This has not been investigated at this stage but should be considered in future research.

In addition, these results go some way to demonstrate why experimentally (though not presented in this thesis) there is a difference in efficiency between the upper and lower injector achieved with the three designs, with lower injector on the whole being slightly less efficient, but the Novel 2 case being the most efficient configuration – indicating that a combination of Novel 1 for upper injector and Novel 2 for lower injector could lead to an inherently higher overall efficiency for this turbine setup.

7 Comparison of CFD and Experimental Results

In this chapter the CFD analysis in Chapter 4 and the experimental results presented in Chapter 5 will be compared and the capability of the CFD model to make a qualitative visual assessment of potential losses due to the casing will be commented upon.

Before comparing the numerical and experimental results, the mechanical losses in the Pelton system are estimated so they can be accounted for in the comparison.

The CFD models used in this research are verified in two ways:

1. Pelton full system modelling: Comparing the absolute experimental hydraulic efficiency to the numerical hydraulic efficiency, taking into account the losses through the pipework and injector as well as the impact of the resultant real jet profile on the runner performance.
2. Pelton injector modelling: By comparing the numerical improvements to the runner performance as a result of changes in the injector nozzle and spear geometry to the measured experimental improvements.

The naked case as the name implies contains no baffle plates and indeed it was the least efficient configuration for both upper, lower and twin jet operation, though for upper jet the spread of results for different housings were minimal so will provide a bench mark to analyse the overall flow patterns that appear from the Z120 runner.

7.1 Loss Analysis of a Typical Experiment

In order to provide a compendium of loss analysis and determine the losses due to the casing, the example of experiment E will be chosen, since it achieved the overall best efficiency results in the experiments for single and twin jet operation. The total efficiency η is composed of the individual efficiencies of the casing η_C , the mechanical losses η_M , losses due to the pipeline η_P , the nozzle η_N , and finally the runner η_R .

$$\eta = \eta_C \cdot \eta_M \cdot \eta_P \cdot \eta_N \cdot \eta_R \quad (7.1)$$

Therefore, it is important to try and quantify these losses in order to establish the casing losses. Firstly the mechanical losses are outlined in 7.1.1 and the pipeline, nozzle and runner losses are established in 7.1.2.

7.1.1 Mechanical Loss Estimation, η_M

The first consideration includes the mechanical losses in the system, which is a result of frictional losses within the bearings.

The mechanical friction torque M_M can be estimated from the mechanical loading on the bearings due to the force of the jets and weight of the runner. The measured torque M_T use to calculate the efficiency η is given by equation (7.2)

$$M_{T(Nj)} = N_j \cdot M_j - M_{M(Nj)} \quad (7.2)$$

For a number of jets, N_j , where M_j is the torque induced by each jet and M_M is the mechanical friction torque. M_M (7.3) can be defined as the sum of the bearing friction torque, M_B , which is dependent on which jet is used and the disc friction torque, M_D .

$$M_{M(Nj)} = M_D + M_{B(Nj)} \quad (7.3)$$

This disc friction torque is defined as the frictional torque arising from the frictional losses of the outer surface of the runner not in contact with the flow passage [108]. The assumption is made that this does not vary with the number of jets used.

7.1.1.1 Disc friction torque, M_D

The disc friction torque can be measured by rotating the turbine shaft at various speeds with and without the runner, since the Pelton used in the test rig at NTUA is the segmented Pelton [112] where the buckets can be removed from the hub, it can be tested with the hub only, and without the hub. Fig. 7-2 shows the test rig in operation with just the hub attached to the shaft. During the experimental injector testing, documented in 6.2 three additional tests were carried out to measure the torque against the rotational speed at $Q = 0 \text{ m}^3/\text{s}$ with 1) the full runner, 2) only the hub but no buckets and 3) no hub or buckets. Therefore, the torque measured with the runner will be the disc friction torque and without the runner the bearing losses, which can be subtracted from the total. The results of these tests are given in Fig. 7-1.

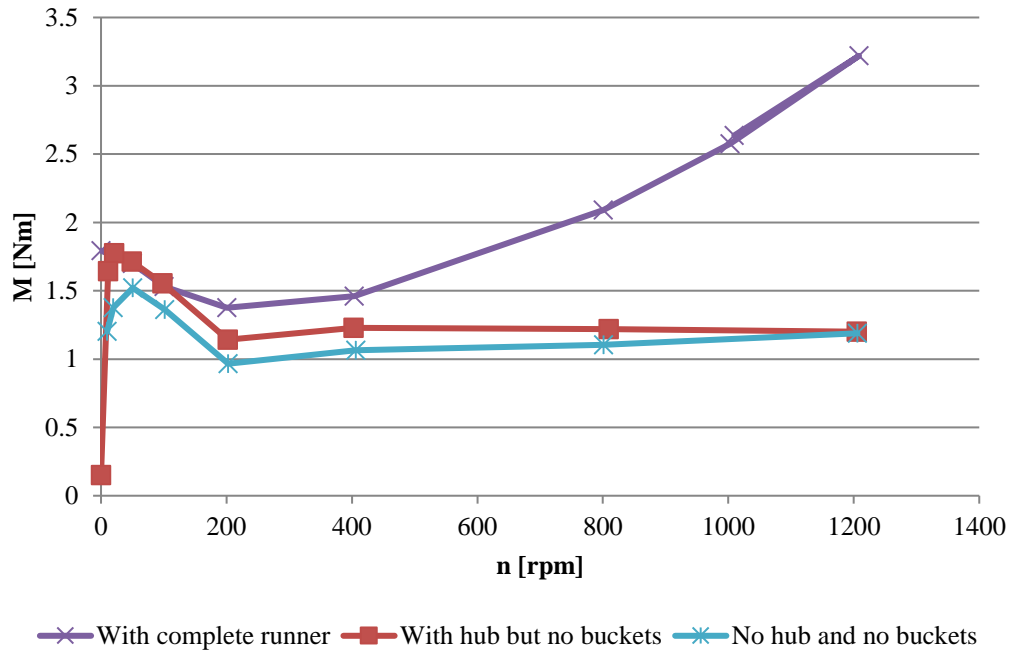


Fig. 7-1 Frictional torque vs rotational speed when $Q = 0 \text{ m}^3/\text{s}$



Fig. 7-2 Friction torque measurements with hub only [18]

Assuming that the bearing friction is not significantly affected by the loading as a result of mass of the runner (23.6 kg), the disk friction, M_D , can be approximated as:

$$M_D = M_f - M_s \quad (7.4)$$

Where M_f is the friction torque of the full runner in rotation and M_s is the friction torque from only the shaft rotating. At the BEP rotational speed, this gives a disk friction of $M_D = 2.4 - 1.1 = 1.3$ Nm.

7.1.1.2 Bearing friction torque, M_B

The hydraulic loads applied to the runner for a twin jet horizontal arrangement are shown in Fig. 7-3 below, where the loading force \mathbf{F}_J , for an ideal jet can be represented as:

$$\mathbf{F}_J = \dot{m} \cdot \mathbf{V} \quad (7.5)$$

Where \dot{m} is the mass flow rate of the fluid and \mathbf{V} is the velocity vector.

For twin jet machines with an angle θ between the jets, the resultant force of the upper jet, \mathbf{R}_{u1} , operation only is given in equation (7.6)

$$\mathbf{R}_{u1} = \sqrt{(\mathbf{F}_J \cos \beta)^2 + (\mathbf{F}_J \sin \beta + W_r)^2} \quad (7.6)$$

Where W_r is the runner weight (acting vertically downwards) and \mathbf{F}_J is the jet force acting downwards at an angle β to the horizontal.

For twin jet operation the resultant forces, \mathbf{R}_{u2} is given in equation (7.7).

$$\mathbf{R}_{u2} = \sqrt{(\mathbf{F}_R \cos \alpha)^2 + (W_r - \mathbf{F}_R \sin \alpha)^2} \quad (7.7)$$

Where $\mathbf{F}_R = 2(\mathbf{F}_J \cos \frac{\theta}{2})$ is the twin jet resultant hydraulic force acting upwards at angle α .

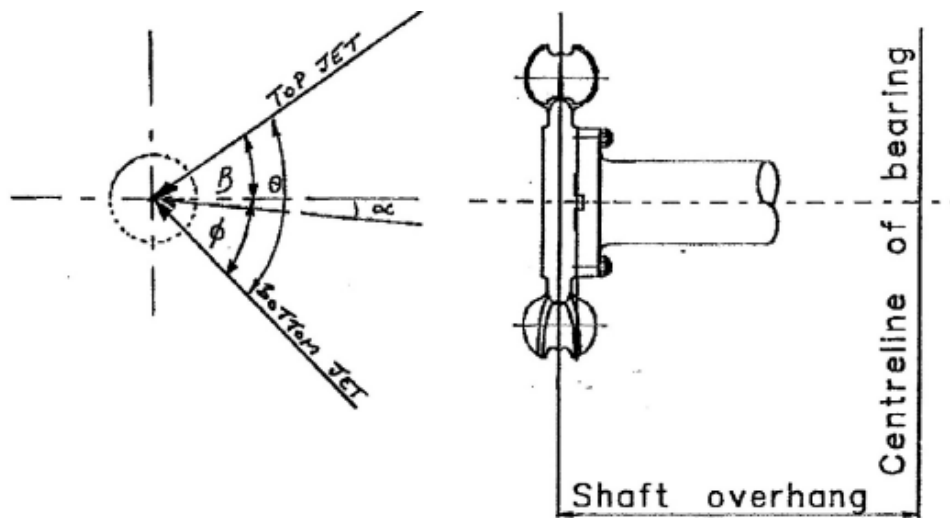


Fig. 7-3 Loads on the runner [113]

Since both the weight and jet loadings are in the same plane, these forces may be considered as radial loads. The axial thrust is very small so will not be calculated in this instance, however thrust bearings are fitted with capability of taking thrust in either direction.

Fig. 7-4 shows the bearing arrangements for the Pelton test rig, taken from the CAD model, and the details for each bearing are given below.

- Bearing 1 – B1 SKF Cylindrical Roller Bearing (SKF N 214 ECP) - designed to support radial loading
- Bearing 2 – B2 SKF Spherical Roller Bearing (SKF 22211 E) - designed to support axial and radial loading

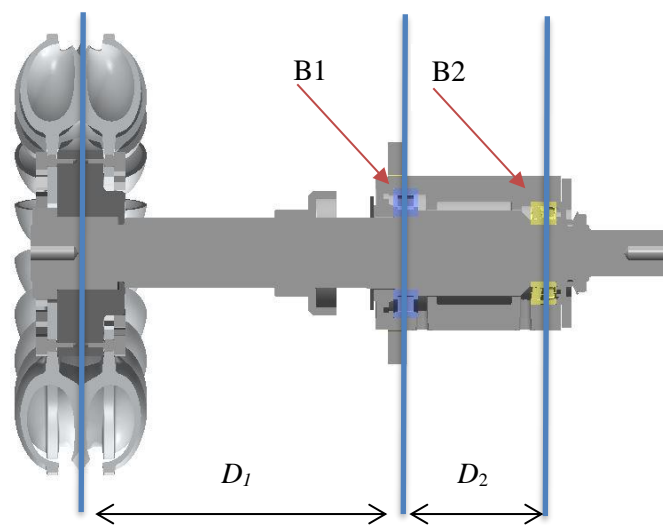


Fig. 7-4 Pelton test rig bearing arrangement

The test rig is equipped with an overhung bearing design with a radial (B1) and thrust (B2) bearing, and the associated bending moment diagram is shown in Fig. 7-5.

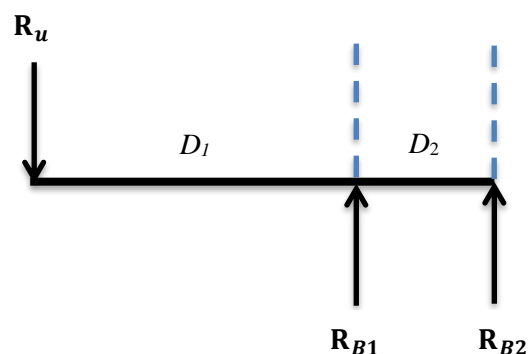


Fig. 7-5 Bending moment diagram for showing radial loads on bearings

Taking moments about B1:

$$\mathbf{R}_u \times D_1 = R_{B2} \times D_2 \text{ therefore, } R_{B2} = \frac{\mathbf{R}_u \times D_1}{D_2}$$

Taking moments about B2:

$$\mathbf{R}_u \times (D_1 + D_2) = R_{B1} \times D_2 \text{ therefore, } R_{B1} = \frac{\mathbf{R}_u \times (D_1 + D_2)}{D_2}$$

Where, R_{B1} is the load at bearing 1 and R_{B2} is the load at bearing 2.

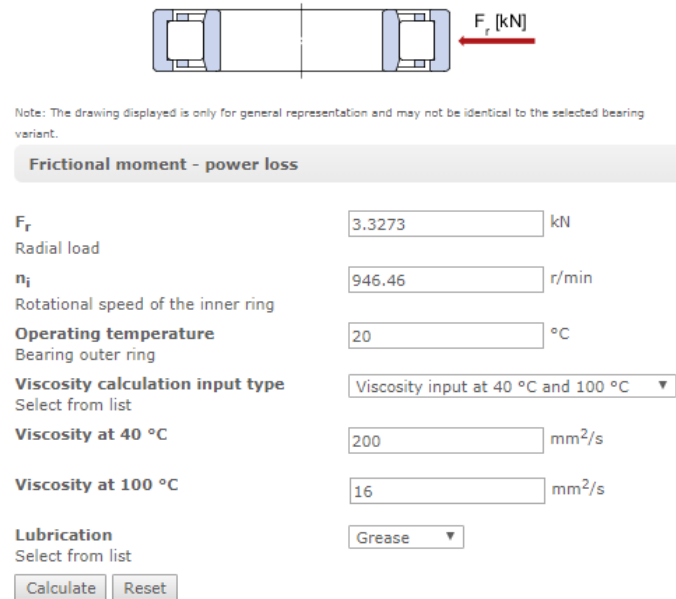
The forces acting on each bearing at the BEP conditions can be resolved using the equations, as shown in Table 7-1 below.

		$N_j = 1$	$N_j = 2$
\dot{m}	[kg/s]	24.4	48.8
H	[m]	60	60
v	[m/s]	34.3	34.3
$\beta = \phi$	[deg]	40	40
m_r	[kg]	23.6	23.6
W_r	[N]	231.5	231.5
$R_{u1,2}$	[N]	998.2	1298.2
D_1	[mm]	315	315
D_2	[mm]	135	135
R_{B1}	[N]	3327.3	4327.3
R_{B2}	[N]	2329.1	3029.1

Table 7-1 Bearing forces for single and twin jet operation

Once these values have been calculated the online tool *SKF Bearing Calculator* [114] can be used to estimate the bearing friction losses. The tool requires the following input data:

- The radial loads on each bearing- given in Table 7-1.
- The operating temperature- this was not measured, however a range of values are looked at in order to establish the impact of the temperature on the performance. The value used for the losses was taken as 40°C.
- Viscosity of lubricant- The lubricant used on these bearings is a Lithium soap, LGEP-2, which has a viscosity of 200mm²/s at 40°C and 16mm²/s at 100°C.



Note: The drawing displayed is only for general representation and may not be identical to the selected bearing variant.

Frictional moment - power loss

F_r
Radial load: 3.3273 kN

n_i
Rotational speed of the inner ring: 946.46 r/min

Operating temperature
Bearing outer ring: 20 °C

Viscosity calculation input type
Select from list: Viscosity input at 40 °C and 100 °C

Viscosity at 40 °C
200 mm²/s

Viscosity at 100 °C
16 mm²/s

Lubrication
Select from list: Grease

Calculate Reset

Fig. 7-6 SKF Bearing calculator tool, showing input values for BEP operation at 20°C

Thus, the frictional torque as a function of temperature for bearings 1 and 2 is plotted in Fig. 7-7.

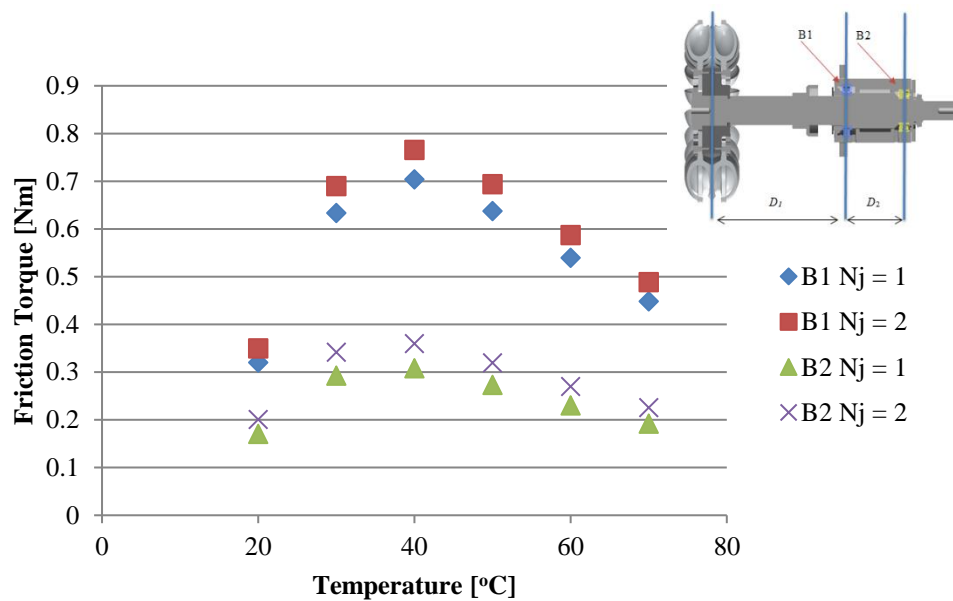


Fig. 7-7 The effect of temperature on bearing friction torque

In order to account for the worst case scenario an operating temperature of 40°C was chosen for the estimation. The resultant bearing friction torques are given in Table 7-2 below. The losses can be determined using M_B/M_t , where M_t is the total torque measured experimentally.

		$N_j = 1$	$N_j = 2$
M_{B1}	[Nm]	0.7037	0.7656
M_{B2}	[Nm]	0.3081	0.3595
$M_B = M_{B1} + M_{B2}$	[Nm]	1.012	1.125
M_t	[Nm]	125.09	234.44
M_B/M_t		0.81%	0.48%

Table 7-2 Bearing friction torques and losses approximated from the SKF bearing calculator

7.1.1.3 Mechanical Friction Torque, M_M

Since the mechanical friction torque, M_M is the sum of the bearing friction from Table 7-1 and disc friction, calculated in 7.1.1.1 the value can now be calculated using equation (7.3) as follows:

For single jet operation: $M_{M1} = 1.3 + 1.012 = 2.312$ Nm

For twin jet operation: $M_{M2} = 1.3 + 1.125 = 2.425$ Nm

Expressing this as a ratio between the friction torque and the total torque, $\frac{M_{M1}}{M_{t1}} = 1.848\%$ and $\frac{M_{M2}}{M_{t2}} = 1.0344\%$, for single and twin jet operation respectively. Therefore the mechanical losses, η_M can be calculated as follows.

$$\eta_M = 1 - \frac{M_{M1}}{M_{t1}} = 98.152\% \quad (7.8)$$

7.1.2 Pelton Turbine System Modelling

The full Pelton system can be broken down into three primary regions of analysis, which introduce hydraulic losses that will be experienced as nozzle losses, these are as follows:

1. Pipework Losses - this includes the bifurcation and pipe downstream of the pressure sensor, outlined in Fig. 7-8.
2. Nozzle Losses - this includes the full injector, which has been modelled in Chapter 8, where the losses at the BEP are predicted using CFD.
3. Runner Losses - this region includes the losses in the runner, which are modelled in Chapter 8 by combining the real jet velocity profiles as an inlet boundary condition to a runner simulation.

7.1.2.1 Pipeline Losses, η_p

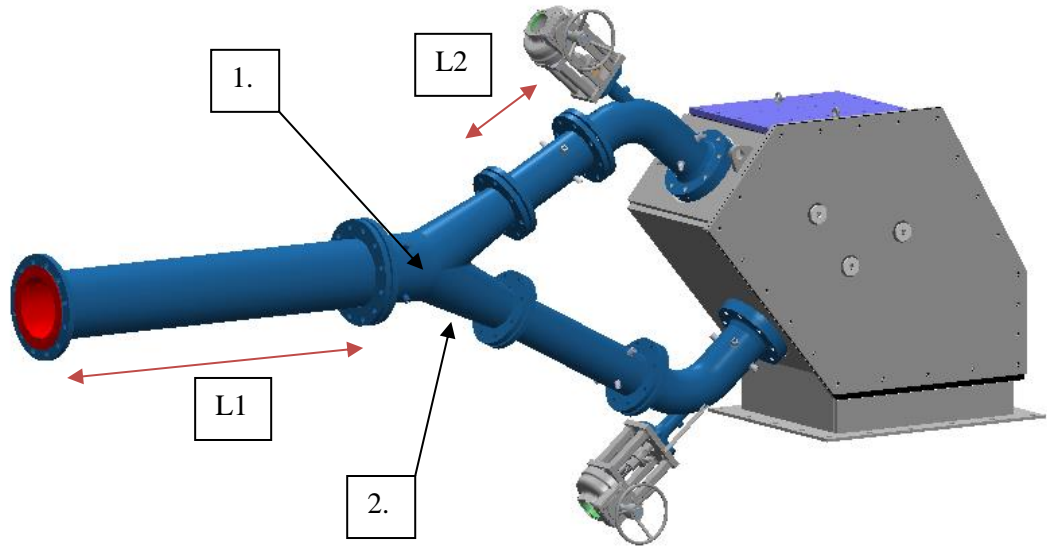


Fig. 7-8 Pelton test rig loss features and straight pipe sections for 1.

The flow in 1. can be generally assumed to follow well established phenomenological equations and can be approximated by examining the individual head losses for each component using the loss factors K .

$$h_l = K \cdot \frac{v^2}{2g} \quad (7.9)$$

Where v is the mean velocity in the pipe calculated from the internal diameter and the mass flow rate, which for the pipe L1 with 196 mm i.d. is calculated as 0.8 m/s and L2 with 128 mm i.d. is calculated as 1.88 m/s.

Region 1 can be broken down into 2 different loss features and 2 straight pipe sections as shown in Fig. 7-8. The loss features are defined as:

1. **Bifurcation:** This is treated as a 45deg metre bend as the lower injector is closed.
2. **Gradual contraction:** this is the section where the pipe diameter steps down from bifurcation to the 128 mm diameter pipe.

The loss factors (K) are given in for each feature and from these the head loss, h_l , can be calculated using equation (7.9). The head loss for each feature as well as the total head loss is shown in Table 7-3 below.

Loss feature	Loss factor (<i>K</i>)	Head loss (<i>h_l</i>)
1	0.20	0.036m
2	0.04	0.0072m
	Total	0.043m

Table 7-3 Head loss from loss features

The head loss from the straight pipe sections can be calculated using:

$$h_l = \frac{4flv^2}{2Dg} \quad (7.10)$$

Where *l* is the total pipe length, (*l*₁ + *l*₂), which is measured as 1.25 m and 0.39 m respectively, *D* is the pipe diameter. *f* is the Fanning friction factor determined by the surface roughness and Reynolds number. The relative surface roughness is equal to the average height of surface irregularities divided by the pipe diameter, Fig. 7-9 shows the corrosion on the inside of the pipe, a conservative estimate of the average height of irregularities would put this number somewhere in the region of 3 mm, which results in a relative roughness of 0.02. Therefore, *f*, is taken from a Moody diagram as 0.0123. This gives a head loss from the pipe section L1 = 0.0103 m and from L2 = 0.0267 giving a total as 0.037 m. The total head loss through region 1 can then be taken as 0.043 + 0.037 = 0.08 m, which equates to **0.13%** loss from the 60 m inlet pressure.



Fig. 7-9 Corrosion on the inside of L2 pipework

7.1.2.2 Nozzle Losses, η_N

The nozzle losses have been determined using a CFD analysis of the full 3D injector at the BEP, outlined in 6.1.2. For the Standard injector design, these losses are calculated as **1.8%**.

7.1.2.3 Runner Losses, η_R

One method of quantifying the nozzle and runner losses has already been explored in 6.4.2.1, where the real jet profiles at the BEP head and flow rate were imported into the runner simulation, therefore calculating the losses from the point beyond the bifurcation to the runner. This method therefore neglects the upstream losses beyond the bifurcation and the mechanical losses, however since these have already been approximated and measured respectively, they can be added to the nozzle and runner losses and by doing so the casing losses may be ascertained.

For the standard injector the numerical efficiency at the BEP was calculated and outlined in Table 6-10. The efficiency has now been normalised to **100%** for comparative purposes.

7.2 Total Efficiency Analysis

The total numerical hydraulic efficiency, η_{nh} , accounting for all the losses in the Pelton system can be calculated using equation (7.11) where η_R is normalised to 100%.

$$\eta_{nh} = \eta_P \cdot \eta_N \cdot \eta_R = 99.87 \times 98.2 \times 100 = 98.1 \% \quad (7.11)$$

The experimental hydraulic efficiency, η_{eh} , excluding the mechanical losses, η_M calculated in equation (7.8), can be calculated from the measured experimental efficiency, η , which has been normalised against η_R , as follows.

$$\eta_{eh} = \frac{\eta}{\eta_M} = \frac{98.58}{98.152} = \mathbf{100.44\%} \quad (7.12)$$

What this result shows is that the numerically predicted efficiency was 0.44 % lower than the efficiency, which was experimentally measured and corrected for the losses. This discrepancy is within the total uncertainty of the experiment as estimated in section 5.1.7. Since the splashing and water interference effect caused by the casing was not included in the CFD model it was expected that numerical results would over predict the efficiency. This indicates that either the CFD model is under predicting the torque or the mechanical or injector losses have been overestimated or more likely a combination of all of these factors.

Since the numerical and experimental results lie very close to each other and are both within the same margin of error another conclusion that can be made is that the effect of the casing is

practically negligible for this casing width. This would explain the flattening of the curves of efficiency with casing width, shown in Fig. 5-34, as the casing tends towards the widest width.

Secondly, these simulations were carried out using a 2-bucket model, which was found during the periodicity study in section 3.3.1.3 to give slightly lower efficiencies (0.12%) compared with the equivalent 6-bucket case. This suggests that using more buckets will increase the numerical efficiency. It is recommended that a larger runner section be modelled with a finer mesh in order to achieve a more accurate absolute numerical result although this will introduce a much higher computational cost.

7.3 Limitations of the CFD modelling

Numerical modelling, mesh generation, computational solving all inherently introduces uncertainties and numerical errors. There are a number of uncertainties, which can be summarised as follows [115] [116]:

1. Physical approximation error due to uncertainty in the formulation of the model (physical modelling error) and deliberate simplifications of the model (geometry modelling error).
2. Computer round-off errors develop with the representation of floating point numbers on the computer and the accuracy at which the numbers are stored. When compared with other errors these are often considered to be negligible.
3. Iterative convergence error exists because the iterative methods used in the simulation must have a stopping point eventually.
4. The discretisation errors are those that occur from the representation of the governing flow equations and other physical models as algebraic expressions in a discrete domain of space and time.
5. Computer programming errors are “bugs” and mistakes made in programming or writing the code.
6. User errors are caused by negligence, lack of knowledge of the complex computational code and of physical phenomena as simplifications are made due to computational cost and lack of resources.

During the computational modelling, decisions related to the methodology were made in order to produce reliable results in a reasonable timeframe, therefore a number of simplifications were introduced. Nonetheless, the methodology has been systematic, followed established guidelines and recognised methods, and wherever possible further simulations were carried out to estimate uncertainties.

The total computational error calculated using the root-sum-square method is 0.97%. However, it is highly likely there are further errors imposed due to the turbulence modelling. During the mesh generation process the first layer height (as outlined in the y^+ explanation in section 3.2.2.1) was kept the same, therefore the level of turbulence resolution will be the same for all three meshes. This is important as the torque will be highly dependent on the appropriate selection of turbulence models and adequate mesh resolution, particularly in the bucket regions where the flow undergoes high shear stresses, such as immediately below the splitter. Although the chosen turbulence model was compared to other Two-Equation RANS models, it was not compared to a Scale Resolving Simulation model such as Large Eddy Simulation which would be more accurate but also computationally more expensive. Furthermore, at this point in time the possibility of using an inviscid¹⁹ solver has been explored, the torque curves comparing the 6 bucket model run using the RANS $k-\epsilon$ and using the inviscid model are shown in Fig. 7-10. Furthermore, the efficiency predicted with this method, normalised to the coarse mesh in 3.4.2, is 102.4%.

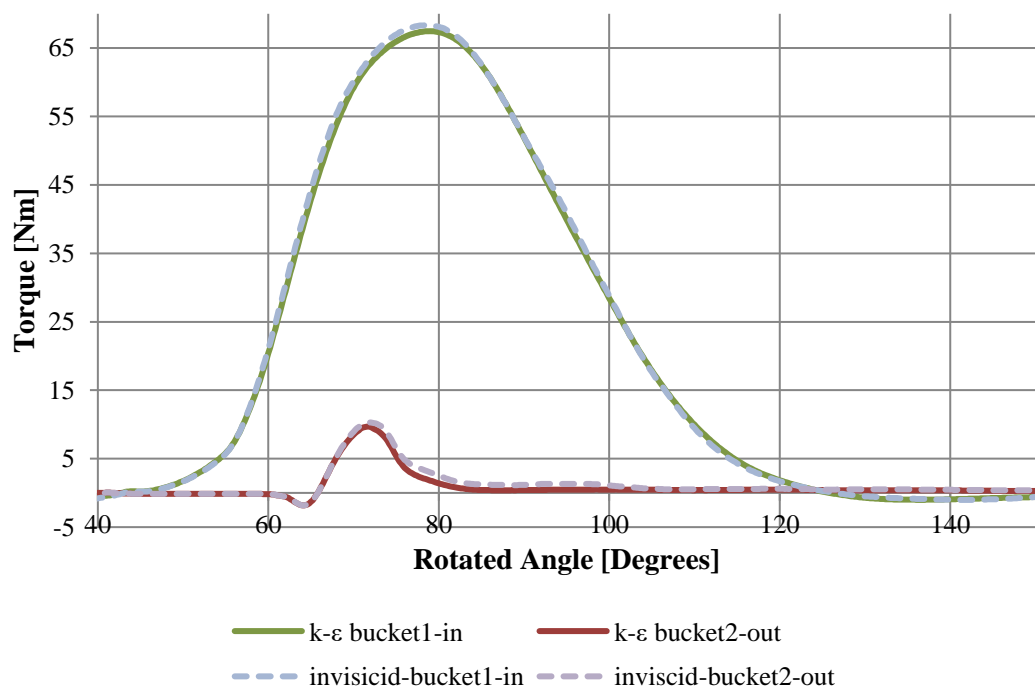


Fig. 7-10 Torque curves comparison of 6-bucket runner simulation with different turbulence models

Discretisation errors caused by the mesh are unpredictable but can be extreme. This error can be quantified and reduced considerably by carrying out successive mesh refinement, using

¹⁹ Inviscid solvers neglect the effect of viscosity on the flow and are appropriate for high-Reynolds-number applications where inertial forces tend to dominate viscous forces [35].

different types of grids and searching for grid-independent solutions. A recognised method for the uniform reporting of mesh refinement studies [103] was performed in sections 3.4.2 and 6.4.2 and the solutions were well within the asymptotic range. However, the runner mesh is unstructured due to a combination of limitations imposed by the ANSYS® Meshing® software and the complex geometry, and as such any discretisation errors could be carried forward through the mesh refinement study. Furthermore, the methodology used in section 6.4.2, whereby the exported jet profile is imported into a separate runner simulation introduces further errors as a result of interpolation, since the cells in the two separate meshes are not aligned and therefore a certain level of false numerical diffusion will be observed due the importing of the free-surface data onto different cell locations. The diffusion could have a dampening effect whereby the kinetic energy of the jet will be slightly lower in the runner simulation as opposed to the jet simulation and therefore the efficiency will be lower as a result.

7.4 Summary of CFD and Experimental Comparison

This chapter has attempted to ascertain the absolute efficiency losses due to the casing by examining the differences in the numerical and experimental efficiencies. This was done by estimating the mechanical losses of the Pelton test rig in order to calculate the experimental hydraulic efficiency, η_{eh} . The losses in the pipework upstream of the injector were then estimated using pipe flow equations which were combined with the losses through the full 3D injector and the runner simulation using the real jet profile giving the numerical hydraulic efficiency, η_{nh} . Comparing these two values showed the numerical models to be under predicting the efficiency by 0.44%, which is inside of the total experimental uncertainty of 0.6% and the total numerical uncertainty of 0.97%.

From this several conclusions can be drawn, firstly it is likely that the numerical torque is being under predicted and several reasons for this have been outlined. Another possibility is that at this width the casing effects are largely negligible (indeed Phase 1 testing indicated a difference of $\approx 0.5\%$ between tests A – H as opposed to Phase 2, which took the most efficient combination from tests A – H, and established a difference of $\approx 3\%$ in efficiency from the widest to narrowest widths).

8 Secondary Investigation of Casing Design

In this chapter the development of the Lancaster University Pelton test rig is documented. Approximately half way through the PhD program it became apparent that a second case study test rig to enable investigation of the effect of casing design on turbine performance was required. The test rig would enable analysis of casing flow in a much more generic way that was not possible in the NTUA laboratory, more specifically its oversized nature meant it was not restricted by existing casing geometry features. Also, a Perspex casing meant that much more flow visualisation was possible. The Lancaster test rig also serves as a second test rig in which to establish the means to demonstrate the versatility of the CFD model and make similar predications of the effects of casing geometry, which can be verified by flow visualisations and experimental testing

8.1 Lancaster University Test Rig

The design of the Lancaster University Pelton test rig has been outlined previously in section 2.3.2. It consists of a considerably oversized casing made of Perspex and unlike a typical Pelton turbine, the nozzles are fixed and there is no spear or spear rod to regulate the flow, therefore only a single flow rate is possible from the set operating pressure.

The test rig was designed and established by the author, the purpose of having a second test rig was to enable the investigation and analysis of more generic designs that can be carried out more easily and in shorter timescales. It also provides a second case study in which to explore and demonstrate the versatility of the CFD modelling methods developed in Chapter 3. However, it should be noted that it was manufactured with a very limited budget and does not meet IEC standards, therefore no assessment of the uncertainties will be given and the experimental results should be treated with some caution.

8.2 Proposed Tests

The proposed tests 1- 8, outlined in the following pages, resulted from observations made during the testing in NTUA, detailed in Chapter 5. Following the experimental testing it was concluded that the Side Shrouds have a slightly negative impact on performance for both upper and lower jet operation and are only marginally detrimental for twin jet. These SSs are both cumbersome but also difficult and expensive to install and questions have been raised in previous reporting as to when they become effective.

Observing the location of the SS in situ, shown in Fig. 8-1, it is logical to determine that all these will simply do is redirect the majority of the water that leaves the runner towards the

highlighted edge and consequently towards the lower injector, hence why the lower jet achieves inferior efficiency than the upper jet.

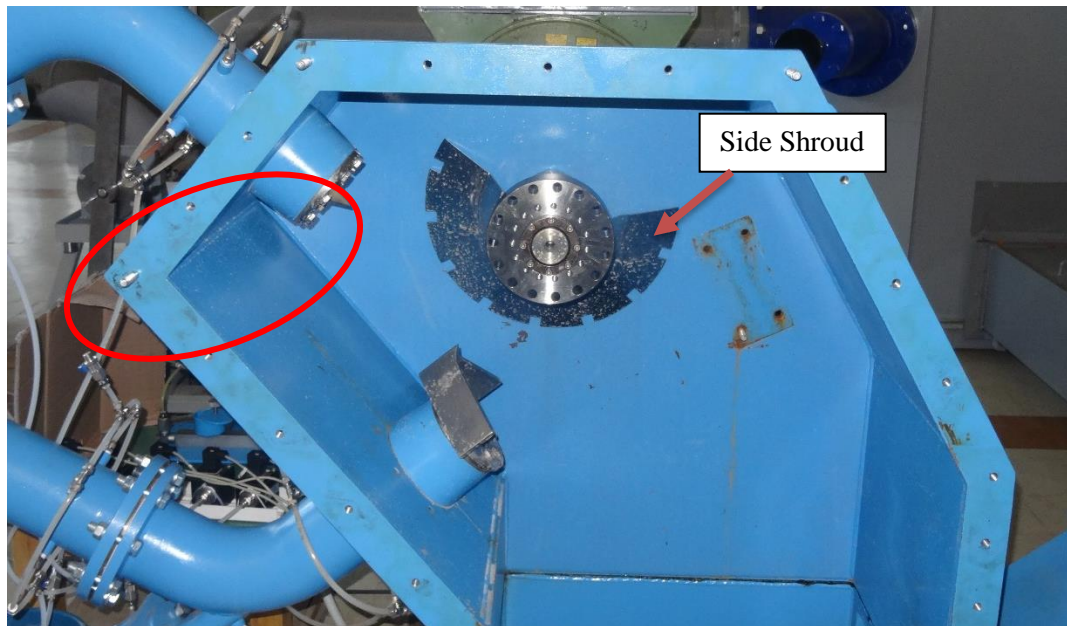
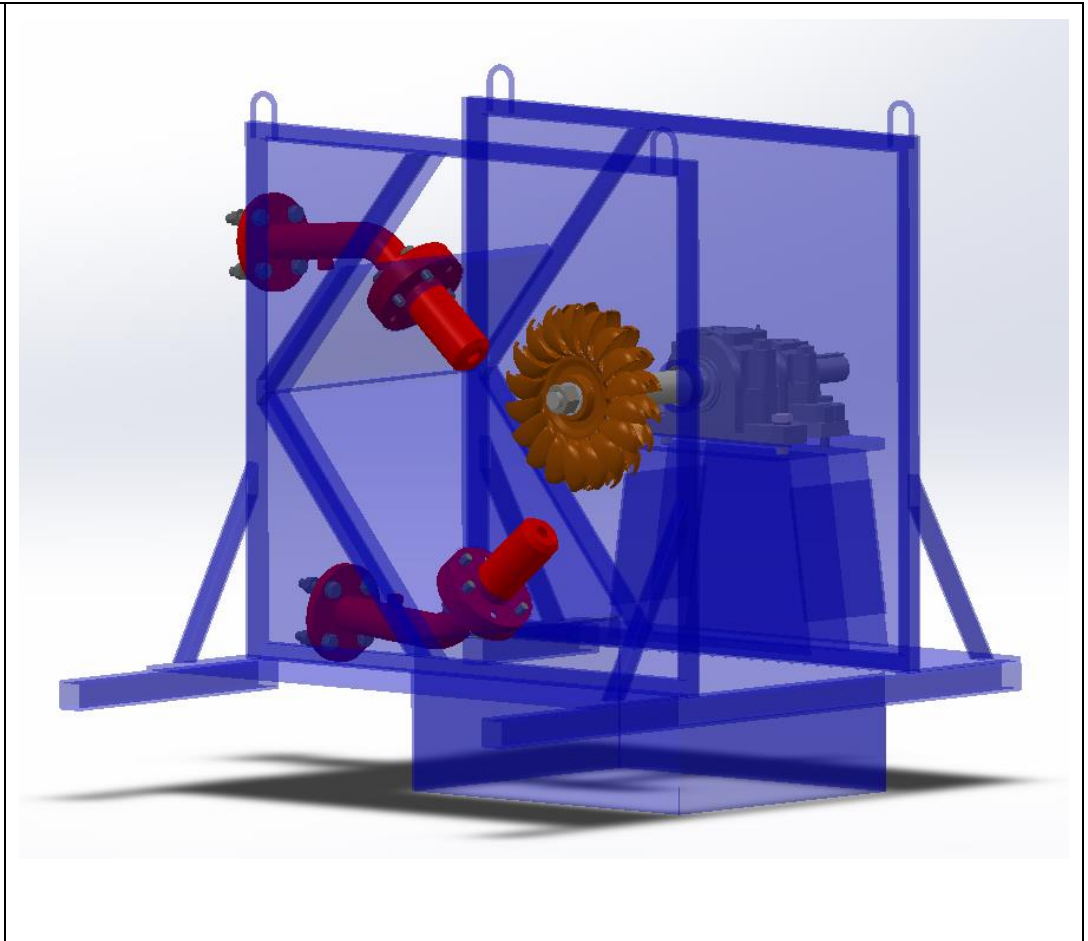
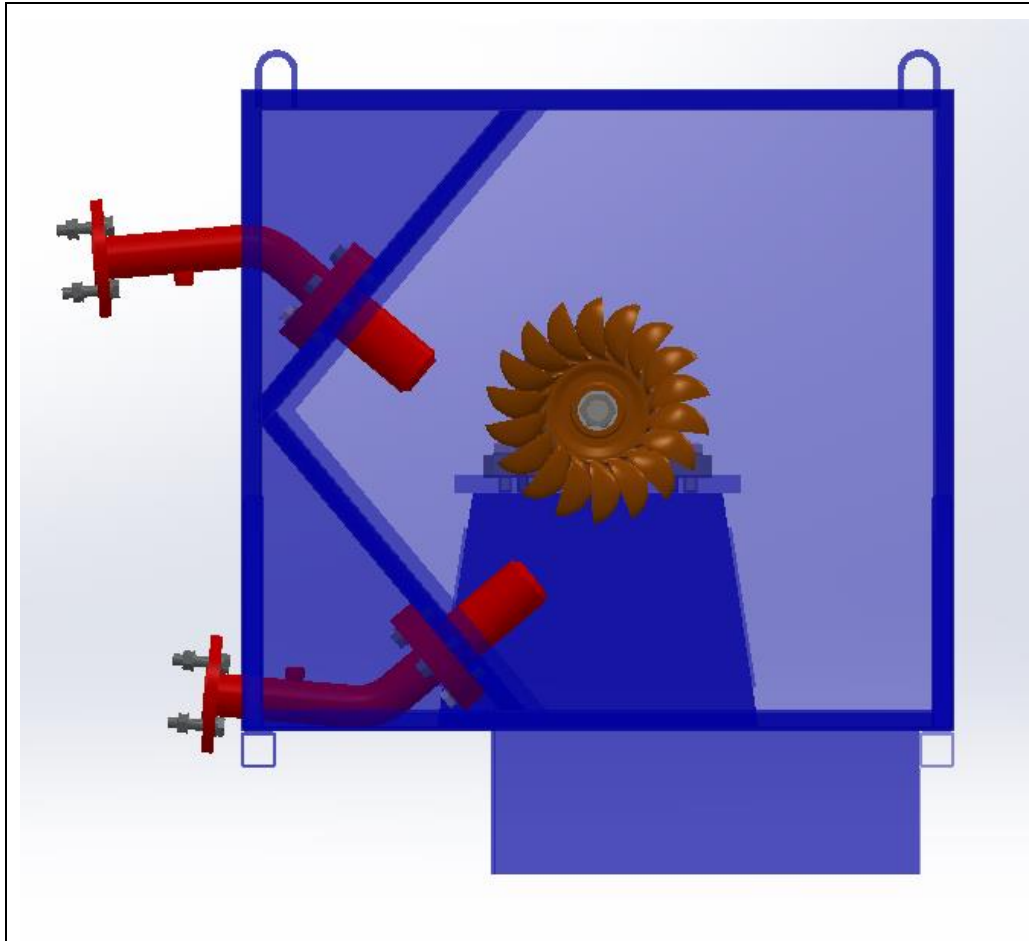


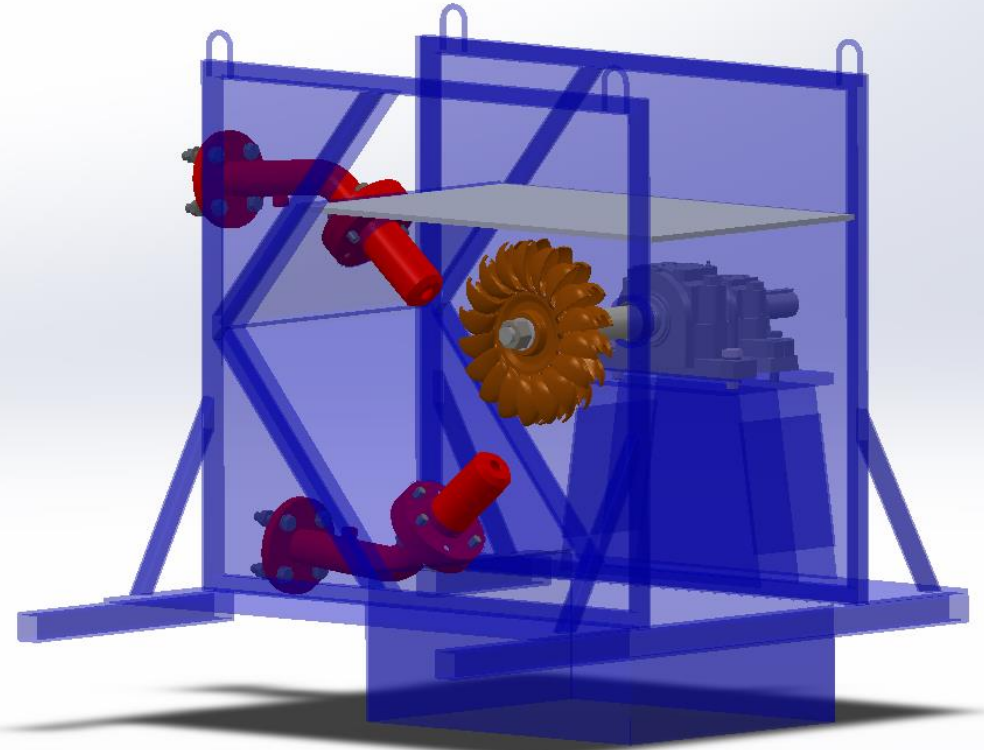
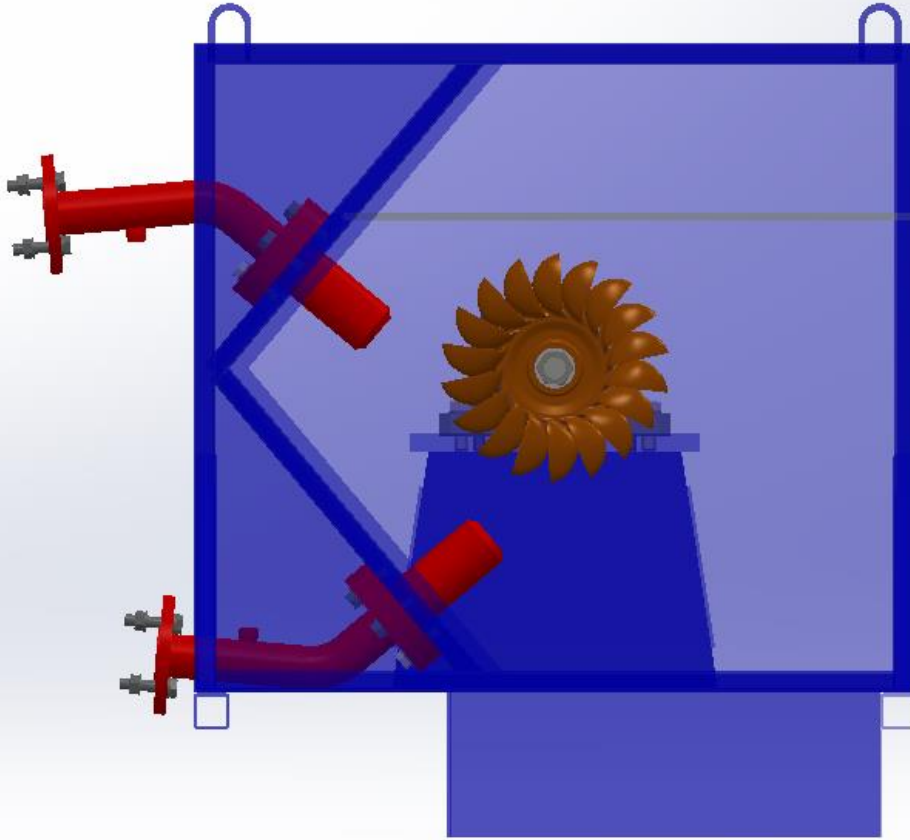
Fig. 8-1 Side Shroud in construction in the Z120 test rig

It should be noted that test 4, 6 and 7 are not included as these were repeat tests and therefore need not be described in any detail.



Test #1

Test #1: the naked test case
Time required: 1/2 day



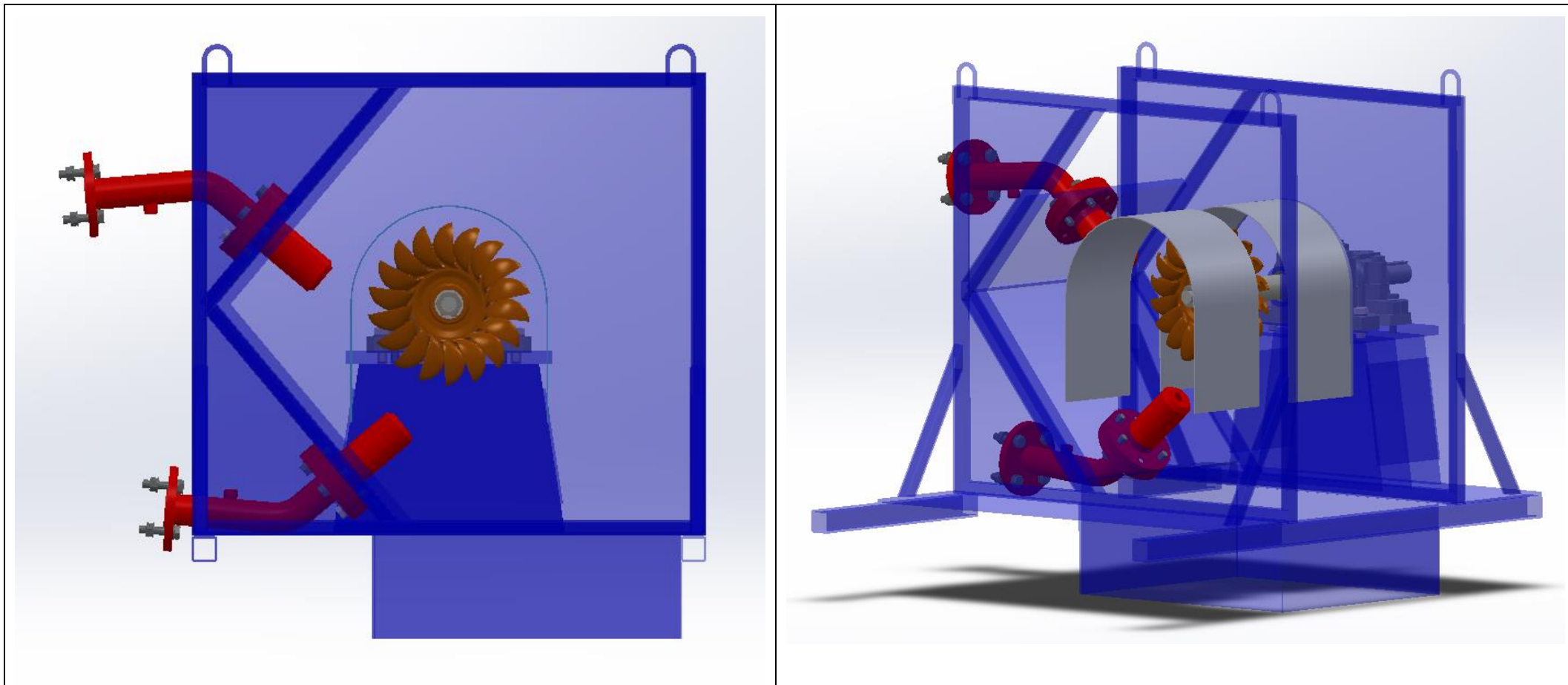
Test #2

Test #2: naked case with flat roof as in Athens dimensions

Material required: 1 x 10 mm acrylic 580 x 900 mm (in stock)

Time required: ½ construction and ½ day testing

Notes: the top lid represents the casing geometry as found in the Athens test rig



Test #3

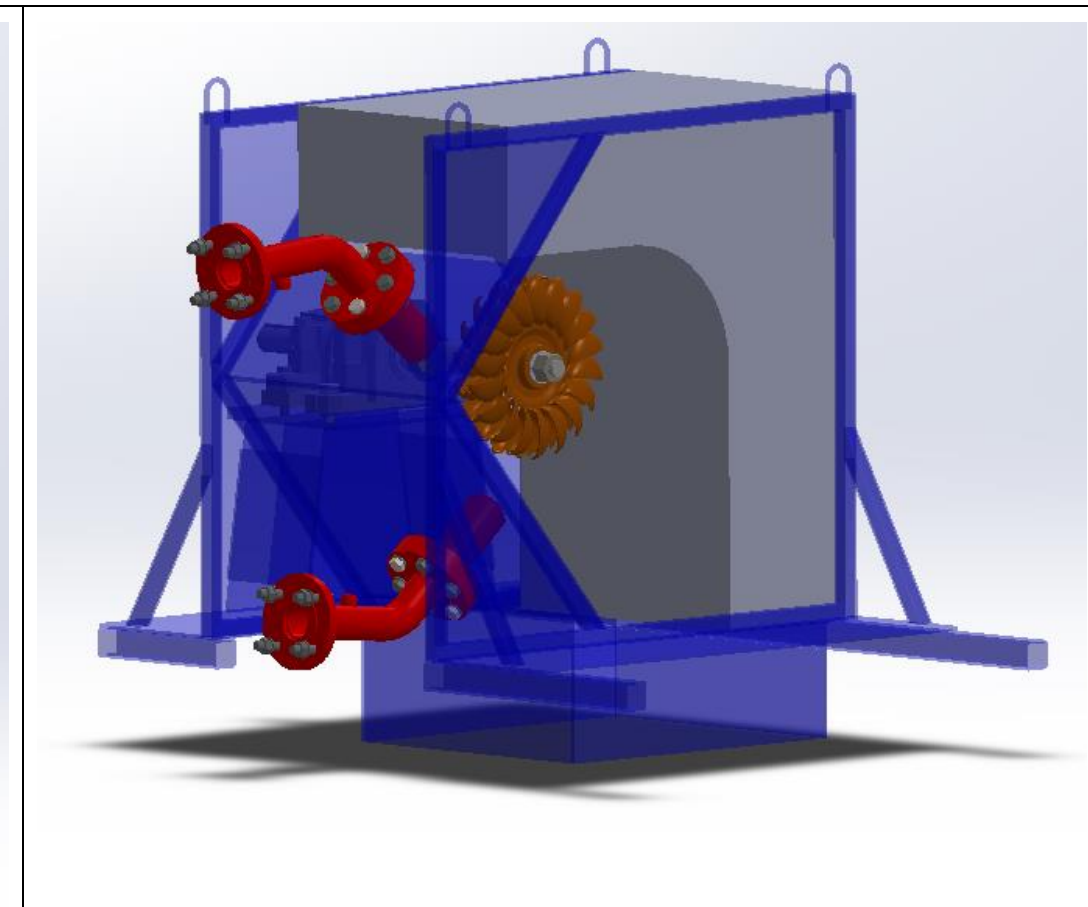
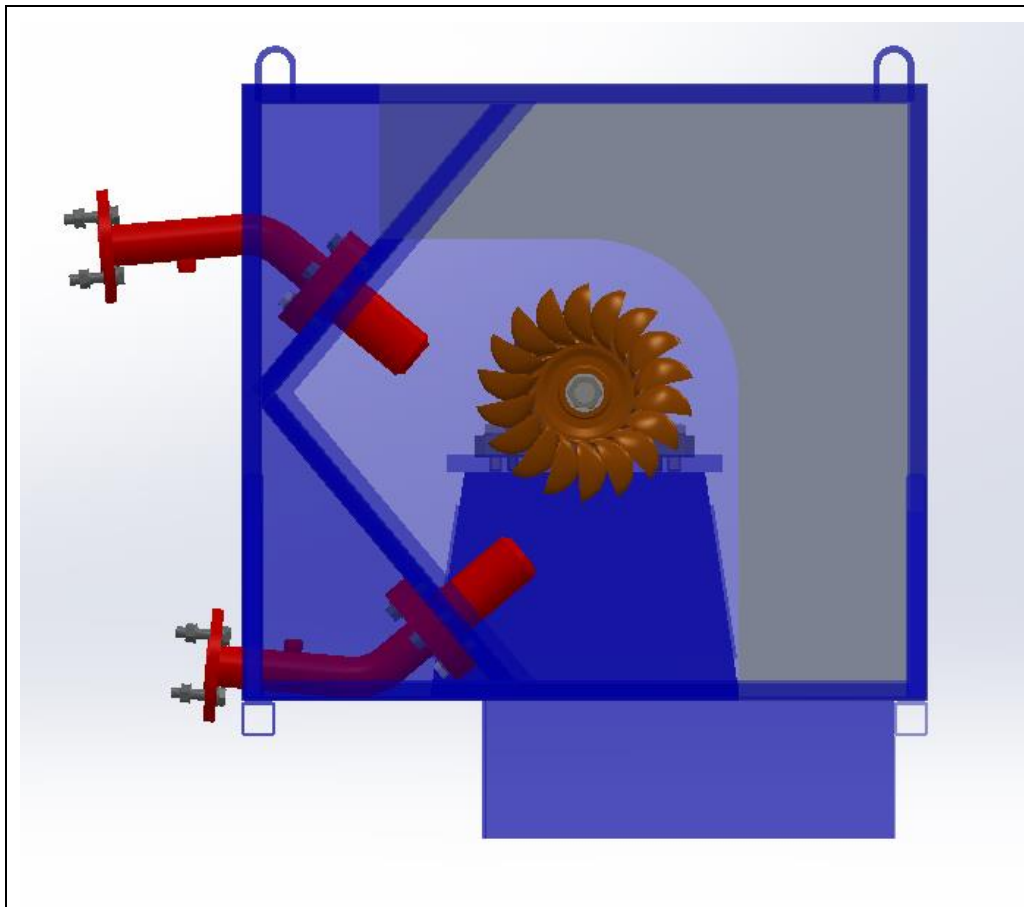
Test #3: new side shroud design 1

Material required: 2 x 3mm Aluminium sheet 1050 x 210 mm

Time required: ½ day construction and ½ day test

Notes: the side shroud radius is ½ bucket width wider than the outer diameter of the runner. The panel will be secured at either end by corner brackets and at the top by longer stud bolts either side of the metal panel. If need be to aid strength bracing strips will be attached between the two shrouds.

Background: from observations made in previous testing it would appear that the side shrouds are ineffective. Their truncated conical shape with the larger diameter at the casing wall meant that the water leaving the runner was redirected towards the nozzles, particularly the lower jet causing interference. Therefore, the new proposed insert for test #3 aims to do the opposite by funnelling the water away from the runner and restricting its path when it reaches the casing wall.



Test #5

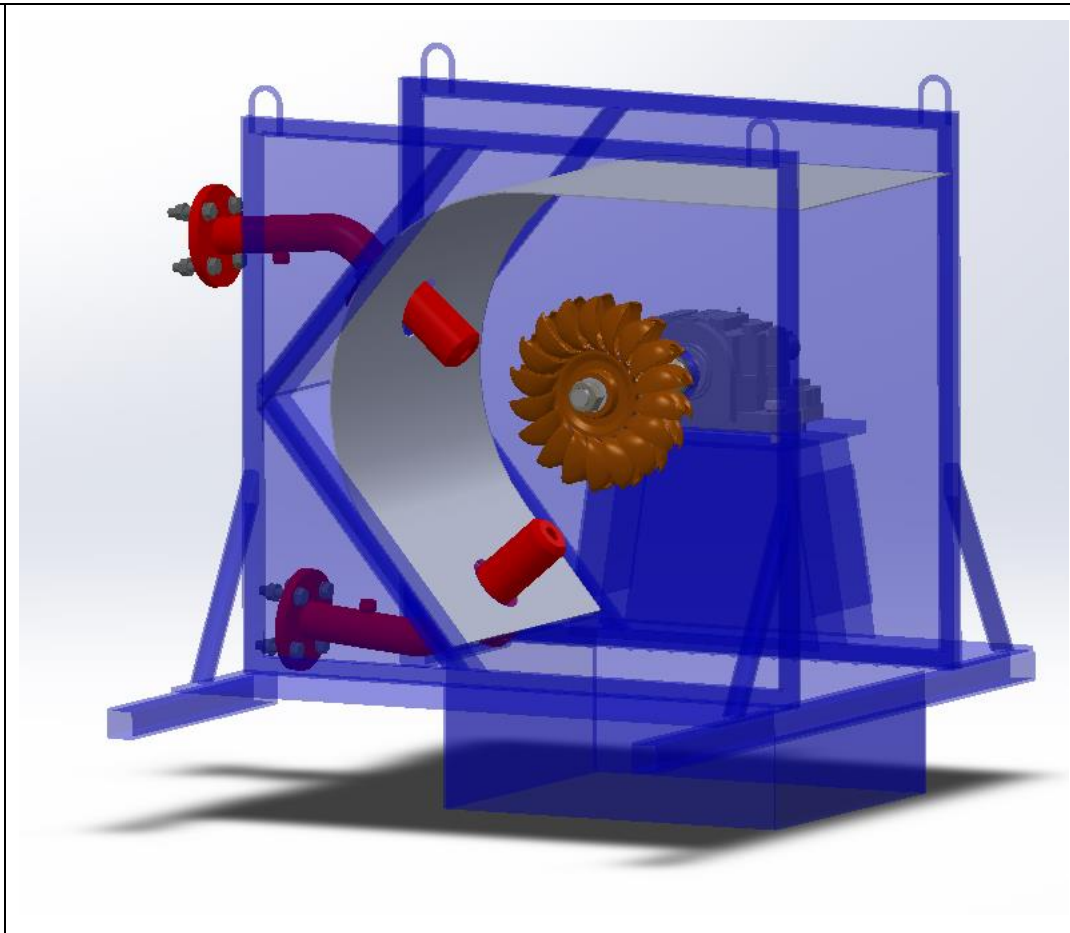
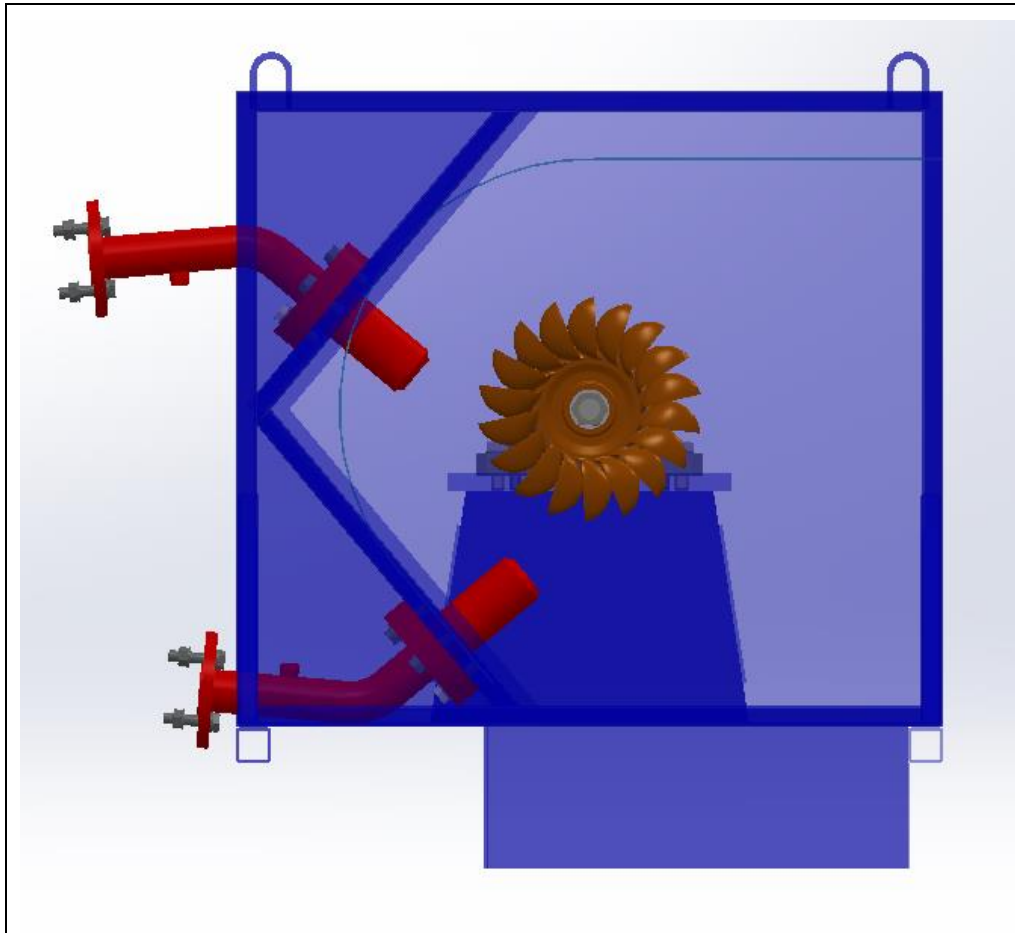
Test #5: bolt on baffle analysis 1

Material required: 1 x 3mm Aluminium sheet 1100 x 510 mm and foam former

Time required: 1 day construction and ½ day test

Notes: the baffle radius is 1 bucket width wider than the outer diameter of the runner

Background: it was noted in the literature that the casing in the upper half of the runner need only be a very small axial and radial opening between the casing and the runner. It is also noted by Nechleba 'a wiper must be arranged behind the discharge side of the wheel' [5], which in the role fulfilled by the bolt on baffle. Therefore the purpose of the insert for test #5 is to incorporate the role of the bolt on baffle as an integral component of the casing wall. Starting with 1 bucket width radius between the runner and casing.



Test #8

Test #8: curved side 1

Material required: 1 x 3mm Aluminium sheet 1500 x 510 mm

Time required: 1 day construction and ½ day test

Notes: the curved side radius is to the extent of the casing, however is very close to 3 bucket width wider than the outer diameter of the runner. The panel will be secured at either end by corner brackets and at the various points along the length by longer stud bolts either side of the metal panel.

Background: the proposed insert for test #8 is a curved side that reaches the extent of the casing wall. Depending on operating speed the water leaving the runner, particularly from the upper jet, hits the top edge of the casing wall, which can then fall back onto the nozzle. The objective of the insert of test #8 is to ensure that the water cascades down the walls and does not bounce back off the edges causing spray and mist within the casing.

8.3 Results of Experimental Tests

The graphs for twin, lower and upper jet testing results are shown in Fig. 8-2, Fig. 8-3 and Fig. 8-4, respectively.

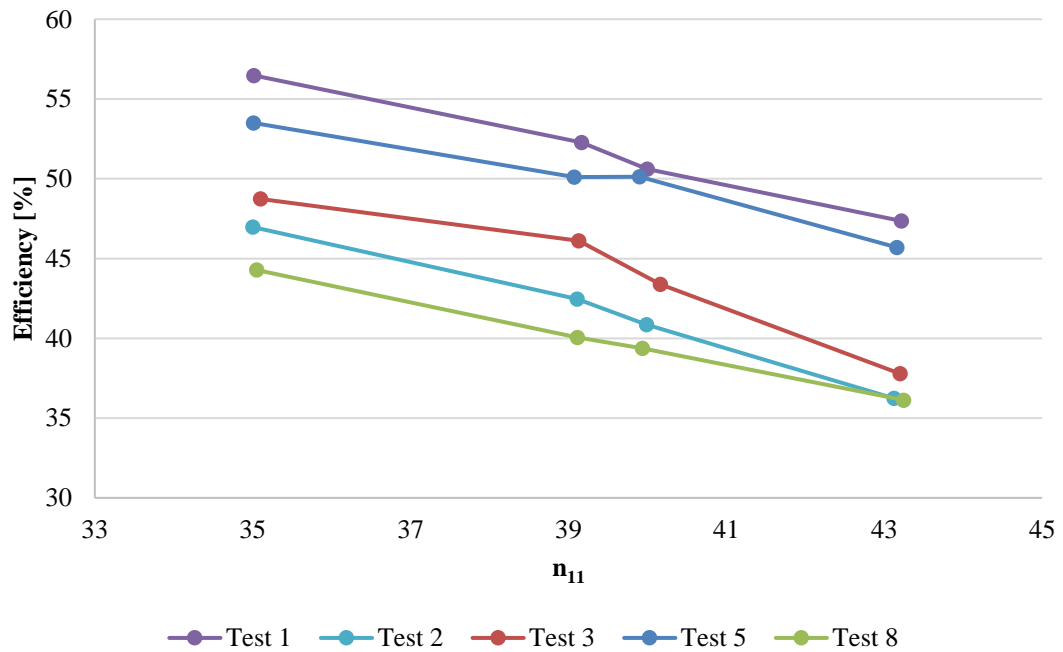


Fig. 8-2 Twin jet testing results across a range of rotational speeds at 20 m head

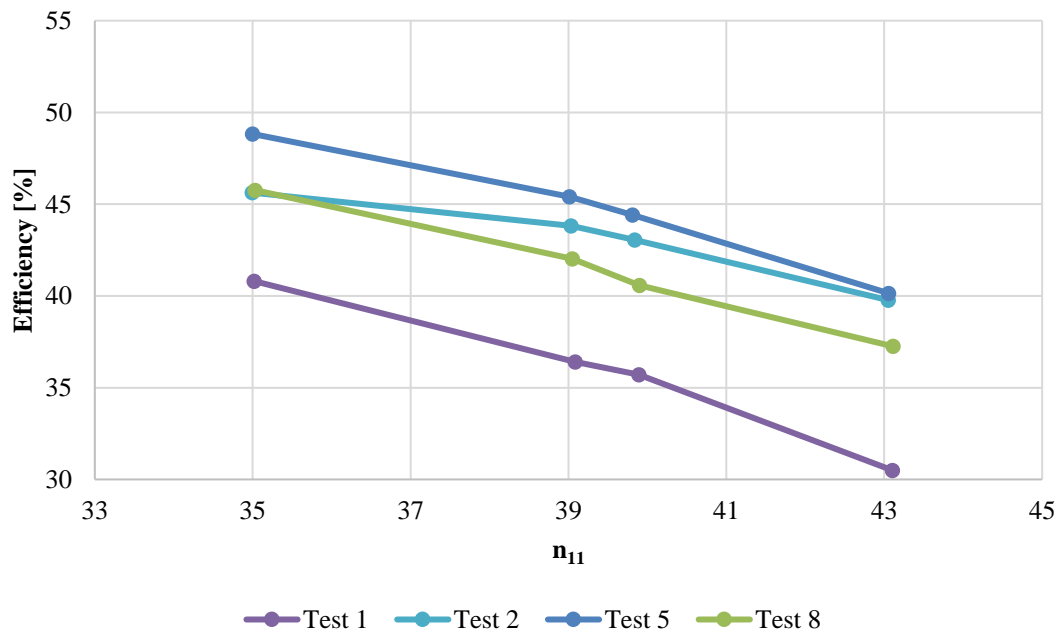


Fig. 8-3 Lower jet testing results across a range of rotational speeds at 20 m head

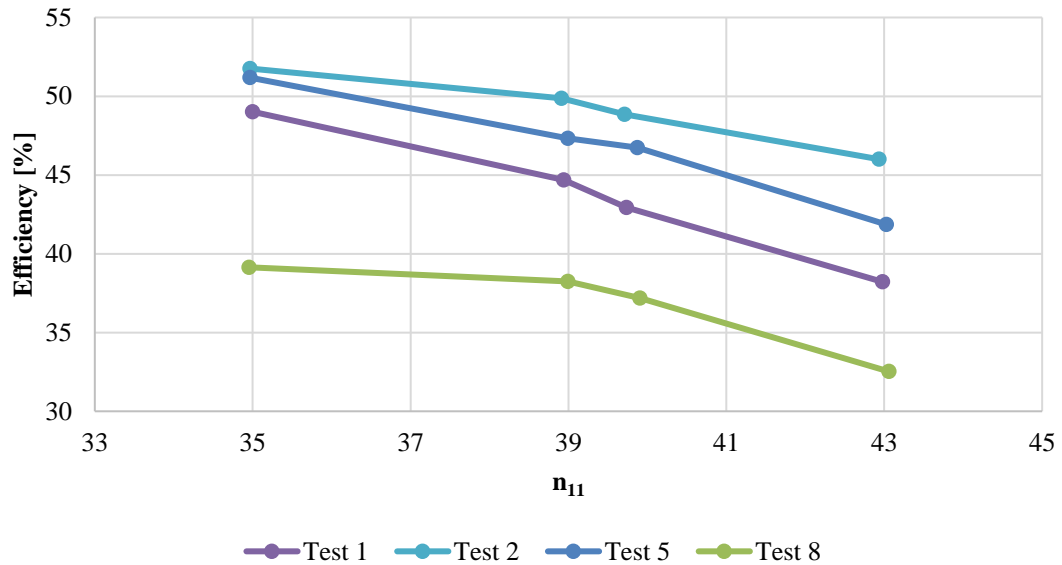


Fig. 8-4 Upper jet testing results across a range of rotational speeds at 20 m head

What is most prominent from the testing is that the efficiency variation is quite large, ~10% from maximum to minimum across all speeds, this is much larger than was measured during the previous experimental testing outlined in Chapter 5. What is also more apparent is that the water leaving appears to be much more ‘irregular’, the surface is not as well defined as the Z120 runner, there appears to be more entrained air and the water dissipates into a number of defined streak lines and mist.

Perhaps the most interesting result is that the completely naked case of test #1 is the most efficient, however strictly speaking the casing configuration most closely resembling the naked case of the Z120 NTUA Pelton test rig is test #2, which is the second from least efficient.

8.4 Visual Documentation of Results

The Lancaster test rig was equipped with a Go-Pro camera fitted above the nozzles, which provided an internal view of the flow within the casing. External images were obtained by means of a digital SLR camera. In the course of the experiments it was found that the camera shutter speed of 1/10,000 s gave a good temporal resolution. At this exposure time the direction and movement of the water masses can be observed since the water droplets can easily be distinguished at this short shutter duration. With a longer exposure time the water motion appears as a white blur. The visual observations during the experiments were made (at night, i.e. no ambient light) by means of two LED floodlights directed from the top and side walls of the casing in order to avoid glare on the Perspex walls of the casing where the photographs are taken.

When describing the direction of flow, for convenience some locations are defined as follows in Fig. 8-5.

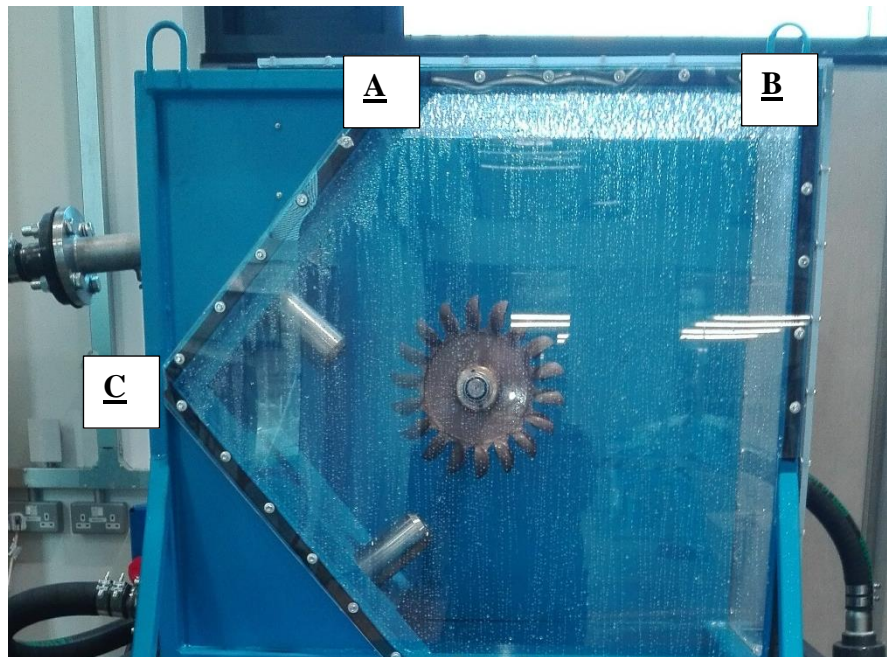


Fig. 8-5 Lancaster Test rig locations

8.4.1 Analysis of Test #1

For lower jet operation at all speeds, the majority of the flow hits the front wall of the casing and the remaining portion hits the top right hand corner at B. At this head and casing width the water tends to cascade down the side walls with little interference with the injectors. At the BEP speed the portion of the flow that hits the top right hand side of the casing tends to recirculate and fall back down onto the runner as is visible from the internal camera images as shown in Fig. 8-6, Fig. 8-7 and Fig. 8-8.

At lower rotational speeds the water leaves the bucket with a considerable radial velocity in the direction back towards the nozzles, which draws it around in an elliptical direction towards the split line at C. This water is then halted from moving any further and cascades down the side wall into the tailrace. As the speed increases this effect is less pronounced. A considerable portion also leaves at a relatively high angle towards B, one could question whether the bolt on baffle with the scraper would indeed be as effective with the Jubilee Pelton, which exhibits a much more ‘irregular’ flow as it would require a very close proximity to the runner and could induce a choking effect.

For upper jet operation at all speeds the water leaves the runner in a crescent shape, with the water making impact with the casing at roughly point A. The internal images show that this

crescent shape means that a large portion of the water is directed towards the right hand wall of the casing B, though some of the flow spreads across the front face and runs down the side walls, though at this head and casing width it misses the injectors.

Unfortunately getting clear images for all of the testing has been difficult. For external images the Perspex side is very prone to reflection, which means that during the afternoon the south facing windows in the laboratory make it very difficult to obtain clear images. The splashing inside the casing also means that acquiring a clear image from the internal camera is difficult. It is perhaps interesting to note that the splashing on the internal camera appears more prominent during lower jet operation, the likely reason for this is due to the large droplets, shown in Fig. 8-9, that form on the roof of the casing as the water hits the top right hand corner B.



Fig. 8-6 Test #1 lower jet $n_{11} = 35$ rpm



Fig. 8-7 Test #1 lower jet $n_{11} = 39$ rpm



Fig. 8-8 Test #1 lower jet $n_{11} = 43$ rpm



Fig. 8-9 Droplets on casing roof



Fig. 8-10 Test #1 upper jet $n_{11} = 35$ rpm

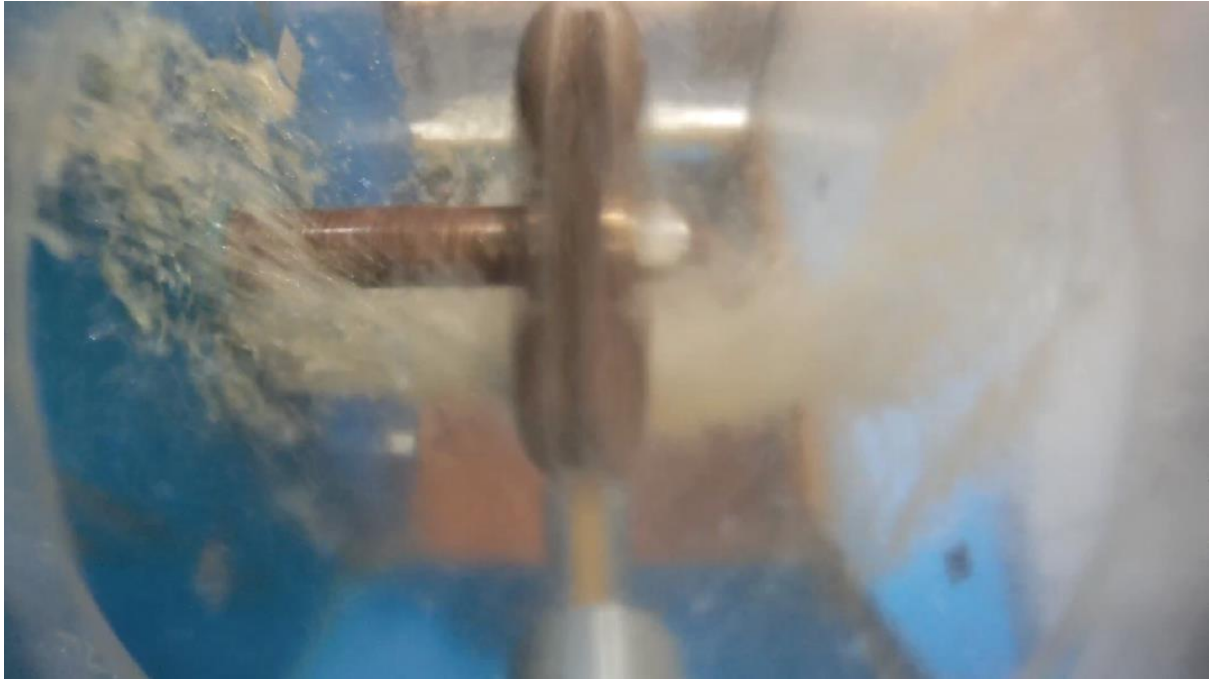


Fig. 8-11 Test #1 Upper jet $n_{11} = 39$ rpm



Fig. 8-12 Test #1 Upper jet $n_{11} = 43$ rpm

Experimental testing was carried out at a reduced width; however the quantitative results are not presented here. The Lancaster test rig has nonetheless offered the opportunity for flow visualisation results. For example, Fig. 8-13 shows the upper jet operation at the BEP for 20 m pressure head at 310 mm and 140 mm wide casing. The most significant difference is the flow that appears around the right hand side of the runner in the reduced width casing, which would

lead to efficiency losses. The water sheet appears to have a similar shape along the front face of the casing, however in the 140 mm casing there is a greater accumulation of water in the casing since the available volume is smaller (the red lines copied from 320 mm). However with a wider casing the splashing and runner entrainment will be significantly reduced.

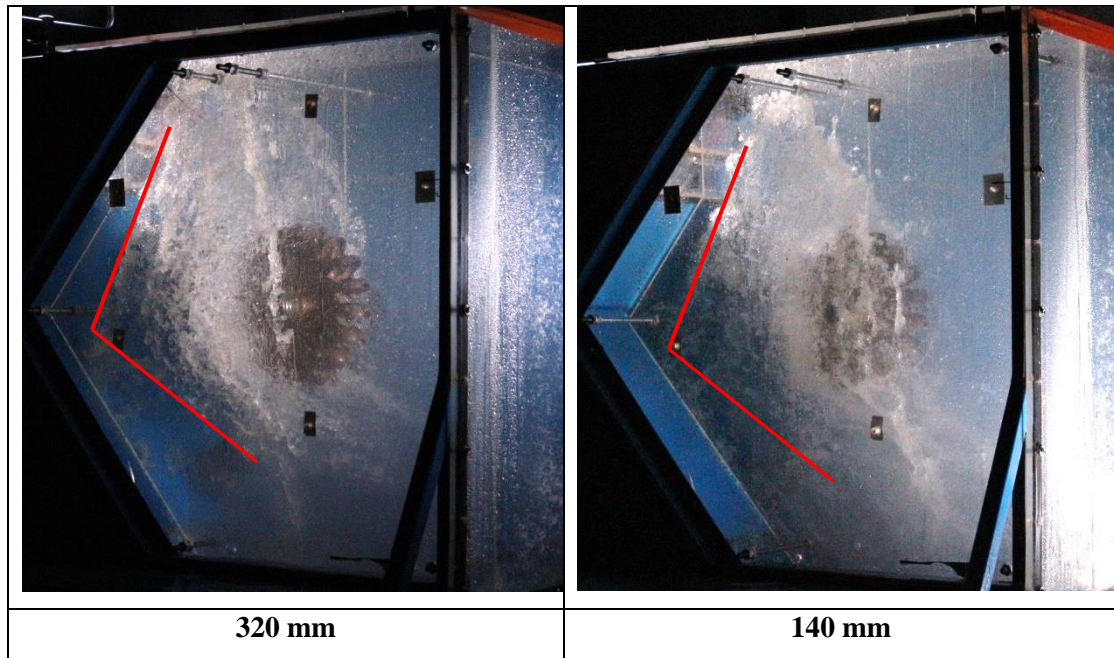


Fig. 8-13 Comparing upper jet operation for test #1 with two different casing widths

8.4.2 Analysis of Test #5

It was shown from the experimental testing at NTUA, outlined in Chapter 7 that the baffle (BAF) and sealing plate (SP) have been shown to be very effective at stopping water from flowing into the roof of the casing and falling back down onto the runner and injectors, therefore it was recommended that the casing can be brought in and the side shroud be incorporated as part of the casing wall, removing the need for the additional manufacture of the insert, hence the geometry configuration of test 5.

The casing was meshed using the ANSYS Mesher tool, following the procedure outlined in Chapter 3 and consisted of five inflation layers on all wall boundaries. The simulation was run using a conservative timestep of 3.5219×10^{-5} s, which equates to 0.2 degree rotation, for the BEP of the turbine. Similar to the CFD analysis investigating the influence of the BAF in 4.1.2, only the lower jet was simulated. Snapshots are shown from 240° rotation to 440° rotation in Fig. 8-14 - Fig. 8-16.

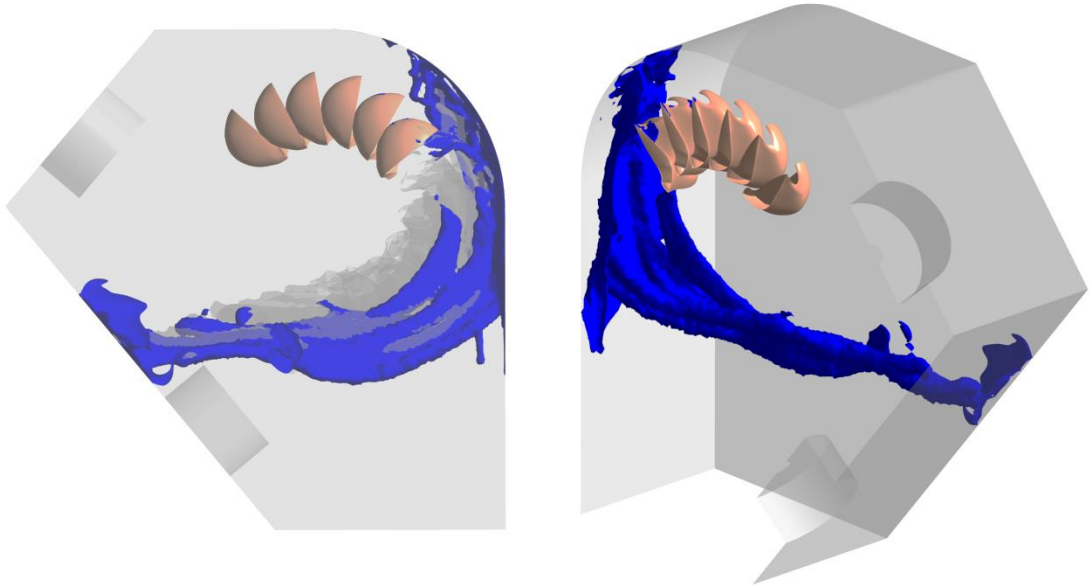


Fig. 8-14 Lancaster test # 5 lower jet: casing flow at 240° rotation

Unlike the standard casing design the curved side wall in test #5 has a smaller distance between the casing and the runner, therefore by 240° the water has already made impact and has started to travel along the curvature of the insert, as shown in Fig. 8-14.

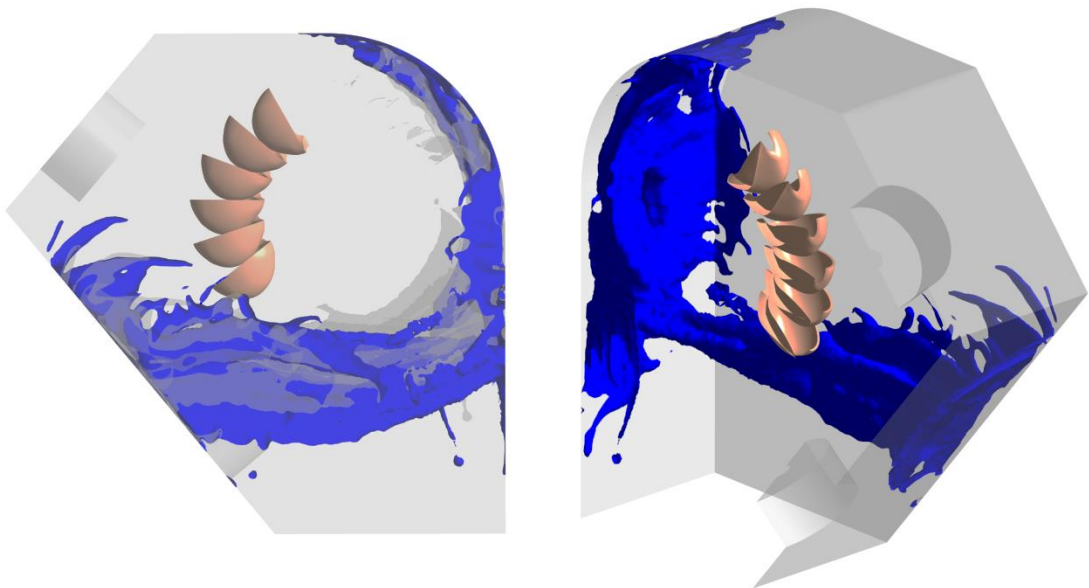


Fig. 8-15 Lancaster test # 5 lower jet: casing flow at 320° rotation

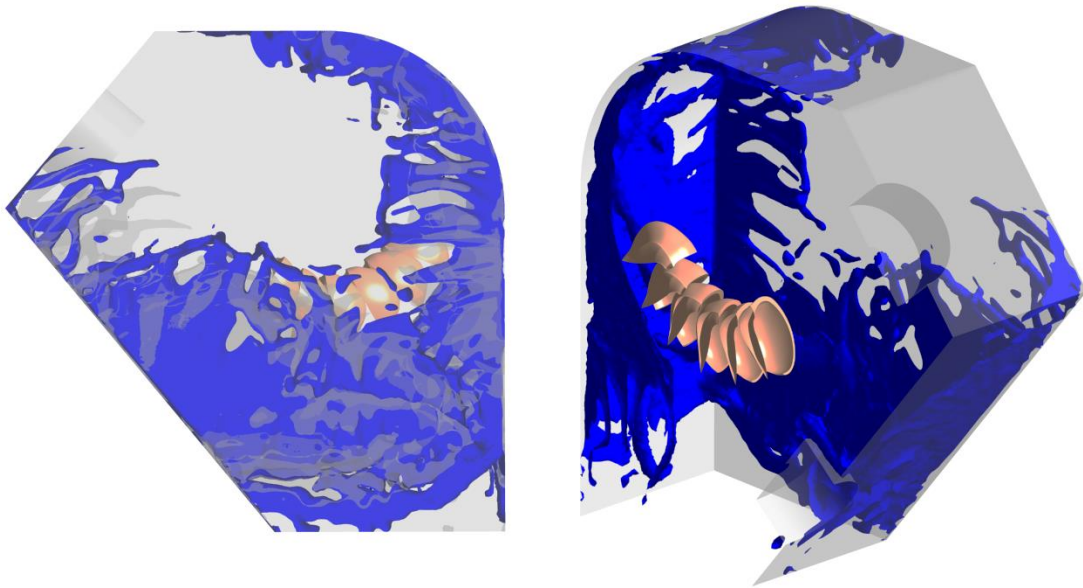


Fig. 8-16 Lancaster test # 5 lower jet: casing flow at 440° rotation

The BAF was particularly effective for lower jet operation as its position and curvature meant that the portion of flow (as highlighted in Fig. 8-17) was directed into the tailrace. The tests have shown that out of the possible casing combinations this configuration was the most efficient across the range of speeds, however due to the absence of the ‘wiper’ that sits around the runner some of the flow recirculates into the roof and falls down onto the runner in large droplets.

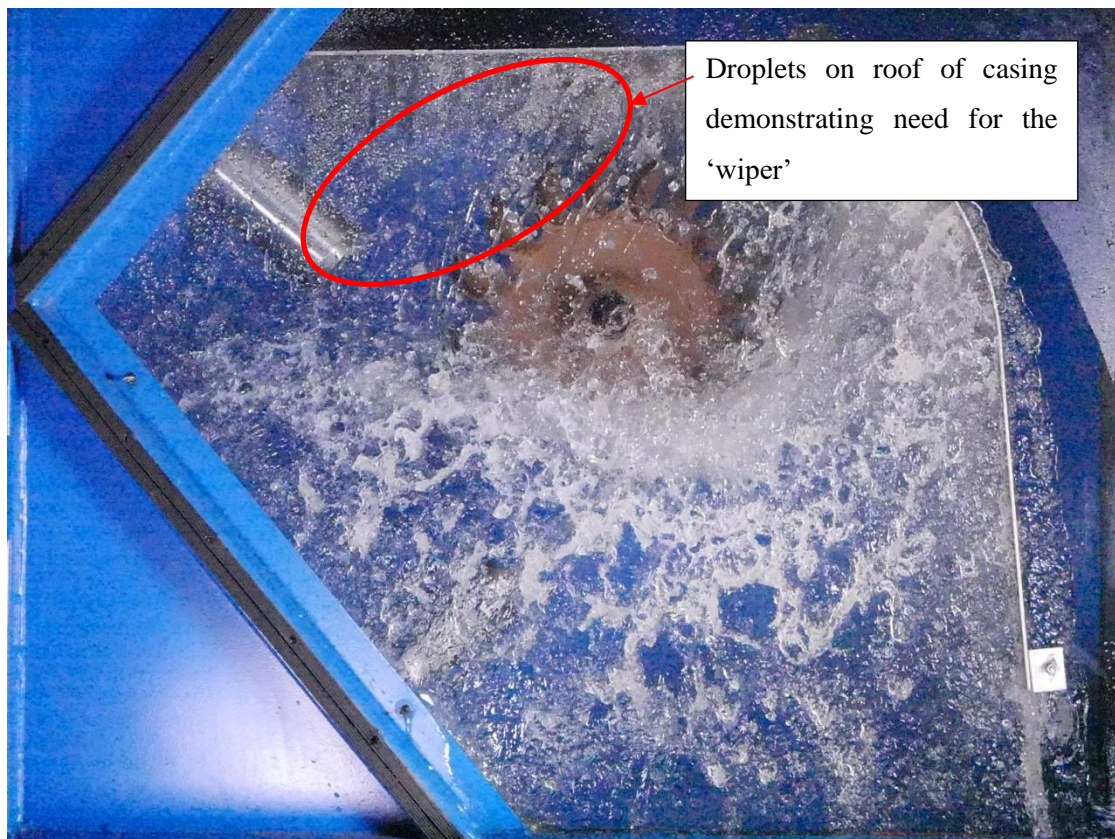


Fig. 8-17 Test # 5 lower jet operation $n_{11} = 39$

What is particularly evident from Fig. 8-17 and shown more clearly in the comparison snapshot highlighted in Fig. 8-18, is the positive role the BAF plays in moving the water which leaves the bucket through the cut-out towards the front face of the casing. This water follows the curvature of the BAF in a forward facing arc, collecting as droplets on the roof of the casing and thereby avoiding further interference with the runner and injectors.



Fig. 8-18 Comparing experimental and CFD snapshots for test #5 with lower jet

8.4.3 Analysis of Test #8

It is interesting to note that the geometry of test 8, applying a curved baffle plate on the side of the nozzles is the least efficient. The motivation for this test came from the observations of the experimental testing outlined in Chapter 7, particularly the slit line in the casing at C, where interference from the upper jet was observed. It was postulated that a curved surface would reduce this interference, however from observation it appears that the shallow slope of the curve promotes the generation of some quite large droplets, which then cascade onto the jets. Similar snapshots taken from the CFD model run for upper jet operation from 280° – 520° rotation are shown in Fig. 8-19 - Fig. 8-22.

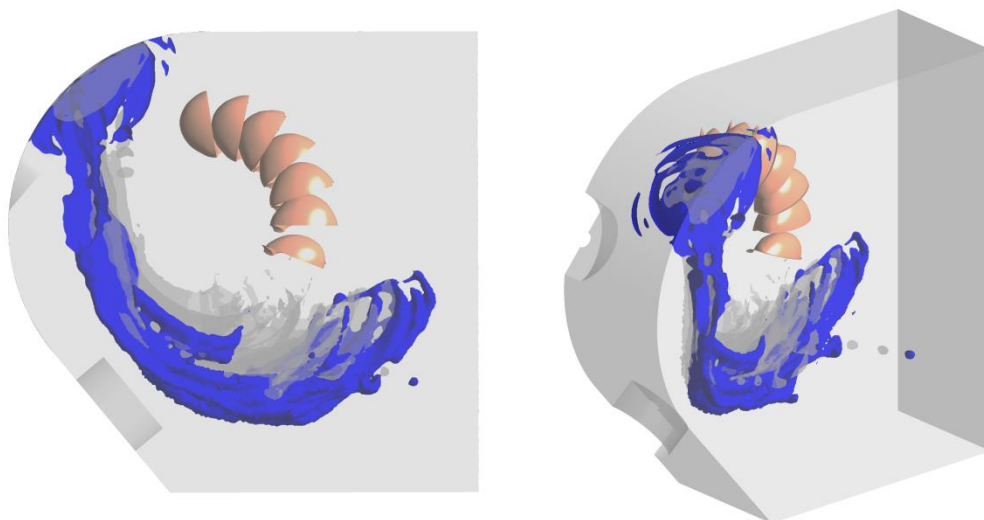


Fig. 8-19 Lancaster test # 8 upper jet: casing flow at 280° rotation

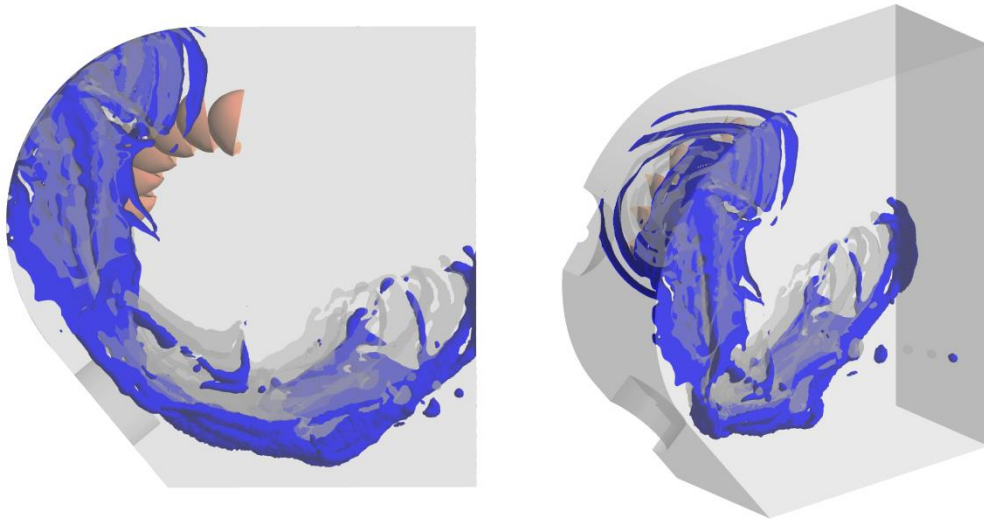


Fig. 8-20 Lancaster test # 8 upper jet: casing flow at 360° rotation

By 360° rotation a significant quantity of water has collected in the corner of the casing at A, this is in contrast to the standard case, the comparison of which is shown in Fig. 8-21, indicating that the curved side caused the impact point of the water to shift, which could cause a greater interference with the upper nozzle and injector.

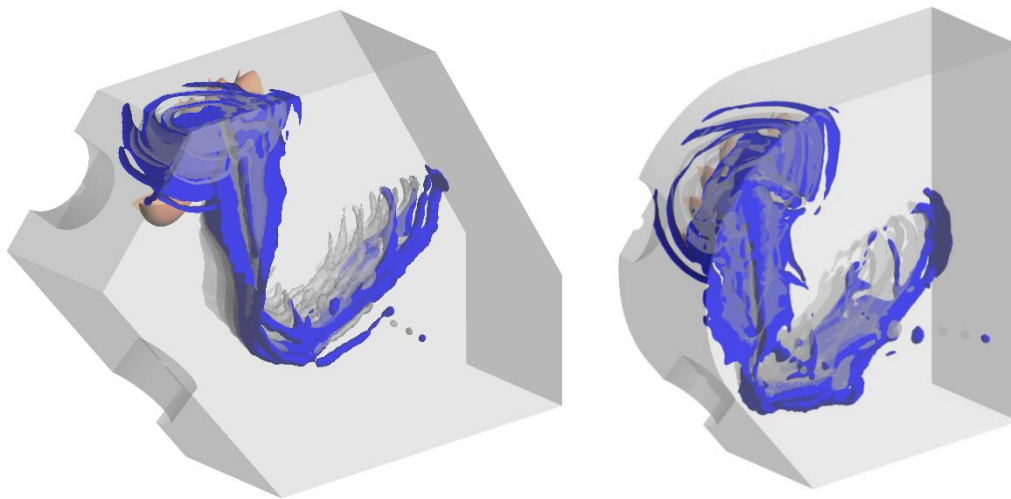


Fig. 8-21 Comparison of test #8 with standard case at 360° rotation

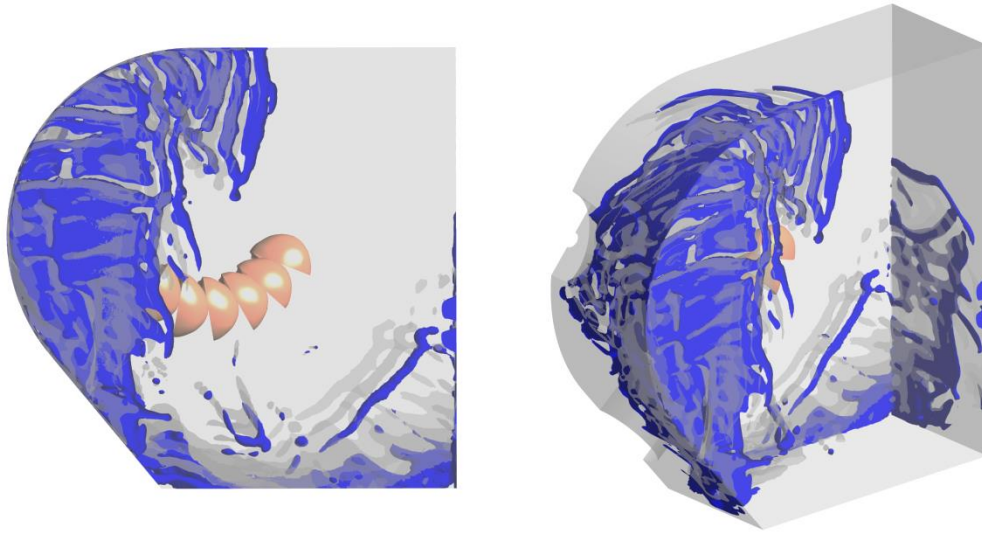


Fig. 8-22 Lancaster test # 8 upper jet: casing flow at 520° rotation

The snapshot shown in Fig. 8-22 shows large ligaments of the water in the centre of the casing cascading down in the line of the runner, this is largely due to gravitational forces now exceeding the inertial forces, these are clearly visible in the photographs taken during operation highlighted in Fig. 8-23, with red arrows tracking one of these ligaments, which breaks up into large droplets over a period of 0.008 s.

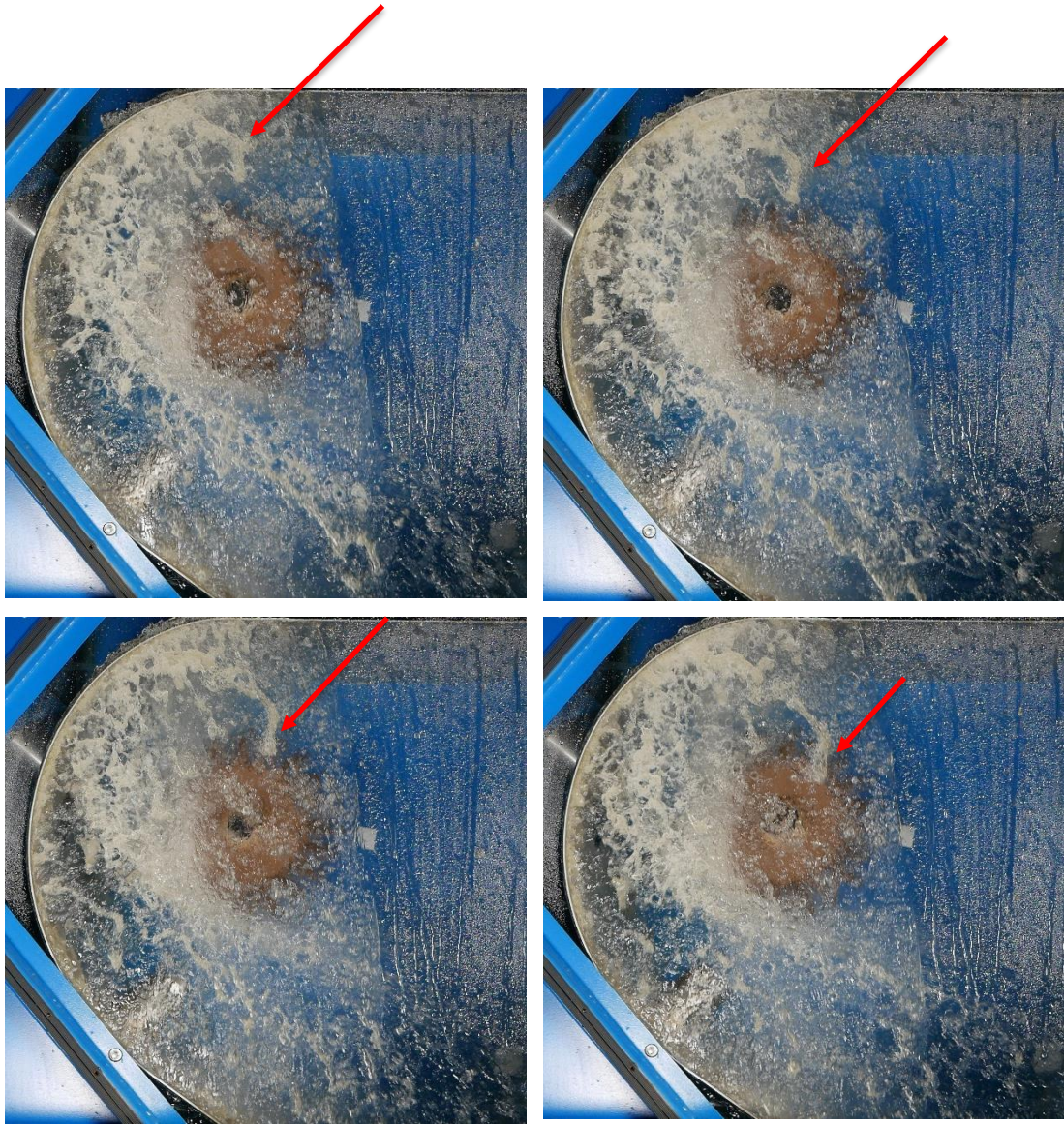


Fig. 8-23 Four photographs taken during test # 8 with upper jet showing flow progression

8.5 Summary of testing at Lancaster University

Several tests were carried out at Lancaster University on the in-house designed Pelton test rig, these included a large naked – case and several casing inserts, which were developed by the author based on experiences at NTUA, as outlined in Chapter 5. The work in this chapter has demonstrated another outlet for flow visualisation and comparative analysis with the CFD and has further outlined the methodology developed for interpreting the flow patterns and understanding the influence this has on hydraulic efficiency. A benefit of this particular test rig is that it was possible in a much more time efficient manner.

The most prominent conclusion is that a wide and tall casing, as in test #1, is the most efficient as it ensures that little to no interference with the nozzle and runner take place, this is not surprising since the ideal scenario would be to have no casing. A surprising outcome has been that the result from test #8 is the least efficient for twin and upper jet operation, this geometry

was devised based on observations made on the NTUA rig and the interaction of the flow with the split line in the casing, therefore it was hypothesised that a curved panel would be much less abrupt and reduce the splashing. However, as a result of the geometry the distance between the nozzle opening and the runner is reduced, therefore there will be greater splash back and interference. Therefore, it can be concluded is that it not about how the flow moves around the casing walls, rather the distance between the nozzles and the casing is more influential and where possible the distance between the casing and these components should be large and the nozzles be extended into the casing as far as is feasible.

9 Summary and Conclusions

The aim of the present thesis was to investigate the flow in a twin jet horizontal axis Pelton turbine. The main aim has been the development of a CFD model suitable to simulate the flow for a number of different casing configurations in a reasonable time frame. In doing so, the simulation aims to provide an overview of the design of Pelton turbine casings and the factors most important to maintaining high efficiency over a range of operating conditions.

The CFD models of the casings were based on sound methodologies that have been widely documented in the literature, in addition a number of assumptions that reduce the timescale were introduced. These assumptions were verified against computationally more demanding simulations, where available, while the whole methodology was validated experimentally.

It can be argued that the key component of the turbine and indeed the most complex to simulate is the runner, since this requires the modelling of a free surface jet interacting with a rotating runner. This is inherently a computationally demanding task as multiphase, turbulent, unsteady time dependent flow physics all need to be calculated simultaneously. For this reason there are few publications showing CFD being used for impulse turbine modelling. Therefore, the objective of present thesis introduces additional complexity since not only is the runner modelled but the casing has also been introduced, which necessitates much stricter model controls to ensure sensible simulation time as the computational domain is much larger. This also highlights the key novelty of this research.

The design basis presented in the thesis is the commercial Gilkes design incorporating the Z120 runner type. The standard Gilkes casing design incorporates a number of baffles and shrouds in order to direct the water away from the critical components, namely the runner and injectors to ensure that there is minimal compromise on efficiency from the splash water. Therefore, a systematic approach was taken where a selection of individual shrouds were added and their effect on the flow field was assessed. Likewise, the effect of varying the overall casing width has been assessed with both CFD modelling and experimental testing. Despite successive levels of mesh refinement and running the simulations for several runner rotations, the water present in the casing was found to have a negligible effect on the calculated runner torque and consequently the ability of the CFD model to quantitatively predict differences in efficiency between different casing designs is not yet possible with current computing capabilities.

Experimental testing was carried out at the Laboratory of Hydraulic Machines within the National Technical University of Athens (NTUA). Out of all of the experimental cases tested, the efficiency loss of different casing designs can be predicted and it was found to be negligible for the best case scenario (experimental test E) and 3% in the worst case scenario (experimental

test K). However, one has to take into consideration both the numerical and experimental uncertainties, which have been detailed accordingly. The experimental width testing has shown that there appears to be a generally linear decrease in efficiency with decrease in width, however a flattening of this curve towards the wider widths suggests a standard width casing (experimental test E) is close to optimum, where the effect of the casing becomes minimal. In retrospect, this result is not surprising, the Pelton turbine has historically been developed through experiment alone and one of the easiest geometrical features to alter is the casing and accordingly one can imagine that previous experience has arrived at the standard casing width via these methods. However, since no historical testing records were available this independent assessment was a necessary learning outcome and highlights a novel aspect of this work contributing to the overall knowledge of Pelton turbines and the effect of casing width on efficiency.

The secondary aim of the present thesis was to analyse the impact of the injector nozzle and spear configuration and examine the influence the obtained real-jet profiles have on runner performance. The full 3D CFD injector simulations reveal some important characteristics of the flow through the injector such as the creation of secondary cross-flow vortices after the pipe bend and their interaction with the spear holding vanes causing fragmentation into more vortices of various size and strength. They also reveal the role of the secondary velocities in the observed disturbances of the jet free surface. Furthermore, the investigation has demonstrated that injectors with noticeably steeper angles of 110° & 70° and 150° & 90° , respectively, attain a higher efficiency than the industry standard of 80° & 55° . Moreover, experimental testing of the upper jet at NTUA showed gains of $\approx 1\%$ in efficiency at the best efficiency point of the turbine can be achieved. The increase in injector efficiency obtained by using steeper nozzle and spear valve angles can also be explained by the observed reduction of the non-symmetric jet structure characteristics, which includes the secondary velocity magnitude.

Further CFD analysis of a 2-bucket runner model is carried out with four different jet configurations. In three configurations the runner has been coupled with the jet profile from the aforementioned injectors and this is compared against an ideal axisymmetric jet profile. It has been demonstrated that a higher peak torque is experienced for the Novel cases with the highest peak torque on the inside of the bucket experienced by the Novel 1 design and consequently results in a higher efficiency. The reason for this is that while the jet velocity may not be as uniform as the Novel 2 case, a more compact jet with less surface disturbance ensures a more optimal exchange of kinetic energy with the runner.

The present thesis has demonstrated some appreciable efficiency gains, both from the analysis of the nozzle and spear configuration and also by assessment of the casing design, where

experimental tests showed that the Side Shrouds (experimental tests F-H) are ineffective. These both have a commercial advantage, since altering the nozzle and spear design has little appreciable cost and removal of the Side Shrouds will reduce the materials and manufacturing time. However, one factor that has not been considered is the maintenance schedule and whether these changes will have appreciable long term effects. For example, it has been postulated that steeper angled nozzle and spear designs could lead to larger high velocity water droplet formations, which could cause erosion damage.

Overall this research has shown how CFD can be used effectively in the analysis of the flow inside Pelton turbine casings and subsequently as a design tool to offer insight into the potential negative influence of new casing designs on this flow, leading to interference and efficiency loss. The CFD tool should not however replace experimental testing but is an ideal complement to it, since in the first instance it can be used to determine design modifications warranting further experimental analysis.

Finally, the author postulates that the maximum efficiency of a Pelton turbine is likely to be no more than 95%. Even in the best case scenario there is a sacrifice in efficiency of the runner since the bucket outflow angle β_2 , which should theoretically be 180° , has to be slightly less to ensure there is little interference of the water outflow with the preceding bucket. A previous PhD project adopted a systematic approach of applying CFD to optimise the design of the runner to the current form presented in this thesis (Z120 type) and managed to improve the efficiency by 2.1% [18]. Likewise, the injectors have undergone a similarly systematic analysis of all major geometric entities and in this case an improvement of 1.8% has been obtained. Nevertheless, the predicted efficiency of the runner remains in the low 90's% region. In light of this it can be concluded that efforts to the development of the entire Pelton system should continue to focus on the improvement of the runner, injector and upstream pipework design. However it may be the case that as time and technology progress these enhancements will be very small. Furthermore, it can be argued that the understanding of the role and influence of the casing is still in the infancy and will therefore likely become the focus of the continued R&D effort in the future as up until now it has largely be overlooked.

Nevertheless, all PhD projects with a commercial sponsor fall foul of the trade-off between academic requirements and economic inevitabilities and this project is no exception. The following Chapter 12 lists the recommendations for future work, some of which will be clearly academic driven recommendations, which the sponsors may or may not pick up.

10 Recommendations for Future Work

The complexity inherent to the understanding of the full Pelton turbine calls for further investigations, both experimentally and numerically. Some will be a purely academic exercise and others will have a commercial advantage.

10.1 Turbulence Modelling and Injector Simulations

As discussed in section 7.3 it is reasonable to imagine that a degree of error will be imposed by the choice of turbulence modelling. The choice of turbulence model needs to be considered carefully and work is required to assess whether Reynolds-Averaged Navier-Stokes models, in which all the scales of the turbulence are modelled rather than solved, are capable of modelling the flow within a Pelton turbine adequately. Further research could consider Scale Resolving Simulation (SRS) options, such as Large Eddy Simulation, Scale Adoptive Simulation and Detached Eddy Simulation. Despite the computationally expensive simulations which use up large quantities of data, these models can resolve the large energy-containing scales while also modelling the influence of the small scales. The SRS method is more accurate when it is important to resolve the large scales. However, it necessitates the use of a very fine mesh and small timesteps to capture the eddy formation.

Furthermore, so far only RANS based numerical modelling of the injectors have taken place. While this is a sound methodology that has been well documented in the literature, it may be possible to obtain a more realistic picture of the injector operation by using more sophisticated techniques. High speed photography of the injectors, available from the literature, demonstrate a much more chaotic free surface and indeed under certain conditions droplets break away from the main portion of the jet. In some cases, these droplets, if significant, could lead to damage to the splitter edge or other components. Being able to fully determine the origin and mechanisms, which lead to their generation, may be crucial.

10.2 Further Analysis of the Jet – Runner Interaction

The purpose of the 3D CFD simulations of the jet – runner interaction carried out in section 6.4.2 was to enable the quantification of casing losses by investigating the differences in the absolute numerical and experimental efficiencies.

The results show an under prediction of the CFD model compared to the experimental tests, this under prediction in the numerical performance can be attributed to insufficient mesh resolution in the runner domain, particularly due to the transition from structured hexahedral cells in the injector to unstructured tetrahedral cells in the runner domain. The result of this will be an under

prediction of the shape and width of the jet as evidenced in the literature [62]. Further modelling errors were introduced by using the profile data exported from the injector simulation and imported as a boundary condition into the runner simulation. This inherently will lead to numerical diffusion as the solver attempts to interpolate cell data on mismatched cell locations in the two meshes. It is recommended that a CFD analysis of the injector including the full pipework is carried out combined with a runner simulation in order to investigate this further and to try to reduce these errors as much as possible.

10.3 Casing Simulations

A key learning outcome from the PhD has been that predicting casing losses numerically is not a trivial task and requires a great deal of patience. Indeed establishing losses due to different casing designs has not been possible with the current CFD methodology²⁰. It may be foreseeable that in the future, with much more refined meshes and improved computer hardware, that the full runner and several runner rotations could enable the quantification of the influence of the splash water on efficiency.

10.4 Further Experimental Testing of Casing Widths

The most promising outcome of the PhD project was the analysis of casing width and the effect this has on the efficiency explored in section 5.3.3. Current classical guidelines on the optimum casing width are based on theoretical assumptions that inevitably include simplifications of complex flow behaviour in the runner and casing. There is a lack of guidelines that were based on experimental or CFD studies. It has been demonstrated experimentally that there is generally a linear trend between reducing width and decreasing efficiency, however the results presented in this thesis showed that there appears to be a peak in this trend, suggesting that beyond certain widths the effect of the casing is minimal. Therefore, repeat and further experimental testing is proposed in order to further verify the casing effects. Hence, the optimum design of the casing is an important issue, in order to minimise such interference and at the same time to reduce as much as possible the material volume and cost of the casing.

10.5 Nozzle and Spear Combinations and Jet Locations

Some initial experimental work not covered in this thesis has shown some promising results regarding the use of different combinations of Novel injector designs for the upper and lower jet. Indeed, the real jet simulations have shown how one particular phenomena, i.e. the bead

²⁰ As noted in the literature review, researchers from Andritz Hydro, who used SPH particle based methodology came to the same conclusions [72]

generation on the underside of the jet as a result of the secondary flow velocities generated by the pipework bend, plays a different role depending on location, i.e. pipework arrangement, which differs for the upper or lower jet operation. This should be explored further by carrying out additional and repeat experimental testing.

Future studies may consider different pipework arrangements in order to reduce the induced secondary velocities and losses experienced through the injectors. For example, currently the Pelton pipework layout consists of the branch pipe and bifurcator all being perpendicular to the runner shaft, however for the Turgo turbine these are in-line with the turbine shaft and bend around the generator. It is very likely that the reason for this is due to cost implications to ensure that the turbine house remains small. It is recommended that a more complete 3D CFD analysis of the injectors could be carried out including the current and different upstream pipework in order to determine if alternative pipework layouts should be considered.

Furthermore, state of the art Pelton turbines now fit the nozzles in such a way that the main splash water outflow is directed downwards to the tailrace channel indicating that further work needs to be carried out to determine the ideal compromise between injector location and casing design. In any casing if the outflow from the bucket has an upwards direction, this can reflect on the housing and partially hit the runner, causing a strong decrease of power output.

References

- [1] United Nations Framework Convention on Climate Change, “The Paris Agreement,” 10 04 2017. [Online]. Available: http://unfccc.int/paris_agreement/items/9485.php. [Accessed 16 05 2017].
- [2] The World Bank Group, “Hydropower in Vietnam: The right way to do it,” 18 08 2016. [Online]. Available: <http://blogs.worldbank.org/climatechange/hydropower-vietnam-right-way-do-it>. [Accessed 16 05 2017].
- [3] Hydro Review, “Small Hydro,” [Online]. Available: <https://www.hydroworld.com/industry-news/small-hydro.html>. [Accessed 03 09 2018].
- [4] ITAIPU Binacional, “Itaipu ends 2016 with a historic production of 103.09 million MWH,” [Online]. Available: <https://www.itaipu.gov.br/en/press-office/news/itaipu-ends-2016-historic-production-10309-million-mwh>. [Accessed 03 09 2018].
- [5] M. Nechleba, Hydraulic Turbines: Their Design and Equipment, Prague: Artia, 1957.
- [6] L. A. Pelton, “Water Wheel”. United States of America Patent 233,692, 26 10 1880.
- [7] Gilbert Gilkes & Gordon Ltd, “Gilkes Turgo Impulse Hydro Turbine,” [Online]. Available: http://www.gilkes.com/user_uploads/turgo%20paper2.pdf.
- [8] G. A. Aggidis and A. Zidonis, “Hydro turbine prototype testing and generation of performance curves: fully automated approach,” *Renewable Energy*, vol. 71, pp. 433-441, 2014.
- [9] A. Zidonis, D. S. Benzon and G. A. Aggidis, “Development of hydro impulse turbines and new opportunities,” *Renewable and Sustainable Energy Reviews*, vol. 51, pp. 1624-1635, 2015.
- [10] A. Zidonis and G. A. Aggidis, “State of the art in numerical modelling of Pelton turbines,” *Renewable and Sustainable Energy Reviews*, vol. 45, pp. 135-144, 2015.
- [11] T. Staubli, A. Abgottspon, P. Weibel, C. Bissel, E. Parkinson, J. Leduc and F. Leboeuf, “Jet quality and Pelton Efficiency,” in *Proceedings of Hydro 2009*, Lyon, 2009.

- [12] A. Zidonis, A. Panagiotopoulos, G. Aggidis, J. S. Anagnostopoulos and D. E. Papantonis, "Parametric optimisation of two Pelton turbine runner designs using CFD," *Journal of Hydrodynamics*, vol. 27, no. 3, pp. 403-412, 2015.
- [13] C. Vessaz, L. Andolfatto, F. Avellan and C. Tournier, "Towards design optimization of a Pelton turbine runner," *Structural and Multidisciplinary Optimization*, vol. 55, no. 1, pp. 37-51, 2017.
- [14] B. W. Solemslie and O. G. Dahlhaug, "A reference pelton turbine - design and efficiency," *IOP Conf. Ser: Earth and Environ. Sci.*, vol. 22, p. 012004, 2014.
- [15] T. Staubli, P. Weibel, C. Bissel, A. Karakolcu and U. Bleiker, "Efficiency increase by jet quality improvement and reduction of splashing water in the casing of Pelton turbine," in *16th International Seminar on Hydropower Plants*, Vienna, 2010.
- [16] R. W. Shortridge, "Lester Pelton and his Water Wheel," 1989. [Online]. Available: <https://www.hydroworld.com/content/dam/hydroworld/downloads/Q%26Aturbine4.pdf>. [Accessed 2018 09 03].
- [17] L. F. Barstad, "CFD Analysis of a Pelton Turbine," Norwegian University of Science and Technology, Trondheim, 2012.
- [18] A. Zidonis, "Optimisation and efficiency improvement of Pelton hydro turbine using computational fluid dynamics and experimental testing," Lancaster University, Lancaster, 2015.
- [19] P. Stein, "Numerical Simulation and Investigation of Draft Tube Vortex FLOW," Coventry University , Coventry, 2007.
- [20] Z. Zhang, *Pelton Turbines*, Springer International Publishing, 2016.
- [21] E. Mosonyi, *Water Power Development Vol B: High-Head Power Plants*, Budapest: Akademiai Kiado, 1991.
- [22] R. S. R. Gorla and A. A. Khan, *Turbomachinery: Design and Theory*, New York: Marcel Dekker, 2003.

- [23] V. Gupta and V. Prasad, "Numerical Investigations for Jet Flow Characteristics on Pelton Turbine Bucket," *International Journal of Emerging Technology and Advanced Engineering*, vol. 2, no. 7, pp. 364-370, 2012.
- [24] P. Bachman, C. Schaerer, T. Staubli and Vullioud, "Experimental flow studies on a 1-jet model Pelton turbine," in *Proceedings of the 15h IAHR Symposium on Hydraulic Machinery, Equipment and Cavitation*, Belgrade, 1990.
- [25] F. David, "Experimental Investigation On Suspended Sediment, Hydroabrasive Erosion And Efficiency Reductions Of Coated Pelton Turbines," ETH Zurich, Zurich, 2017.
- [26] A. Perrig, "Hydrodynamics of the Free Surface Flow in Pelton Turbine Buckets," Ecole Polytechnique Federale de Lausanne, Lausanne, 2007.
- [27] A. Rai , A. Kumar and T. Staubli, "Hydro-abrasive erosion in Pelton buckets: Classification and field study," *Wear*, Vols. 392-393, pp. 8-20, 2017.
- [28] G. K. Batchelor, *An Introduction to Fluid Dynamics*, Cambridge University Press, 2012.
- [29] "Diary of a Powerspout Installation," [Online]. Available: <https://water-to-wire.blogspot.co.uk/search/label/Windage>. [Accessed 16 04 2018].
- [30] K. Bergeles, "Liquid Atomisation Processes in the Crankcase of an IC Engine: A computational and experimental study," Imperial College, London, 2017.
- [31] J. Leduc, "Etude physique et numerique de l'ecoulement dans un dispositif d'injection de turbine Pelton," Ecole Centrale de Lyon, Lyon, 2010.
- [32] A. R. Frost, "Rotary atomization in the ligament formation mode," *Journal of Agricultural Engineering Research*, vol. 26, no. 1, pp. 63-78, 1981.
- [33] N. Ashgriz, *Handbook of atomization and sprays*, Springer, 2011.
- [34] J. Liu, Q. Yu and Q. Guo, "Experimental investigation of liquid disintegration by rotary cups," *Chemical Engineering Science*, vol. 73, pp. 44-50, 2012.
- [35] M. Brocchini and D. H. Peregrine, "The dynamics of strong turbulence at free surfaces. Part 1. Description," *Journal of Fluid Mechanics*, vol. 449, pp. 225-254, 2001.

- [36] D. P. Busker and A. P. Lamers, "The non-linear breakup of an inviscid liquid jet," *Fluid Dynamics Research*, vol. 5, no. 3, pp. 159-172, 1989.
- [37] F. Savart, "Memoire sur le choc d'une veine liquide lancee sur un plan circulaire," *Ann. Chem Phys*, vol. 53, pp. 177-386, 1833 .
- [38] L. Rayleigh, "On the Instability of Jets," *Proceedings of the London Mathematical Society*, vol. 1, no. 1, pp. 4-13, 1878.
- [39] N. I. Kolev, "Liquid and gas jet disintegration," in *Multiphase Flow Dynamics 2*, Springer, 2012, pp. 287-210.
- [40] M. J. McCarthy and N. A. Molloy, "Review of Stability of Liquid Jets and the Influence of Nozzle Design," *The Chemical Engineering Journal*, vol. 7, pp. 1-20, 1974.
- [41] M. Birouk and N. Lekic, "Liquid Jet Breakup in Quiescent Atmosphere: A Review," *Atomization and Sprays*, vol. 19, no. 6, pp. 501-528, 2009.
- [42] J. W. Hoyt and J. J. Taylor, "Waves on water jets," *Journal of Fluid Mechanics*, vol. 83, no. 1, pp. 119-127, 1977.
- [43] T. Staubli and H. P. Hauser, "Flow Visualization - A Diagnosis Tool for Pelton Turbines," in *IGHM*, Lucerne, 2004.
- [44] M. Peron, E. Parkinson, L. Geppert and T. Staubli, "Importance of Jet Quality on Pelton Efficiency and Cavitation," in *IGHM*, Milan, 2008.
- [45] Z. Zhang and M. Casey, "Experimental studies of the jet of a Pelton Turbine," *Proceeding of the Institution of Mechanical Engineers, Part A: Journal of Power and Energy*, vol. 221, pp. 1181-1192, 2007.
- [46] Z. Zhang and E. Parkinson, "LDA Application and the dual-measurement method in experiemental investigations of the free surface jet at a model nozzle of a Pelton Turbine," in *Proceedings of the 11th International Symposium on Applications of laser anemonometry to fluid mechanics*, Lisbon, Portugal, 2002.
- [47] Z. Zhang, "Dual-Measurement-Method and its extension for accurately resolving the secondary flows in LDA (Laser Doppler Anemometry) applications," *Flow Measurement and Instrumentation*, vol. 16, pp. 57-62, 2005.

- [48] T. Staubli, "Die Auswirkung der Strahlqualität auf den Wirkungsgrad von Pelton-turbinen," *Wasser Energie*, vol. 101, no. 3, 2009.
- [49] J. Leduc, "Theoretical and numerical analysis of a Pelton turbine jet," Ecole Centrale de Lyon, Lyon, 2007.
- [50] R. Fiereder, S. Riemann and R. Schilling, "Numerical and experimental investigation of the 3D free surface flow in a model Pelton turbine," in *25th IAHR Symposium on Hydraulic Machinery and Systems*, Timisoara, 2010.
- [51] M. Gass, "Mechanical Rehabilitation: Lessons Learned at Moccasin Powerhouse," *Hydro Review*, pp. 10-12, 2003.
- [52] M. Gass, "Modification of Nozzles for The Improvement of Efficiency of Pelton Type Turbines," in *Hydrovision*, Portland , 2002.
- [53] F. Avellan, P. Dupont, S. Kvicinsky, L. Chapuis, E. Parkinson and G. Vullioud, "Flow calculations in Pelton turbines - part 2: Free surface flows," in *Proceedings of the 19th IAHR Symposium on Hydraulic machinery and cavitation*, Singapore, 1998.
- [54] S. Kvicinsky, "Methode d'analyse des 'écoulements 3D a surface libre: application aux turbines Pelton," Ecole Polytechnique Federale de Lausanne, Lausanne, 2002.
- [55] S. Kvicinsky, J. L. Kueny and F. Avellan, "Free surface flows: experimental validation of volume of fluid (VOF) method in the plane wall case," in *Proceedings of the 3rd ASME/JSME Joint Fluids Engineering Conference*, San Francisco, 2002.
- [56] B. Zoppe, C. Pellone, T. Maitre and P. Leroy, "Flow analysis inside a Pelton turbine bucket," *Trans. AMSE J. Turbomachinery*, vol. 128, pp. 500-511, 2006.
- [57] A. Perrig, F. Avellan, J. L. Kueny, M. Farhat and E. Parkinson, "Flow in a Pelton turbine bucket: numerical and experimental investigation," *ASME J. Fluids Eng.*, vol. 128, no. 4, pp. 350-358, 2006.
- [58] V. Gupta, V. Prasad and R. Khare, "Numerical simulation of six jet Pelton turbine model," *Energy*, vol. 104, pp. 24-32, 2016.

- [59] P. K. Koukouvini, "Development of a meshfree particle method for the simulation of steady and unsteady free surface flows: application and validation of the method on impulse hydraulic turbines," National Technical University Athens, Athens, 2012.
- [60] B. W. Solemslie, "Experimental methods and design of a Pelton bucket," Norwegian University of Science and Technology, Trondheim, 2016.
- [61] A. Santolin, G. Cavazzini, G. Ardizzon and G. Pavesi, "Numerical investigation of the interaction between jet and bucket in a Pelton turbine," *Proc. Inst. Mech. Eng. Part A: Journal of Power and Energy*, vol. 223, pp. 721-728, 2009.
- [62] D. Jost, P. Mezner and A. Lipej, "Numerical prediction of Pelton turbine efficiency," *IOP Conf. Ser.: Earth and Environ. Sci.*, vol. 12, p. 012080, 2010.
- [63] Y. Xiao, T. Cui, Z. Wang and Z. Yan, "Numerical and experimental analysis of the hydraulic performance of a prototype Pelton turbine," *IOP Conference Series: Earth and Environmental Science*, vol. 15, no. 5, p. 042033, 2012.
- [64] X. Z. Wei, K. Yang, H. J. Wang, R. Z. Gong and D. Y. Li, "Numerical investigation for one bad-behaved flow in Pelton turbine," *IOP Conference Series: Materials Science and Engineering*, vol. 72, no. 4, p. 042033, 2015.
- [65] M. Sick, E. Keck, E. Parkinson and G. Vullioud, "New Challenges in Pelton Research," in *Proceedings of Hydro 2000*, Bern, 2000.
- [66] J. R. Rygg, "CFD Analysis of a Pelton Turbine in OpenFOAM," Norwegian University of Science and Technology, Trondheim, 2013.
- [67] OpenFOAM Foundation, "OpenFOAM User Guide, Version 2.1.1," 2012.
- [68] L. Quartz and K. Meerwarth, *Wasserkraftmaschinen: Eine Einführung in Wesen, Bau und Berechnung von Wasserkraftmaschinen und Wasserkraftanlagen*, Berlin und Heidelberg: Springer-Verlag, 1963.
- [69] J. Raabe, *Hydraulische Maschinen und Anlagen. Teil 2 Wasserturbinen*, Düsseldorf: VDI-Verlag, 1970.
- [70] J. Giesecke, S. Heimerl and E. Mosonyi, *Wasserkraftanlagen: Planung, Bau und Betrieb*, Berlin Heidelberg: Springer-Verlag, 2014.

- [71] H. B. Matthias, J. Prost and C. Rossenger, "Investigation of the Flow in Pelton Turbines and the Influence of Casing," *International Journal of Rotating Machinery*, vol. 3, no. 4, pp. 239-247, 1997.
- [72] B. List, J. Prost and H. B. Matthias, "Using PIV on the splash water in a Pelton turbine," in *Proceedings of the International Measurement Confederation World congress*, Vienna, 2000.
- [73] Gilbert Gilkes and Gordon Ltd, "Streamline Turbine Range," 2017. [Online]. Available: <http://www.gilkes.com/Streamline-Turbine-Range>. [Accessed 17 05 2017].
- [74] C. Vessaz, "Finite particle flow simulation of free jet deviation by rotating Pelton buckets," Ecole Polytechnique Federale de Lausanne, Lausanne, 2015.
- [75] J. C. Marongiu, F. Leboeuf and E. Parkinson, "Numerical simulation of the flow in a Pelton turbine using the meshless method smoothed particle hydrodynamics: a new simple solid boundary treatment," *Proc. Inst. Mech. Eng. Part A: Journal of Power and Energy*, vol. 221, pp. 849-856, 2007.
- [76] J. C. Marongiu, F. Leboeuf, J. Caro and E. Parkinson, "Free surface flows simulations in Pelton turbines using an hybrid SPH-ALE method," *Journal of Hydraulic Research*, vol. 48, pp. 40-49, 2010.
- [77] M. Neuhauser, F. Leboeuf, J. C. Marongiu, E. Parkinson and D. Robb, "Simulations of Rotor-Stator Interactions with SPH-ALE," in *Advances in Hydroinformatics: SIMHYDRO 2012 - New Frontiers of Simulation*, Springer Hydrogeology, 2012, pp. 349-361.
- [78] M. Rentschler, M. Neuhauser, J. C. Marongiu and E. Parkinson, "Understanding casing flow in Pelton turbines by numerical simulation," *IOP Conf. Seri.: Earth Environ. Sci*, vol. 49, p. 022004, 2016.
- [79] M. Neuhauser, "Development of a coupled SPH-ALE/Finite Volume method for the simulation of transient machines," Ecole Centrale de Lyon, Lyon, 2014.
- [80] J. Anderson, *Computational Fluid Dynamics: The basics with applications*, McGraw Hill, 1985.

- [81] S. Rane, "Grid generation and CFD analysis of variable geometry screw machines," City University, London, 2015.
- [82] ANSYS Inc, "ANSYS Fluent Theory Guide, Release 17.2," ANSYS Inc, Canonsburg, USA, 2016.
- [83] W. E. Schiesser, *The Numerical Method of Lines*, Academic Press, 1991.
- [84] H. Rusche, "Computational Fluid Dynamics of Dispersed Two-Phase Flows at High Phase Fractions," University of London, London, 2002.
- [85] R. Courant, E. Issacson and M. Rees, "On the solution of nonlinear hyperbolic differential equations by finite differences," *Communications of Pure and Applied Mathematics*, vol. 5, pp. 243-255, 1952.
- [86] S. Patankar and D. Spalding, "A calculation procedure for heat, mass and momentum transfer in three-dimensional parabolic flows," *Int. J. Heat Mass Transf.*, vol. 15, pp. 1787-1806, 1972.
- [87] L. Richardson, *Weather prediction by numerical process*, Cambridge University Press, 1922.
- [88] H. Versteeg and W. Malalasekera, *An introduction to Computational Fluid Dynamics: The Finite Volume Method*, Pearson Education Ltd, 2007.
- [89] A. Dewan, *Models Based on Boussinesq Approximation*. In: *Tackling Turbulent Flows in Engineering*, Berlin: Springer, 2011.
- [90] F. R. Menter, "Two-equation eddy-viscosity turbulence models for engineering applications," *AIAA*, vol. 32, no. 8, pp. 1598-1605, 1994.
- [91] D. C. Wicox, "Simulation of Transition with a Two-Equation Turbulence Model," *AIAAJ*, vol. 32, no. 2, pp. 247-255, 1994.
- [92] R. Scardovelli and S. Zaleski, "Direct numerical simulation of free-surface and interfacial flow," *Annual Review of Fluid Mechanics*, vol. 31, no. 1, pp. 567-603, 1999.
- [93] S. Osher and R. P. Fedkiw, "Level set methods: an overview and some recent results," *Journal of Computational Physics*, vol. 169, no. 2, pp. 463-502, 2001.

- [94] M. Shams, "Modelling two-phase flow at the micro-scale using a volume-of-fluid method," Imperial College, London, 2018.
- [95] C. W. Hirt and B. D. Nichols, "Volume of Fluid (VOF) Method for the Dynamics of Free Boundaries," *Journal of Computational Physics*, vol. 39, no. 1, pp. 201-225, 1981.
- [96] D. Benzon, A. Zidonis, A. Panagiotopoulos, G. Aggidis, J. S. Anagnostopoulos and D. E. Papantonis, "Impulse turbine injector design improvement using Computational Fluid Dynamics," *ASME J. Fluids Eng*, vol. 137, no. 4, p. 041106, 2015.
- [97] D. Benzon, A. Zidonis, A. Panagiotopoulos, G. Aggidis, I. Anagnostopoulos and D. Papantonis, "Numerical investigation of the spear valve configuration on the performance of Pelton and Turgo turbine injectors and runners," *ASME J. Fluids Eng*, vol. 137, no. 11, p. 111201, 2015.
- [98] D. S. Benzon, "The Turgo impulse turbine; a CFD based approach to the design improvement with experimental validation," Lancaster University, Lancaster, 2016.
- [99] B. E. Launder and D. B. Spalding, "The Numerical Computation of Turbulent Flows," *Computer Methods in Applied Mechanics and Engineering*, vol. 3, pp. 269-289, 1974.
- [100] Pointwise, "Online yplus calculator," [Online]. Available: <http://www.pointwise.com/yplus/>. [Accessed 24 01 2017].
- [101] J. U. Brackbill, D. B. Kothe and C. Zemach, "A Continuum Method for Modeling Surface Tension," *Journal of Computational Physics*, vol. 100, no. 2, pp. 335-354, 1992.
- [102] I. Malgarinos, N. Nikolopoulos and M. Gavaises, "Coupling a local adaptive grid refinement technique with an interface sharpening scheme for the simulation of two-phase flow and free-surface flows using VOF methodology," *Journal of Computational Physics*, vol. 300, pp. 732-753, 2015.
- [103] P. J. Roache, "Perspective: A Method for Uniform Reporting of Grid Refinement Studies," *ASME J. Fluids Eng.*, vol. 116, pp. 405-413, 1994.
- [104] NASA National Program for Applications-Orientated Research in CFD, "Examining Spatial (Grid) Convergence," [Online]. Available:

<https://www.grc.nasa.gov/www/wind/valid/tutorial/spatconv.html>. [Accessed 15 01 2018].

- [105] Z. Zhang, *LDA Application Methods - Laser Doppler Anemometry for Fluid Dynamics*, Springer, 2010.
- [106] M. Raffel, C. E. Willert, S. Wereley and J. Kompenhans, *Particle Image Velocimetry A Practical Guide*, Springer, 2007.
- [107] T. Kumashiro, H. Fukuhara and K. Tani, “Unsteady CFD simulation for bucket design optimization of Pelton turbine runner,” *IOP Conf. Ser.: Earth and Environ. Sci*, vol. 49, p. 022003, 2016.
- [108] International Electrotechnical Commission, “Hydraulic turbines, storage pumps and pump-turbines - Model acceptance tests,” IEC, 1999.
- [109] A. Zidonis, S. Benzon, A. Panagiotopoulos, S. Petley, G. A. Aggidis, I. Anagnostopoulos and D. Papantonis, “Experimental investigation and analysis of the spear valve design on the performance of Pelton turbines: 3 case studies,” in *Hydro*, Seville, 2017.
- [110] A. Zidonis and G. Aggidis, “Pelton turbine: Identifying the optimum number of buckets using CFD,” *Journal of Hydrodynamics*, vol. 2, no. 1, pp. 75-83, 2016.
- [111] Z. Chongji , X. Yexiang, X. Wei, W. Tao, Z. Jin and W. Zhengwei, “Numerical Analysis of Pelton Nozzle Jet Flow Behavior Considering Elbow Pipe,” *IOP Conf. Ser.: Earth and Environ. Sci*, vol. 49, p. 022005, 2016.
- [112] G. A. Aggidis and R. Cattley, “Fastening of Pelton turbine buckets”. European Patent 1452731, September 2004.
- [113] Gilbert Gilkes and Gordon Ltd, “Technical Design Manual Section 820 Horizontal Shaft Pelton Turbines,” 2015.
- [114] SKF Group, “SKF Bearing Calculator,” [Online]. Available: <http://webtools3.skf.com/BearingCalc/>. [Accessed 15 05 2018].
- [115] J. F. Gülich, *Centrifugal pumps*, 2nd ed., Berlin: Springer, 2010.

- [116] NASA, “Uncertainty and Error in CFD Simulations,” 2008. [Online]. Available: <https://www.grc.nasa.gov/www/wind/valid/tutorial/errors.html>. [Accessed 9 August 2017].
- [117] E. Parkinson, C. Neury, H. Garcin, C. Vullioud and T. Weiss , “Unsteady analysis of a Pelton runner with flow and mechanical simulation,” *International Journal on Hydropower and Dams*, vol. 13, no. 2, pp. 101-105, 2006.
- [118] J. Erlach and P. Erlach, “The first up to Six Jets Horizontal Pelton Turbine,” in *Hidroenergia*, Istanbul, 2014.
- [119] NASA, “Speed of Sound,” [Online]. Available: <https://www.grc.nasa.gov/www/k-12/airplane/sound.html>. [Accessed 15 01 2019].
- [120] J. D. Anderson, Fundamentals of Aerodynamics, McGraw Hill, 2007.
- [121] I. Babuska and J. T. Oden, “Verification and validation in computational engineering and science: basic concepts,” *Computer Methods in Applied Mechanics and Engineering*, vol. 193, pp. 4057-4066, 2004.